The Dissertation Committee for Jose Sergio de Araujo Cavalcante Filho certifies that this is the approved version of the following dissertation:

Mobility Control of Gas Injection in Highly Heterogeneous and Naturally Fractured Reservoirs

APPROVED BY

SUPERVISING COMMITTEE:

Kamy Sepehrnoori, Supervisor

Mojdeh Delshad

Kishore Mohanty

Lee Chin

Ali Moinfar

Mobility Control of Gas Injection in Highly Heterogeneous and Naturally Fractured Reservoirs

by

Jose Sergio de Araujo Cavalcante Filho, B.S.; M.S.

DISSERTATION

Presented to the Faculty of the Graduate School of

The University of Texas at Austin

in Partial Fulfillment

of the Requirements

for the Degree of

DOCTOR OF PHILOSOPHY

THE UNIVERSITY OF TEXAS AT AUSTIN

May 2016

To my beloved wife Cristiane, my daughter Beatriz, and my son Bernardo, for their love, patience and support.

To my parents Jose Sergio (Cel Cavalcante) and Leonia, for their continuous effort in guiding, educating and orienting since my first steps.

To my grandfather Waldemar Cavalcante (in memoriam), for his example of strength and perseverance.

Acknowledgments

I would like to express my appreciation and gratitude to my advisor, Dr. Kamy Sepehrnoori. More than an advisor, he has been a mentor who helped me to succeed not only academically but personally. I am proud to have been part of such a friendly and cooperative research group.

Technical advices given by Dr. Mojdeh Delshad, Dr. Kishori Mohanty, and Dr. Francisco Marcondes have been a great help in understanding mobility control using foaming agents in heterogeneous reservoirs. I would like to thank other members of my dissertation committee, Dr. Lee Chin and Dr. Ali Moinfar, for their time and effort to participate in my committee and review my dissertation.

I am particularly grateful by the assistance given by Dr. Jalil Varavei, on the development of the last chapter of this dissertation, and Dr. Chowdhurry Mamun, on the revision of my papers and my dissertation.

Technical discussions with my friends and office-mates were of great importance for the development of this dissertation. I express my gratitude to Rodolfo Victor, Elton Ribeiro, and Rahul Verma for their invaluable technical discussions during the courses and qualifying exams. I would like to thank Dr. Aboulghasem Kazemi-Nia, Dr. Hamid Lashgari, Dr. Emad Waleed, Mahmood Shakiba, and Yifei Xu for our discussions on numerical methods and reservoir simulation.

I am grateful to the staff of the Department of Petroleum and Geosystem engineering for their technical and administrative support.

This work was only possible thanks to the financial support provided by PETROBRAS. I acknowledge PETROBRAS and STATOIL for providing some of

the data used in this dissertation.

My deepest gratitude belongs to my beloved wife, Cristiane, who helped me in every step of this journey. Thanks for your patience and understanding during my absences. As in her own words, what started as the dream of an individual became the goal of a whole family, our family. I cannot forget to thank my daughter, Beatriz, the 11 months beautiful baby girl who moved with us to a foreign country and helped us to live and learn the American culture from her own experiences. Last, but not least, thanks to my younger son, Bernardo, for arriving at this family and for bringing so much joy and love. I love y'all!

Special thanks for those who guided and educated since my first steps, my father Jose Sergio (Cel Cavalcante) and my mother Leonia. Your examples lead me on the right path and that path brought me to this moment. Thank you for all your love and understanding. I also would like to thank my sisters Liane, Debora, and Camila.

I also thank God for the blessing of life, my family and my work; faith keeps me calm and gives me the equilibrium and patience required during hard times.

Mobility Control of Gas Injection in Highly Heterogeneous and Naturally Fractured Reservoirs

Publication No. _____

Jose Sergio de Araujo Cavalcante Filho, Ph.D.
The University of Texas at Austin, 2016

Supervisor: Kamy Sepehrnoori

Since a significant portion of the world's oil reserves resides in naturally fractured reservoirs (NFR), it is important to maximize oil production from these reservoirs. Mobility control EOR techniques, such as water alternating gas (WAG) and foam injection, may be used in NFRs to improve oil recovery. Foam injection may be modeled by empirical or mechanistic models, the latter being capable of representing foam generation and coalescence effects. Numerical models are needed to evaluate EOR techniques in NFR. The Embedded Discrete Fracture Model (EDFM) is capable of representing conductive faults or fractures and describing NFR and unconventional reservoirs as a triple porosity medium (hydraulic fractures, natural fractures, and matrix). This work aims at developing a general EDFM framework to allow the evaluation of different mobility control EOR methods in NFR. The mobility control EOR methods evaluated were the WAG and continuous foam injection. The formulation used to evaluate mobility control by foam injection in NFR was the population balance assuming local equilibrium and the P_c^* models. Nanoparticle transport models (Two Site and Two Rate models) were implemented and validated to allow simulation of nanoparticle stabilized foam injection. An EDFM preprocessor was further developed and validated against the in-house fully

implicit simulator, unstructured grid models from the literature and fine-grid models using a commercial simulator. Simulation run time was reduced by applying a porosity cut-off in the fracture cells assuming constant fracture conductivity. Validation case studies included multi-fractured wells producing through depletion and a 2D quarter five-spot production scheme (water and miscible gas injection) in NFR. We obtained a good agreement between EDFM, unstructured grid, and fine-grid models. Application case studies included 3D models under water, miscible gas and WAG injection, which confirmed the efficiency of the EDFM in modeling complex fracture networks. We used the EDFM to simulate multilateral well stimulation and we performed an automated history matching of the production data of a field test. The foam model and the nanoparticle transport models were validated against experimental data from the literature. It is concluded that the effect of fractures on hydrocarbon production depends on fracture network connectivity, which may be modeled using the EDFM preprocessor. Simulation results using mobility control EOR methods show considerable improvements in oil recovery due to a postponement in gas breakthrough.

Table of Contents

List of Tables

List of Figures

Chapter 1

Introduction

Narr *et al.* (2006) defined a naturally fractured reservoir (NFR) as a reservoir in which fractures are present in sufficient quantity and extent to impact reservoir behavior, enhance the permeability field, affect well productivity, and change recovery efficiency. NFRs can be found in sandstones, carbonates, shales, cherts, siltstones, and basement rock (Aguilera, 1995). These kinds of reservoirs present strong anisotropy, heterogeneity, and distinct production behavior. Fractures are mechanical discontinuities caused by brittle failure. The geometry elements of a fracture are the following: aperture, height, length and orientation. Types of fractures are joints and faults, which are differentiated by the nature of their displacement. Joints are extension fractures generated by an opening mode; they generally occur in joint sets (groups of parallel, spaced joints). Faults are shear fractures, or extension fractures, on which later shearing has occurred; they can enhance fluid flow or act as barriers and are of great importance due to compartmentalization. Figure 1.1 shows a conceptual representation of a fractured sandstone with joints and faults (Narr *et al.*, 2006).

Since a significant portion of the world's oil reserves resides in naturally fractured reservoirs (NFR), oil production from these reservoirs must be maximized. Among the mechanisms applied for improved oil recovery (IOR), the most common are water and gas injection. The efficiency of water injection for displacing oil and maintaining pressure in a NFR is highly dependent on reservoir wettabilitty. In water-wet reservoirs, the water enters the matrix by a natural process called spontaneous imbibition, which allows oil displacement and production from the

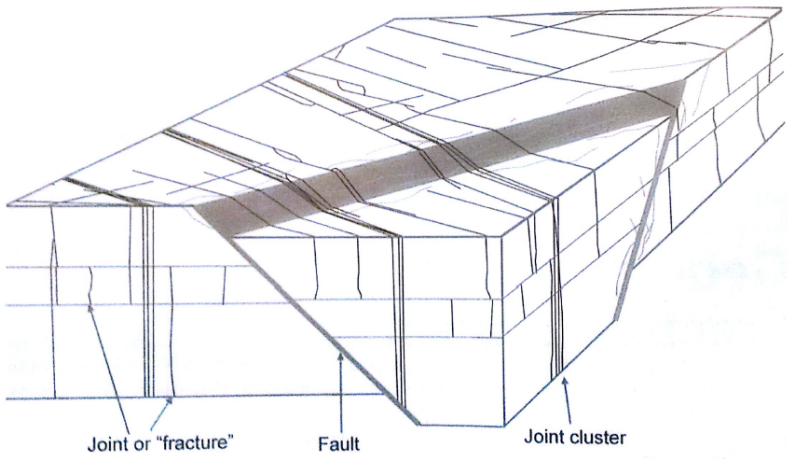

Figure 1.1: Conceptual view of fracture sandstones presented by Narr et al. (2006)

matrix to the fractures. The spontaneous imbibition is less pronounced (or even absent) in mixed to oil-wet reservoirs due to the occurrence of negative capillary pressure. Gas injection is also used in NFR projects to maintain reservoir pressure and/or to promote miscible displacement of the oil from the matrix to the fracture. However, because of the unfavorable mobility ratio between the displacing and displaced fluids most gas injection projects suffer from mobility problems, leaving a considerable amount of oil in the matrix which could be produced by combining water or gas injection with enhanced oil recovery (EOR) methods.

The target of an EOR application is to minimize the residual oil in the matrix and to accelerate the recovery rate for rapid production of oil (Babadagli, 2001). Minimizing residual oil is a critical issue for reservoirs with a high recovery factor, while accelerating production is critical for those with a low recovery factor. Allan and Sun's (2003) systematic study includes hundred NFRs throughout the world and they found that the average recovery factor for a NFR is 26%, ranging from 9 to 56%. The authors evaluated the effect of reservoir parameters and reservoir management techniques (application of EOR, for example) on the recovery efficiency. Allan and Sun (2003) determined that for most NFRs the choice of an appropriate

EOR method is key to improving final oil recovery. Chemical flooding and miscible gas injection are EOR techniques used in NFR. The first is useful for water injection into mixed to oil-wet NFRs where the use of chemicals promotes wettability alteration, reduces interfacial tensions (IFT) between water and oil phases, and/or promotes mobility control (polymer). Miscible gas injection in NFR has low efficiency because of mobility control issues (early breakthrough of injected phase). Foam and water alternating gas injection are used as mobility control EOR methods to avoid early breakthrough.

Numerical models are used to evaluate the efficiency of EOR applications in NFRs. Among the numerical formulations available for NFR modeling are explicit fracture representation and dual continuum approaches. The use of explicit fracture modeling is well-known for its detailed representation of fractures at the cost of a demanding computational effort. Dual continuum models fail to represent complex and heterogeneous NFRs but present fewer computational issues. Recently, embedded discrete fracture models (EDFM) have proven to be a numerically efficient approach to model long conductive fractures along with small fractures. The dual continuum (2ϕ2K), unstructured discrete fracture model (USDFM), and EDFM were compared by Moinfar *et al.* (2011). The 2ϕ2K formulations were originally introduced to study densely fractured reservoirs (represented as a sugar-cube model) with good connectivity. It was found that this formulation is reasonably accurate in predicting the behavior of sparsely fractured systems. For sparse fractures (distance between fractures bigger than the block dimensions), the formulation can capture the general trend, and when the fracture density is greater and the fracture pattern more irregular, the formulation is unable to capture details of the complex flow paths and the highly localized anisotropy. The EDFM gives a good representation in all cases and is able to accurately model highly heterogeneous NFRs (such as those with conductive faults and fracture corridors associated to faults). Integrating the equations used in the EDFM approach,

Moinfar *et al.* (2013) developed an approach to model small fractures by borrowing the concept of conventional $2\phi 2K$ formulation. A complex NFR composed of natural and hydraulic fractures was evaluated as a triple porosity medium with a reasonable numerical effort.

Foam is a special kind of colloidal dispersion composed of a gas phase dispersed in a liquid phase and stabilized by a surfactant (Kovscek and Radke, 1994). A foam is composed of the lamellae (region of the thin film, the two interfaces on either side of the film and part of the junction to the other lamellae) and the plateau border (connection of three lamella at a 120 degree angle). Foam quality is defined as the ratio of gas volume to the total volume of gas and liquid. Given the difficulty of measuring foam quality into the porous media, the injection foam quality is used as a reference. Kovscek and Radke (1994) described the mechanisms of foam generation (snap-off, lamella division, and leave-behind) and destruction (capillary suction coalescence, and gas diffusion). Many studies in the literature have shown the advantages in using foam as a mobility control agent (Farajzadeh *et al.*, 2010; Ashoori and Rossen, 2010, 2012; Haugen *et al.*, 2012), and compared its performance to other EOR methods (Srivastava *et al.*, 2009; Abbasi Asl *et al.*, 2010; Kharrat *et al.*, 2012).

In order to evaluate the efficiency of the application of foam as a gas mobility control agent in NFR, reliable numerical models are needed to represent the foam flow in both matrix and fracture systems. Methods currently used to model foam flow are local-equilibrium (or semi-empirical alteration of gas phase mobilities), population balance, percolation, and fractional flow theories (Kovscek and Radke, 1994; Cheng *et al.*, 2000; Delshad *et al.*, 2002; Chen *et al.*, 2010). The population balance model and local-equilibrium are the most used. Commercial simulators currently use local equilibrium models for foam flow (STARS, 2011; ECLIPSE, 2014). Another mechanistic representation of the foam flow process is the population balance model (Kovscek and Radke, 1994; Kovscek *et al.*, 1993, 1994, 1997; Apaydin and Kovscek, 2000). To simplify the numerical solution and make

the population balance model more suitable to real field models, Chen *et al.* (2010) assumed a local equilibrium between foam generation and coalescence rates. STARS (2011) allows the use of a more mechanistic approach for foam modeling, also referred to as the lamella density approach.

Foam injection is an efficient mechanism for improving oil recovery in gas injection projects in NFRs by reducing gas mobility, reducing gravity override, providing wettability alteration, and providing IFT reduction. The use of foam in gas injection projects increases the residence time of the injected gas in the porous media benefiting the occurrence of miscible processes (first or multiple-contact miscibility). Although there are occasional works in the literature on surfactant selection for foaming processes and foam modeling, few have evaluated the use of foam in miscible and immiscible gas injection in NFRs. Some works in the literature have compared the efficiency of foam and other mobility control methods in NFRs (Yanze and Clemens, 2012; Kharrat *et al.*, 2012; Ameri Ghasrodashti *et al.*, 2012; Taheri *et al.*, 2013).

1.1 Objectives

The present work aims to study the numerical modeling and representation of foam as a mobility control agent in gas injection projects (miscible or immiscible) applied to NFRs (triple porosity systems composed of both natural fractures, conductive faults, and/or fracture corridors acting as conduits for the fluid flow). State-of-the-art numerical models for NFR (the EDFM approach) and foam flow in porous media (local equilibrium models) are used to guarantee a better physical representation.

The general objective of this work is described below. For didactic purposes the general objective was divided in four specific objectives.

General Objective. Improve the efficiency of gas injection (miscible and/or

immiscible) in highly heterogeneous NFRs by the use of mobility control methods (foam and alternated injection methods)

Specific Objective 1. Implement a general EDFM preprocessor capable of accurately modeling complex fracture networks

Specific Objective 2. Extend the use of the EDFM preprocessor to allow modeling of multilateral well stimulation techniques

Specific Objective 3. Evaluate the numerical representation of foam flow into fractures using different foam models

Specific Objective 4. Compare the efficiency of gas injection processes combined with mobility control EOR techniques in simple and real field reservoir models

Specific Objective 5. Implement nanoparticles transport in porous media to allow their use as a foaming agent

The accomplishment of these specific objectives allows this work to contribute to the recent technical literature as follows:

1. Development of a robust EDFM preprocessor for fracture modeling and simulation capable of
   (a) Embedding fracture planes in irregular corner point reservoir grids
   (b) Incorporating variable fracture conductivity in a given fracture plane to allow complex fracture model
   (c) Using the Oda's tensor to calculate full permeability tensor and average permeabilities for a set of fractures modeled with the integrated EDFM approach

(d) Calculating shape factors to be used for NFR simulation in conventional dual porosity formulations

(e) Applying a fracture porosity cutoff to enhance simulation run time

2. Implementation and evaluation of a new approach to model multilateral well stimulation using the EDFM formulation and real pilot field data

3. Evaluation of numerical modeling of foam diversion in explicitly modeled fractures using local equilibrium models and the EDFM

4. Simulation of a real field gas injection project in a highly heterogeneous reservoir with explicit representation of conductive faults

5. Evaluation of the advantages and disadvantages of EOR methods for mobility control

1.2 Description of Chapters

In Chapter 2 we introduce basic concepts on naturally fractured reservoirs and foam. We perform a brief literature review on the formulation available to model naturally fractured reservoirs, including dual continuum and discrete fracture formulations. Numerical modeling of foam flow in porous media is also described, focusing on the description of foam models classified as local equilibrium models. Chapter 3 describes the equations and methods used in this dissertation. We comment on the work presented in the literature and we highlight our contribution to the state of the art of each method. Chapter 4 presents a thorough verification of our EDFM preprocessor. We perform our EDFM simulations using our in-house IMPEC compositional simulator. We verify our results with fine models and unstructured grid models from the literature. The modeling of multilateral well stimulation using the EDFM is described in Chapter 5. We perform sensitivity analysis and we history match data from a pilot test implemented in the Austin

Chalk Formation. Chapter 6 shows the validation of the foam model we implemented in our in-house IMPEC reservoir simulator, the population balance model assuming local equilibrium. The validation was performed using experimental data from the literature. In this chapter we also present the results of the method proposed for fitting foam model parameters (with and without the influence of the oil saturation on foam degradation). Chapter 7 presents two applications of foam injection for mobility control during gas injection in a simple and a complex model. In Chapter 8 we describe the use nanoparticles in the petroleum industry. We show the equations used for implementing nanoparticle transport using Two Site and Two Rate models in our in-house IMPEC simulator and we validate the implementation by comparing results with experimental data from the literature. As an illustrative example, we perform one run of foam injection using the nanoparticle as a foam stabilizing agent. The foam model used was the population balance model assuming local equilibrium. Chapter 9 summarizes the dissertation and enumerates the main contributions and conclusions of this work.

Chapter 2

Literature Review

2.1 Numerical Models for Naturally Fractured Reservoirs

Numerical models are used to evaluate the efficiency of EOR applications in Naturally Fracture Reservoirs (NFR). Among the methods available for numerical representation of NFRs are the dual continuum formulations and the unstructured grid (Finite Element Methods). The dual continuum formulation assumes that matrix and fractures may be modeled as two separate continua, connected by means of a shape factor which is a function of the fracture network. Unstructured grids use finite element or finite volume methods to explicitly represent the fractures, but their disadvantages are the need of complex gridding techniques and computational inefficiency. Recently, embedded discrete fracture models (EDFM) have shown to be a numerically efficient approach capable of modeling long explicit fractures along with small fractures. This section presents a literature review about dual continuum and EDFM formulations, which are in the scope of this work.

2.1.1 Dual Continuum Formulations

The first application of dual continuum formulations in the oil industry was described by Warren and Root (1963). Warren and Root (1963) assumed that the primary porosity was contained in a homogeneous and isotropic material modeled as a systematic array of identical, rectangular parallelepipeds and the secondary porosity was contained in an orthogonal system of continuous uniform fractures oriented to the main permeability axes (IJK) and uniformly spaced with constant width (sugar cube model as shown in Figure 2.1). Fluid exchange between matrix and fracture was

governed by a transfer function; the geometry of the fracture and matrix elements was defined by a shape factor, σ (Warren and Root, 1963; Kazemi *et al.*, 1976; Lim and Aziz, 1995).

Kazemi *et al.* (1976) extended the Warren and Root (1963) approach to multiphase flow and developed the first two-dimensional, two-phase, dual porosity simulator. Kazemi *et al.*'s (1976) shape factor is shown in Equation 2.1, its advantage over Warren and Root's (1963) shape factor was the incorporation of different fracture spacing in I,J and K directions.

$$\sigma_f = 4\left[\frac{1}{L_x^2 + L_y^2 + L_z^2}\right], \tag{2.1}$$

where L_x, L_y, and L_z are the matrix block dimensions.

Efforts were made to make the dual porosity formulation more realistic, such as the multiple interacting continua (MINC) method (Pruess and Narasimhan, 1985), subdomain method (Saidi, 1983), and pseudo-capillary pressure and relative permeability techniques (Thomas *et al.*, 1983; Gilman and Kazemi, 1983). Blaskovich *et al.* (1983); Hill and Thomas (1985); Dean and Lo (1986) handled matrix-matrix connections using dual permeability formulations.

Among the disadvantages of dual continuum formulation are the demand of a large quantity of data, the high computational effort, and the inability to represent fractures with all their characteristics directions.

Karimi-Fard and Firoozabadi (2003); Li and Lee (2008); Moinfar *et al.* (2011) mentioned that dual-porosity models were most often used when the sugar-cube model was applicable to fractured media (well connected fractures with regular spacing). Limitations of the dual porosity formulation are cited as follows: inability to model heterogeneity of disconnected fractured media and inability to represent gravity effects in a mixed-wet system using transfer functions. Hui *et al.* (2013) evaluated various approaches for NFR numerical simulation in terms of

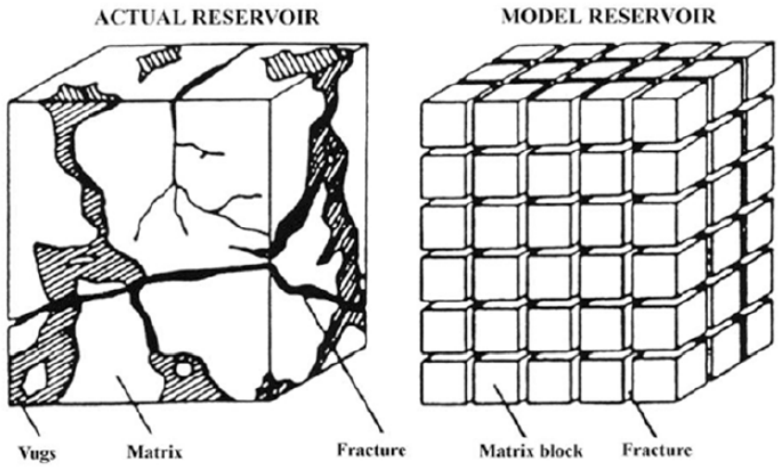

Figure 2.1: Sugar cube representation of a fractured media (Warren and Root, 1963).

accuracy and computational speed. The authors used a flow-based multiple sub-region technique (MSR) to create unstructured coarse fracture models, directly based on discrete fracture models (DFM). An upscaling was applied to generate structured DFM-based, dual porosity/dual permeability ($2\Phi 2K$) models (shape factors and effective fracture permeability were calculated). The DFM results were used as a reference solution, and the authors ordered the formulations in terms of decreasing accuracy: MSR, DFM based $2\Phi 2K$, and conventional $2\Phi 2K$.

Diagonal representation of permeability is only valid when the flow is aligned to the principal axes and the full-tensor permeability matrix is diagonally dominant. The assumption that the full-tensor permeability matrix is diagonally dominant may not always apply for a fractured reservoir, since fractures may have any direction in the space.

Oda (1985) developed a method to calculate the permeability tensor based on the geometrical properties of the fracture. The authors assumed an uniform field gradient over the flow region, which is only valid if there is a sufficient number of fractures. Oda (1985) applied the Darcy's law to a single fracture and projected the pressure gradient in the fracture plane (function of the unit vector of the i^{th} fracture

plane). The author obtained Equation 2.2.

$$\overrightarrow{u_i} = -\frac{k_{f_i}}{\mu}\begin{bmatrix} 1-n_x^2 & -n_x n_y & -n_x n_z \\ -n_y n_x & 1-n_y^2 & -n_y n_z \\ -n_z n_x & -n_z n_y & 1-n_z^2. \end{bmatrix}\overrightarrow{\nabla} P, \tag{2.2}$$

where u_i is the Darcy velocity of fracture i, k_{f_i} is the permeability of fracture i, μ is the fluid viscosity, n_x, n_y, and n_z are the components of the unit vector defining the fracture plane. Assuming matrix permeability equals to zero, the average flux over a network of fractures is obtained by integrating the flux over all fractures and weighted by the fracture void volume, as shown in Equation 2.3.

$$\overrightarrow{u_{i\,average}} = \frac{\int \overrightarrow{u_i} dW_i}{V_{bulk}}, \tag{2.3}$$

where $u_{iaverage}$ is the average Darcy's velocity at a given block, dW_i is a differential volume of the fracture, and V_{bulk} is the bulk volume of the grid cell representing the matrix. Comparing Equations 2.2 and 2.3 the average permeability tensor of a well connected fractured medium is calculated using Equation 2.4.

$$\bar{k} = \frac{\sum_{i=1}^{nf}\left[k_{f_i}\begin{pmatrix} 1-n_x^2 & -n_x n_y & -n_x n_z \\ -n_y n_x & 1-n_y^2 & -n_y n_z \\ -n_z n_x & -n_z n_y & 1-n_z^2. \end{pmatrix}_i\right]}{V_{bulk}} \tag{2.4}$$

Tarahhom (2008) implemented a full-tensor dual porosity formulation in a fully implicit compositional chemical reservoir simulator. The author showed that the full-tensor permeability allows capturing the fracture system directionality and heterogeneity.

2.1.2 Discrete Fracture Model

Lee *et al.* (2000, 2001) proposed a hierarchical modeling approach based on the ratio of fracture length to grid size (l_f/l_g), upon which three classes of fractures

were defined: short fractures ($l_f/l_g << 1$), grid block scale fractures ($l_f/l_g \approx 1$), and long fractures ($l_f/l_g >> 1$). The effect of short fractures was computed using a simple analytical equation and was included by means of an enhanced (or effective) matrix conductivity. The contribution of gridblock scale fractures was calculated using the boundary element method. Long fractures were modeled as major fluid conduits. Li and Lee (2008) adopted the transport index concept from Lee *et al.* (2001) and extended their method to include networks of long fractures, modeling them as two dimensional planes crossing several layers. Fracture to matrix transmissibilities were calculated using Equation 2.5.

$$TI = A\frac{\bar{\bar{k}} \cdot \vec{n} \cdot \vec{n}}{\bar{d}}, \tag{2.5}$$

where A is the fracture surface area in the block, $\bar{\bar{k}}$ is the matrix permeability tensor, $\vec{n}$ is the unit vector normal to the fracture plane, and $\bar{d}$ is the average normal distance from the fracture. The authors also included the intersection of fractures and wellbores assuming the following: the pressure drop along the fracture in the wellblock is negligible; the productivies from the fracture and wellbore are superposed; Peaceman's equation can be directly used. Both medium and long fractures were perpendicular to the bedding plane. Hajibeygi *et al.* (2011) applied an iterative multiscale finite volume (i-MSFV) to model multiphase flow in fractured porous media. The i-MSFV method was extended to model fractures using a hierarchical framework. For high conductivity fractures (small gradient pressures) the authors use the mean fracture network pressure, which reduces the degree of freedom (DOF) of the fracture network (one for each fracture); the authors mention the term "agglomeration of highly connected DOFs." For low conductivity fractures (greater pressure gradients) the fracture domain should be divided into more DOFs to allow for a better convergence of the problem. Moinfar *et al.* (2013) implemented the Li and Lee (2008) formulation in an in-house, fully-implicit, compositional reservoir simulator. Non-Neighboring Connections

(NNC) were used to account for the flow between matrix and fracture blocks. The NNC contribution (a convection term) was added to the component mass balance equation as a source/sink term. Moinfar (2013) first presented the concept of an EDFM preprocessing code to calculate the transmissibilities between NNC blocks. The transmissibilities were used as input data for the fully implicit compositional simulator used in his work. The preprocessing code was able to account for orthogonal and slanted fractures, assuming they penetrate the whole reservoir domain (from top to bottom of the simulation grid). Three kinds of NNC were calculated by the preprocessing code: between a fracture cell and its neighboring matrix block (FM), between two intersecting fractures cells (FINT), and between two cells of an individual fracture (FF). The equation for the FM transmissibility presented by Moinfar (2013) was Equation 2.6 .

$$T = \frac{A^{nnc} \times k^{nnc}}{\bar{d}^{nnc}}, \tag{2.6}$$

where A^{nnc}, k^{nnc} and $\bar{d}^{nnc}$ are the area open to flow, the harmonic average of permeability, and the characteristic distance, respectively, between two control volumes associated with a NNC. Equation 2.7 was used to calculate the average normal distance between the fracture and the matrix gridblock (Li and Lee, 2008; Hajibeygi *et al.*, 2011; Moinfar, 2013),

$$\bar{d}^{nnc} = \frac{\int_{V_{bulk}} w_n dv}{V_{bulk}}, \tag{2.7}$$

where dv is a volume element in the matrix gridblock, w_n is the normal distance of the volume element to the center of the fracture plane, and V_{bulk} is the bulk volume of the gridblock. For FINT transmissibility Equation 2.8 was used.

$$T = \frac{T_1 T_2}{T_1 + T_2}, \tag{2.8}$$

where T_1 and T_2 are defined in Equation 2.9.

$$T_1 = \frac{k_{f1}\omega_{f1}L_{f,int}}{\bar{d}_{f1}} \; and \; T_2 = \frac{k_{f2}\omega_{f2}L_{f,int}}{\bar{d}_{f2}}, \tag{2.9}$$

where k_f is the fracture permeability, ω_f is the fracture aperture, L_f, int is the length of the fracture intersections, and $\bar{d}_{f1}$ and $\bar{d}_{f2}$ are the distances between the center of the fracture plane and the center of the intersection line. To calculate FF transmissibility, Moinfar (2013) defined k^{nnc} equal to the fracture permeability, d^{nnc} was defined as the distance between the centers of two fractures segments into the block, and A^{nnc} is the fracture aperture times the length of the intersection line. Moinfar's (2013) formulation to calculate FF transmissibility assumes that fracture planes have homogeneous conductivity and that it cannot the used to model fractures with varying conductivity. The intersections between well and fractures (FW) were modeled using Equation 2.10, derived with an approach similar to Peaceman (1983) (Li and Lee, 2008; Moinfar, 2013).

$$WI_F = \frac{k_F\omega_F}{ln\left(\frac{r_o}{r_w}\right)}, \tag{2.10}$$

where r_o is the Peaceman's radius evaluated to the dimensions of a fracture block, given in Equation 2.11

$$r_o = 0.14\sqrt{L_f^2 + h_F^2}, \tag{2.11}$$

where L_f is the fracture length and h_F is the fracture height in the well block. Moinfar's (2013) formulation to calculate FW transmissibility assumes that the geometry of the intersection of the fracture plane and the matrix gridblock will always be rectangular, what might not be true for three dimensional cases which may be a triangle, pentagon, or even an hexagon.

To model small and medium scale fractures, Moinfar *et al.* (2013) integrated the EDFM equations borrowing the concept of dual porosity/dual permeability

formulation derived from the dual continuum assumption, as shown in Equation 2.12. The authors were able to simulate a triple porosity medium composed of natural and hydraulic fractures, in which hydraulic fractures were modeled explicitly. This approach is promising for unconventional reservoirs modeling.

$$T_{m-f} = \sum_{i=1}^{N_{nf}} W_i \frac{k_{m-f,i} A_{f,i}}{\bar{d}_{m-f,i}}, \tag{2.12}$$

where N_{nf} is the number of embedded natural fractures in a matrix gridblock, W_i is the volume of the i-th fracture bounded in that gridblock divided by the total volume of fractures in that cell, $T_{m-f,i}$ is the transmissibility between the i-th fracture and the matrix gridblock, $k_{m-f,i}$ is the harmonic average of the matrix and fracture permeabilities, $A_{f,i}$ is the fracture surface area in the gridblock, and $d_{m-f,i}$ is the average normal distance of the fracture from the matrix gridblock. The work of Hajibeygi *et al.* (2011) mentioned that for highly connected matrix and fracture cells the effect of $\bar{d}$ is small as long it is larger than a minimal value. Jiang *et al.* (2015) studied the application of hybrid models to unconventional reservoirs neglecting gravity effects (2D models). The hybrid model is composed of a discrete fractures modeles explicitly and coupled to natural fractures represented by a dual-continuum approach. The link between the discrete fracture network and the natural fractures is denoted as the critical issue to hybrid modeling. Two hybrid models were proposed: coupling of the EDFM with the MINC and coupling of an unstructured DFM with continuum type models. The EDFM/MINC hybrid model was validated against refined single porosity models and the unstructured DFM/continuum hybrid model is validated against a fine scale unstructured DFM model.

Panfili *et al.* (2013) implemented the EDFM approach as described by Li and Lee (2008) and coupled it to a commercial reservoir simulator. Two cases were studied: the pressure transient behavior of a multi-fractured horizontal well and a

first contact miscible injection process. The authors concluded that the EDFM may be coupled with commercial reservoir simulators and that it allows efficient modeling of complex fractured reservoirs characterized using discrete fracture network model embedded in corner point grids. Jiang *et al.* (2014) developed a multi-continuum, multi-component model to study gas injection in fractured shale reservoirs. Their hybrid model included three domains: matrix, major conductive fractures (modeled with the EDFM), and microfractures (modeled using the dual porosity and multiple interacting continua, MINC, approach). The authors used single-phase, multi-component flow in order to simplify the simulation studies. The Knudsen diffusion and gas slippage effect were included in the formulation, along with multi-component adsorption and desorption. Different production scenarios were evaluated to calculate production from multi-fractured horizontal wells. Results showed that fracture networks influence methane production; CO_2 and N_2 injections were found to be effective in enhancing shale gas recovery. Aiming to improve the efficiency and the accuracy of the numerical solution of fractured reservoirs, Zhou *et al.* (2014) developed a two-phase finite difference formulation assuming 1D flow in fractures. Different levels of flux were assigned for both sides of the fractures to model saturation changes due to multiphase flow within the fracture. Matrix blocks covering the fracture do not join the numerical solution scheme because they are included as boundaries. The pressure field near the fracture was defined by unilateral interpolation between fracture and matrix blocks; fluxes were calculated and used as boundary conditions. Results showed a better match for the Zhou *et al.* (2014) formulation than for Lee *et al.* (2000). Zhou *et al.*'s (2014) work does not define intersection between fractures.

Some authors in the literature have attempted to create flexible fracture models. Edwards *et al.* (2013) modeled hydraulic fractures as part of the well model instead of explicitly setting the fractures using grid local refinement. The fracture is defined as a mesh of interconnected branches of multilateral, multi-segmented wells.

The authors indicated advantages of this model as follows: the independence of the fracture mesh to the simulation grid, fractures can intersect the grid at any angle and geometry, properties of the fracture can be fully honored, and improved numerical stability. The authors' proposed approach presented a match with results obtained from traditional grid refinement models.

2.2 Multilateral Well Stimulation

Many works in the literature describe the application of multilateral stimulation to increase well productivity in field projects. Those wellbore laterals may be created using different methods, such as mechanical drilling from the main wellbore using small drill bits and high velocity fluid injection to perforate the formation by diversion and dissolution. One way to perform multilateral stimulation is to use fishbone wells. The definition of a fishbone well presented at Schlumberger Oilfield Glossary (2014) is the following: "A series of multilateral well segments that trunk off a main horizontal well. The appearance closely resembles the ribs of a fish skeleton trunking off the main backbone."

Maricic *et al.* (2008) studied the influence of different horizontal-well shapes on the production of coal-bed methane reservoirs. Five horizontal wells were used: single-lateral, dual-lateral, tri-lateral, quad-lateral, and fishbones (also referred to as pinnate wells). The objective functions used for ranking were the gas recovery factor and the NPV. The study reported that quad-laterals wells had a better performance in terms of gas recovery factor, followed by the fishbones wells; quad-laterals presented the better NPV of all alternatives. The authors discussed the need to optimize the spacing between laterals. Xiance *et al.* (2009) performed a comparison between multi-fractured and fishbone wells for tight gas field development. To compare both performances, material balance and nodal analysis techniques were applied. The net present value (NPV) was used for an economic analysis; the authors assumed that the cost of two fishbone laterals is equivalent to the cost of

one hydraulic fracture. The NPV of gas fields developed with fishbone wells increased with the number wells and fishbone laterals (not proportionally). The NPV increased with the increase of fishbone laterals length and decreased with the increase of the fishbone laterals spacing. The multifractured wells provided better NPVs for number of fractures greater than four, while fishbones provided better results when the number of fishbone laterals was less than six. Ding *et al.* (2012) evaluated the use of a fishbone well geometry to inject water in buried hills reservoir, Liahoe oilfield, in China. The fishbone injector was positioned at the bottom of the reservoir, while the horizontal producer was located at the top. A dual porosity and single permeability formulation was used for the reservoir simulation. The number, length, and branching angles of the fishbone were investigated. The authors showed that the horizontal injector with fishbones had a greater injectivity than the horizontal injector without fishbones; the producer anticipated production, but an earlier breakthrough occurred for the case of the fishbones injector rather than for the case of the horizontal injection well. Xun (2013) reported an overview of horizontal well drilling technologies applied to Liaohe Oilfield, China. Among the presented technologies, the authors mention the application of a maximum reservoir contact (MRC) fishbone-shaped horizontal well technology. The authors indicated that the MRC technology maximizes reservoir contact surface, increasing the well productivity. The following key features of the MRC technology were listed: fishbone construction sequence (from front to rear), application of open-hole suspended sidetracking, and the use of bits of different sizes to drill main wellbore and branches. Xun (2013) pointed out that the daily production of a fishbone-shaped horizontal well in buried-hill reservoir in Xinglongtai is 162% of what is produced from a conventional horizontal well.

Freyer and Shaoul (2011) and Rice *et al.* (2014) described a multilateral stimulation technology (MST), known as fishbones technology. The technology was made possible by the development of a liner sub which houses four small-diameter

high strength tubes called needles, each measuring 40 feet. Fishbones are created when the liner sub is hanged off into the wellbore with a standard liner hanger and HCl fluid is pumped, jetting out of the nozzles located in each needle (Figure 2.2). Lateral tunnels of half to a quarter inches are created by jetting and dissolution. Although the needles exit the sub at 40^o angle, the bending located at the exit port results in laterals of approximately 90^o angle relative to the wellbore. This multilateral stimulation technology may be applied to compartmentalized, layered, or naturally fractured reservoirs. In the well screening process the presence of geological barriers is not an issue as it is in hydraulic fracturing. This stimulation technique is applicable to depleted reservoirs even when the accuracy of the depth is insufficient for sweet spot well placement (Rice *et al.*, 2014). Freyer and Shaoul (2011) attempted to model the fishbones using a 3D reservoir simulator and computational fluid dynamics (CFD) modeling. The fishbone needles modeled with a 3D grid are shown in Figure 2.3. Fishbones with 12 meters lateral extensions presented a productivity increase of 20-30% (compared to the base case well) in a high temperature gas/condensate reservoir consisting of layered and faulted sandstones. A case of a hydraulic fracture was used for comparison and the fishbones produced less water due to the limited height of the branches and the evenly distributed connection with the reservoir. In a low permeability sandstone gas reservoir the fishbones stimulation proved to be as efficient as two longitudinal propped fractures. Fishbones performance was compatible to three propped fractures when longer needles were assumed. Freyer and Shaoul's (2011) performed CFD studies to estimate friction pressure losses at the fishbone laterals. The calculated pressure loss was less than 0.07 MPa (10 psi) in all simulations performed. Rice *et al.* (2014) presented a pilot well in the Austin Chalk formation, a tight limestone formation with porosity of 5% and 0.5 mD permeability located in Brazos County, Texas. Sixty laterals with 40 ft penetration length were successfully installed. Results showed a 8.3 times increase in IP-30 (cumulative production of

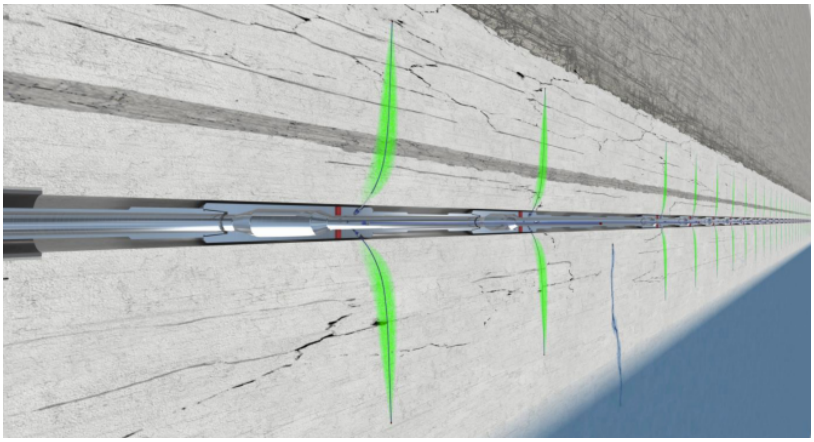

Figure 2.2: Fishbones (Rice et al., 2014).

first 30 days) and 30 times increase in the well productivity index.

2.3 Foams

Foam is a specific kind of colloidal dispersion; it is composed of a gas phase dispersed in a liquid phase and stabilized by a surfactant which is adsorbed at the gas-liquid interface (Kovscek and Radke, 1994). A foam is composed of the lamella (thin liquid phase film which separates the gas phase) and the plateau border (connection of three lamella at a 120 degree angle). Figure 2.4 shows a cut in a symmetric stable

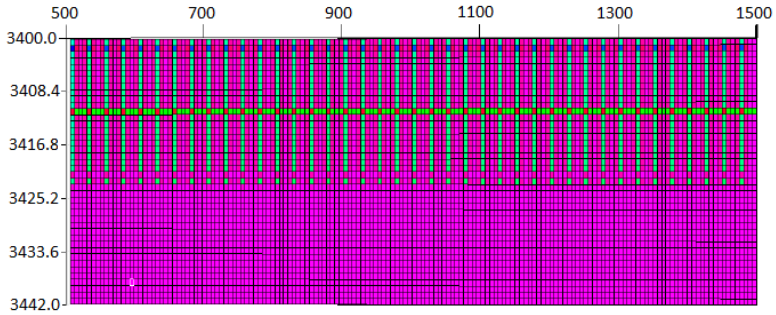

Figure 2.3: Fishbones' 3D model used by Freyer and Shaoul (2011); vertical needles are shown in green.

foam and its parts as described by Schramm and Wassmuth (1994). Foam quality is defined as the ratio of gas volume to the total volume of gas and liquid. Given the difficulty of measuring foam quality in the porous media, injection foam quality is used as a reference.

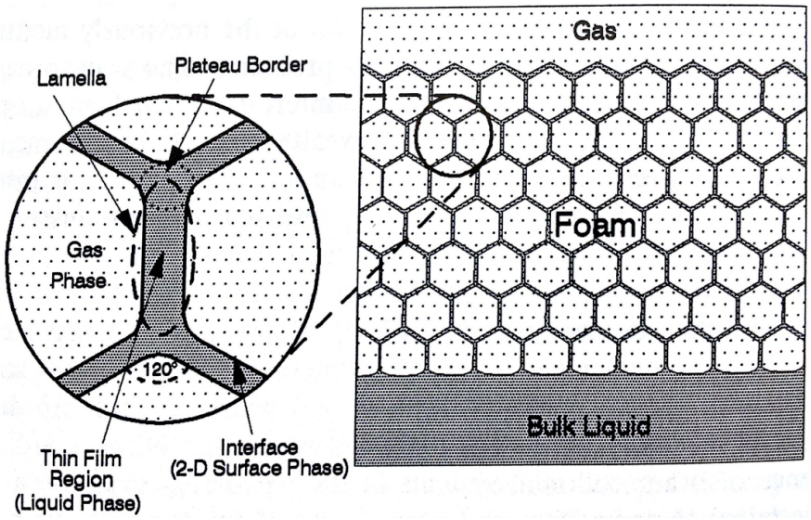

Figure 2.4: Representation of symmetric foam (Schramm and Wassmuth, 1994)

Kovscek and Radke (1994) described the mechanisms of foam generation (snap-off, lamella division, and leave-behind) and destruction (capillary suction coalescence, and gas diffusion).

As described in Falls *et al.* (1988) and Kovscek and Radke (1994), the *snap-off* is a mechanical process due to multiphase flow in porous media regardless of the presence or the absence of surfactant. Snap-off is the dominant mechanism of foam generation and happens when a finger enters a pore constriction initially filled with wetting fluid. Upon reaching the throat, the interface curvature and corresponding capillary pressure rise to the equilibrium entry value. As the bubble enters the downstream body, wetting liquid remains in the corners. Bubble's front curvature and corresponding local capillary pressure are reduced due to expansion of the interface. The resulting capillary pressure leads to a gradient in the liquid

pressure moving it toward the pore throat, initiating the formation of what we call a collar. As the collar grows, the bubbles are created. Snap-off or germination sites must exhibit a body-throat size aspect ratio larger than 2 and be gently sloped. Figure 2.5 shows the schematic of the snap-off mechanism. A lamella cannot be generated directly from snap-off, but will be formed when the bubble meets another previously generated one in the same site. Without a stabilizing agent (surfactant), bubbles generated by snap-off will quickly coalesce. Snap-offs are classified into three types (Kovscek and Radke, 1994): neck or roof snap-off (prevalent at high wetting liquid saturations), rectilinear and preneck constriction snap-off (both phases are flowing in steady state at lower wetting liquid saturations), and preneck snap-off (gas bubble lodges upstream of a pore throat and blocks liquid flow, and thus causes deformation in the gas-liquid interface).

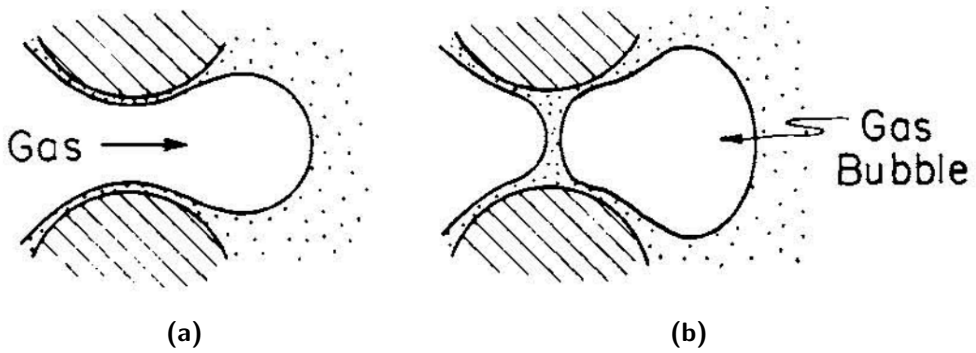

Figure 2.5: Illustration of the snap-off mechanism presented by Ransohoff et al. (1988): gas enters the liquid filled pore throat forming a gas finger and a wetting collar (a) and a bubble is formed after snap-off (b).

Foam bubbles may be generated by the *division of preexisting mobile bubbles or lamella* (Falls *et al.*, 1988; Kovscek and Radke, 1994). When a moving bubble encounters a point where the flow branches into two directions, the bubble's interface stretches around this point and enters both flow paths, dividing the initial bubbles in two. Bubbles smaller than the pore body size do not divide, while larger ones divide

(Kovscek and Radke, 1994). Figure 2.6 shows a schematic of the bubble division. This mechanism also depends on the occupancy of surrounding pores, once existence of trapped bubbles may prevent the division from occurring.

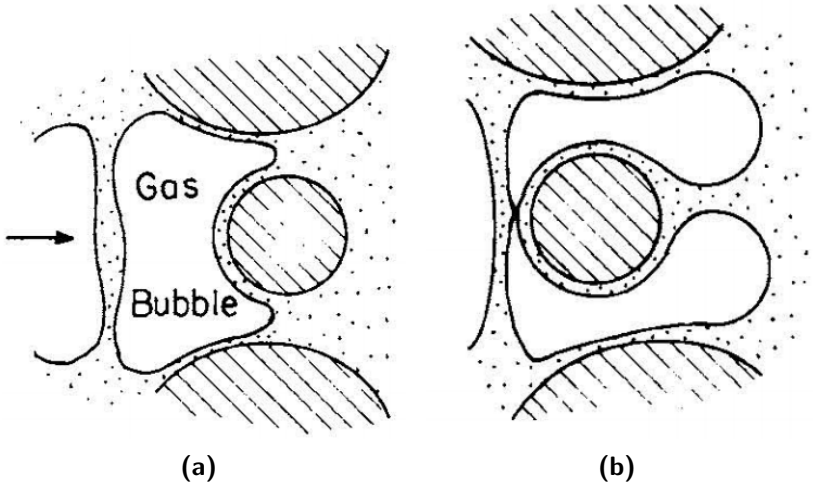

Figure 2.6: Illustration of the division mechanism presented by Ransohoff et al. (1988): gas bubble approaches entry point (a) and is divided in two gas bubbles (b).

The *leave-behind* bubble generation process initiates when two gas menisci invade an adjacent liquid-filled pore-body (Kovscek and Radke, 1994). As the two menisci converge downstream a lens is left behind. If the capillary pressure of the system is not high and the pressure gradient is not large, a stationary stable lens emerges and the lens may drain to a thin film. Figure 2.7 shows a schematic of the leave-behind mechanism. Normally the lenses are oriented in the direction of flow and do not make the gas phase discontinuous.

Thin lamella are thermodynamically unstable and exist because of normal forces within the films originated from long-range concerted intermolecular interactions. *Capillary suction coalescence* is related to the film disjoining pressure (Π), which is a function of film thickness, h (Jimenez-Laguna, 1991; Kovscek and Radke, 1994; Aronson *et al.*, 1994). Π is the net pressure between the gas phase (bubbles) and the bulk liquid from which the lamellae extend. The three primary

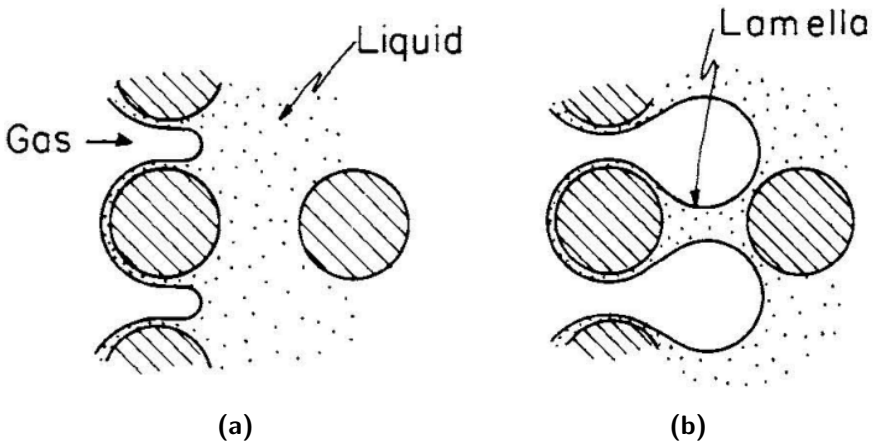

Figure 2.7: Illustration of the leave-behind mechanism presented by Ransohoff et al. (1988): gas invasion (a) and stable lens (b).

components of Π are electrostatic repulsion (Π_{el}), van der Walls attraction (Π_{vw}), and steric/hydration forces (Π_{sh}) (Aronson *et al.*, 1994). The combination of these three forces leads to an S-shaped disjoining pressure isotherm that is similar in form to a pressure-volume isotherm for real gases and liquids, as shown in Figure 2.8. Positive values of Π denote net repulsive film forces, while negative values indicate net attractive forces. The dashed lines in Figure 2.8, labeled P_{c1} and P_{c2}, correspond to different capillary pressures applied by the porous medium on the lamellae. Both flowing and stationary foam films thins or thickens to achieve an equilibrium thickness in accordance with the capillary pressure value calculated by the augmented Young-Laplace equation (Equation 2.13).

$$P_c = 2\sigma C_m + \Pi(h), \tag{2.13}$$

where P_c is the local capillary pressure, C_m is the mean interfacial curvature of the thin film and σ is the bulk surface tension. Note that in the limit of thick films $\Pi(h)$ tends to zero. Aronson *et al.* (1994) stated that at P_{c1} the film can exist in two equilibrium states: common black film (CBF) or Newton black film (NBF). The CBF equilibrium state occurs due to the electrostatic diffuse double layers overpowering

van der Walls attraction, while the NBF equilibrium state occurs due to the steep repulsive branch initiated by the steric /hydration forces. At the higher pressure P_{c2} the film thins to a critical thickness near Π_{max} and jumps to an NBF. Rupture of the film occurs when capillary pressure is greater than Π_{max} (Aronson *et al.*, 1994).

For the static trapped lamella, the film reaches an equilibrium thickness set by the local capillary pressure and the film curvature. As the capillary pressure in the porous media rises during drainage, the film thickness decreases until Π_{max} is attained. At still higher, Π_{rup} is attained, where the film eventually breaks. The capillary pressure that corresponds to Π_{rup} is termed the critical capillary pressure for rupture, P_c^* (Khatib *et al.*, 1988; Rossen and Zhou, 1995). The coalescence behavior for flowing bubbles is more complicated (Jimenez-Laguna, 1991; Osterloh and Jante Jr, 1992; Kovscek and Radke, 1994; Farajzadeh *et al.*, 2012). The thickness of the transporting lamella oscillates about the equilibrium thickness established in the stationary lamella in a sequence of squeezing-stretching and draining filling events (the oscillation is proportional to the P_c - Π pressure difference). Thickness oscillations are wider for high gas flow rate and for large pore-body to pore throat aspect ratios. Jimenez-Laguna (1991) argued that the lamella would break instantaneously when film thickness diminishes to h_{min}, corresponding to Π_{max}; the film is stretched so rapidly that the surfactant cannot flow into the film to stabilize it. The capillary pressure at which moving lamella breaks is defined as P_c^*, the limiting capillary pressure (Khatib *et al.*, 1988; Jimenez-Laguna, 1991; Osterloh and Jante Jr, 1992; Kovscek and Radke, 1994; Rossen and Zhou, 1995). Khatib *et al.* (1988); Vassenden *et al.* (2000); Farajzadeh *et al.* (2012) indicated that there is a limiting water saturation for foam stability, or the foam breakdown saturation (S_w^*) associated with the limiting capillary pressure (Fig. 2.9). Since lamellae is generated in porous media, the capillary pressure increases up to a limit as the gas fractional flow is raised. Any further increase in the gas fractional flow would not result in an increase of the capillary pressure,

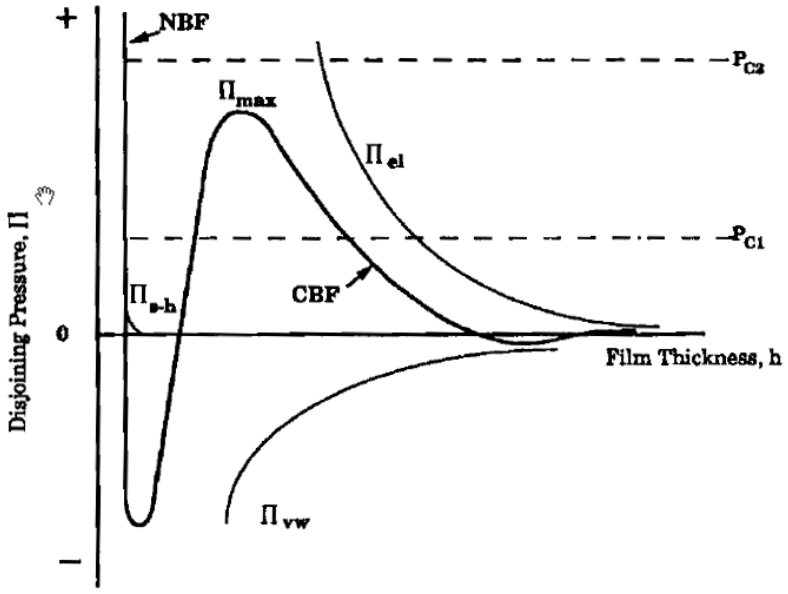

Figure 2.8: Idealized disjoining pressure isotherm (Aronson et al., 1994)

instead would cause the foam texture to become coarser. Khatib *et al.*'s (1988) work showed that the value of this limiting capillary pressure for foams in porous media varies not just with surfactant formulation, but also with the gas velocity and the permeability of the medium. Farajzadeh *et al.* (2012) stated that surfactant solutions that exhibit large rupture disjoining pressures lead to strong foam in porous media with large flow resistance. Different surfactant structures and conditions such as concentration and temperature lead to different disjoining pressure isotherms for single foam films and thus different limiting capillary pressure characteristics.

Gas diffusion occurs mostly to stagnant and trapped bubbles. This process is based on the premise that the gas in the concave part of a bubbles is at a higher chemical potential than the one located in the convex side. That difference in chemical potential between both gases leads to a transport by diffusion through the liquid film from the concave to the convex side (Kovscek and Radke, 1994).

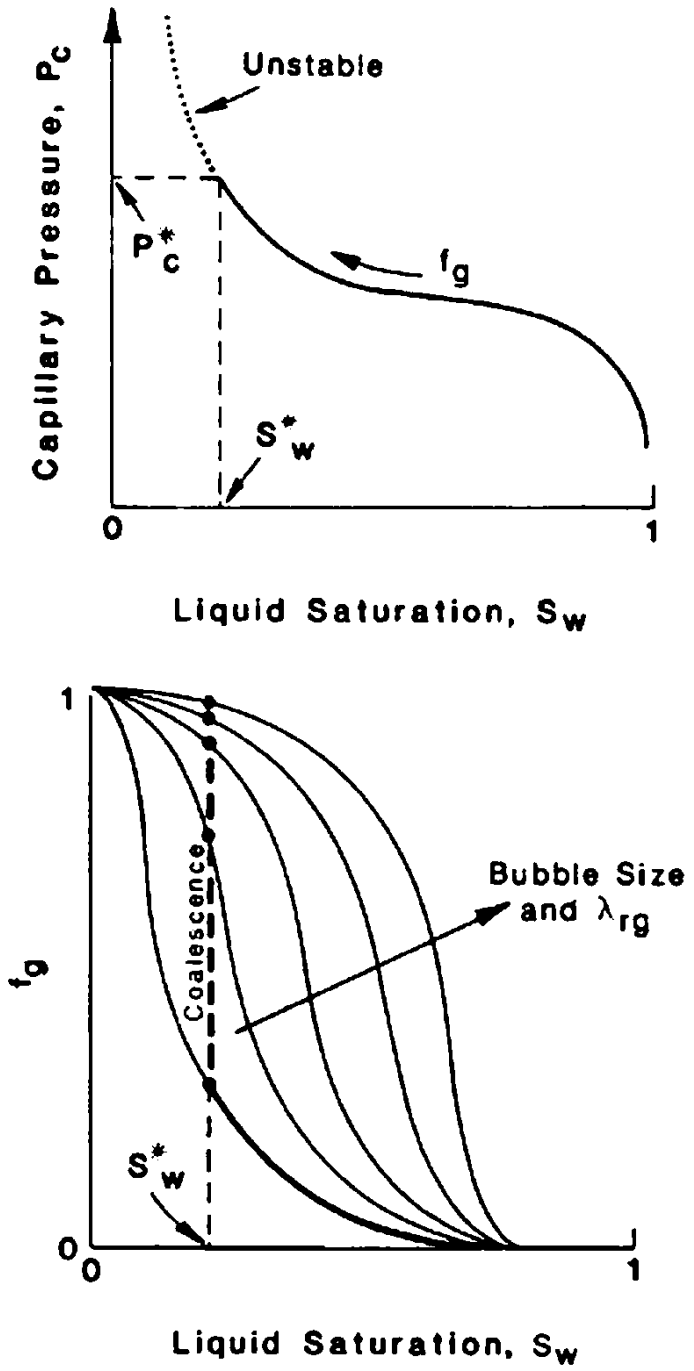

Figure 2.9: Sketches of capillary pressure and fractional flow curves operating during a 2-phase displacement Khatib et al. (1988)

2.3.1 Interfacial Properties and Foam Stability

The total surface area of a bubble increases as the bubble size decreases for a constant fractional flow of gas. The free energy is inversely proportional to the surface area. A dispersion of small bubbles is obtained when energy is added to the system (Kovscek and Radke, 1994). Hence the free energy of the foam is increased by adding mechanical energy or by using a foam agent to reduce the interfacial free energy (or interfacial tension). The interfacial tension is an imbalance of intermolecular forces which tend to contract in the direction of the liquid located at the interface forcing the interface to adopt a geometry that minimizes the interfacial free energy. The sum of these contracting forces that act parallel to the interface is known as the interfacial tension. The lamella has two gas-liquid interfaces, each with its own interfacial tension, for this reason the term film tension is defined as twice the interfacial tension of surfaces. Examples of foam agents are surfactants, macromolecules or finely divided solids. They act reducing the surface tension and increasing the interfacial area with a reduced mechanical energy input. When surfactants concentrate in an adsorbed monolayer at a surface they lower the interfacial tension and increase the interfacial viscosity, resulting in an increase of the mechanical resistance of the interfacial liquid (increase in foam stability). In aqueous solution, dilute concentrations of surfactant act more like normal electrolytes but at higher concentrations the molecules form organized aggregates called micelles (Schramm and Wassmuth, 1994). The lipophilic parts of the surfactants associate in the interior of the micelle and the hydrophilic part faces the aqueous medium. The concentration at which micelles formation become significant is called the critical micelle concentration (CMC). At concentrations higher than the CMC the effect of surface rheological properties is less pronounced and plays a secondary role in foam stability. However, foam stability increases even with concentrations above the CMC because of the formation of an ordered microstructure (stratification) in the draining foam films (Wasan *et al.*, 1994). At

very high surfactant concentrations, ordering of micelles occurs inside the liquid film and the bulk phase volume. At surfactant concentrations below or around the CMC the drainage and stability of the film are controlled by the adsorption of the surfactant molecules in the film surface and the properties of the adsorbed layers.

Foam stability is not necessarily a function of bubble size although there may be an optimum size for an individual foam type. Changes in the size distribution with time yield a measure of the stability of foam. Foams that have drop-size distribution heavily weighted toward the smaller sizes will represent the most stable foam (Friedmann and Jensen, 1986; Schramm and Wassmuth, 1994). The cause of instability in foams with larger bubbles may be the mass transfer of gas between foam bubbles or lamella rupture due to film drainage (Friedmann and Jensen, 1986). Foam stability also has an important influence in viscosity because the increased interfacial area and thinner films increases the resistance to flow (Roof, 1970; Falls *et al.*, 1988). The viscosity will also be higher when the bubble size distribution is narrow rather than wide (for a given foam quality).

The effectiveness of the foam injection is favored by water-wet conditions. Any degree of oil-wet character reduces the effectiveness of the flowing foam. If the foam forming surfactant is adsorbed onto the solid surfaces altering the wettability, less surfactant would be available for foam generation.

The presence of other dissolved species, an additional liquid phase such as oil in an aqueous foam or fine solids, may also affect the foam stability. The effect of stabilizing or destabilizing depends on the affinity of the third phase to the liquid in the interfacial film, what determines if they tend to accumulate at the gas-liquid interface (Schramm and Wassmuth, 1994). Friedmann and Jensen's (1986) results showed that the ability of the surfactant to reduce the gas relative permeability was impacted by the presence of the residual oil phase. Without oil, gas phase mobility was substantially reduced by the surfactant. One possible explanation is that when the oil is present in the porous media during surfactant injection it occupies the larger

pores (water wet sandstone). Without space the gas-surfactant interface would not expand freely from the pore throats to form bubbles (snap-off). As the oil saturation decreases more space is available and then more bubbles are formed. According to Farajzadeh *et al.* (2012) foam can be destabilized by oil by the following mechanisms:

1. Foam-forming surfactant may be absorbed by the oil when there is emulsion or adsorbed by the rock, causing depletion of surfactant in the aqueous phase and in the gas-liquid interface

2. Surfactants from the oil may be adsorbed by the foam lamella forming either a mixed or a replaced adsorption layer producing a less favorable state of foaming

3. Components from the oil may be adsorbed by the porous media altering the wettability of the solid phase which would make more difficult the generation or regeneration of foam

4. Oil may spread on foam lamella and displace the foam stabilizing interface

5. Oil may emulsify and allow drops to break the stabilizing interface

2.3.2 Fundamentals of foam flow in porous media

Several authors in the literature reported two steady state flow regimes for foams: high and low quality regimes (Osterloh and Jante Jr, 1992; Vassenden *et al.*, 2000; Cheng *et al.*, 2000) . Those regimes are function of foam quality (f_g) or injected gas volume fraction. At the high quality or coalescence regime the pressure gradient ∇P is independent of the gas flow rate and the flow is controlled by coalescence at the limiting capillary pressure. In this regime both capillary pressure and water saturation remain at the limiting capillary pressure and limiting water saturation, being independent of gas and water flow rates. For the low quality regime, the pressure gradient (∇P) is independent of the liquid flow rate; bubble size is fixed

but water saturation changes with flow rates. Foam rheology during flow is shear-thinning as a function of overall flow rate. There is a transition between regimes characterized at a given foam quality (f_g^*). Falls *et al.* (1988) classifies the foam in the porous media in terms of continuity: (1) discontinuous-gas foam (entire gas phase is made discontinuous by the lamella and no gas channels are continuous) and (2) continuous-gas foam (porous media contains one or more interconnected gas channels that are interconnected by the lamella over macroscopic distances). Figure 2.10 shows a schematic representation of the discontinuous and continuous gas phase.

Foam can influence the phase mobilities in different ways. The liquid mobility does not depend on whether the gas exists as a continuous phase or as a foam. The gas mobility is reduced because the foam diminishes the cross-section area through which the gas is able to flow, and Falls *et al.* (1988) consider this to be strictly a relative permeability effect; in other words, the foam creates a large effective trapped gas saturation. When all the gas phase is discontinuous, not only the relative permeability is smaller, it also appears to have an increased viscosity because of the movement of the lamellae into the porous media. About relative permeability effects, Falls *et al.* (1988) believe that the gas relative permeability is proportional to the area through which gas flows. The area open to flow should depend on the pressure gradient and density of stationary bubbles (texture), so the gas relative permeability increases only if the pressure gradient is large enough to mobilize stationary lamellae.

The consequences of a limiting capillary pressure for the foam flow in porous media are listed by Khatib *et al.* (1988). The authors believe that the critical capillary pressure limits how high above the free water level the discontinous-gas foams (containing moving lamellae) and the continuous-gas foams (containing only stationary lamellae) can exist in a reservoir where gravity can segregate gas and liquid. The limiting capillary pressure could be used as a parameter to screen surfactants for EOR processes, by recognizing that when lamellae can support higher capillary pressures they should have greater potential for reducing gas-phase

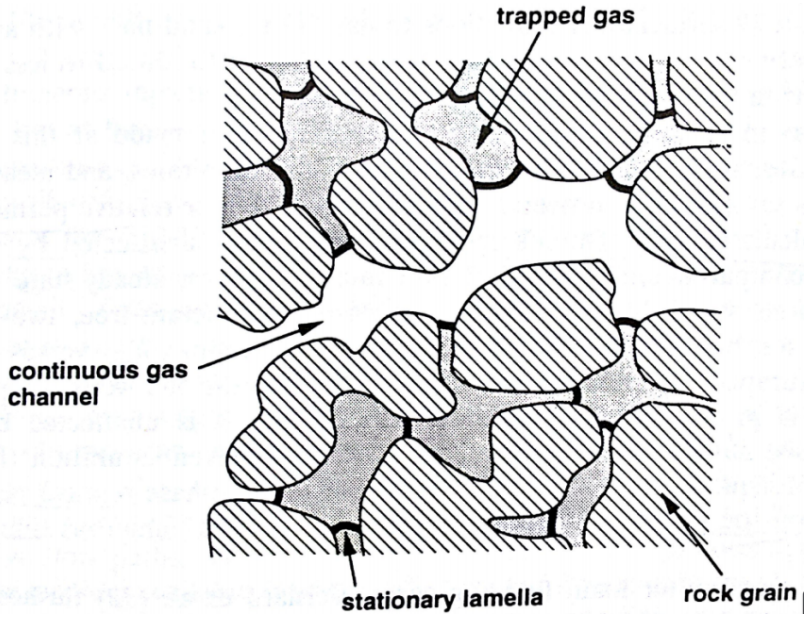

Figure 2.10: Continuous and discontinuous gas phase (Kovscek and Radke, 1994)

mobility. Whenever this limiting capillary pressure is maintained in the porous medium, relative gas mobility can be calculated by the capillary pressure curve, relative liquid mobility function, and ratio of gas-to-liquid fractional flow. The relative gas mobility is greater than or equal to its value at the limiting capillary pressure, for a given gas fraction flow curve.

2.3.3 Foams bulk properties

Density of foam is calculated ignoring the mass of gas, as shown in Equation 2.14.

$$\rho_F = \frac{m_L}{V_F}, \tag{2.14}$$

where m_L is the mass of liquid in foam and V_F is the total volume of foam.

Equation 2.15 is used for foams made from a liquid of density ρ_L and volume

V_L.

$$\frac{\rho_L}{\rho_F} = \frac{V_F}{V_L}, \tag{2.15}$$

where V_F/V_L is termed the expansion factor (or ratio) of a foam.

A reformulation of the factor $\frac{\rho_L}{\rho_F}$ yields the so called increase of volume upon foaming, or foaming power, calculated as $100\left[\left(\frac{\rho_L}{\rho_F}\right) - 1\right]$.

A simple description of foam viscosity applies Newtonian behavior in laminar flow (Equation 2.16).

$$\tau = \eta\dot{\gamma}, \tag{2.16}$$

where η is the coefficient of viscosity (milli pascal-seconds), τ is the shear stress and $\dot{\gamma}$ is the shear rate. For non-Newtonian fluids η is not a constant ($\eta(\dot{\gamma})$).

Foams are frequently pseudo-plastic (as shear rate increases, viscosity decreases), also termed shear thinning. Persistent foam usually exhibits a yield stress. There is relatively lack of data for foam viscosity, compared to other colloidal systems because measurements are not reproducible or not representative. For wet foams the viscosity can be estimated the same way as emulsion viscosities using an empirical extension of Einstein's equation for a dilute dispersion of spheres, which assumes Newton behavior (Equation 2.17).

$$\eta = \eta_0(1 + \alpha_0\phi + \alpha_1\phi^2 + \alpha_2\phi^3 + ...), \tag{2.17}$$

where η_0 is the liquid viscosity, ϕ is the gas phase volume fraction, and the αs are empirical constants. In dry foams, the internal phase has a high volume fraction, and the foam viscosity increases strongly because of bubble generation or structural viscosity. Fluid becomes non-Newtonian and frequently exhibits a yield stress. Roof (1970) and Falls *et al.* (1988) developed a theory for the apparent gas viscosity including the resistance of the transport of lamellae through constricted pore

channels. The model defines two main components: the resistance from flow through smooth, uniform pores (μ_s), and that resulting from constrictions. When the average bubble density in the flowing phase is less than the density of pore constrictions and $K_{rg} << 1$, measured apparent viscosities are well correlated by Equation 2.18.

$$\mu_{g,app} = \mu_s + G\sigma n_L \frac{r}{v_g}, \tag{2.18}$$

where $\mu_{g,app}$ is the apparent gas viscosity, G is a geometrical factor, σ is the gas/liquid interfacial tension, n_L is the number of lamellae per unit length, r is the equivalent capillary radius of porous medium, and v_g is the interstitial velocity of the gas.

2.3.4 Numerical Models for Foam Flow in Porous Media

Foam generation into porous media causes a reduction in the gas mobility, which may be due a decrease in relative permeability or an increase in the foam viscosity. Since both parameters influence foam mobility, different foam models were developed where changes in relative permeability or viscosity (or both) altered the foam mobility. The work of Ma *et al.* (2015) discussed the applicability and limitation of different foam modeling techniques (analytical, empirical, and mechanistic); the authors described the function of foam generation mechanisms in different mechanistic models from the literature.

Semi empirical Alteration of Gas Phase Mobilities

In STARS (2011) a simple (quasi-equilibrium) approach to foam modeling is employed. The basic assumption is that foam creation and coalescence mechanisms occur rapidly relative to flow such that whenever gas and surfactant coexists, foam exists. A simple interpolation scheme based on surfactant concentration, gas flow velocity, and the presence of oil employs a dimensionless interpolation factor FM

(Equation 2.19) varying between $FM = 1$ (no foam) and $FM \approx (MRF) - 1$ (strongest foam), where MRF is the mobility reduction factor (Equation 2.20). This dimensionless interpolation factor is then used to modify the relative permeability of the gas, as in Equation 2.21.

$$FM = \left[1 + MRF\left(\frac{ws}{ws^{max}}\right)^{es}\left(\frac{S_o^{max} - S_o}{S_o^{max}}\right)^{eo}\left(\frac{N_c^{ref}}{N_c}\right)^{ev}\right]^{-1}, \tag{2.19}$$

where w_s^{max} is the maximum surfactant concentration, N_c^{ref} is the reference capillary number (no oil in the core), and w_s^{max}, S_o^{max} and N_c^{ref} are interpolation parameters.

$$MRF = \frac{(\Delta P)_{foam}}{(\Delta P)_{nofoam}}, \tag{2.20}$$

where $(\Delta P)_{foam}$ is the pressure gradient of the foam and $(\Delta P)_{nofoam}$ is the pressure gradient of the gas.

$$k_{rg}^f = k_{rg} \times FM, \tag{2.21}$$

where k_{rg} is the gas relative permeability with no foam and k_{rg}^f is the gas relative permeability with foam.

STARS (2011) also allows the use of a more mechanistic approach to foam modeling, also referred as the lamella density approach. A lamella component in the gas phase is defined whose concentration determines flow properties (viscosity, relative permeability, resistance factor) of the gas phase. In situ generation and coalescence also affect lamella, and these processes may be modeled by non-equilibrium mass transfer rate expressions.

Although foam is essentially a mixture of water, surfactant and gas, in ECLIPSE (2014) it is modeled as an effective concentration of surfactant transported either by gas or water phase. Adsorption of the foam is assumed to be instantaneous and desorption may be specified. Foam effectiveness over time is

modeled by foam decay $\lambda(S_w, S_o)$. The gas mobility reduction is accomplished by the use of a simple multiplier, supplied as a function of foam concentration. The mobility modification is applied explicitly in the subsequent iteration or time-step. Two methods of modeling gas mobility reduction are available: a tabular model and a functional form. In the latter, the gas mobility reduction factor is represented in terms of a set of functions which represents the individual reduction factors due to surfactant concentration, oil saturation, water saturation, and capillary number.

Rossen *et al.* (1994, 1999); Cheng *et al.* (2000); Delshad *et al.* (2002) described an empirical foam model known as the UT model. Originally developed for the high quality regime, the model also exhibit reasonable results for the low quality regime. The UT model modifies the gas relative permeability for the effect of the foam as in Equations 2.22, 2.23 and 2.24.

$$If\ S_w < (S_w^* - \epsilon)\ and\ C_s < C_s^o,\ then\ k_{rg}^f = k_{rg}^o(S_w), \tag{2.22}$$

$$If\ (S_w^* - \epsilon) < S_w < (S_w^* + \epsilon)\ and\ C_s \geq C_s^o,\ then\ k_{rg}^f = \frac{k_{rg}^o(S_w)}{\left(1 + \frac{(R-1)(S_w - S_w^* + \epsilon)}{2\epsilon}\right)}, \tag{2.23}$$

$$If\ S_w > (S_w^* + \epsilon)\ and\ C_s \geq C_s^o,\ then\ k_{rg}^f = \frac{k_{rg}^o(S_w)}{R}, \tag{2.24}$$

where C_s is the surfactant concentration in the aqueous phase, C_s^o is a threshold surfactant concentration for foam formation, k_{rg}^f is the effective gas relative permeability modified for foam, $k_{rg}^o(S_w)$ is the gas relative permeability as a function of water saturation in the absence of foam, and S_w^*, ϵ, and R are model parameters. S_w^* is the critical water saturation at which foam collapses, it is a function of surfactant and rock properties, not a function of flow rate.

Population Balance Model

Kovscek and Radke (1994); Kovscek *et al.* (1993, 1994, 1997); Apaydin and Kovscek (2000); Chen *et al.* (2010) described the population balance model. The mass balance equation for the gas/foam phase and for the surfactant are shown in Equation 2.25 (non-wetting foam or gas phase in an one-dimensional medium).

$$\frac{\partial[\phi\rho_g S_g]}{\partial t} + \frac{\partial(\rho_g u_g)}{\partial x} = Q_g, \tag{2.25}$$

where t denotes time, x gives the axial location, ϕ is the porosity, ρ_g is the mass density, S_g is the saturation of the gas phase, u_g is the superficial or Darcy velocity and Q_g is a source-sink term. The mass balance for water is written by changing the subscript g by w. A mass balance for the surfactant is given in Equation 2.26.

$$\frac{\partial[\phi(C_s S_w + \Gamma_s)]}{\partial t} + \frac{\partial(u_w C_s)}{\partial x} = Q_s \tag{2.26}$$

where C_s is the number or molar concentration of the surfactant in the aqueous phase, Γ_s is the amount of surfactant adsorption on the rock surfaces in units of moles per void volume, and Q_s is the source-sink term for surfactant in units of moles per unit volume per unit time.

Because the mobility of foam is a strong function of texture, mechanistic prediction of foam flow in porous medium is impossible without a conservation equation to account for the evolution of foam bubble size. The unidimensional transient population balance on the mean bubble size may be written as in Equation 2.27 (Kovscek and Radke, 1994; Kovscek *et al.*, 1993, 1994, 1997; Apaydin and Kovscek, 2000; Chen *et al.*, 2010):

$$\frac{\partial[\phi(S_f n_f + S_t n_t)]}{\partial t} + \frac{\partial(u_f n_f)}{\partial x} = \phi S_g(r_g - r_c) + Q_b, \tag{2.27}$$

where subscripts f and t refer to flowing and trapped foam, and n is the foam texture or bubble concentration. n_f and n_t are, respectively, the number of foam bubbles

per unit volume of flowing and stationary gas. The total gas saturation is given by $S_g = 1 - S_w = S_f + S_t$, and Q_b is the source/sink term for foam bubbles in unit of number per unit volume per unit time. The first term in the time derivative ($\phi S_f n_f$) is the rate at which texture of flowing foam becomes fine or coarser per unit rock volume, and the second ($\phi S_t n_t$) is the net rate at which foam bubbles trap. The spatial term deals with the foam convective transport. On the right side of the equation, generation and coalescence rates (r_g and r_c) are expressed on a per volume of gas basis, both being fundamental terms since they control the foam texture. Chen *et al.* (2010) proposed Equation 2.28 as the foam generation term. Others have proposed different generation term equations (Kam and Rossen, 2003; Kam *et al.*, 2007).

$$r_g = k_1 v_f^a v_w^b, \tag{2.28}$$

where $v_w = u_w/\phi S_w$ is the local interstitial liquid velocity and $v_f = u_f/\phi S_f$ is the local interstitial velocity of the flowing foam. These velocities depend upon the local saturation of flowing liquid or gas and the local pressure gradient (capillary pressure plus gravitational effects). Exponents a and b are power indices, with index b close to unity. Coefficient k_1 is the generation rate constant reflecting the number of foam germination sites. Chen *et al.* (2010) modified the foam generation term to predict foam flow behavior in both the high-quality and the low-quality regimes by writing the foam generation constant k_1 as in Equation 2.29.

$$k_1 = k_1^0 \left[1 - \left(\frac{n_f}{n^*}\right)^{\omega}\right], \tag{2.29}$$

where ω is a constant determining the shape of inverse proportionality of foam-germination sites to pre-existing gas bubbles and n^* is an upper limit for the concentration of foam bubbles that is related to pore size. Equation 2.29 reflects fewer foam-germination sites as bubbles texture increases. The dependence of k_1 on S_w is not included. Chen *et al.* (2010) asserts in their conclusion that the foam texture dependence of the foam generation term successfully predicts the

steady-state pressure gradient trends in the high- and low-quality flow regimes, as well as the smooth transition between regimes. For the coalescence term Chen *et al.* (2010) proposes Equation 2.30.

$$r_c = k_{-1}(S_w) v_f n_f, \tag{2.30}$$

where $k_{-1}(S_w)$ is a coalescence rate constant which varies strongly with local aqueous-phase saturation, surfactant concentration and surfactant formulation. Note that higher v_f would lead to higher coalescence rates since stretched lamella are more vulnerable to breakage. Coalescence also depends on P_c^*, on account of the reason why the coalescence constant depends on surfactant formulation, concentration and S_w. Khatib *et al.* (1988) proposed a function to model $k_{-1}(S_w)$ using Equation 2.31,

$$k_{-1}(S_w) = k_{-1}^o \frac{(1 - S_w)}{(S_w - S_w^*)}. \tag{2.31}$$

Kovscek *et al.* (1993, 1994, 1995, 1997); Chen *et al.* (2010) write the coalescence rate constant (k_{-1}) as function of the capillary pressure (Equation 2.32), which also allows the coalescence rate to increase smoothly from zero at S_w equal to 1 to very large values as P_c approaches P_c^* at S_w equals to S_w^*. In the vicinity of the P_c^* the slopes tend to infinity.

$$k_{-1}(P_c) = k_{-1}^o \left(\frac{P_c}{P_c^* - P_c} \right)^2. \tag{2.32}$$

The confined foam is divided into intermediate-wetting trapped and nonwetting flowing portions. To consider the flow of the moving foam one could use the Darcy's law, but μ_f is not constant. The gas viscosity is then replaced with the effective viscosity or the foam viscosity (Roof, 1970; Kovscek *et al.*, 1993). For the relative permeability a Stone-type model is used and the relative permeability of the aqueous wetting phase is assumed to be unaffected by the presence of foam (Kovscek *et al.*, 1993, 1994, 1995, 1997; Kam and Rossen, 2003; Kam *et al.*, 2007;

Chen *et al.*, 2010). Knowledge of the fraction of foam trapped in the porous medium is needed to complete the flow model (Kovscek *et al.*, 1993, 1994, 1995, 1997; Kam and Rossen, 2003; Kam *et al.*, 2007; Chen *et al.*, 2010). The fraction of trapped foam is written as $X_t = S_t/S_g$. Tang and Kovscek (2006) worked with the fraction of mobile foam in porous media, X_f (Equation 2.33). According to the authors, there were few steady-state flow measurements in the literature, most of which had sparse measurements and no quantification of the size of the bubble at the core's exit. The authors obtained experimental results and developed a statistical model based on the percolation theory to scale mobile gas fraction. The model is applicable to predict foam's relative permeability during foam flow into the porous media. Foam's relative permeability is a function of the pressure gradient, permeability, and bubble density.

$$X_f = \frac{\Psi}{S_g}\left[\frac{f_c|\nabla p|}{k^{1/2}n_f}\right]^{\eta}, \tag{2.33}$$

where Ψ is a constant of proportionality, S_g is the gas saturation, ∇P is the pressure gradient, k is the rock permeability, and n_f is the foam texture. f_c and η are parameters with values of 0.25 and 0.4, respectively (assuming cubic lattices filled with largely immobile gas).

Inspired by the bubble-population correlation (Bertin *et al.*, 1998a,b), Chen *et al.* (2010) introduced the population-balance model with the local-equilibrium approximation, which is useful for large scale calculations. In their derivation, the transient balance on the mean foam bubble size (Equation 2.27) in dimensionless form is given in Equation 2.34.

$$\frac{\partial}{\partial \tilde{t}}[\phi(S_f\tilde{n}_f + S_t\tilde{n}_t)] + \frac{\partial}{\partial \tilde{x}}(\tilde{u}_f\tilde{n}_f) = \phi S_g Da_{-1}\left(\frac{Da_1}{Da_{-1}}|\tilde{v}_w||\tilde{v}_f|^{1/3} - |\tilde{v}_f|\tilde{n}_f\right), \tag{2.34}$$

where S_f and S_t are the flowing and trapped foam saturations, respectively; S_g is the gas saturation; ϕ is the porosity; $\tilde{n_f}$ and $\tilde{n_t}$ are the dimensionless density of

flowing and trapped foam bubbles, respectively; $\tilde{u_f}$ is the dimensionless Darcy foam velocity; $\tilde{v_w}$ and $\tilde{v_f}$ are the dimensionless interstitial water and foam velocity, respectively; $\tilde{t}$ and $\tilde{x}$ are the dimensionless time and distance in x direction, respectively. Two dimensionless Damkohler numbers , Da_1 and Da_{-1} (Equations 2.35 and 2.36, respectively) are defined as the ratio of the characteristic fluid motion time scale to the characteristic reaction (foam generation/coalescence) time scale. A large Damkohler number ($Da >> 1$) corresponds to very rapid foam generation/coalescence in comparison to transport processes. A small Damkohler number ($Da << 1$) corresponds to very slow foam generation/coalescence in comparison to transport processes.

$$Da_1 = \frac{t_c}{t_{1,c}} = \frac{LU_c^{1/3}k_1}{n_c}, \tag{2.35}$$

$$Da_{-1} = \frac{t_c}{t_{-1,c}} = Lk_{-1}, \tag{2.36}$$

where t_c is a characteristic time, L is the core length, U_c is the characteristic velocity, and n_c is the characteristic density of foam bubbles.

Chen *et al.* (2010) show that when Da_1 and $Da_{-1} >> 1$, the in situ foam texture is dominated by local foam generation and coalescence, what is particularly true for applications at field-scale since Da_1 and Da_{-1} are proportional to the length scale. Chen *et al.* (2010) set the net rate of foam generation in Equation 2.27 equal to zero, assuming that generation and coalescence rates are in equilibrium. The authors obtained an equation for the density of the flowing foam shown in Equation 2.37.

$$n_f^{\omega} + \frac{n^{*\omega}k_{-1}|v_f|^{1-a}}{k_1^0|v_w|^b}n_f - n^{*\omega} = 0, \tag{2.37}$$

where n^* is the upper limit of the concentration of foam bubbles that is related to the pore size, and ω is a constant determining the shape of inverse proportionality of foam

germination sites to pre-existing gas bubbles. For $\omega = 3$, Equation 2.37 becomes a cubic equation that presents a single real root and can be easily solved for n_f at given liquid velocity, gas velocity, and capillary pressure using analytical formulas. Hence, a simple check must be done for the presence of surfactant before solving Equation 2.37 and if there is no surfactant the local equilibrium foam texture is set to zero.

Balan *et al.* (2012) investigated the effect of the density of the flowing foam on the viscosity and relative permeability of foam using a 3D pore-network model. Three viscosity models were used to evaluate the apparent foam viscosity of the flowing foam: linear, power-law, and Hirasaki-Lawson model. The authors observed that the foam density has low influence on the relative permeability of the gas, which showed a non-linear correlation with the flowing gas fraction. The phase trapping was cited as an important aspect of the foam flow modeling.

Estimation of Foam Parameters

Cheng *et al.* (2000) developed a simple approach to match foam modeling parameters (STARS and the P_c^* foam models) to both high- and low-quality regimes in a steady-state core-flood data; non-linear optimization could be used to match all parameters. The authors mention the importance of having experimental data in both flow regimes once using foam model parameters fitted to the wrong flow regime of a single coreflood datum would cause incorrect predictions. Boeije and Rossen (2013a) proposed a foam parameter fitting procedure for the STARS foam model adequate to model foam injection at finite water fraction; their approach is based on the work of Cheng *et al.* (2000) but is a more simple and flexible method that may be used for a single gradient pressure curve. The authors mention that for surfactant-alternate-gas the behavior of foam at low water fraction is important, while behavior at higher water fractions is less important. The transition between high- and low-quality foam regimes is assumed to be abrupt. Boeije and Rossen (2013b) proposed an approach to estimate foam parameters in the STARS foam model using

steady-state laboratory foam data and the fractional-flow theory (for foam injection without oil). The authors claim that the approach to estimate foam parameters for local equilibrium models depends on the foam injection method. The approach using fractional-flow curves would be appropriate for SAG foam injection processes. The water saturation must be measured during the experiment to allow fractional-flow curve plotting. Two examples were discussed. The authors mention that least-square optimization could be used, but they alert the importance of user judgment during the optimization. Ma *et al.* (2013) performed an experimental study and proposed a method to improve the estimation of the dry-out function parameters in the STARS foam model. They proposed a transient experiment (gas displacing a surfactant solution) to quantify the foam model parameters. The authors evaluated the effect of the gas fractional flow on the foam apparent viscosity, calculated with Equation 2.38), using a hybrid contour plot method.

$$\mu_{foam,eff} = \frac{-k\nabla p}{u_w + u_g}. \tag{2.38}$$

2.3.5 Foam as a Mobility Reduction Agent in Heterogeneous Reservoirs

Before studying the use of mobility control techniques in fractured and heterogeneous reservoirs we define conformance as in Sydansk and Romero-Zeron (2011): "The term conformance in its truest and original form is defined as the measure of the volumetric sweep efficiency during an oil recovery flood or process being conducted in an oil reservoir." We define the volumetric sweep efficiency (E_V) as the percentage of the pore volume swept by the injected fluid (Equation 2.39). Based on this definition, the goal of applying foam as a mobility control agent is to improve conformance in heterogeneous reservoirs under fluid (water or gas) injection.

$$E_V = E_A E_l, \tag{2.39}$$

where E_A is the areal sweep efficiency and E_l is the vertical sweep efficiency.

Sydansk and Romero-Zeron (2011) explains the difference between conformance problems in heterogeneous and fractured reservoirs. In the upper part of Figure 2.11 there is a representation of two wells (a producer and an injector) in an heterogeneous reservoir with a high permeability layer; if that was a homogeneous reservoir the injection saturation front would move as a vertical line from left to right, but since there is a high permeability layer the breakthrough of the injected fluid happens early and oil is left behind (poor vertical sweep efficiency). In the lower part of Figure 2.11 there is a representation of a reservoir with one conductive fracture between the injector and the producer in a 5-spot injection scheme. The high contrast of conductivity between matrix and fractures in a fractured reservoir reduces the performance and the efficiency of most of the improved oil recovery techniques, as the injected fluids prefer to flow through fractures. In that case the fracture serves as a conduct which causes an early breakthrough of the injected fluid (poor areal sweep efficiency). Assuming an homogeneous reservoir and no conductive fracture the saturation front should move radially from the injector to the producer well.

In real field cases a combination of both vertical and areal conformance problems might occur, depending on the reservoir characteristics; hence the application of a conformance improvement method should be used to delay the injected fluid breakthrough by stabilizing the saturation front of the injected fluid and reducing gravity override. A conformance improvement method will also benefit miscible injection, since the residence time of the injected fluid is increased allowing more time for miscible processes to take place. Many works in the literature have attempted to evaluate the use of foam as a mobility reduction agent.

Bertin *et al.* (1999) studied the flow of foam into an annular, heterogeneous porous media with permeability ratio of 67. Experiments were done with and without crossflow between zones. Water saturation was measured by the use of

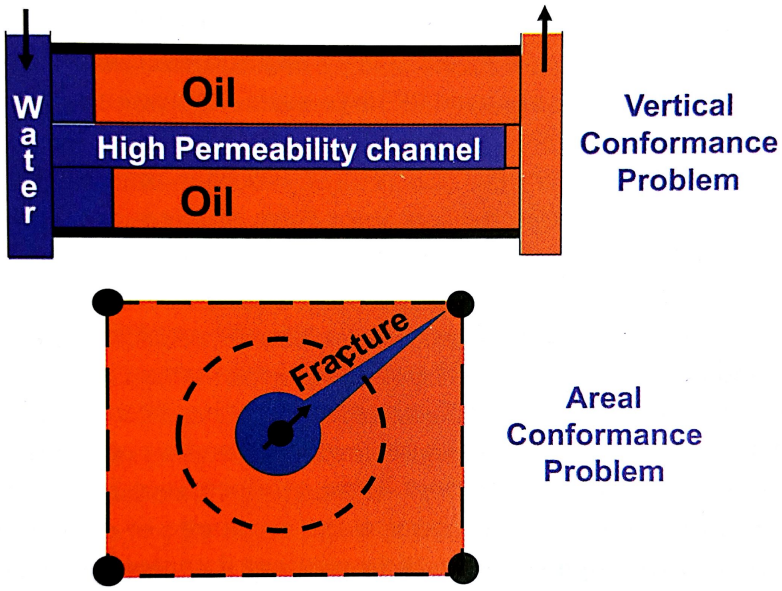

Figure 2.11: Example of conformance problems in heterogeneous and fractured reservoirs (Sydansk and Romero-Zeron, 2011).

X-ray computed tomography. Fronts moved at the same rate when zones were in capillary contact, but when the capillary contact was suppressed by one sealant layer, the gas was blocked in the high permeability zone and diverted to the low permeability zone. Cheng *et al.* (2000) observed that the foam diversion depends on permeability in high-quality regime, whereas, for low-quality regime the permeability has a very small influence. Bertin (2000) modeled the foam diversion in heterogeneous media using the bubble population correlation. The authors considered a 1D model and solved the equation using the IMPES scheme; numerical results were qualitatively in good agreement with experimental data from literature. Yan *et al.* (2006) mention few studies about foam flow in fractures. They studied the mechanism of foam flow in fractures to predict foam diversion in heterogeneous media. The authors adapted the capillary tube theory to predict the foam apparent viscosity to the case of a uniform fracture. Also a heterogeneous fracture was considered and used to study foam diversion. Three contributions to the apparent

viscosity of foam were considered: liquid between bubbles (μ_{app}^{liq}, in Equation 2.40), bubble deformation (μ_{app}^{shape}, in Equation 2.41), and surface tension gradient. The latter was found to be insignificant for the studied system. The proposed analytical model was validated against experimental data.

$$\mu_{app}^{liq} = (1 - f_g)\mu^{liq}, \tag{2.40}$$

$$\mu_{app}^{shape} = \frac{n_L \Delta p_{dynamic} b^2}{12U}, \tag{2.41}$$

where μ^{liq} is the viscosity of pure liquid, f_g is the gas fractional flow, n_L is the number of equivalent lamella per unit length, b is the fracture aperture, U is the velocity of the bubble, σ is the surface tension, r_c is the radius of curvature of gas-liquid interface (when bubbles are not in contact r_c is equal to the capillary tube radius). Srivastava *et al.* (2009) cited the foam as an alternative to polymer injection, stating that it can provide mobility control in chemical-EOR processes. They associate the improvement in sweep efficiency with the resistance to movement and the reduction of the liquid effective permeability provided by the foam phase. The authors mention that an advantage of foam over polymer is that foam is stronger in high permeability region. The strong foam formed in high permeability regions diverts the injected fluid to low permeability regions providing conformance control. Srivastava *et al.* (2009)'s work clearly states that the use of foam in chemical EOR can reduce the technical disadvantages associated with polymers in low permeability and fractured reservoirs. Haugen *et al.* (2012) states that the occurrence of foam generation primarily in high permeable zones is a favorable property of foams, since it diverts flow to low permeability regions and increases sweep efficiency. The authors investigated the possibility of using foam to divert flow from open fractures into matrix blocks. They carried out experiments using foam to reduce fracture transmissivity and to produce unswept residual oil in highly

fractured low permeable oil-wet limestone. Two approaches to generate foam were adopted, in-situ generation of foam in the fracture during co-injection of surfactant solution and N_2 gas and injection of pre-generated foam from a Bentheimer sandstone foam generator. Four injection schemes were tested. The results showed low recovery levels for the water flood and gas injection, capillary imbibition was not observed and no significant pressure increase across the fractures was obtained. Low recovery was obtained after surfactant injection. In-situ foam generation was not observed in fractures with smooth fracture surfaces, and the gas mobilities were not reduced. Pre-generated foam greatly enhanced oil recovery, and a decrease in fractures transmissivity was observed, associated with increasing differential pressures, leading to the displacement of the oil in the matrix. The foam front progression in the matrix appears to be inhibited by the oil presence, so apparently foam was sensitive to the presence of oil and wettability of the system. The surfactant also acted by altering the wettability of the matrix. Recovery rate was sensitive to fracture/matrix permeability ratio, and the most efficient recovery was for low ratios.

Khalil and Asghari (2006) performed a series of experiments to select a suitable surfactant for CO_2-foam flooding in carbonate porous medium. Effects of various parameters on the CO_2-foam mobility were evaluated and compared to a WAG injection scheme. Results have shown that higher foam quality leads to lower foam mobility, higher temperatures and lower pressures reduce the mobility of CO_2-foam system, and that brine concentration has a minor effect on CO_2-foam mobility. The comparison with the water and WAG injection resulted in an additional oil recovery for the CO_2-foam injection. Zhang *et al.* (2010) studied immiscible CO_2 flooding aiming to investigate the phase behavior of reservoir oil and injected solvents (such as pure CO_2 and enriched flue gas), measure interfacial tensions and viscosity when chemicals are added to brine, examine immiscible WAG and immiscible WAG augmented with chemicals, and study the displacement and

sweep efficiency during WAG coreflooding tests. The authors observed that when a chemical, such as surfactant, was added in the WAG injection the displacement efficiency was improved due to the generation of foam and consequent reduction in injected gas mobility. Emadi *et al.* (2011) presented results of vizualization experiments carried out in high pressure transparent models to investigate the performance of subcritical CO_2 and CO_2 foam injection in heavy crude oil. Three tests were done: the tertiary injection of CO_2, the CO_2 foam flood with pre-flush of surfactant, and the CO_2 foam flood without pre-flush of surfactant. Experiments show that foam improves heavy oil production and reduces the volume of injected CO_2, but strong foam is needed; otherwise displacement and oil recovery efficiency are reduced. The authors mention that the CO_2 foam injection improves the sweep efficiency and micro-scale displacement efficiency (pore scale). The effect of the surfactant partition between water and super critical CO_2 was studied by Ren *et al.* (2011). Corefloods were used to estimate foam parameters and a commercial simulator was used to evaluate the effect of foam partitioning coefficient from lab to field scale. The authors concluded that surfactant structure has a greater effect on the surfactant partitioning than temperature or pressure and that an increase in the surfactant partitioning coefficient reduces foam propagation. Mukherjee *et al.* (2014) evaluated a CO_2 gas injection project for the Salt Creek Field, Natrona County, WY. The followed steps were as follows: selection of pilot area, evaluation of laboratory results, reservoir modeling, evaluation of the injection strategy, and the implementation on the field. The injection pattern used was an inverted 5-spot, defined by simulation results and operational aspects. A foam model was used to model the chosen surfactant formulation behavior and allow predictions. The authors observed a 40% reduction of gas injectivity, which was attributed to the foam generation. Norris *et al.* (2014) evaluated the foam injection pilot of the Salt Creek Field using production and injection profiles. Data indicated diversion of the CO_2 to the bottom of the reservoir, and chemical tracers, which showed that the

foam injection was able to delay tracers' breakthrough. Reservoir simulations showed the foam diversion (streamline analysis) and the gas relative permeability reduction due to the foam (finite differences).

Kiani *et al.* (2011) presented the results of a conceptual model to evaluate the performance of a surfactant injection in a pilot test configuration using three different models with different approaches to gridding and grid refinement. The models used were dual porosity, dual permeability and single porosity formulation. Results using a commercial and an in-house numerical simulator showed that the dual porosity, dual permeability formulation led to smaller additional oil recovery than the single porosity model because of the inability to model gravity and viscous forces Skoreyko *et al.* (2011, 2012) developed an workflow for foam flow modeling using a commercial numerical simulator. Their model was validated against laboratory experiments and production data from a foam injection pilot in a single well located in the Aka field, Cantarrel complex. Foam injection was proposed to control flow mobilities and to take advantage of the surfactant transport to the matrix, which would consequently reduce the interfacial tension. The mechanistic foam model developed by the authors considered a set of reactions in order to properly model the foam behavior. The main influencing parameters were the trapped foam, foam regeneration, low concentration limit, and high foam quality cut-off. A total of ten reactions were used and the model provided a good history match with the production data. Hou *et al.* (2012) studied foam flood as a candidate EOR mechanism for a heterogeneous reservoir in Daqing oil field, where water flooding and polymer flooding were conducted previously. Systematic laboratory experiments were performed in order to evaluate recovery efficiency, study foamability and stability of the foam under different injection modes (co-injection, alternative injection, and direct injection of foam were considered), and verify the effect of different gas-liquid injection ratio (for the direct injection mode). Results indicated that foam successfully blocked thief zones in highly

heterogeneous reservoirs after polymer injection. The direct injection model was the most effective, with approximately 10% difference in oil recovery for the co-injection and 15% difference for WAG. The foam formulations were optimized for foamability and stability with the use of polymers. Foam was stabilized with surfactant and polymer. The polymer helped to stabilize the foam by improving the viscoelasticity of the foam film and avoiding liquid draining. Spirov *et al.* (2012) used ECLIPSE (2014) (black-oil formulation) empirical foam model to model foam injection in a complex geological model of two Norwegian Reservoirs. The new model was used for sensitivity study and for history matching process of a Foam Assisted Water Alternated Gas Injection (FAWAG) pilot. A reasonable history matching was obtained by the authors and the differences between simulated and history data were due to complexity of fluid flow controls inside the reservoir. Afonja *et al.* (2012) used the empirical method incorporated in STARS to evaluate and identify critical parameters that can be used to obtain the minimum but most effective concentration of surfactant to maximize oil recovery in CO_2 foam injection. STARS (2011) empirical model was used to model a 1D displacement of oil, water, and gas in the presence of foam, with foam parameters obtained from laboratory corefloods. The simulation results were successfully matched to experimental data. The authors state that additional work should be carried out to investigate and optimize surfactant concentration and foam injection. Kharrat *et al.* (2012) studied a mature field with more than sixty years of production. Several EOR processes were evaluated, such as continuous gas injection (GI), water alternate gas flooding (WAG), simultaneous water and gas injection (SWAG), foam assisted WAG (FAWAG) and gas assisted gravity drainage (GAGD). Experimental tests using cores and numerical simulations were done. Due to the high fracture frequency of the reservoir, the GI and GAGD were considered unfeasible because of early gas breakthrough. The FAWAG process resulted in the higher recovery due to the reduction in IFT. The authors mention the great influence of the fracture density in

the selection of the optimum injection/production pattern.

The Gas Oil Gravity Drainage (GOGD) is considered the main recovery mechanism for non-water-wet naturally fractured reservoirs, but care should be taken since this method needs a balance between the oil production and the gas injection rate in order to avoid gas-out or water-out. GOGD is a slow process and requires continuous gas injection to replace the produced oil and avoid the rise of the oil rim into the fracture. Farajzadeh *et al.* (2010) studied how to improve the GOGD by reducing the gas mobility of the injected gas adding a foaming agent before injecting into the fracture. A sensitivity study of different parameters was performed. Results show that the amount of oil produced increases with an increase in the foam strength for the same gas constraint. Foam generation in the fractures creates a viscous pressure drop directly transferable to the matrix and accelerating oil production. Ashoori and Rossen (2012) cite the SAG (surfactant-alternating-gas) as the preferred EOR method for foam injection. They show a connection between the SAG effectiveness and the K_{rw}, independent of the process related to the gas mobility reduction by foam. The work assumes that if the foam process does not succeed in the absence of mobile oil, it will not succeed in the presence of immobile oil. Their analysis used the method of characteristics, or fractional flow analysis, of foam processes. The authors state that foam is useful as a mobility control agent provided that the total mobility of foam is lower than the mobility of the swept bank ahead of the foam. Ashoori and Rossen (2012) also concluded that SAG is inappropriate for naturally fractured reservoirs if straight line relative permeabilities apply, even if strong foams can be stabilized into the fractures. They show that if foam collapses at $S_w > S_{wc}$ it is difficult to achieve a successful SAG process for a medium with linear $k_{rw}(S_w)$ functions.

Talebian *et al.* (2013) performed an extensive literature survey on the foam-assisted CO_2 EOR, focusing in miscible and immiscible WAG using CO_2-foam injection (considered as a combination of chemical and gas EOR methods). The

authors state that CO_2 recovers more oil due to miscibility generation (lowering the interfacial tension of CO_2 and oil interface). The immiscible process is also economically attractive due to reduction in oil viscosity and oil swelling (primary mechanisms of immiscible CO_2 flood). The adverse mobility ratio due to viscosity differences between CO_2 and oil can lead to conformance and/or mobility issues, generating instabilities in the displacement front; those were the most critical dynamic concerns. Talebian *et al.* (2013) proposed new chemical EOR techniques to overcome these issues, among them the CO_2 foam injection. Foam stabilizes the displacement front by increasing the viscosity of the injected gas and reduces the interfacial tension in oil and water interface by presence of the surfactant (wettability alteration, which may occur because of foam rupture in the porous media). Talebian *et al.* (2013) cite that there is still lack of understanding of the phenomena and mechanisms involved in different applications and conditions of the FAWAG process. The authors also mention a consensus of its benefits when applied at the right condition. Their work found open questions and debates in oil industry concerning foam-assisted CO_2 injection: upscaling from core test to pilot and field levels, representative and predictive tools, lack of pilot and field trials, and challenges in operations and logistics.

2.4 Summary

2.4.1 Numerical Models for Naturally Fractured Reservoirs

- The EDFM has proven to be an efficient and accurate method to model fractured reservoirs, but many issues must still be studied to increase accuracy in complex cases. The harmonic average have been used to calculate matrix to fracture connections in the EDFM, but that approach is simplistic and does not account for fracture anisotropy. The full permeability tensor of the matrix and the unit vector of the fracture plane should be used to transform the direction of the vector representing the flow from the matrix to the fracture

and correct anisotropy.

- Hydraulic fractures or even conductive faults are heterogeneous and present diverse geometries and varying conductivity. The EDFM must be improved by allowing the connection between fracture blocks into the same fracture to account for heterogeneous fractures with different geometries.

- Well productivity between horizontal wells and fractures are calculated using an approach based on Peaceman's equation. That approach assumes that the intersection between the fracture and the matrix gridblock will always assume a quadrilateral geometry. For three dimensional cases the well productivity index must be calculated using an approach similar to what has been used in unstructured grids.

- The integration of the EDFM equations allows the modeling of a greater number of fractures as a dual continuum media. Averaged permeability calculation must be improved by using existing methods to allow a better representation of the fractures heterogeneity.

2.4.2 Multilateral Stimulation Methods

- Multilateral stimulation methods have been successfully used to increase well productivity in conventional and unconventional reservoirs. The main difficulty on using multilateral stimulation is the cost to create wellbore lateral.

- A new technology called Fishbones was developed that allows to create wellbore laterals by acid injection at affordable operational costs.

- Although many authors have tried to model wellbore lateral stimulation using analytical or numerical methods, there is a need of a numerical method capable of modeling multilateral well stimulation in a flexible and accurate way.

2.4.3 Foam

- Foam have been successfully used to reduce mobility control of miscible and immiscible gas injection in heterogeneous reservoirs. The foam is capable of diverging the flow from fractures (or high permeability channels) to low permeability matrix.

- Among the foam models used to simulate foam flow in porous media there are the population balance model assuming local equilibrium and the P_c^* model.

- The population balance model assuming local equilibrium needs a large set of parameters to be defined; hence there is a need to develop a method to fit and evaluate those parameters in a practical and timely manner.

- Some works in the literature attempted to model foam flow in fractures using the conventional dual porosity dual permeability formulation with limited success. There is a need to couple foam models to numerically efficient and accurate fracture modeling tools, such as the EDFM.

Chapter 3

Methodology[1,2,3]

In this chapter we address the issues identified in the literature review. Applying few assumptions, we propose and derive solutions to contribute to the state of the art of fractures and foam modeling and characterization.

The Embedded Discrete Fracture Model (EDFM) is a methodology originally developed to model large scale conductive fractures. Although many authors have mentioned the implementation of the EDFM in reservoir simulators most of them actually refer to the implementation of non-neighboring connections (off-diagonal terms in the Jacobian matrix). The EDFM itself consists of the calculation of the appropriate non-neighboring connections and respective transmissibilities which allow to model matrix, fractures and interactions between those elements with a production or injection well. Moinfar *et al.* (2013) was the first to cite the need for a preprocessing code to create EDFM input data. The authors explained how the

[1]Cavalcante Filho, J. S. D. A., Shakiba, M., Moinfar, A., & Sepehrnoori, K. (2015). Implementation of a Preprocessor for Embedded Discrete Fracture Modeling in an IMPEC Compositional Reservoir Simulator. In SPE Reservoir Simulation Symposium. Society of Petroleum Engineers. Cavalcante Filho is the writer and main author, Shakiba is the support on the reservoir simulator, Moinfar is a reviewer, and Sepehrnoori is the supervisor.

[2]Cavalcante Filho, J. S. D. A., Xu, Y., Sepehrnoori, K., & Hogstol, H. (2015). Modeling Fishbones Using the Embedded Discrete Fracture Model Formulation: Sensitivity Analysis and History Matching. In SPE Annual Technical Conference and Exhibition. Society of Petroleum Engineers. Cavalcante Filho is the writer and main author, Xu is a collaborator and a reviewer, Sepehrnoori is the supervisor, and Hogstol is the provider of the production data.

[3]Cavalcante Filho, J. S. D. A., Delshad, M., & Sepehrnoori, K. (2016). Estimation of Foam Flow Parameters for Local-Equilibrium Methods using Steady-State Flow Experiments and Optimization Algorithms. In SPE Improved Oil Recovery Conference. Society of Petroleum Engineers. Cavalcante Filho is the writer and main author, Delshad is a collaborator and a reviewer, and Sepehrnoori is the supervisor.

preprocessing code was implemented to handle non-neighboring connections. Based on Moinfar *et al.*'s (2013) work we improved the EDFM fracture description and developed a general EDFM preprocessor capable to handle complex cases and to be integrated with commercial reservoir simulators. The focus of this work is to increase the accuracy of the EDFM and develop a general EDFM preprocessor, the first fundamental step to use the EDFM. The tasks of the EDFM preprocessor are the following: (1) read a discrete fracture network (fractures represented as planes in the three-dimensional space) and a simulation grid (regular Cartesian or Corner Point), (2) calculate the intersections between fracture planes and the simulation grid, as well as between wells and fractures, (3) add fracture blocks to the existing simulation grid with a proper indexing, (4) automatically define non-neighboring connections, (5) calculate transmissibilities between non-neighboring connections, and (6) export connections and transmissibilities in an appropriate format to be used by any reservoir simulator capable of handling non-neighboring connections.

We used UTCOMP, our in-house IMPEC compositional simulator, developed by Chang (1990). The feature of non-neighboring connections was added in UTCOMP by Shakiba (2014) to allow the simulation of fractured media using the EDFM.

The workflow we idealized for the EDFM application is shown in Figure 3.1. Once the EDFM preprocessor exports the appropriate input data for a given reservoir simulator, all the physics modeled by that simulator is able to be applied to the fractures. The EDFM preprocessor may be coupled to uncertainty analysis and optimizations tools for further evaluation of fracture networks. In this work we also implemented and evaluated different foam models, represented as bubbles on the reservoir simulation side of the workflow, and the coupling of those models to the EDFM. In Section 3.1 we derive and present improvements on the EDFM transmissibility equations and the implementation of our EDFM preprocessor. In Section 3.2 we explain how to use the EDFM to model multilateral well stimulation and propose a new EDFM connection (lateral to the matrix) based on the

Peaceman's equation. In Section 3.3 we present foam models used in this work, the P_c* mode, originally implemented in our compositional reservoir simulator, and the population balance model assuming local equilibrium, that we simplified and implemented for further evaluation. We also developed an automated procedure to evaluate and estimate foam model parameters using the Simplex optimization method.

3.1 Embedded Discrete Fracture Model

3.1.1 Discretization of Fractures

The EDFM preprocessing code works with linear (2D domain) and planar (3D domain) fractures. The procedure for discretization is as follows: (1) identify matrix blocks which contain fractures, (2) calculate the area of the fracture polygon (A_f) into the block, (3) calculate fracture porosity (ϕ_f) using Equation 3.1, (4) create a new fracture gridblock adding blocks to the x direction of the grid, and (5) create connections and calculate respective transmissibilities. Figure 3.2 shows the basic shapes of fracture and gridblock intersections.

$$\phi_f = \frac{A_f \omega_f}{V_{bulk}}, \tag{3.1}$$

where ϕ_f is the fracture porosity, A_f is the area of the fracture intersection into a matrix gridblock, ω_f is the fracture aperture, and V_{bulk} is the bulk volume of the gridblock.

The last two steps of the EDFM preprocessing are fundamental because fracture gridblocks are created, transmissibilities are calculated, and NNC connections are assigned. Fracture gridblocks are created as additional blocks added to the x direction of the Cartesian grid; the preprocessor calculates the indexes of the new fracture blocks, the non-neighboring connections between matrix and fracture gridblocks, and the transmissibilities assigned to each non-neighboring

connection. Errors in those calculations lead to material balance errors in the simulation run.

An illustration of how the fracture blocks are created is shown in Figure 3.3 for a 2D reservoir and two linear fractures. Figure 3.3a shows the matrix gridblocks (blocks 1 to 25) and the fractures in the physical domain represented as a black and a red line; the fracture blocks are represented in the computational domain as additional blocks in the x direction (blocks 26 to 31). Figure 3.3b shows how the matrix and fractures are connected to represent fracture to matrix flow.

Figure 3.4 shows the connections generated by the EDFM preprocessor for matrix block 8 and fracture block 28; note that fracture to matrix, neighboring fracture blocks and fracture intersections are created. Figure 3.5 shows the full list of EDFM connections for the matrix and fractures. Transmissibilities must be properly calculated.

3.1.2 Fracture to Matrix (FM)

Lee *et al.* (2000, 2001) states that the counterpart of long fractures modeling is the modeling of wells. The authors assumed that the length of the fracture was greater than the height and they distributed singularities at the horizontal center line of the fracture to model the flow. The authors also reported that the flow into a fracture asymptotically converges as the transmissibility increases. To calculate the matrix to fracture connection Li and Lee (2006) assumed that the pressure gradient around a well is much larger than around a fracture and that the pressure around the fracture is linearly distributed. The authors used Equation 3.2 to model transmissibilities between fracture and matrix.

$$T_{FM} = \frac{(\overline{\overline{k}} \cdot \vec{n} \cdot \vec{n}) A_f}{d}, \tag{3.2}$$

where $\overline{\overline{k}}$ is the permeability tensor of the matrix, $\vec{n}$ is the unit vector of the fracture

plane, A_f is the area of the fracture, and d is the characteristic distance between the fracture and the matrix block.

To derive the transmissibility between the fracture and the matrix we first define the flux as Equation 3.3. We assume that the flow from the matrix to the fracture comes from both sides of the fracture, as shown in Figure 3.6, so the flux from matrix to fracture is calculated with Equation 3.4.

$$q = (\overline{\overline{k}} \cdot \vec{n} \cdot \vec{n}) \nabla \Phi, \tag{3.3}$$

where q is the flux and $\nabla \Phi$ is the potential gradient.

$$q_{FM} = q_{FM1} + q_{FM2}, \tag{3.4}$$

where q_{FM} is the flux from the fracture to the matrix and q_{FM1} and q_{FM2} are the flux from the fracture to matrix blocks 1 and 2 (as shown in Figure 3.6), respectively. Expanding Equation 3.4 we obtain Equation 3.5.

$$q_{m-f} = (\overline{\overline{k}} \cdot \vec{n} \cdot \vec{n}) \left(\frac{\Phi_{m1} - \Phi_f}{d_1} + \frac{\Phi_{m2} - \Phi_f}{d_2} \right), \tag{3.5}$$

where Φ_{m1} and Φ_{m2} are the potential in matrix blocks 1 and 2, Φ_f is the potential in the fracture, and d_1 and d_2 are the distance between the matrix block 1 and matrix block 2 to the fracture, respectively. Note that this derivation allows to discretize even further the original matrix block dividing it in two blocks; hence two different potential gradients between the matrix and fracture blocks are needed. In reality the EDFM connects a fracture block to a single matrix block; hence to allow the calculation of this transmissibility we must assume that the potential gradient in the matrix block is constant and that the pressure in the fracture follows the same potential gradient of the matrix (Figure 3.7). That assumed we might continue our

derivation to obtain Equation 3.6.

$$q_{m-f} = \frac{2(\overline{\overline{k}} \cdot \vec{n} \cdot \vec{n})}{d}(\Phi_m - \Phi_f), \tag{3.6}$$

where d is the characteristic distance from the fracture to the matrix block, Φ_m is the potential in the fracture, and Φ_f is the potential in the fracture. Note that the constant potential gradient is calculated as $\nabla\Phi = \frac{\Phi_m - \Phi_f}{d}$.

Following the assumptions and derivations above, the transmissibility equation between the fracture and the matrix is defined as in Equation 3.7.

$$T_{FM} = \frac{2A_f(\overline{\overline{k}} \cdot \vec{n} \cdot \vec{n})}{d} \tag{3.7}$$

By performing the dot product between the permeability tensor and the fracture unit vector $\vec{n}$ we obtain the permeability vector normal to the fracture surface. For that calculation we need the matrix tensor as an input; as default we assume the matrix permeability tensor as a diagonal tensor with $k_{xx} = k_x$, $k_{yy} = k_y$, and $k_{zz} = k_z$ (off diagonal component are equal to zero, assuming k is aligned with the grid coordinate system). If the user has the tensor for matrix blocks the EDFM preprocessor is able to read that input and perform the appropriate calculations.

Characteristic Distance Calculation

A numerical integration scheme must be used to calculate the characteristic distance defined in the fracture to matrix transmissibility equation (Equation 2.7). In the numerical integration we calculate the volume of each differential element as $dv_i = (w_i - w_{i-1}) \times A_i$. After the calculation of the differential volume we obtain a curve of $w \times v$ with $v_i = \sum_{i=1}^{n_{steps}} (w_i - w_{i-1}) \times A_i$, as illustrated in Figure 3.8; n_{steps} is the number of steps in the numerical integration. The Trapezoidal rule is used to integrate the curve. The algorithm is used for both sides of the fracture, sweeping the whole grid block and the final result is the sum of both integrations. We extended the

numerical integration to calculate the characteristic distance for corner point grids. We calculated the bulk volume of a corner point grid cell (V_b) using the equations presented by Ponting (1989).

Similarly to Li and Lee's (2006) work, when a fracture partially penetrates a matrix gridblock, we extend the area of the fracture to calculate the characteristic distance as described above. The transmissibility for a partially penetrating fracture is assumed to be linearly proportional to the fracture area in the gridblock.

Porosity Cut-off for Fracture Blocks

The IMPEC formulation is well known by its conditional stability, consequence of the explicit treatment for the composition calculations. The conditional stability limits the time step size, which is smaller than the time step used in Fully Implicit formulations. The problem gets worst when the formulation faces blocks with low pore volume where great variations in composition are observed and where small time steps must be used to allow convergence. To overcome the time step limitations of the IMPEC formulation we applied the generally known solution: a porosity cut-off in the fracture blocks. When fracture porosity is below cut-off we overwrite the porosity with the cut-off value. Assuming constant conductivity through the fracture plane, we calculate an equivalent fracture permeability as $k_F^{eq} = C_F/\omega_F^{eq}$, where k_F^{eq} is the equivalent fracture permeability, C_F is the fracture conductivity, and ω_F^{eq} is an equivalent fracture aperture calculated as $\omega_F = V_F/A_F$, where A_F is the fracture area into the block and V_F is the fracture volume. We present a workflow of the porosity cut-off procedure in Figure 3.9.

3.1.3 Fracture to Fracture (FF)

We obtain the constant portion of the transmissibility term between two matrix blocks (in x direction) with different permeabilities in a regular, Cartesian grid as in

Equation 3.8. Other directions (y and z) may be derived similarly.

$$T_x = \frac{2}{\left(\frac{1}{T}\right)_x + \left(\frac{1}{T}\right)_{x+1}}, \tag{3.8}$$

where $T = k/\Delta x$.

The constant portion of the transmissibility for a two blocks of a given fracture may be derived as follows. First we define the flux (q) as in Equation 3.9.

$$q = k\frac{\Phi_1 - \Phi_2}{L}, \tag{3.9}$$

where Φ_1 and Φ_2 are the potentials at the center of each fracture block and L is the distance between the center of each fracture block. Equating the flux between two fracture cells of the same fracture plane as illustrated in Figure 3.10 we obtain Equation 3.10.

$$-k_{f1,b1}\frac{\bar{\Phi} - \Phi_{f1_b1}}{d_{f1-int,b1}} = k_{f1,b2}\frac{\bar{\Phi} - \Phi_{f1_b2}}{d_{f1-int,b2}}, \tag{3.10}$$

where $d_{f1-int,b1}$ and $d_{f1-int,b2}$ are the distances between the midpoint of each fracture block (1 and 2) and the interface between blocks, $\bar{\Phi}$ is the potential at the interface between the two fracture cells, Φ_{f1_b1} and Φ_{f1_b2} are the potentials in the center of block 1 and 2 of fracture f_1, and the midpoint of the intersection of the fracture and the gridblock plane, and $k_{f1,b1}$ and $k_{f1,b2}$ are the permeabilities in each fracture block (1 and 2). Defining $T_{f1,b1} = k_{f1,b1}/d_{f1-int,b1}$ and $T_{f1,b2} = k_{f1,b2}/d_{f1-int,b2}$ and solving Equation 3.10 for $\bar{\Phi}$, we obtain

$$\bar{\Phi} = \frac{T_{f1,b1}\Phi_{f1_b1} + T_{f1,b2}\Phi_{f1_b2}}{T_{f1,b1} + T_{f1,b2}}. \tag{3.11}$$

Inserting Equation 3.11 in the left side of Equation 3.10,

$$q = \frac{1}{1/T_{f1,b1} + 1/T_{f1,b2}}(\Phi_{f1_b1} - \Phi_{f1_b2}), \tag{3.12}$$

The calculation of the transmissibility between fracture blocks (T_{FF}) of a complex fracture was done using Equation 3.13.

$$T_{FF} = \frac{\bar{\omega} L_{int}}{\frac{d_{f1-int,b1}}{k_{f1,b1}} + \frac{d_{f1-int,b2}}{k_{f1,b2}}}, \tag{3.13}$$

where $\bar{\omega}$ is the harmonic average of the different apertures in the same fracture, L_{int} is the length of the intersection of the fracture and gridblock plane. Note that Equation 3.8 has a multiplier 2, which appears because the distance of the center of the block to the interface is $\Delta x/2$; since $d_{f1-int,b1}$ and $d_{f1-int,b2}$ are the distance between the center of the fracture block and the interface this multiplier does not appear in Equation 3.12. Figure 3.11 shows a workflow of the identification and calculation of transmissibilities for neighboring fractures blocks in the same fracture.

3.1.4 Fracture Intersections (FINT)

Connections between intersecting fracture were generalized for 3D cases as presented by Karimi-Fard and Firoozabadi (2003). The transmissibility between two control volumes is given by Equation 3.14, which is the generalized transmissibility calculation for a corner point system. For fractures in 2D the authors derived an equation similar to Equation 3.14 by using a small sized intermediate control volume representing the fracture intersection with a permeability equal to the surrounding fractures and assuming $n_i \cdot f_i = 1$. A generalized equation for a three dimensional fracture was proposed (Equation 3.15) to calculate the transmissibility between three or more fracture segments.

$$T_{12} = \frac{\alpha_1 \alpha_2}{\alpha_1 + \alpha_2}, \tag{3.14}$$

where $\alpha_i = \frac{A_i k_i}{D_i} n_i \cdot f_i$.

$$T_{ij} = \frac{\alpha_i \alpha_j}{\sum_{k=1}^{n} \alpha_k}. \tag{3.15}$$

We used Equation 3.15 to calculate the transmissibility between two planar fractures. Figure 3.12a shows an example of the intersection of two planar fractures. A front view of the fracture presented in Figure 3.12b allows a better visualization of the nodes of each fracture segment located in a matrix gridblock. Using Karimi-Fard and Firoozabadi (2003) equation we obtain the transmissibilities of each fracture segment connected in series to each other (Figure 3.12c). We use a harmonic average of all 4 transmissibilities to calculate the connection between two intersecting fractures, as shown in Equation 3.16. Figure 3.13 shows a simplified workflow of how the fracture intersections are calculated for a general case. Note that if the length of the fracture segment is less than a percentage of the whole length the segment must be suppressed from the transmissibility calculation. Figure 3.14a and Figure 3.14b show a case where three and two segments, respectively, are used for calculating T_{FINT}.

$$T_{FINT} = \frac{4}{\frac{1}{T_{12}} + \frac{1}{T_{23}} + \frac{1}{T_{34}} + \frac{1}{T_{41}}}. \tag{3.16}$$

In multiphase flow cases the transmissibility changes with variations of pressure and saturation. The method proposed to calculate T_{FINT} is an approximation for the geometrical part of the problem. Since the transformation is applied only to the geometrical part of the transmissibility a local error is introduced, which is small for typical cases (Karimi-Fard and Firoozabadi, 2003).

3.1.5 Fracture to Well Intersections (FW)

Fracture may be intercepted by horizontal or vertical wells, hence the appropriate well index must be assigned to connect the well block to the fracture block.

Horizontal Well

Moinfar *et al.* (2013) calculated the fracture to well intersection using an equation derived from Peaceman's equation (Equations 2.10 and 2.11). Those equations apply to cases where fracture to block intersections assume a quadrilateral geometry, as shown in Figure 3.2b and Figure 3.2c (2D cases or 3D cases with regular Cartesian grids and fractures in 90 degrees dip). To model fracture to well intersections, we calculate the well index assuming that fracture length and height are much bigger than fracture aperture; hence the well and fracture intersection will always be a point. We assume a radial flow in the well vicinities into the fracture and that the average pressure in the fracture block equals the calculated fracture block pressure, pressure loss along the fracture is negligible, productivity from fracture and wellbore are superposed, and that the well rate (either injection or production) equals to the summation of the flow in each fracture block interface. Applying those assumptions and starting from the analytical solution for the radial flow (Equation 3.17).

$$P_{@re} - P_{wf} = \frac{q_w \mu}{2\pi k h} ln \frac{r_e}{r_o}, \tag{3.17}$$

where $P_{@r_e}$ is the pressure at radius r_e, P_{wf} is the well bottom-hole pressure, q_w is the well flow rate, μ is the fluid viscosity, k is the rock permeability, h is the reservoir height, r_e is the reservoir external radius, and r_o is the well radius. Assuming well flow rate is the summation of the flow into the fracture we start from Equation 3.18.

$$q_f = \oint_A \frac{k_f}{\mu} \frac{\Delta P}{L} dA \tag{3.18}$$

In Equation 3.19 we define the transmissibility between fracture blocks.

$$T_i = \frac{k_f A}{L}, \tag{3.19}$$

where A is the area open to flow into the fracture and L is the distance between the center of each fracture block. The closed integral in Equation 3.18 becomes Equation 3.20.

$$q_f = \sum_{i=1}^{n_f} \frac{T_i}{\mu}(P_i - P_b) \tag{3.20}$$

From the equation of the radial flow into the fracture we obtain Equation 3.21, which is simplified to Equation 3.22.

$$q_f = \sum_{i=1}^{n_f} \frac{T_i}{\mu}\left(\frac{q_f \mu}{2\pi kh} ln \frac{r_e}{r_o}\right) \tag{3.21}$$

$$\sum_{i=1}^{n_f} T_i \left(\frac{1}{2\pi kh} ln \frac{r_e}{r_o}\right) = 1 \tag{3.22}$$

From Equation 3.22 the equivalent well radius may be derived as in Equation 3.23 (Fung *et al.*, 1992).

$$r_o = \exp\left[\frac{(\sum T_i ln r_i - 2\pi k_f \omega_f)}{\sum T_i}\right], \tag{3.23}$$

where r_o is the equivalent well radius, T_i is the transmissibility between each fracture block, r_i is the distance between the center of each fracture block and the point of intersection of the well and the fracture plane, k_f is the fracture permeability, and ω_f is the fracture aperture. Figure 3.15 shows an example of the calculation of the equivalent well radius for a fracture block with five sides. In Figure 3.15 the well is assumed to be at the center of the fracture block. For cases where the well is not located in the center of the fracture block we calculate the proper r_i but we use the transmissibilities between fracture blocks. This simplification comes from the assumptions that the flow in the well equals the summation of the flows in each interface of the fracture block and pressure drop in fracture plane is negligible. Figure

3.16 shows a workflow used for the calculation of fracture to well transmissibilities.

Vertical Well

For a vertical well the distance between the well and the fracture is calculated and the transmissibility calculated using Equation 3.24.

$$WI_{vertical} = \frac{\omega_f k_f \Delta z}{d_{w-f}}, \tag{3.24}$$

where Δz is the height of the gridblock containing the fracture and the well, ω_f is the fracture aperture, k_f is the fracture permeability, and d_{w-f} is the distance between the fracture and the well.

3.1.6 Integration of EDFM Equation

We explain the modeling of natural fractures (joints and joint sets) with the integration of the EDFM equations first by explaining the Oda's method to calculate the crack permeability tensor and the average fracture network permeability.

Crack Permeability Tensor

Oda's (1985) work shows that when applying Darcy's law to a single fracture and writing the pressure gradient in the fracture as a projection on the fracture plane (function of the unit normal of the i^{th} fracture) one obtains Equation 3.25.

$$\overrightarrow{u_i} = -\frac{k_f}{\mu} \begin{bmatrix} 1-n_x^2 & -n_x n_y & -n_x n_z \\ -n_y n_x & 1-n_y^2 & -n_y n_z \\ -n_z n_x & -n_z n_y & 1-n_z^2. \end{bmatrix} \overrightarrow{\nabla} P, \tag{3.25}$$

where u_i is the Darcy velocity of fracture i, μ is the fluid viscosity, n_x, n_y, and n_z are the components of the unit normal vector defining the fracture plane. Assuming impermeable matrix (permeability equals to zero) and that the matrix fully crossed by a great number of fractures (well connected fractured media), the average flux over

the network of fractures is obtained by integrating the flux over all fractures weighted by the fracture void volume, as shown in Equation 3.26.

$$\overrightarrow{u_i}_{average} = \frac{\int \overrightarrow{u_i} dV_i}{V_{f_{bulk}}} \approx \frac{\sum_{i=1}^{N_f} \overrightarrow{u_i} V_i}{V_{f_{bulk}}}, \tag{3.26}$$

where $\overrightarrow{u_i}_{average}$ is the average Darcy velocity at a given block, V_i is the fracture void volume (fracture area times the aperture), $V_{f_{bulk}}$ is the bulk volume of the fracture network into the matrix grid cell, and N_f is the total number of fractures embedded in a gridblock.

Average Permeability of the Fracture Network

Comparing Equations 2.2 and 2.3 the average permeability tensor of a well-connected fractured media is calculated using Equation 3.27. The average permeability of a fracture block generated with the integrated EDFM is calculated using Equation 2.3.

$$\bar{k}_f = \sum_{i=1}^{nf} \left[\frac{V_{f_i}}{V_{f_{bulk}}} k_{f_i} \begin{pmatrix} 1-n_x^2 & -n_x n_y & -n_x n_z \\ -n_y n_x & 1-n_y^2 & -n_y n_z \\ -n_z n_x & -n_z n_y & 1-n_z^2. \end{pmatrix}_i \right], \tag{3.27}$$

where V_f is the volume of the fracture.

Integrated EDFM

Moinfar *et al.* (2013) proposed Equation 3.28 to integrate the EDFM equations and model naturally fractured reservoirs.

$$T_{f-m} = \sum_{i=1}^{N_{nf}} W_i T_{f-m,i} = \sum_{i=1}^{N_{nf}} W_i \frac{k_{m-f,i} A_{f,i}}{d_{f-m,i}}, \tag{3.28}$$

where N_{nf} is the number of embedded natural fractures in a matrix gridblock, W_i is the volume of the i-th fracture bounded in that gridblock divided by the total

volume of fractures in that cell, $T_{f-m,i}$ is the transmissibility between the i-th fracture and the matrix gridblock, $k_{f-m,i}$ is the harmonic average of the matrix and fracture permeabilities, $A_{f,i}$ is the fracture surface area in the gridblock, and $d_{f-m,i}$ is the average normal distance of the fracture from the matrix gridblock.

Borrowing the assumptions from Oda's (1985) work, we extend the equation of the integrated EDFM approach to use the geometric position of the fracture plane in the space and use the full tensor of the fracture network by applying Equations 3.29 and 3.30.

$$T_{f-m} = \sum_{i=1}^{nf} \frac{\bar{k}_{m-f_i} A_{f_i}}{d_{f-m_i}}, \tag{3.29}$$

where $\bar{k}_{m-f_i}$ is the harmonic average of the matrix permeability (k_m) with the average fracture permeability ($\bar{k}_{f_i}$), defined as

$$\bar{k}_{f_i} = \left[\frac{V_{f_i}}{V_{f_{bulk}}} k_{f_i} \begin{pmatrix} 1-n_x^2 & -n_x n_y & -n_x n_z \\ -n_y n_x & 1-n_y^2 & -n_y n_z \\ -n_z n_x & -n_z n_y & 1-n_z^2. \end{pmatrix}_i \right]. \tag{3.30}$$

Note that Moinfar *et al.* (2013) defines $W_i = \frac{V_{f_i}}{V_{f_{bulk}}}$.

Transmissibilities between blocks with natural fractures are calculated using Equation 3.31.

$$T_{f-f} = \sum_{f=1}^{n_f} \bar{k}_{f_i} \frac{\omega_f L_f}{d_f}. \tag{3.31}$$

Intersection between large scale fractures (LSF) and natural fractures (NF) are calculated using Equation 3.32.

$$T_{LSF-NF} = \sum_{f=1}^{n_{fblock}} W_f \frac{T_{NF} T_{LSF}}{T_{NF} + T_{LSF}}, \tag{3.32}$$

where n_{fblock} is the number of fracture blocks, T_{NF} is the constant part of the

transmissibility of each natural fracture, and T_{LSF} is the constant part of the transmissibility of the long scale fracture.

Figure 3.17 shows the workflow for the small and medium scale fractures modeling. The EDFM equations are integrated using Equation 3.28 to upscale fracture properties, which are embedded in the simulation grid. The equations presented above are able to calculate the transmissibilities of a fractured medium using the integrated EDFM approach and the full permeability tensor of the fractured media. If we assume that the full permeability tensor of the fractured medium is diagonally dominant only the permeabilities of the main diagonal are used to calculate the transmissibility aligned to the main axes.

Equivalent Shape Factor

In a conventional dual porosity formulation two parameters are defined to control the flow between matrix and fracture blocks: the shape factor and the average permeability of the fracture network. The shape factor is a geometrical factor that controls the flow from the fracture to the matrix, while the average permeability of the fracture network controls flow between fracture blocks. Note that there are in the literature many approaches to calculate both the shape factor and the average permeability of the fracture network. This formulation was developed under the assumption of highly connected fractured media. Developed under the same assumption, the integrated EDFM approach also has equivalent parameter to control the flow in fractures, the transmissibility between fracture and matrix blocks (Equation 3.29) and the transmissibility between fracture blocks (Equation 3.31). Additionally, the integrated EDFM is able to represent connections between large scale fractures and the fracture network (Equation 3.32).

We extended the EDFM preprocessor to calculate an equivalent shape factor using Equation 3.33 (Kazemi *et al.*, 1992). To calculate the shape factor we calculate the distance between the center of each fracture plane in all directions aligned to the

grid main axis. The angle that defines the main direction of fractures is defined by the user.

$$\sigma_{Kazemi} = 4\left(\frac{1}{L_{x_f}^2} + \frac{1}{L_{y_f}^2} + \frac{1}{L_{z_f}^2}\right), \tag{3.33}$$

where L_{x_f}, L_{y_f}, and L_{z_f} are the fracture spacing in x, y, and z directions. The EDFM preprocessor exports L_{x_f}, L_{y_f}, and L_{z_f} to serve as input for dual porosity dual permeability formulations.

Equivalent fracture network permeability is calculated using Equation 3.27. Besides the extension of the use of the EDFM preprocessor to conventional dual porosity formulations, we also used this equivalent shape factor and equivalent fracture network permeability to verify the integrated EDFM approach.

3.1.7 Translation of Fracture Properties

The method used to embed spatial properties of a planar fracture into a simulation grid is based on the normalization of the dimensions of the fracture. The input is a contour map defined by three columns: height of the fracture, length of the fracture, and the magnitude of the spatial property (e.g., fracture conductivity). The normalized dimensions of the fracture are calculated (Equations 3.34a and 3.34b) and the properties are assigned to the corresponding normalized coordinates.

$$L_d = \frac{L}{L_f}, \tag{3.34a}$$

$$H_d = \frac{H}{H_f}, \tag{3.34b}$$

where L_d is the normalized length of the fracture, L is the length of a given point into the fracture plane, and L_f is the fracture length. H_d is the normalized height of the fracture, H is the height of a given point in the fracture plane, and H_f is the fracture height. The fracture plane is superimposed by the simulation grid to

perform the embedding process. Blocks of the simulation grid containing the fracture are identified and the normalized coordinate and fracture property are assigned to the center of each block. Figure 3.18 illustrates the described procedure. If a negative number is assigned to the fracture property the fracture block is deactivated, which allows diverse fracture geometries to be discretized. Figure 3.19 illustrates the hydraulic fracture modeling for multifractured wells; note that the presented methodology coupled with the EDFM preprocessing code allows field-scale modeling of multiple multifractured wells in reasonable computational time.

3.2 Multilateral Well Stimulation Modeling

A new well stimulation technique was recently developed to increase well productivity index and improve reservoir connectivity to the well, which is an alternative to the widely used hydraulic fracturing (Freyer and Shaoul, 2011; Rice *et al.*, 2014). This technique called Fishbones consists of creation of several holes in the well by the application of acid injection. As a result, one obtains a set of "holes" of small diameter and average length of 40 feet. The main advantages of this technique compared to the hydraulic fracture are competitive price and reduced operation time.

The EDFM preprocessor was modified to account for multilateral stimulation. Lateral segments are treated in this model as equivalent fractures with same flowing properties as the laterals. A representation of the model and all the connections used (matrix to lateral, between lateral segments, and between the lateral and the well) is shown in Figure 3.20. Equivalent fractures are modeled assuming that they have 1 ft width and that the aperture is defined as the area open to flow inside a wellbore lateral (Equation 3.35).

$$\omega = A_{lat} = \pi \times r_{lat}^2, \tag{3.35}$$

where ω is the equivalent aperture, A_{lat} is the area open to flow inside a lateral, and r_{lat} is the lateral internal radius.

Transmissibilities between the blocks of the laterals are calculated using Equation 3.36,

$$T = \frac{A_{lat} \times k_{lat}}{d_{lat}}, \tag{3.36}$$

where k_{lat} is as equivalent fracture permeability for the fishbone and d_{lat} is the distance between the centers of two equivalent fracture segments. We neglect pressure drop into the lateral and we assume that Hagen-Poiseuille equation is valid to model the flow into a lateral. The permeability k_{lat} may be properly calculated and will consist of a high permeability number. Our simulations have shown that results asymptotically converge as we increase the permeability of the lateral, so a smaller value of permeability may be defined to avoid convergence problems.

The transmissibility between laterals and matrix is calculated using the Peaceman's equation. Equation 3.37 is obtained for a Fishbone in x direction, the other directions can be obtained by similarity. Figure 3.21 illustrates the connection between the lateral and the matrix.

$$T = 2\pi\sqrt{k_y k_z}\Delta x_{lat}\frac{1}{ln(r_o/r_{lat})}, \tag{3.37}$$

where T is the transmissibility, k_y and k_z are the matrix permeabilities in y and z directions, Δx_{lat} is the length of the Fishbone in a given block in x direction, r_o is a term similar to the Peaceman radius (Equation 3.38), and r_w is the well radius.

$$r_o = 0.28\frac{(k_y\Delta z^2 + k_z\Delta y^2)^{1/2}}{(k_y)^{1/2} + (k_z)^{1/2}}, \tag{3.38}$$

where Δz and Δy are the block dimensions in direction z and y, respectively. Figure 3.21 shows a schematic representation of the lateral to matrix block connection and the respective equations.

When a lateral intersects one or more natural fractures the transmissibility is calculated using Equation 3.39.

$$T_{lat-nf} = \sum_{i=1}^{N_{nf}} W_i T_{lat-nf,i}, \tag{3.39}$$

where N_{nf} is the number of embedded natural fractures in a matrix gridblock, W_i is the volume of the i-th fracture bounded in that gridblock divided by the total volume of fractures in that cell, and $T_{lat-nf,i}$ is the transmissibility between the i-th natural fracture and the lateral's gridblock (Equation 3.40). Note that if a lateral does not intersect the ith natural fracture, $T_{lat-nf,i} = 0$.

$$T_{lat-nf,i} = \frac{T_{lat} T_{nf,i}}{T_{lat} + T_{nf,i}}, \tag{3.40}$$

where

$$T_{lat} = \frac{A_{lat} \times k_{lat}}{d_{lat,int}}, \tag{3.41}$$

where $d_{lat,int}$ is the distance between the center of the lateral block and the lateral to natural fracture intersection.

$$T_{nf,i} = \frac{\omega_{nf,i} L_{int,lat-nf} k_{nf,i}}{< d >_{nf,i}}, \tag{3.42}$$

where $\omega_{nf,i}$ is the natural fracture aperture, $L_{int,lat-nf}$ is the length of intersection between the natural fracture and the fishbone, $k_{nf,i}$ is the permeability of the natural fracture, and $d_{nf,i}$ is the distance between the centers of natural fracture block and the fishbone to natural fracture intersection.

3.3 Foam modeling

3.3.1 Population Balance Model Assuming Local Equilibrium

Chen *et al.* (2010) introduced the population-balance model with the local-

equilibrium approximation, which is useful for large scale calculations. Chen *et al.* (2010) set the net rate of foam generation in Equation 2.27 equal to zero, assuming that generation and coalescence rates are in equilibrium. The authors obtained an equation for the density of the flowing foam bubbles which may then be obtained as in Equation 3.43.

$$n_f^{\omega} + \frac{n^{*\omega} k_{-1} |v_f|^a}{k_1^0 |v_w|^b} n_f - n^{*\omega} = 0, \tag{3.43}$$

where n^* is the upper limit of the concentration of foam bubbles that is related to the pore size, and ω is a constant determining the shape of inverse proportionality of foam germination sites to pre-existing gas bubbles. For $\omega = 3$, Equation 3.43 becomes a cubic equation that presents a single real root and can be easily solved for n_f at given liquid velocity, gas velocity, and capillary pressure using analytical formulas. Hence, a simple check must be done for the presence of surfactant before solving Equation 3.43; if there is no surfactant, the local equilibrium foam texture is set to zero. For the generation term Equation 3.44 was used (Chen *et al.*, 2010).

$$r_g = k_1 v_f^a v_w^b, \tag{3.44}$$

where $v_w = u_w/\phi S_w$ is the local interstitial liquid velocity and $v_f = u_f/\phi S_f$ is the local interstitial velocity of the flowing foam. These velocities depend upon the local saturation of flowing liquid or gas and the local pressure gradient (capillary pressure plus gravitational effects). Exponents a and b are power indices, with index b close to unity. Coefficient k_1 is the generation rate constant reflecting the number of foam germination sites. Chen *et al.* (2010) modified the foam generation term to predict foam flow behavior in both the high quality and the low quality regimes by writing the foam generation constant k_1 as in Equation 3.45.

$$k_1 = k_1^0 \left[1 - \left(\frac{n_f}{n^*}\right)^{\omega}\right], \tag{3.45}$$

where ω is a constant determining the shape of inverse proportionality of foam-germination sites to pre-existing gas bubbles and n^* is an upper limit for the concentration of foam bubbles which is related to pore size. Equation 3.45 reflects fewer foam-germination sites as bubbles texture increases. The dependence of k_1 on S_w is not included. Chen *et al.* (2010) asserts in their conclusion that the foam texture dependence of the foam generation term successfully predicts the steady-state pressure gradient trends in the high and low quality flow regimes, as well as the smooth transition between regimes. For the coalescence term, one may consider Equation 3.46 (Chen *et al.*, 2010):

$$r_c = k_{-1}(S_w) v_f n_f, \tag{3.46}$$

where $k_{-1}(S_w)$ is a coalescence rate constant which varies strongly with local aqueous-phase saturation, surfactant concentration and surfactant formulation. Note that a higher v_f would lead to higher coalescence rates since stretched lamella are more vulnerable to breakage. Coalescence also depends on P_c^*, on account of the reason why the coalescence constant depends on surfactant formulation, concentration and S_w. Khatib *et al.* (1988) proposed a function to model $k_{-1}(S_w)$ (Equation 3.47).

$$k_{-1}(S_w) = k_{-1}^o \frac{(1 - S_w)}{(S_w - S_w^*)}. \tag{3.47}$$

Tang and Kovscek (2006) worked with the fraction of mobile foam in porous media. According to the authors, there is few steady state flow measurements in the literature, most of which had sparse measurements and no quantification of the size of the bubble at the core's exit. Tang and Kovscek (2006) performed experiments and developed a statistical model to evaluate mobile gas fraction based on laws of scaling from percolation theory (Eq. 3.48). The model is applicable to predict foam's relative permeability during foam flow into the porous media; foam's relative permeability

may be a function of the pressure gradient, permeability, and bubble density.

$$X_f = \frac{\Psi}{S_g}\left[\frac{f_c|\nabla p_g|}{k^{1/2}n_f}\right]^{\eta}, \tag{3.48}$$

where Ψ is a constant of proportionality, S_g is the gas saturation, parameter $\eta = 0.4$ and $f_c = 0.25$ are appropriate for cubic lattices filled with largely immobile gas, ∇p_g is the gradient of pressure of the gas phase, and k is the absolute permeability.

The effects of the oil saturation on foam coalescence may be included by extending Equation 3.43 as follows (Chen, 2009):

$$n_f^{\omega} + \frac{n^{*\omega}\left[k_{-1} + k_2^0\left(\frac{S_o - S_{or}}{S_{o,lim} - S_o}\right)\right]|v_f|^a}{k_1^0|v_w|^b} n_f - n^{*\omega} = 0, \tag{3.49}$$

where k_2^0 is a constant related to the effect of the oil saturation on foam coalescence, $S_{o,lim}$ is the limiting oil saturation above which foam coalesce, S_o is the oil saturation, and S_{or} is the residual oil saturation.

3.3.2 P_c^* (UT Model)

Cheng *et al.* (2000) described an empirical foam model known as the UT model. Originally developed for the high quality regime, the model also exhibits reasonable results for the low quality regime. The UT model modifies the gas relative permeability for the effect of the foam as in Equations 3.50, 3.51, and 3.52.

$$If\ S_w < (S_w^* - \epsilon)\ or\ C_s < C_s^o,\ then\ k_{rg}^f = k_{rg}^o(S_w), \tag{3.50}$$

$$If\ (S_w^* - \epsilon) < S_w < (S_w^* + \epsilon)\ or\ C_s = C_s^o,\ then\ k_{rg}^f = \frac{k_{rg}^o(S_w)}{\left(1 + \frac{(R-1)(S_w - S_w^* + \epsilon)}{2\epsilon}\right)}, \tag{3.51}$$

$$If\ S_w > (S_w^* + \epsilon)\ or\ C_s = C_s^o,\ then\ k_{rg}^f = \frac{k_{rg}^o(S_w)}{R}, \tag{3.52}$$

where C_s is the surfactant concentration in the aqueous phase, C_s^o is a threshold surfactant concentration for foam formation, k_{rg}^f is the effective gas relative permeability modified for foam, $k_{rg}^o(S_w)$ is the gas relative permeability as a function of water saturation in the absence of foam, and S_w^*, ϵ, and R are model parameters. S_w^* is the saturation at which foam collapses; it is a function of surfactant and rock properties, not function of flow rate (this is equivalent to the Fixed-P_c^* model described in Zhou and Rossen (1995), and it also controls mobility in the high-quality regime).

3.3.3 Estimation of Foam Parameters

There are two ways to estimate foam parameter from experimental data: history match transient flow experiments or analytically match steady-state flow experiments. We propose a method to estimate foam model parameters by using an optimization algorithm to match the pressure gradient as function of fluid velocities. An example of the chart of pressure gradient as function of fluid velocities is shown in Figure 3.22a. After the algorithm finds a good match we perform a quality control comparing the effective viscosity (Equation 2.38) calculated with the experimental data, as illustrated in Figure 3.22b. We assume that the pressure gradient provides a different effective viscosity curve (as observed in the experiments), but in many cases effective viscosities for different pressure gradient may superpose each other. The proposed methodology allows comparison of other parameters for quality control purposes, such as the foam density or the fractional flow curve. The quality control allows a better understanding of the foam flow behavior and is a reference for the application of the foam model in field scale problems.

In this work we borrow all the assumption of local equilibrium foam models and fractional flow theory. From the local equilibrium we assume that when gas, water, and surfactant are present foam is created and that the strong-foam state is instantaneously attained. From the fractional flow theory we assume that phases are incompressible, gas and water are not soluble in each other, degradation of the surfactant due to temperature variations are neglected, and the flow of the foam in porous media follows the Newtonian behavior. Additional assumptions are as follows: relative permeabilities for the coreflood are known, effects of gas compression along the core were minimum during the coreflood (or that the data was corrected).

The optimization algorithm we used is the Simplex method based on Nelder and Mead (1965). The Simplex method is capable to optimize a function y of n variables. The simplex is defined by $(n+1)$ points (P_0,P_1,P_2,...,P_n,) located in a n-dimensional space. The operations used are reflection, contraction, and expansion. To briefly explain the Simplex method we first define the subscripts h, meaning the highest value of a set of points, and l, meaning the lowest value of a set of points. A reflection is done by calculating $P^* = (1+\alpha)P_{centroid} - \alpha P_h$, where P^* is the reflected variable, $P_{centroid}$ is the centroid of the points with $i \neq h$, α is the reflection coefficient, P_h is the highest value of P_i, and P_i is the set of $(n+1)$ points defining the simplex. y^* is calculated and if it is between y_h and y_l, P_h is replaced by P^* and a new simplex is started. If $y^* < y_l$ it means that the reflection produced a new minimum, then we expand P^* to P^{**} using $P^{**} = \gamma P^* + (1-\gamma)P_{centroid}$, where γ is the expansion coefficient (greater than unity). If $y^{**} < y_l$, P_h is replaced by P^{**} and the operation is restarted. If $y^{**} > y_l$ the expansion failed and P_h is replaced by P^* before restarting. When the reflection from P to P^* results in $y^* > y_l$ for all $i \neq h$ (y^* is the maximum), a new P_h is redefined to be either the old P_h or P^*, whichever has the lower y value, and we form $P^{**} = \beta P_h + (1-\beta)P_{centroid}$, where β is the contraction coefficient (always between zero and unity). P^{**} is then accepted to restart as P_h unless $y^{**} > min(y_h, y^*)$, i.e. the contracted point is worse than the

better of P_h and P^*. For the failed contraction P_i's is replaced by $(P_i + P_l)/2$ and the process is restarted. Nelder and Mead's (1965) work presents an example of the Simplex method workflow, shown in Figure 3.23.

Functions used in the Simplex method loop are the population balance assuming local equilibrium model and the P_c^* (UT model). For the population balance model assuming local equilibrium we optimize parameters used to calculate foam viscosity (S_w^*, n^*, k_{-1}, k_1^0, α) and foam relative permeability (Ψ, f_c, and η). For the P_c^* (UT model) we optimize parameters used to calculate the foam relative permeability (S_w^*, R_f, and ϵ). Figure 3.24 shows how we calculate the velocities of the gas and the liquid. The objective function minimized by the simplex method is the summation of the absolute differences between experimental and calculated velocities.

3.4 Summary

EDFM

- We derived the equation used for the transmissibility between the fracture and the matrix blocks. The main assumption of this derivation is the linear pressure behavior in the matrix and that the fracture pressure follows the same pressure gradient of the matrix. We also explained that the full permeability tensor of the matrix should be used to allow the transformation that allows the flux to be perpendicular to the fracture plane. For partially penetrating fractures we extend the fracture area to calculate the characteristic distance and assume that the transmissibility of the partially penetrating fracture is linearly proportional to its area.

- We derived and proposed a new equation for the transmissibility between two fracture blocks of a same fracture that allows the modeling of complex fracture with varying conductivity.

- We explained how the transmissibility between intersecting fractures are calculated and we modified the previous method by accounting for all fracture segments and neglecting small segments when needed.

- We derived and proposed a new transmissibility equation for the transmissibility between a horizontal well intersecting a planar fracture. We assumed radial flow from the fracture to the well and that the intersection between the well and the fracture plane was a point.

- We explained how the average permeability of a set of fractures was calculated to be used in the integrated EDFM approach. We used the Oda's method and assumed that the fracture system is highly connected.

- We identified the need to translate fracture properties in the space to allow the coupling of the EDFM with fracture propagation tools. We proposed a method where we define a local system of coordinates for the fracture plane using dimensionless variables. This local system can be translated in space to any fracture plane in any position and dimensions.

- We extended the EDFM preprocessor to model multilateral well stimulation techniques. Wellbore laterals are modeled as equivalent fractures. We propose a new transmissibility equation based on Peaceman's equation to calculate the connection between the lateral and the matrix.

Foam Modeling

- We described and derived the population balance model assuming local equilibrium. We assumed that the foam destruction rate was a function of the S_w^* instead of P_c^* and we used Tang and Kovscek's (2006) equation to calculate the fraction of flowing foam.

- We describe the P_c* model, which was implemented in our in-house IMPEC simulator.

- We propose an automated methodology to fit foam model parameters using steady state experimental data (pressure gradient versus fluid velocity). Simplex method was used to optimize the absolute difference between the calculated and the experimental data. Quality control of the data may be performed by evaluating the effective foam viscosity and/or foam fractional flow curves.

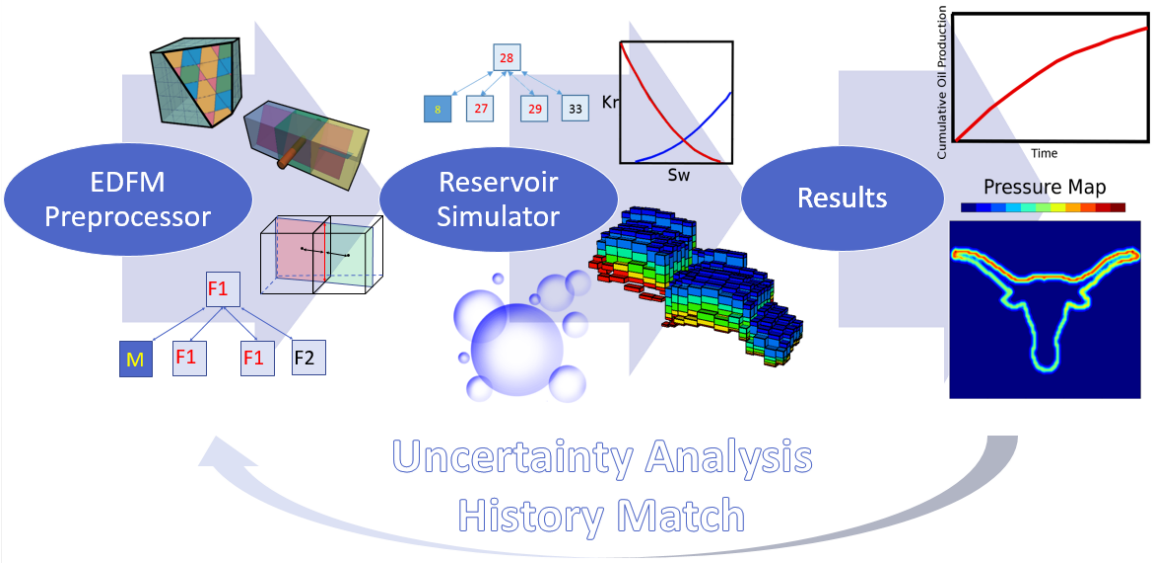

Figure 3.1: Workflow for the EDFM: the present works focus on the development of a general EDFM preprocessor and foam models.

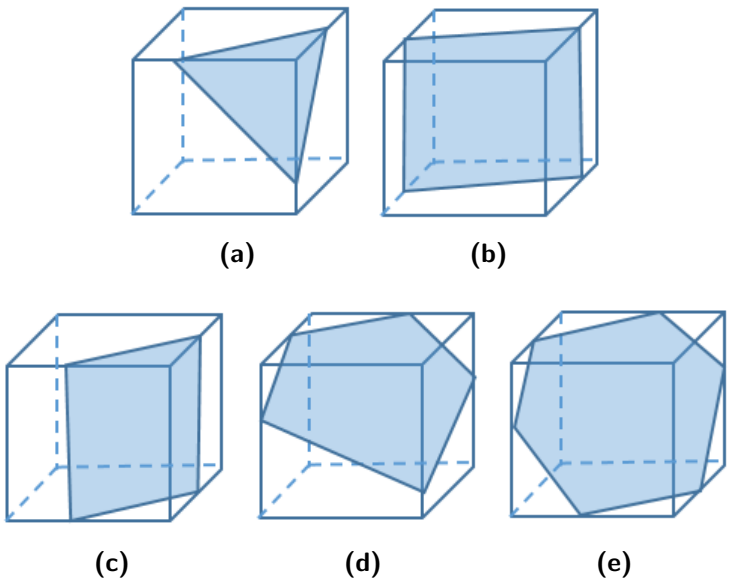

Figure 3.2: Fracture basic shapes when intersecting a matrix gridblock.

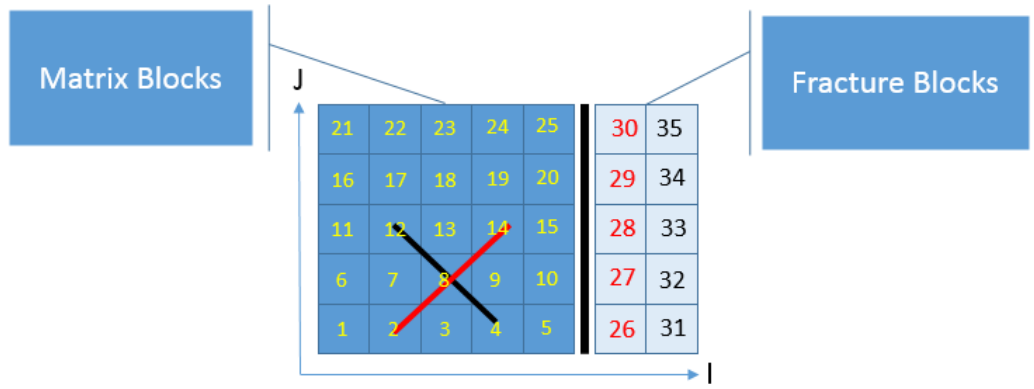

(a) Matrix and Fracture Representation

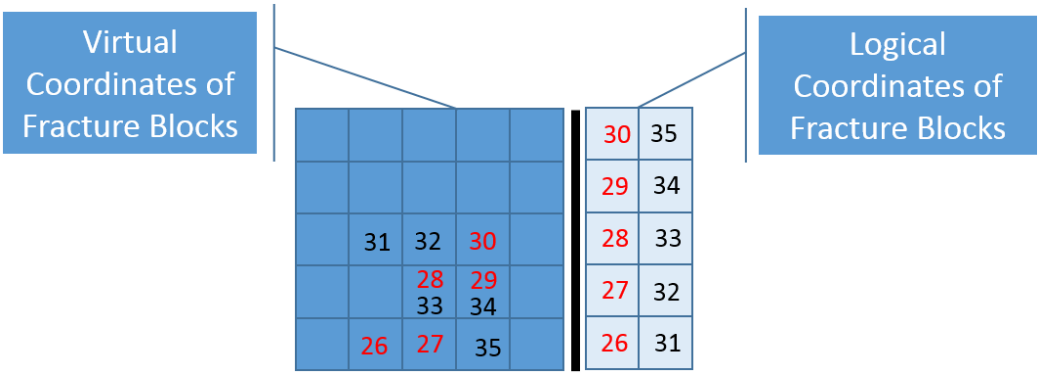

(b) Physical and Computational Fracture Positioning

Figure 3.3: Illustration of how the fracture blocks are added: (a) shows the simulation grid with matrix and added gridblocks and (b) shows the virtual position of each fracture block in the matrix grid.

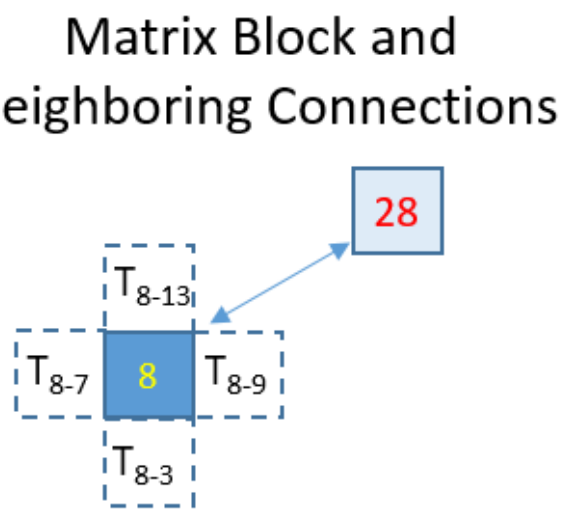

(a)

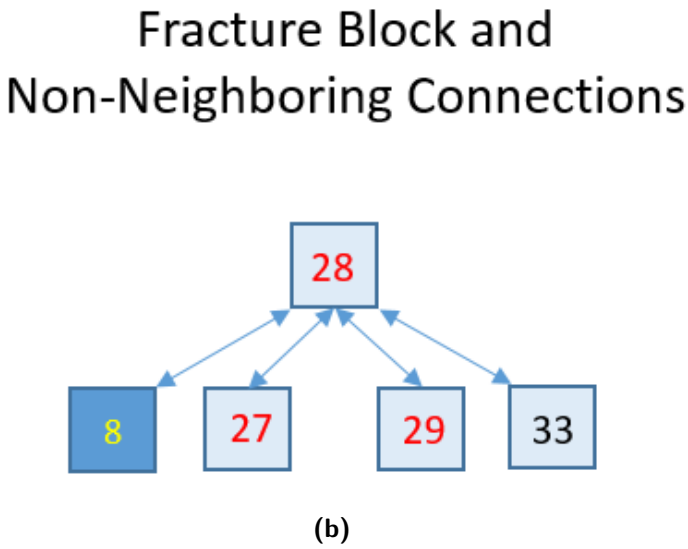

(b)

Figure 3.4: Illustration of fracture and block connections: (a) shows regular matrix connections handled by the simulator and a non-neighboring connection from fracture block 28 to matrix block 8 and (b) shows non-neighboring connections for fracture block 28, which is connected to the matrix block 8, neighboring fracture blocks 27 and 28, and fracture block 33 (intersection between the red and black fracture).

Matrix Connections

Block	Connections	
2	26	
3	27	
4		35
8	28	33
9	29	34
12		31
13		32
14	30	

Fracture Connections

Block	Connections			
26	2	27		
27	3	26	28	
28	8	27	29	33
29	9	28	30	
30	14	29		
31	12	32		
32	13	31	33	
33	8	32	34	28
34	9	33	35	
35	4	34		

Figure 3.5: EDFM connections for case shown in Figure 3.3.

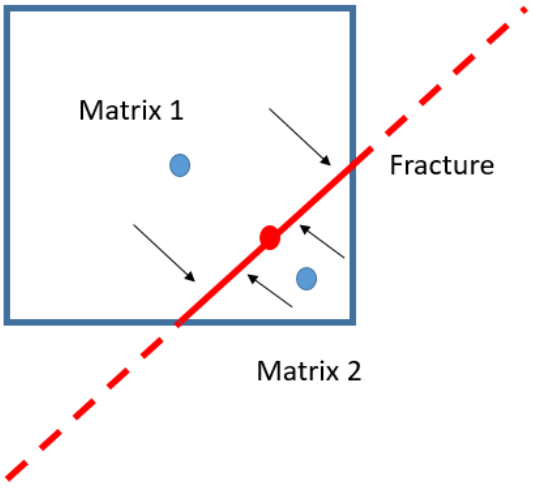

Figure 3.6: Flux from both matrix blocks to the frature.

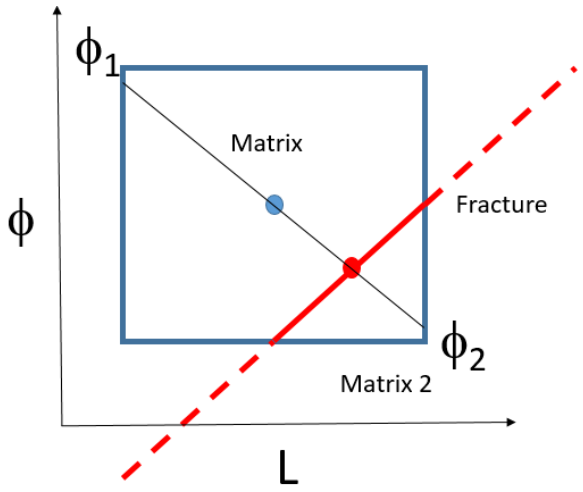

Figure 3.7: Single matrix block connected to a fracture block: the figure shows that the potential gradient is linear in the matrix.

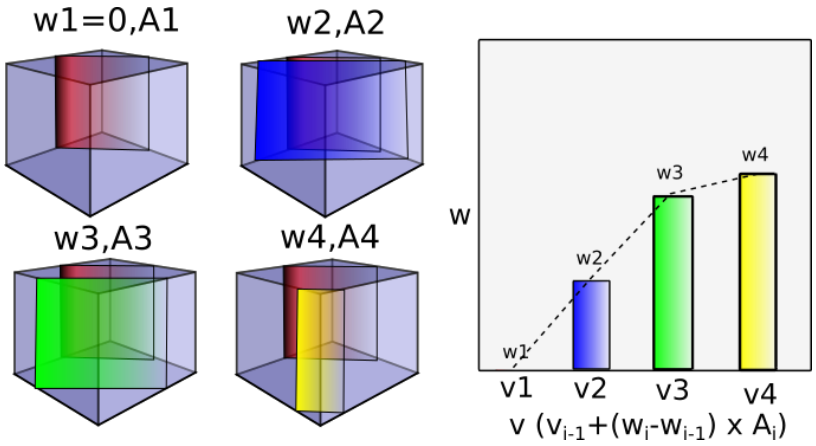

Figure 3.8: Scheme representing the numerical procedure implemented in this work to calculate $d^{nnc} = \frac{\int_V w_n dv}{V_b}$ for fractures at any dip and strike angle in irregular gridblocks .

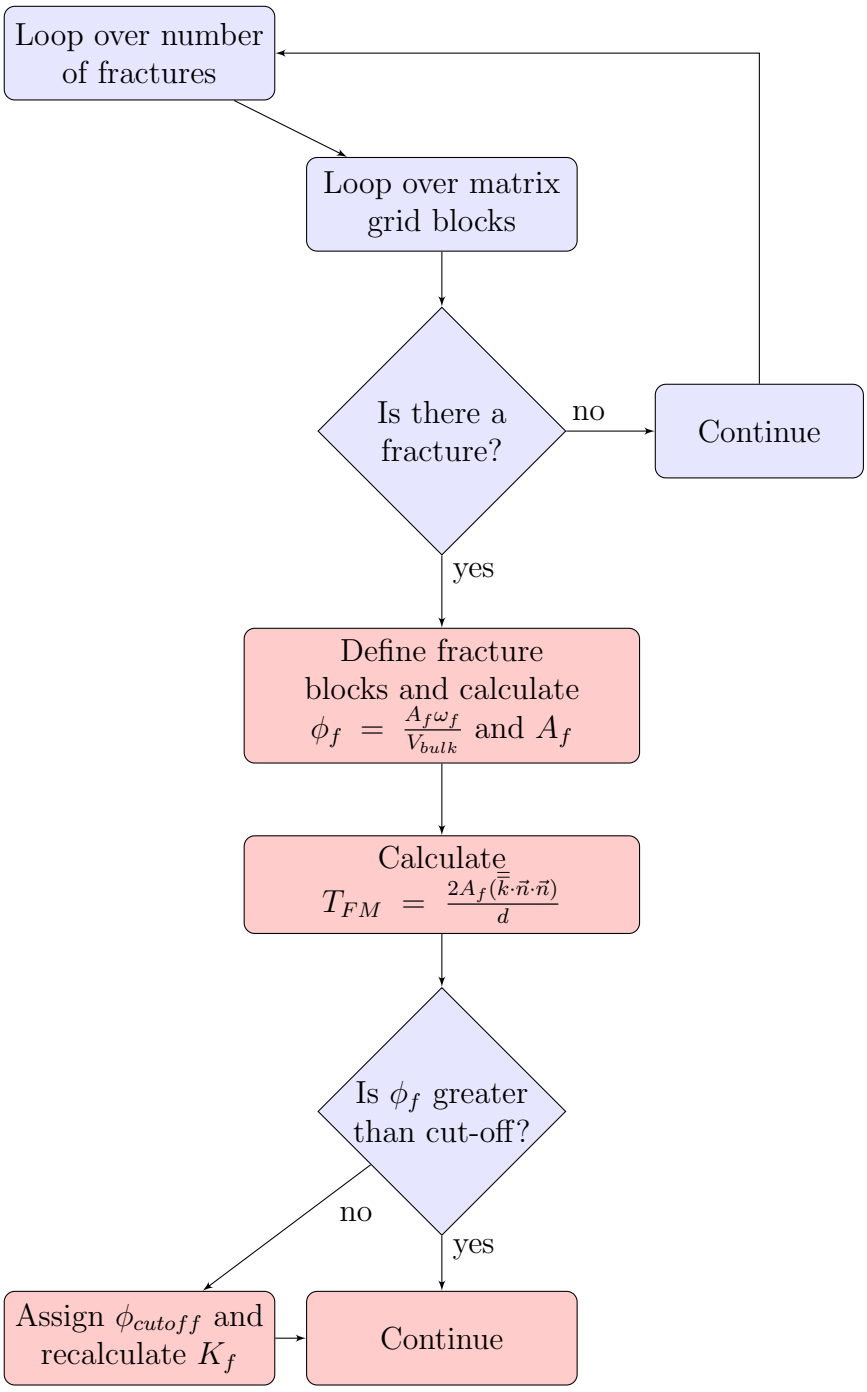

Figure 3.9: Porosity cut-off.

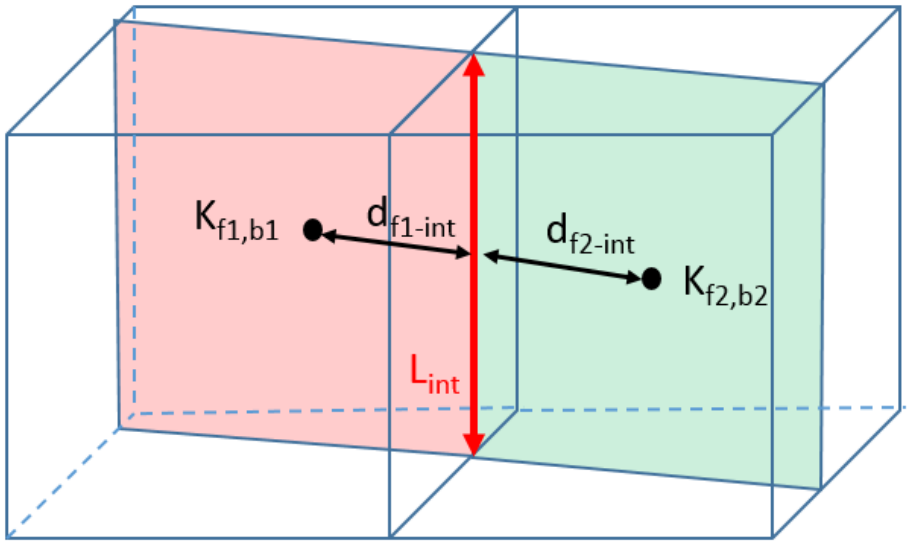

Figure 3.10: Example of transmissibility between fracture blocks with different properties.

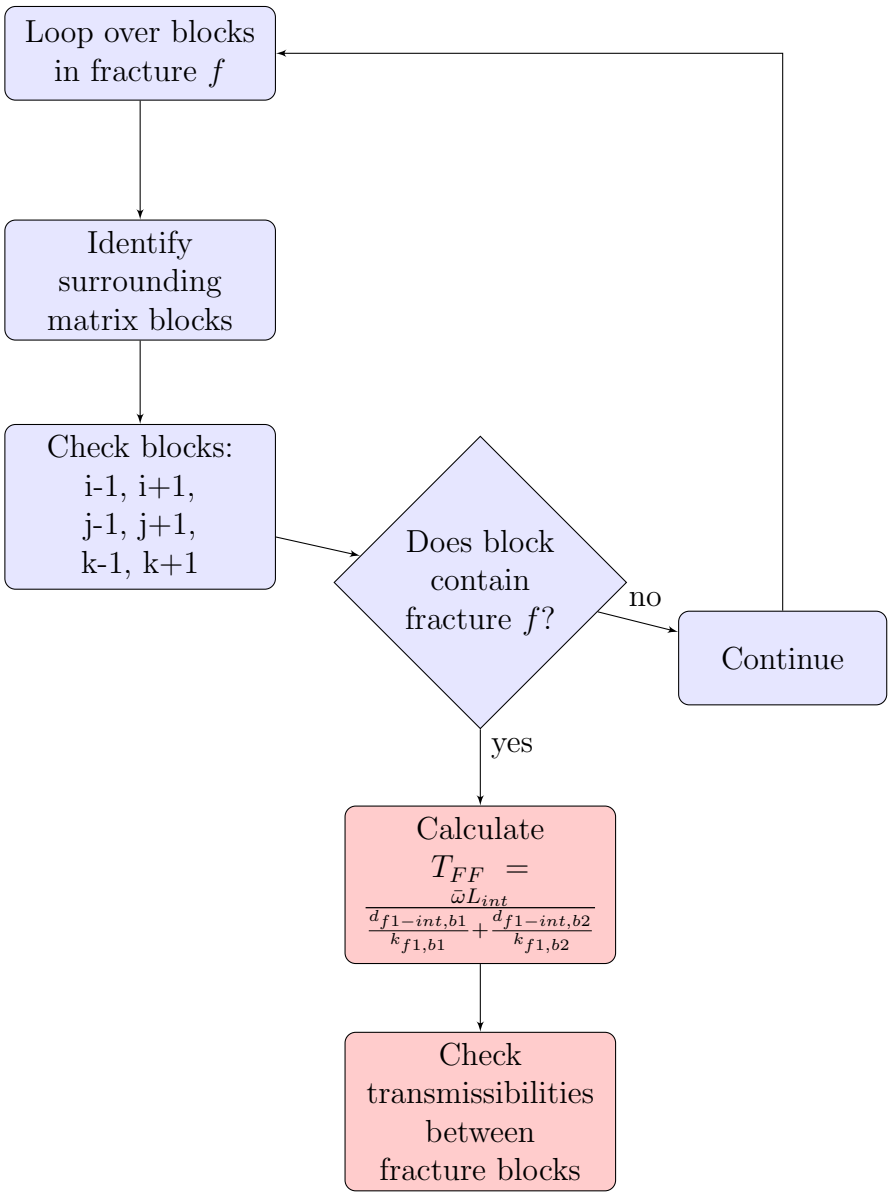

Figure 3.11: Explicit fractures: fracture to fracture transmissibility.

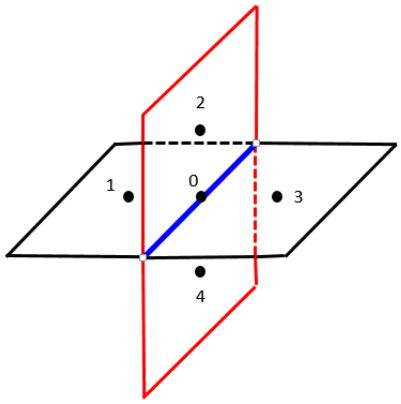

(a) Fracture intersections in 3D (Karimi-Fard and Firoozabadi, 2003)

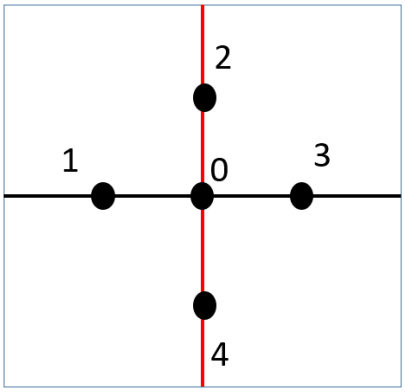

(b) Front view of (a)

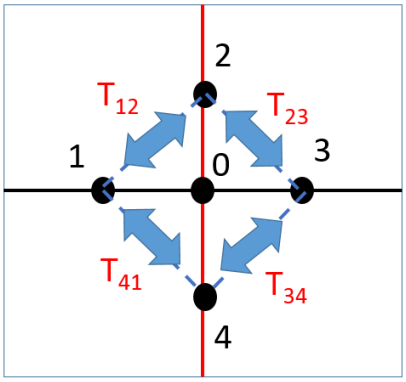

(c) Transmissibilities (series flow)

Figure 3.12: Calculation of the fracture intersections: (a) shows a 3D view of two intersecting fractures and their intersection line (blue), (b) a front view of the fracture, and (c) shows the transmissibilities between the centroid of each fracture element (series flow).

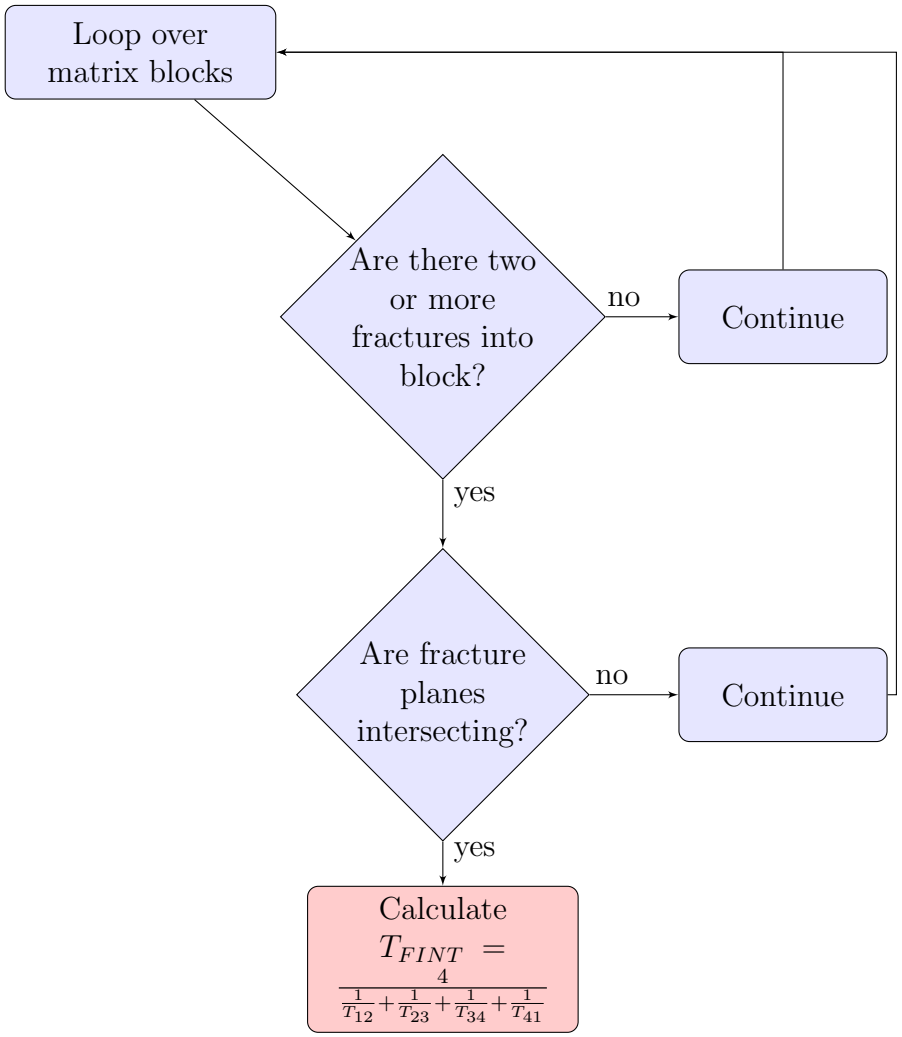

Figure 3.13: Explicit fractures: fractures intersection transmissibility.

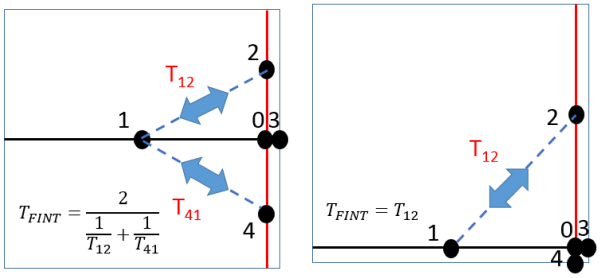

(a) **(b)**

Figure 3.14: Example of fracture intersection cases.

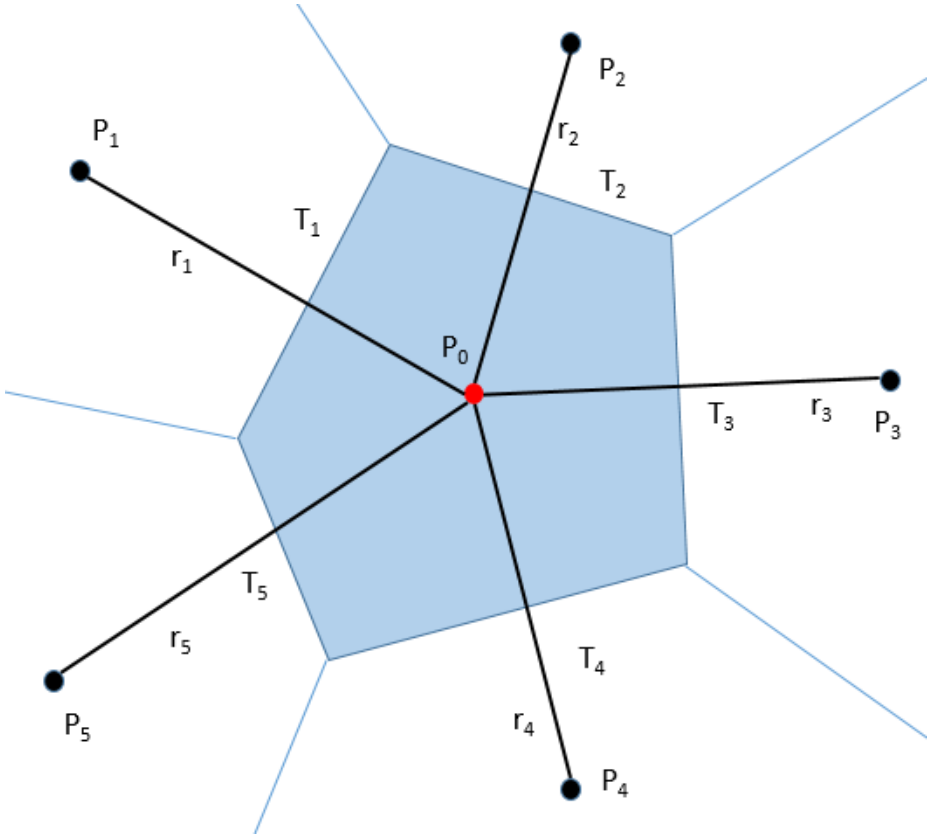

Figure 3.15: Example of equivalent well radius calculation.

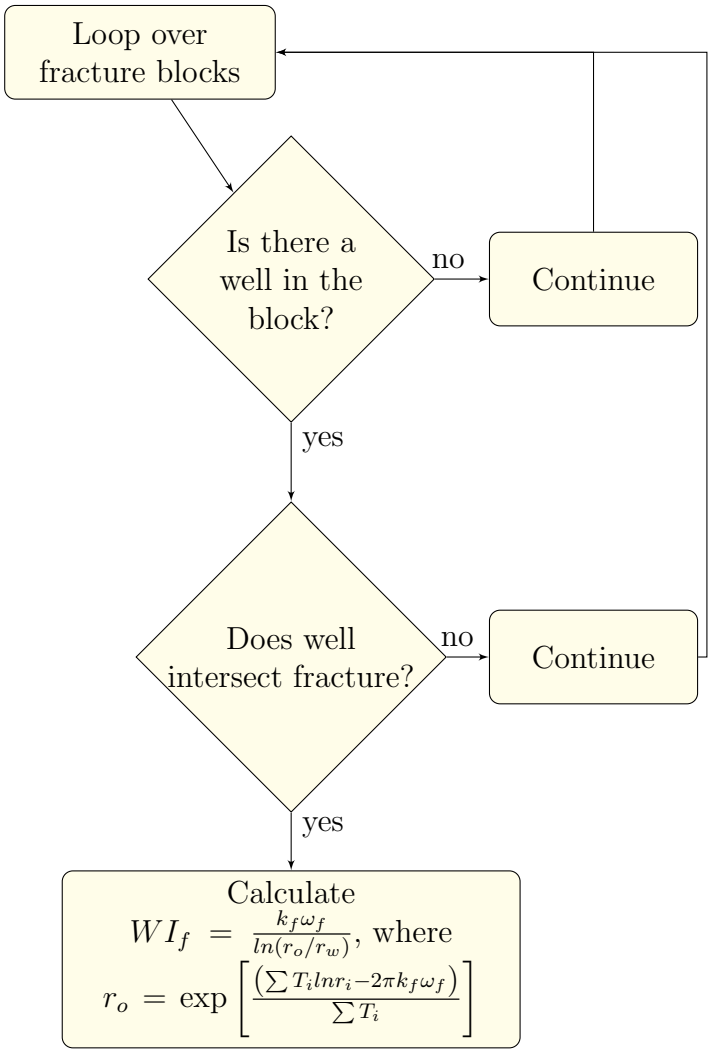

Figure 3.16: Calculation of the well index of a horizontal well crossing a fracture.

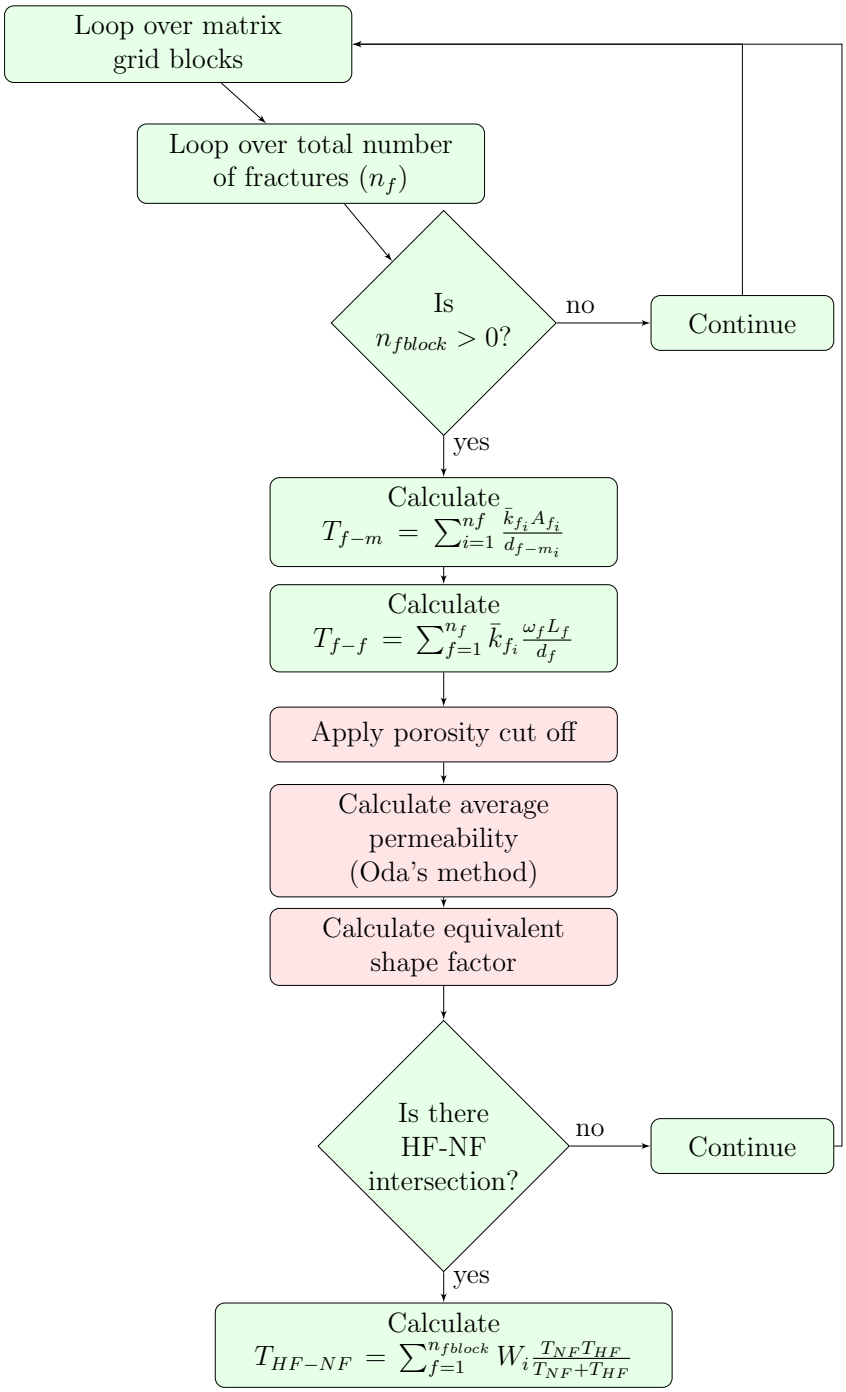

Figure 3.17: Dual continuum: fractures to matrix transmissibility, fracture to fracture, and natural fractures (NF) to hydraulic fracures (HF) intersection.

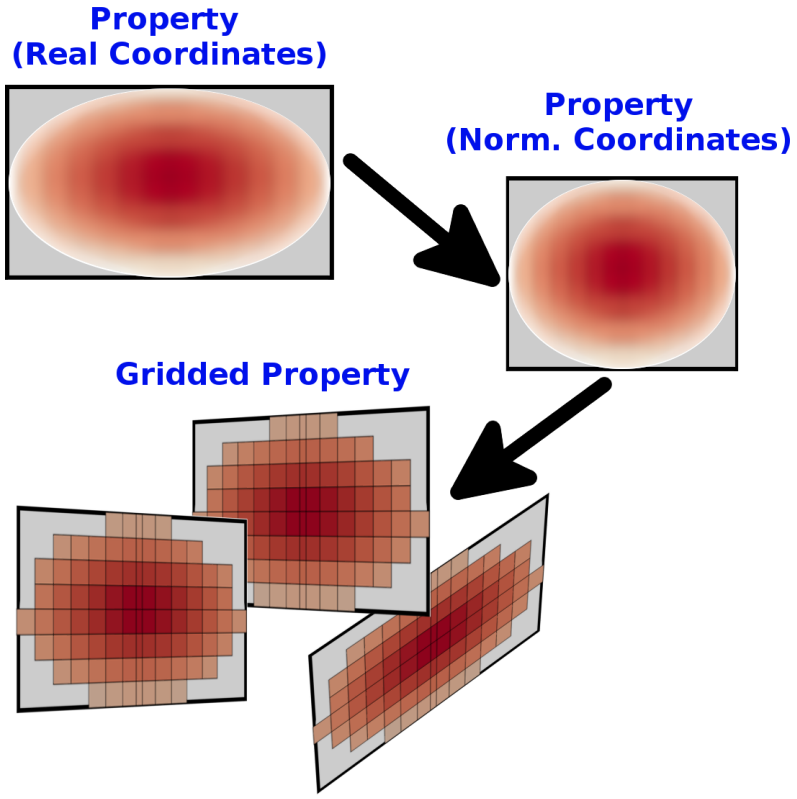

Figure 3.18: Embedding fracture properties to a simulation grid.

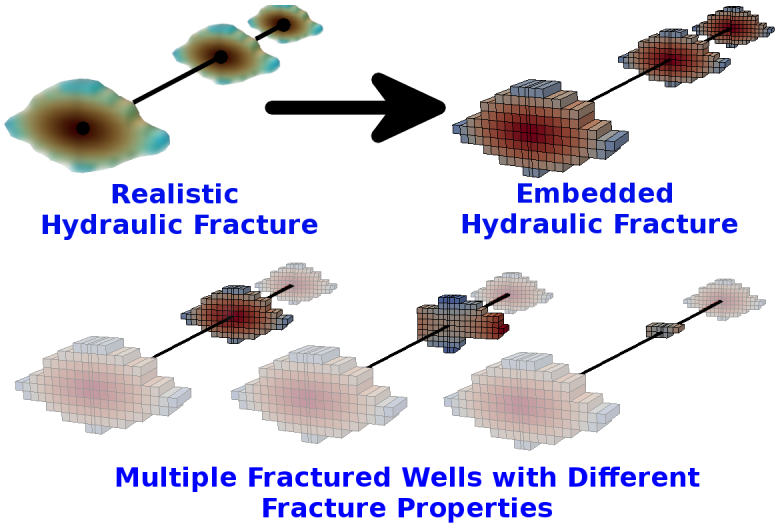

Figure 3.19: Hydraulic fracture modeling using the EDFM preprocessing code.

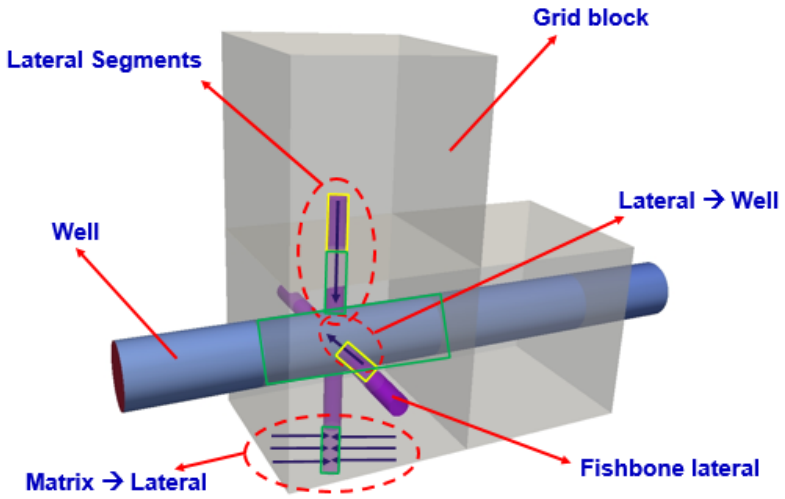

Figure 3.20: Fishbones transmissibilities for the EDFM approach.

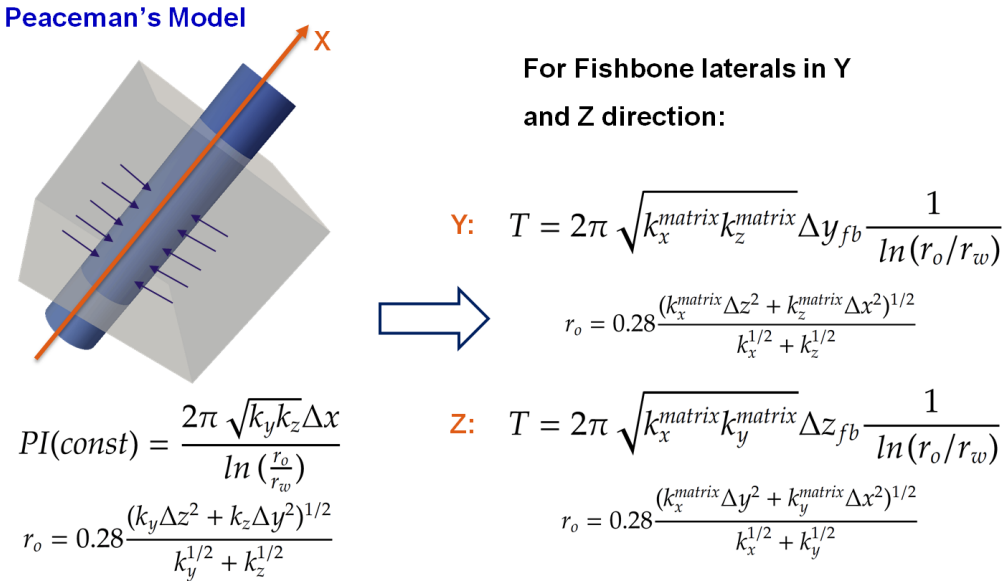

Figure 3.21: Fishbones-matrix transmissibility based on Peaceman's equation for direction y and z.

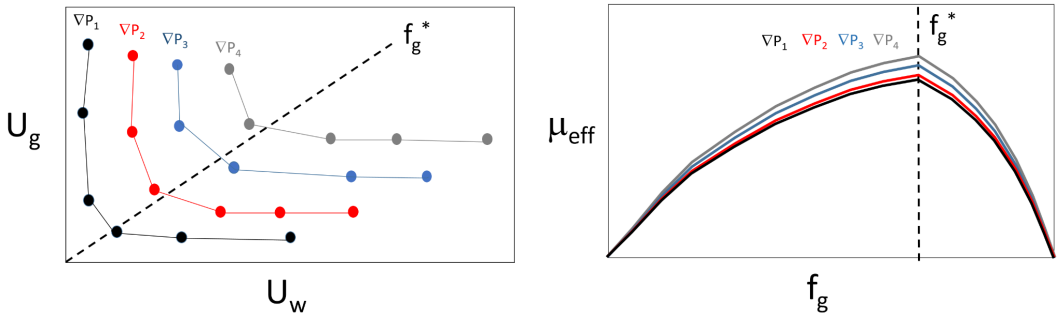

(a) Pressure drop as a function of flow rate

(b) Effective viscosity

Figure 3.22: Illustration of the pressure drop as function of flow rate chart and the effective viscosity.

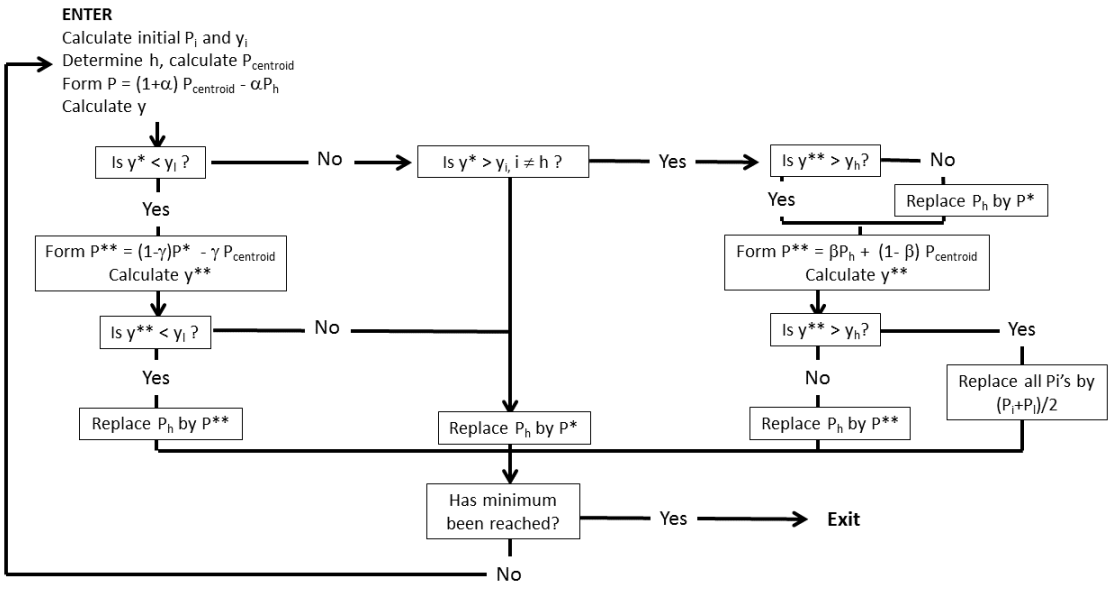

Figure 3.23: Workflow of the Simplex method (Nelder and Mead, 1965).

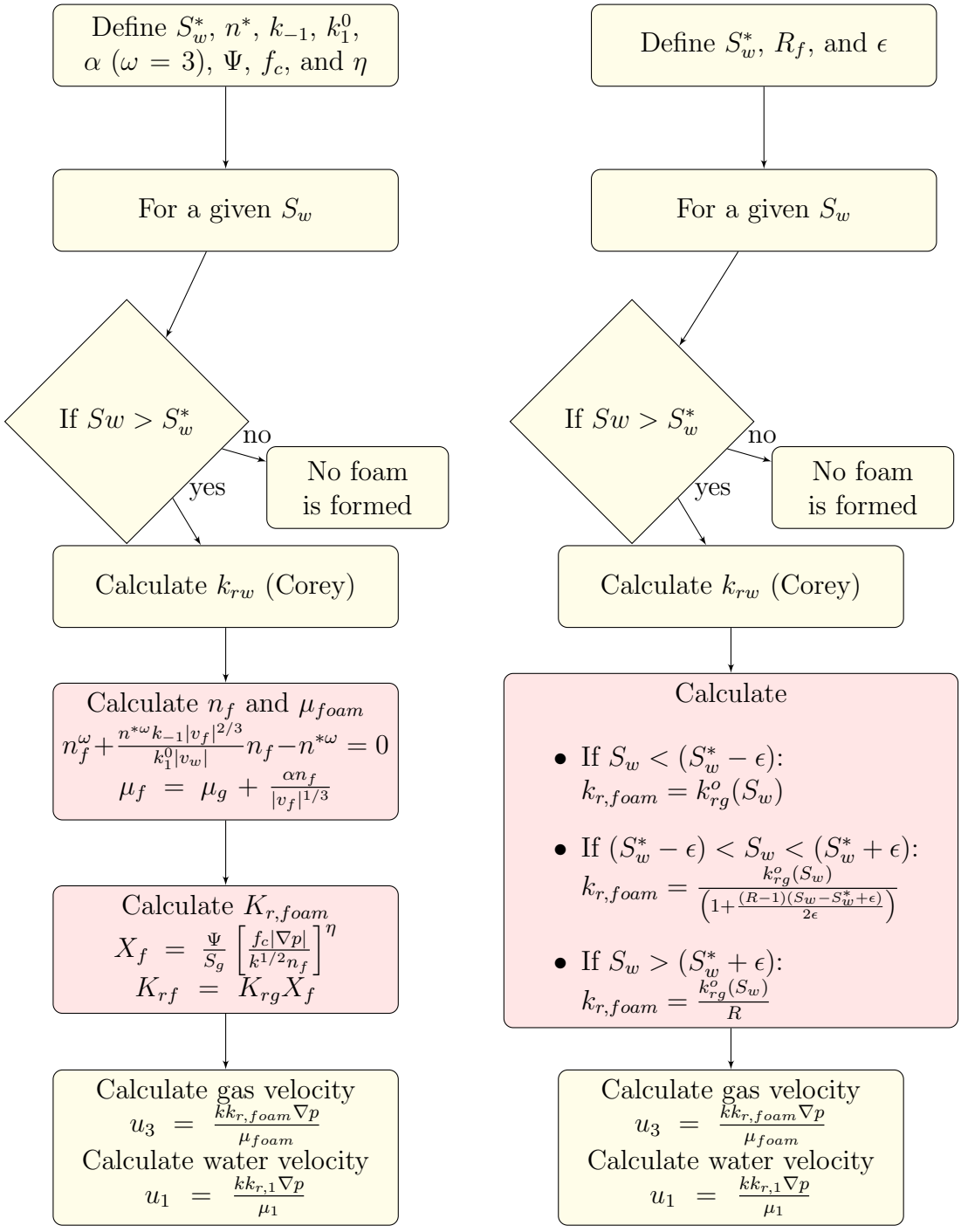

(a) Population Balance (LE) **(b) P_c^***

Figure 3.24: Workflow of the proposed methodology for the population balance (LE) and P_c^* models; we assume $C_s \geq C_s^0$ (foam is always formed).

Chapter 4

Verification and Application of the EDFM[1]

4.1 Introduction

Numerical simulation tools are used to evaluate economic feasibility and to manage production from naturally fractured reservoirs (NFR). NFRs may be modeled by explicit fracture representation (discrete fracture models) or dual porosity/dual permeability formulations. The first is well-known by its detailed representation of fractures with high computational cost, while the latter fails in the representation of complex and heterogeneous NFR but incurs less computational issues. Lee *et al.* (2000, 2001) proposed a hierarchical modeling approach based on the ratio of fracture length to the grid size (l_f/l_g); three classes of fractures were defined: short fractures ($l_f/l_g << 1$), grid block scale fractures ($l_f/l_g \approx 1$), and long fractures ($l_f/l_g >> 1$). The effect of short fractures was computed using a simple analytical equation and was included by enhancing matrix conductivity (permeability). The contribution of gridblock scale fractures was calculated using the boundary element method. Long fractures were modeled explicitly as major fluid conduits. Li and Lee (2008) adopted the transport index concept from Lee *et al.* (2001) and modeled networks of long fractures, which were represented as two dimensional planes crossing several layers. The authors included intersections between fractures and wellbores. A source/sink term was derived to model the flux between matrix and long fractures network in a

[1]Cavalcante Filho, J. S. D. A., Shakiba, M., Moinfar, A., & Sepehrnoori, K. (2015). Implementation of a Preprocessor for Embedded Discrete Fracture Modeling in an IMPEC Compositional Reservoir Simulator. In SPE Reservoir Simulation Symposium. Society of Petroleum Engineers. Cavalcante Filho is the writer and main author, Shakiba is the support on the reservoir simulator, Moinfar is a reviewer, and Sepehrnoori is the supervisor.

black-oil reservoir simulator.

The embedded discrete fracture model (EDFM) is a numerically efficient approach that allows modeling of explicit long fractures along with small fractures (Moinfar *et al.*, 2013). Non-Neighboring Connections (NNC) are used to handle fluid flow between matrix and fracture blocks. Moinfar *et al.* (2013) implemented non-neighboring connections and used the EDFM in an fully-implicit compositional simulator. The NNC contribution (which is mathematically similar to a convection term) was added to the component mass balance equation as a source/sink term. Moinfar *et al.* (2012, 2013) defined three kinds of NNC: between a fracture cell and its neighboring matrix block, between two intersecting fractures cells, and between two cells of an individual fracture. Intersections between well and fractures were modeled using an equation derived from Peaceman (1983), similarly to Li and Lee (2008). To model small and medium scale fractures Moinfar *et al.* (2013) integrated the EDFM equations using the concept of dual continuum from conventional dual porosity dual permeability formulation (Equation 3.28). The authors were able to simulate a complex NFR composed of natural and hydraulic fractures as a triple porosity medium (hydraulic fractures were modeled explicitly and the natural fractures using integrated EDFM equations). Moinfar (2013) described the use of a preprocessing code to calculate the matrix-fracture, fracture-fracture, fracture intersections, and well-fracture transmissibilities. The author's preprocessing code accounted for orthogonal and slanted fractures, assuming they penetrate the whole reservoir domain. Panfili *et al.* (2013) applied the EDFM as described by Li and Lee (2008) in a commercial reservoir simulator. Two cases were studied: a pressure transient test in a multi-fractured horizontal well and a first-contact miscible injection process. The authors concluded that the EDFM coupled with standard simulation technology allows efficient modeling of complex fractured reservoirs characterized by discrete fracture network (DFN) models. Jiang *et al.* (2014) developed a multi-continuum, multi-component model to study gas injection in

fractured shale reservoirs. Their hybrid model includes three domains: matrix, large scale fractures modeled with the EDFM, and microfractures modeled with the multiple interacting continua (MINC) approach. The authors assumed single-phase multi-component flow to simplify the numerical simulation problem. Knudsen diffusion and gas slippage effect were included in the formulation, along with multi-component adsorption and desorption. The authors concluded that fracture properties do influence the production and that simulations show that CO_2 injection is feasible in shale gas reservoirs. Zhou *et al.* (2014) developed a two-phase finite difference formulation assuming 1D flow in fractures to study the efficiency and the accuracy of the numerical solution for fractured reservoirs. The authors assumed that the fluxes in both sides of the fractures were different in order to model saturation changes due to multiphase flow within the fracture. Matrix blocks covering the fracture do not participate in the numerical solution scheme and are included as boundaries. The pressure field near the fracture was defined by unilateral interpolation between fracture and matrix blocks; fluxes were calculated and used as boundary conditions. Results showed a better match for Zhou *et al.*'s (2014) results than that of Lee *et al.* (2000). In the work of Zhou *et al.* (2014) the intersections between fractures were neglected.

In this chapter we verify our EDFM preprocessor with other works from the literature and fine models. We apply the EDFM to evaluate the effect of the gravity on oil production and to model reservoirs with different geological structures using a Cartesian grid. Transmissibility equations are found in Chapter 3.

4.2 Results and Discussions

4.2.1 Verification

We used our in-house IMPEC compositional simulator with added feature of non-neighboring connections (Shakiba, 2014) to validate our EDFM preprocessing code. Reservoir properties used in the simulation runs are shown in Table 4.1. The

fluid used in the compositional simulations was characterized and a regression was performed with a commercial thermodynamic simulator to match the Peng-Robinson equation of state with experimental data as explained in Appendix A. The period of the simulation was defined to allow evaluation of the injected fluid breakthrough.

4.2.1.1 Moinfar *et al.*'s (2013) Model

We verified the implementation of the EDFM preprocessor in our IMPEC simulator (UTCOMP) against one Fully Implicit simulator (GPAS) used by Moinfar (2013). The reservoir has 500 ft in x and y directions and 20 ft in z direction. The model is 2D with 20 x 20 x 1 blocks and has 14 long vertical fractures at different orientations, as shown in Figure 4.1. The injection scheme is a quarter of five-spot pattern. Fracture aperture and permeability are 0.025 ft and 700,000 md, respectively. Matrix porosity and permeability are 0.1 and 20 md, respectively. Straight line relative permeability curves are assumed for the fractures. Initial pressure of the reservoir is 3000 psi. The producer has a constant bottom hole pressure constraint set to the initial reservoir pressure. Water is injected at 100 bbl/day. For more details in the model description refer to Moinfar *et al.* (2013) (page 95). Figure 4.2 shows a good match between our results and Moinfar *et al.*'s (2013).

We evaluated the use of a porosity cut-off in Moinfar *et al.* (2013) model. A significant improvement in the simulation run time was observed, as presented in Figure 4.3. Figure 4.3a shows that the application of porosity cut-off does not affect the simulation results. For that particular case (Moinfar *et al.*, 2013), the simulation run time was reduced by 10 times (Figure 4.3b). The presence of low pore volumes in fracture blocks has a great impact on the time-stepping and on the simulation run time.

4.2.1.2 Multifractured Horizontal Wells

In this section we verify the use of the EDFM in multifractured horizontal wells.

Homogeneous Fractures

We evaluated two cases of multi-fractured horizontal wells with 3 and 5 fractures (Figure 4.4) producing under depletion; the EDFM solution was compared to a fine model to verify the well to fractures connections (Equations 2.10 and 3.23). Reservoir properties used in the simulation runs are shown in Table 4.1. Well operational constraints is contant bottom-hole pressure (8534 psi).

Figure 4.5 and Figure 4.6 show comparisons of oil production rate, gas-oil ratio and average reservoir pressure between the fine model and the EDFM (UTCOMP) solution for multi-fractured well with 3 and 5 hydraulic fractures producing via pressure depletion. A good match is observed for the case with 3 hydraulic fractures. For the case with 5 hydraulic fractures we observe a small difference in the early times which is related to gridding differences; an overall good match is obtained at late times.

Heterogeneous Fracture

The transmissibility equation used in this work to model the connection between fracture blocks was verified using a multifractured horizontal well with 3 fractures, shown in Figure 4.4a. Figure 4.7 shows the fracture permeability map for all three cases named Case 1, 2, and 3. We investigate fractures with low and high conductivity. In Case 1 fractures have a homogeneous fracture permeability of 1,000 mD. In Case 2 fractures have a homogeneous fracture permeability of 10 mD. In Case 3 fractures have an heterogeneous fracture permeability with 1,000 mD in the center block and 10 mD in the lateral blocks. Fracture aperture was 0.3 ft. Our

transmissibility equation must be able to appropriately model the flow and match fine model results. Other reservoir properties in Table 4.1. Well operational constraints are presented in Table 4.2. Figure 4.8 shows the results of the verification cases. We observe a good match between the EDFM and the fine model simulation run using a commercial simulator.

Non-Planar Fractures

The EDFM allows the modeling of non-planar fractures by combining different fracture planes which may have different fracture properties (conductivity). Here we validate the use of the EDFM to model non-planar fractures by comparing EDFM results with a fine model where the fractures are modeled using refined grid blocks. Figure 4.9 shows the multifractured horizontal well with 4 non-planar hydraulic fractures with different sizes. We used a commercial Black-oil simulator to illustrate the use of the EDFM in commercial simulators. For that verification we assumed a tight gas reservoir with porosity of 12% and permeability of 0.5 μd. Gas viscosity is shown in Figure 4.10. Reservoir initial pressure is 4500 psi. Figure 4.11 shows a good agreement between the gas production rate and the cumulative gas production for the fine model and the EDFM. Figure 4.12 shows the pressure map after 2 years of production for the fine model and the EDFM.

Xu's (2015) work evaluated the use of the EDFM in commercial simulators. The author reinforced that the EDFM is a non-intrusive methodology that may be used in any reservoir simulator capable of handling non-neighboring connections. Orthogonal, non-orthogonal, and inclined fractures modeled with the EDFM in 2D and 3D cartesian grids were successfully verified against single porosity fine models.

4.2.1.3 Fractured reservoirs (Unstructured Grid)

We compare the EDFM to unstructured grid and fine grid solutions presented by Karimi-Fard and Firoozabadi (2003). Figure 4.13 shows the geometry of the model,

a 2D reservoir with three fractures (one isolated and two intersecting fractures). The matrix porosity is 0.2 and the matrix permeability is 1 md. Fracture aperture is 0.1 mm and the fracture permeability is obtained by the Poiseuille law ($k_f = \omega_f^2/12 \approx 844,170$ md). The matrix is saturated with an oil of 0.45 cp and the water is injected at 0.01 PV/day (water viscosity is 1 cp). Relative permeabilities are assumed to be straight lines for matrix and fractures. For detailed information on the model refer to Karimi-Fard and Firoozabadi (2003). Figure 4.14 shows the match for the cumulative oil production and Figure 4.15 presents the water saturation maps for a fine single porosity model, unstructured grid, and the EDFM. The EDFM solution presented a good match against Karimi-Fard and Firoozabadi's (2003) results, for both the fine and the unstructured grid models.

4.2.1.4 Fractured reservoirs (Fine Model)

We verified the EDFM and the integrated EDFM approaches with single porosity fine models containing variable number of fractures. A complex fractured reservoir may be modeled using single porosity fine models, to illustrate that we show in Appendix B a drawdown test simulated in a 2D reservoir model with 800 fractures which presented the dual porosity signature in the well test derivative.

The EDFM was verified against three different cases with different number of fractures: 2 fractures (Figure 4.16a and Figure 4.17a), 10 fractures (Figure 4.16b and Figure 4.17b), and 100 fractures (Figure 4.16c and Figure 4.17c). Single porosity and EDFM models were compared for water and miscible gas injections. In the miscible gas injection, the injected stream composition is 50% CO_2 and 50% CH_4. Well operational constraints are given in Table 4.2. Reservoir properties used in the simulation runs are shown in Table 4.1.

To model fractures using a single porosity grid the fracture permeabilities must be corrected to account for the tortuosity of the grid caused by the stair step representation (Moinfar, 2013). We corrected fractures permeabilities using Equation

4.1, which was derived using the stair step representation shown in Figure 4.18.

$$k_F^{corrected} = \frac{\omega_F}{L_F}(N_{b,frac} - 1)k_F, \tag{4.1}$$

where $k_F^{corrected}$ is the corrected absolute permeability for the fracture in the single porosity fine model, ω_F is the fracture aperture, L_F is the total length of the fracture, $N_{b,frac}$ is the number of fracture gridblocks intersected by the fracture plane, and k_F is the absolute permeability of the fracture.

Water Injection

Figure 4.19 and Figure 4.20 show oil and water production rates for a 2D NFR with 2, 10, and 100 fractures. The analysis was conducted for the fine model and the EDFM for the cases with 2 and 10 fractures, and the fine model and the integrated EDFM for the case with 100 fractures. The curves obtained with the fine model and the EDFM approaches show a good agreement for the cases with 2 and 10 fractures. For the case with 100 fractures the connection between fractures in a given block are integrated and represented with the use of equivalent transmissibilities and permeabilities and the integrated EDFM solution presented a good match with the fine model. Note that as the number of fractures increases e the use of the integrated EDFM approach is recommended to reduce the number of off-diagonal terms on the solution matrix and improve simulation run time.

Continuous Gas Injection

Figure 4.21 and 4.22 show oil and gas production rates for a 2D NFR with 2, 10, and 100 fractures. Results show a good agreement especially for the cases with 10 and 100 fractures. For the 2 fractures case, fine model evaluation using the commercial simulator showed oscillation for some periods of the simulation, but a good agreement was obtained for the initial and the final periods of simulation. The oscillations are due to a instability in the phase identification algorithm in the presence of CO_2 at

low temperatures and high pressures (near critical conditions). At high pressures and low temperatures, the CO_2 has high density, close to the oil density, and the phase identification algorithm fails for some gridblocks. We used the phase identification algorithm by density and critical temperature and both presented oscillations; phase identification using the critical temperature of the fluid presented less oscillations. It is worth mentioning that the result shown in the previous figures for the fine model case is the best out of many trials.

4.2.1.5 Fractured reservoirs (Dual Porosity Dual Permeability)

To further validate the EDFM preprocessor, we implemented an equivalent shape factor and equivalent fracture permeability in our EDFM preprocessor (Section 3.1.6). Figure 4.23 shows a good agreement between the EDFM solution (UTCOMP) and the conventional dual porosity formulation (commercial reservoir simulator) for a case with 10 fractures. By increasing the number of fracture to 100, we obtain Figure 4.24, where a good agreement is also observed. Note that the conventional dual porosity results for the case with 10 fractures do not accurately predict the water breakthrough, while the case with 100 fractures accurately predicts the breakthrough. This difference in water breakthrough prediction is expected once the conventional dual porosity formulation was derived for a highly connected fracture network; hence, for greater number of fractures we expect better accuracy in the results. Since the EDFM was developed to model highly conductive large scale fractures, the prediction of the water breakthrough for the case with 10 fractures is more accurate. Results also show that the integrated EDFM formulation is able to provide similar results to the conventional dual porosity formulation, once the shape factors and the equivalent fracture network permeability are properly calculated.

4.2.2 Application

In this application we used 3D models with different geologic structures (horizontal, dipping and anticline reservoirs, as shown in Figures 4.25a, 4.25b, and 4.25c). To embed the fractures we project the reservoir grid to the horizontal position and calculate the fracture intersections; the next step is to fix the gridblock positions to honor the original reservoir geometry. The methodology used to model fractures in different reservoir structures must assume fractures with 90 degree dip angle, which allows the fractures to be embedded in the matrix gridblocks without distorting or curving the fracture planes. Once the fractures cross the whole reservoir, the strike angle may vary. A more efficient way to model a fracture in reservoirs with complex structures is to use a Corner Point Grid to represent the geological structure.

4.2.2.1 Miscible Injection in Fractured Reservoirs

Both continuous gas and WAG injections were evaluated and compared. Gravity effects were assessed by the comparison of a horizontal reservoir model with other non-horizontal models (dipping and anticline). The WAG injection ratio was calculated to be 1 at the initial condition of the reservoir for all cases, but it might change with production and pressure variations in the reservoir during the simulation run. Wells operating constraints are shown in Table 4.2.

Continuous Gas Injection

Figure 4.26 shows the results for 2, 10, and 100 fractures under gas injection, both for 2D and 3D cases. As may be noted, the gravity effect is noted as soon as we turn from the 2D to the 3D model. In cases with 2, 10, and 100 fractures, 2D models resulted in a later breakthrough because of the absence of gravity effects. The 3D model provides a different sweep area in all layers, once the gas tends to segregate in the top, resulting in an earlier breakthrough. In the case with 100

fractures, the gravity effect played a more important role for the dipping and the anticline cases. Differences in production observed between the horizontal reservoir, dipping, and anticline were caused by the greater number of fractures, which provides a better connectivity to the reservoir, resulting in a different reservoir pressure distribution. Figure 4.27 shows the gas saturation maps after 600 days of production for 3D horizontal, dipping and anticline models, where we observe the differences in gas distribution generated by the reservoir geometry and gravity effects.

For lower number of fractures, the gravity effects due to different reservoir structures is not pronounced because of the low connectivity among matrix blocks (low permeability). As we increase the reservoir connectivity, an increase in the gravity effects is expected to occur. The gravity effects are higher for 100 fractures case because the overall connectivity of the reservoir increases, allowing the fluids to flow by gravity potential, in addition to viscous forces.

WAG

In order to compare continuous gas and WAG injections in fractured reservoirs, a WAG injection was performed in both horizontal, anticline, and dipping NFR with 100 fractures. Figure 4.28 shows that the alternated injection of water and gas in the horizontal reservoir provides a greater oil production, since the viscosity and density variations in the alternated injected slugs allow a better sweep by improving mobility ratio and maintaining reservoir pressure. One may also note the premature gas breakthrough for the continuous gas injection case. Figure 4.29 compares the WAG injection in horizontal, anticline, and dipping reservoirs, where one may note a higher production for the horizontal reservoir, which is mainly caused by differences in the magnitude of the gravity effects due to the reservoir geometry (earlier gas breakthrough occurs in the dipping case). The difference may also be justified by a change in the WAG ratio during the simulation run time.

4.2.2.2 Complex Fractures

In this application, we show how to model complex fractures with propped and non-propped regions using the EDFM. We evaluate the following: (1) the influence of the hydraulic fracture geometry (Case 1, Figure 4.30), (2) the influence of the fracture conductivity distribution in the fractures (Case 2, Figure 4.31), (3) the effect of the size of the middle fracture (Case 3, Figure 4.32), and (4) the influence of geometry and fracture conductivity distribution on non-planar fractures (Case 4, Figure 4.33). The cumulative oil production is used to compare each case. The equation of a paraboloid surface (Figure 4.34) was used to model the conductivity distribution in the fracture plane. Since conventional reservoir simulators handle hydraulic fractures as rectangular planes with constant conductivity, we define case 1a as the base case to be compared to Cases 2 and 3. For Case 4 we built four comparable cases, where the fractures have equivalent properties and the same wing length. Reservoir properties are described in Table 4.3.

Figure 4.35 presents the cumulative oil production curves for all cases evaluated in this work. Figure 4.35a shows the cumulative oil production of Cases 1a and 1b. The assumption of a rectangular fracture results in an optimistic cumulative oil production. When we assume a different geometry for the fracture, the cumulative oil production is reduced. This result illustrates the importance of modeling the correct fracture geometry. Figure 4.35b presents the comparison of a rectangular fracture to non-rectangular fractures with heterogeneous conductivity through the fracture plane. The effect of the fracture geometry has a greater impact than the fracture heterogeneity for the cases presented in this work. The pressure map in the complex fracture in Case 2a is shown in Figure 4.36; note the influence of the fracture geometry on the pressure map. Wu and Olson (2013) mention that due to local changes in the stress state field because of multiple fracturing, the center fracture tend to have small apertures and size. In Figure 4.35c we evaluate the influence of the size of the center fracture in the production; Case 2a (non-rectangular with heterogeneous

conductivity fractures) is also presented since the only difference between this case and Case 3 is the size of the center fractures. As the center fracture decreases in size, the cumulative oil production is reduced, which reinforces the importance of correctly modeling fracture geometries. Many authors in the literature mention that most hydraulic fractures may present non-planar geometries due to stress field anisotropy or presence of natural fractures (Siriwardane and Layne, 1991; Yamamoto *et al.*, 2004; Olson, 2008; Weng *et al.*, 2011; Dahi-Taleghani and Olson, 2011; Wu and Olson, 2013, 2014). Figure 4.35d shows the effect of non-planar fractures on the cumulative oil production. When the geometry of non-planar fractures are rectangular, the results are similar to a planar fracture with similar properties. The planar fracture cases result in slightly reduced cumulative oil production because the limits of the reservoir are reached faster, as shown in Figure 4.37. Figure 4.37a and Figure 4.37b show the pressure map after 50 days of production for the non-planar and for the planar fractures. Figure 4.37c and Figure 4.37d present the pressure map after 250 days for the non-planar and for the planar fractures; an isopressure line was drawn in red to show the different drainage area of each case. After including a different fracture geometry (Case 4b) we observe a reduction in the cumulative oil production. Adding a varying conductivity to the elliptical fracture planes (Case 4c) causes another small reduction in the cumulative oil production. Note that Cases 4b and 4c resulted in a reduced cumulative oil production compared to Case 4a, which reinforces the importance of correctly modeling fracture geometry.

4.3 Summary

Verification

- Due to restrictions imposed by the IMPEC formulation, a porosity cut-off was applied to fracture blocks to avoid low pore volumes and the simulation run time was reduced about 10 times without loss in the quality and precision of the results.

- The EDFM was verified against an unstructured grid model presented by Karimi-Fard and Firoozabadi (2003). A good match was observed for the cumulative production and water saturation maps.

- The EDFM was verified against fine grid models run in a commercial simulator for water and miscible gas injection. We verified multi-fractured horizontal wells with different fracture properties (homogeneous, heterogeneous and non-planar fractures) and naturally fractured reservoirs with 2, 10, and 100 fractures. A good match between the EDFM and fine model results was observed.

- In the case of 2 fractures the commercial simulator presented oscillations in the miscible gas injection cases due to phase identification issues; at high pressures and low temperature the CO_2 has a density close to the oil density, causing the phase identification algorithm to fail for some gridblocks. We evaluated the phase identification by density and critical temperature. Cases of 10 and 100 fracture presented less pronounced oscillations in the phase identification.

Application

- Different application case studies were investigated upon which the gravity effect was highlighted when the 2D models were converted to 3D grid. Gravitational effect was not pronounced for models with low number of fractures because of the low matrix permeability. We evaluated the EDFM in fracture reservoirs with different geologic structures assuming that all fractures have 90 degrees dipping angle and crossed the whole reservoir grid.

- For the continuous gas injection, we noticed gravity effects for the case with 100 fractures, once the high number of fractures increases the reservoir connectivity. The WAG injection showed a lower oil production for anticline and dipping reservoirs, which are caused by gravity effects (earlier gas breakthrough than the horizontal reservoir case). WAG provides a better mobility control when

compared to continuous gas injection, but it may have its efficiency reduced depending on the reservoir geometry.

- We performed an application with complex fractures where it was observed that correct modeling of fracture geometry is important to accurately predict production from multi-fractured horizontal wells.

Table 4.1: Reservoir properties of models used in validation and application.

Reservoir Dimension	500 x 500 x 80 ft
Initial Pressure	8534 psi
Reservoir Temp.	147.2^o F
Matrix Porosity	0.3
Matrix Permeability	10 mD
Fracture/Matrix Perm. Ratio	500
Fracture Aperture	1 ft
Matrix Irr. Water Sat.	0.25
Matrix Res. Oil Sat. (Water Inj.)	0.25
End Point for Water Rel. Perm.	0.5
Corey Exponent for Water Rel. Perm.	3
End Point for Oil Rel. Perm.	1.0
Corey Exponent for Oil Rel. Perm.	3
End Point for Gas Rel. Perm.	0.5
Corey Exponent for Gas Rel. Perm.	3
Fracture Rel. Perm.	Straight Lines

Table 4.2: Well operating constraints for WAG injection cases; WAG cycles (water or gas) of 90 days.

Well	Operating Constraint
Producer	Pressure (8534 psi)
Water Injector	Rate (392.2 bbl/day)
Gas Injector	Rate (1000 MSCF/day)

Table 4.3: Reservoir properties of cases used in this work.

Reservoir Dimensions	1000 x 3000 x 100 ft
Initial Pressure	8534 psi
Reservoir Temp.	147.2^o F
Matrix Porosity	0.15
Matrix Permeability	0.1 mD
Matrix Irr. Water Sat.	0.25
Matrix Res. Oil Sat. (Water Injection)	0.25
End Point for Water Rel. Perm.	0.5
Corey Exponent for Water Rel. Perm.	3
End Point for Oil Rel. Perm.	1.0
Corey Exponent for Oil Rel. Perm.	3
End Point for Gas Rel. Perm.	0.5
Corey Exponent for Gas Rel. Perm.	3
Fracture Rel. Perm.	Straight Lines

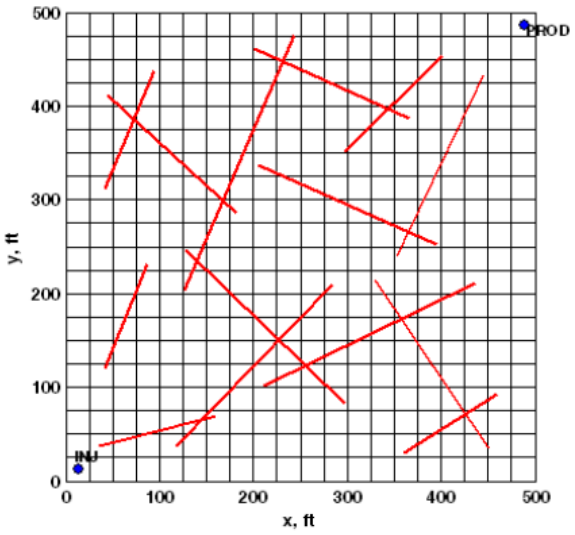

Figure 4.1: Moinfar et al.'s (2013) 2D model with 14 long vertical fractures.

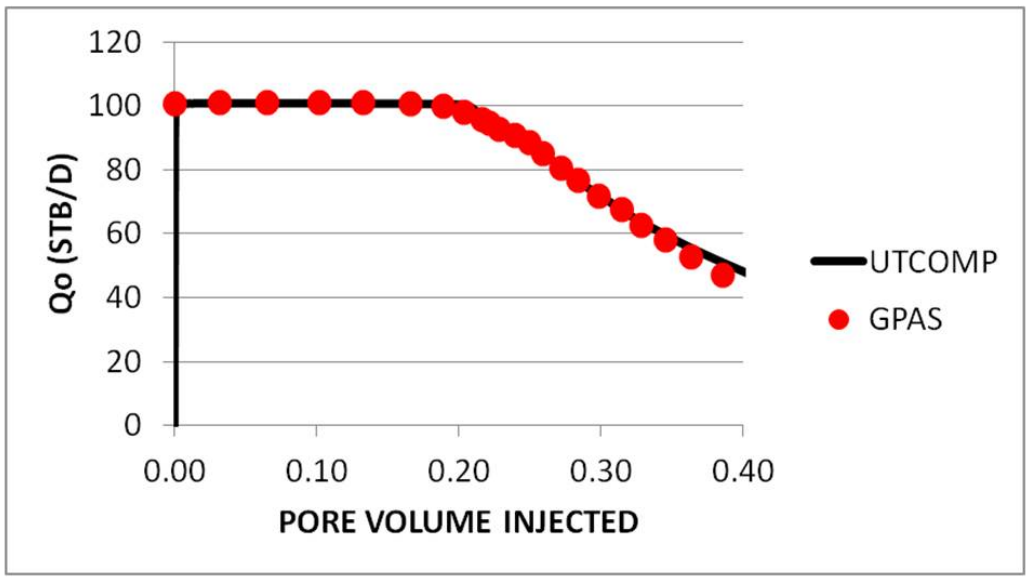

Figure 4.2: Verification of EDFM implementation in our IMPEC simulator (UTCOMP) against the Fully Implicit simulator (GPAS) developed by Moinfar et al. (2013) (GPAS).

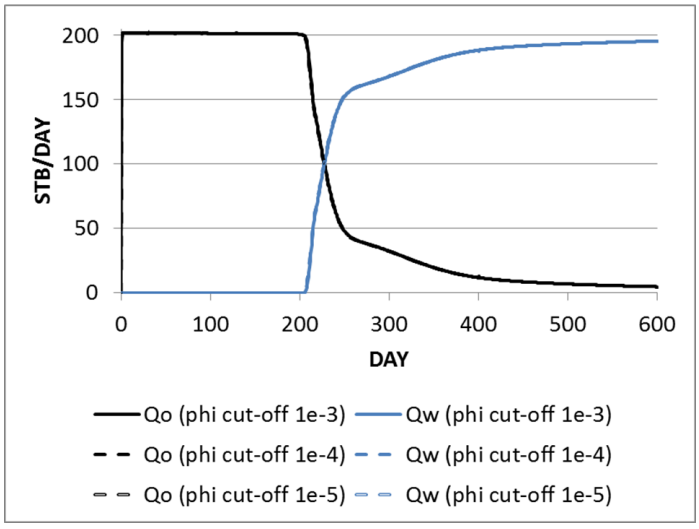

(a) Production results

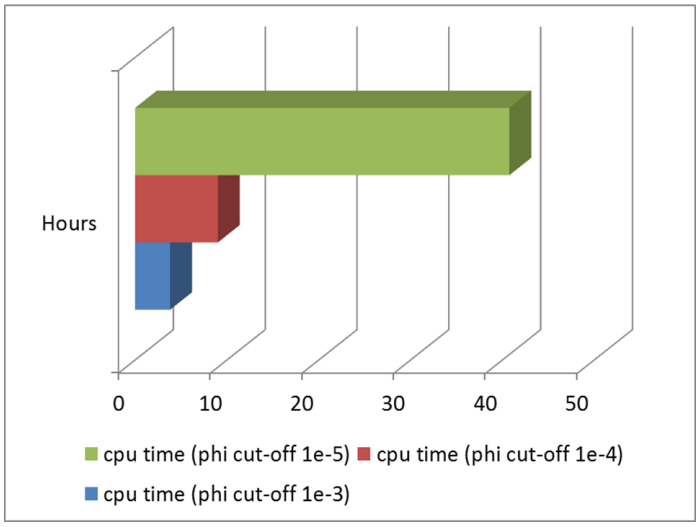

(b) Improvement in simulation run time

Figure 4.3: Fracture porosity cut-off application.

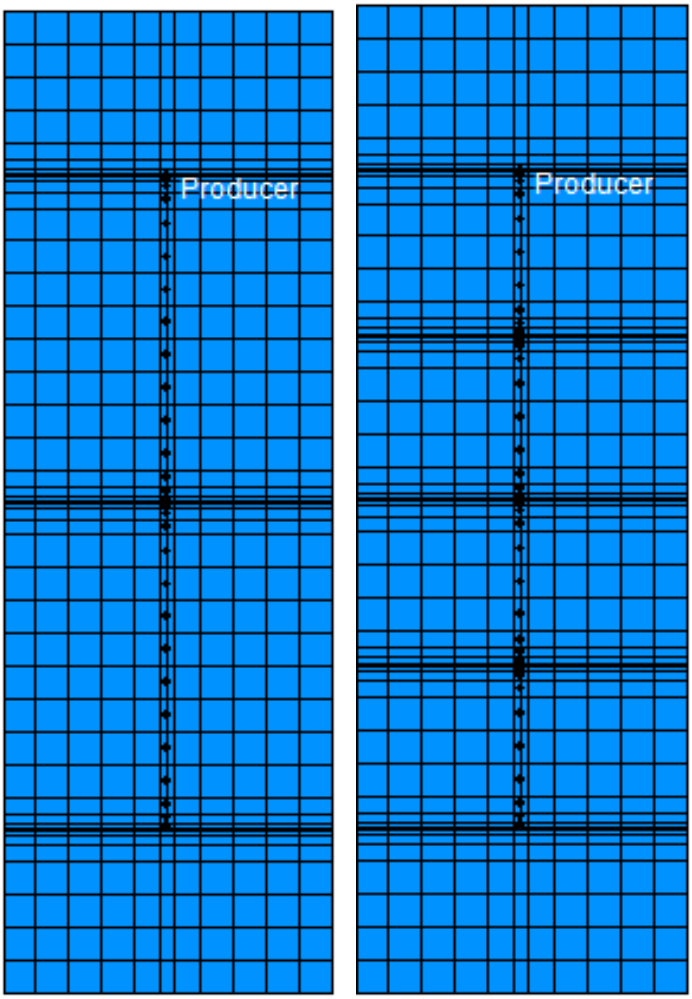

(a) 3 Fractures (b) 5 Fractures

Figure 4.4: Representation of multifractured wells.

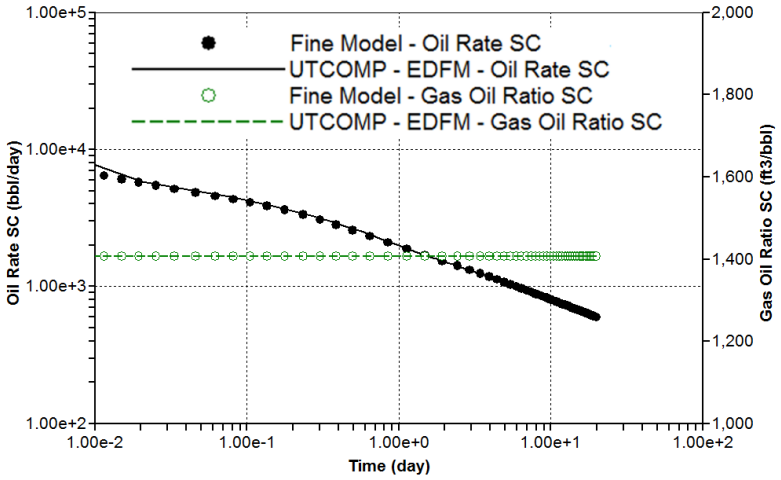

(a) Oil and gas production

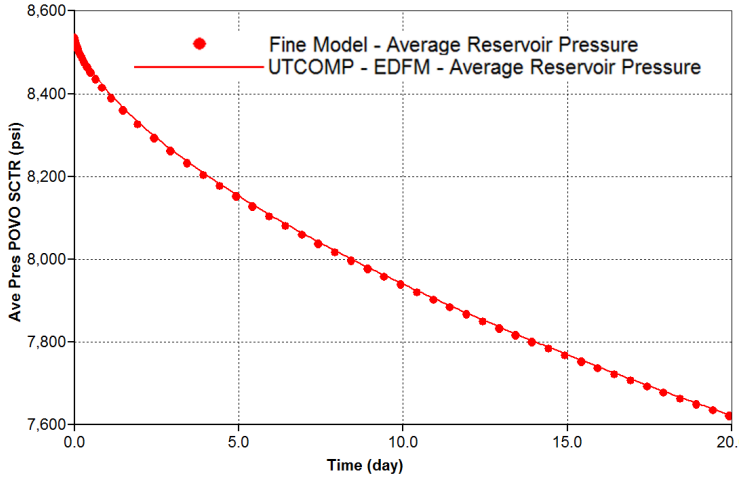

(b) Average reservoir pressure

Figure 4.5: Representation of multifractured wells (3 fractures).

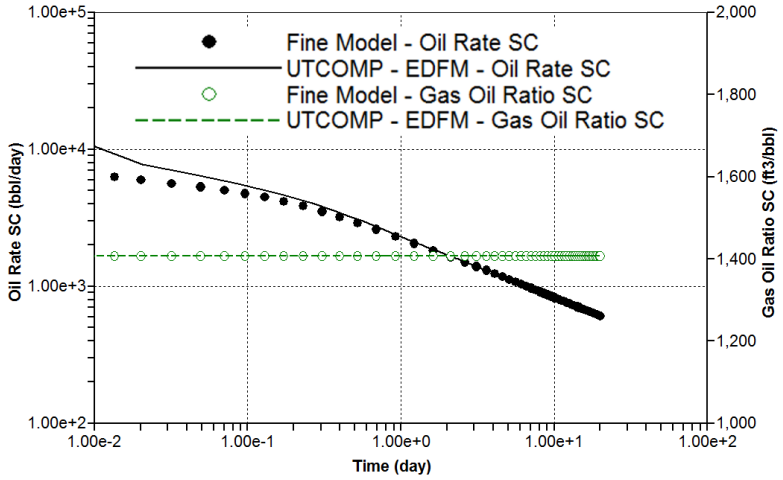

(a) Oil and gas production

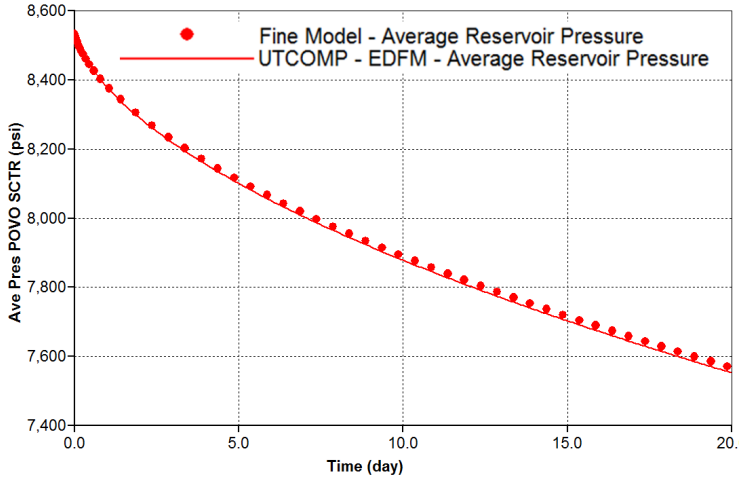

(b) Average reservoir pressure

Figure 4.6: Representation of multifractured wells (5 fractures).

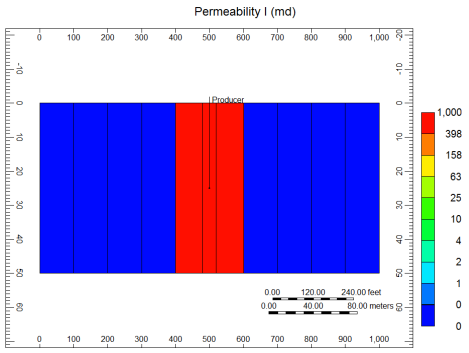

(a) Case 1

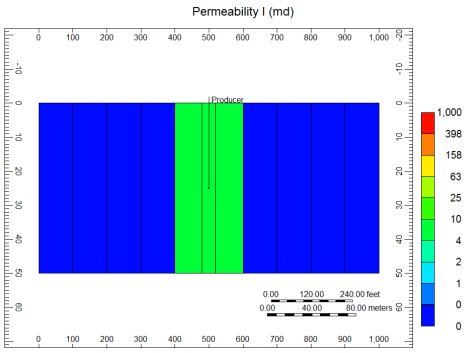

(b) Case 2

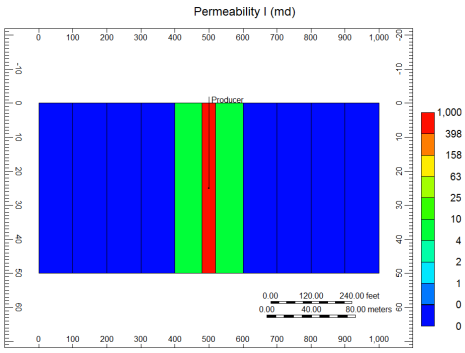

(c) Case 3

Figure 4.7: Permeability maps of the hydraulic fractures used in the verification cases.

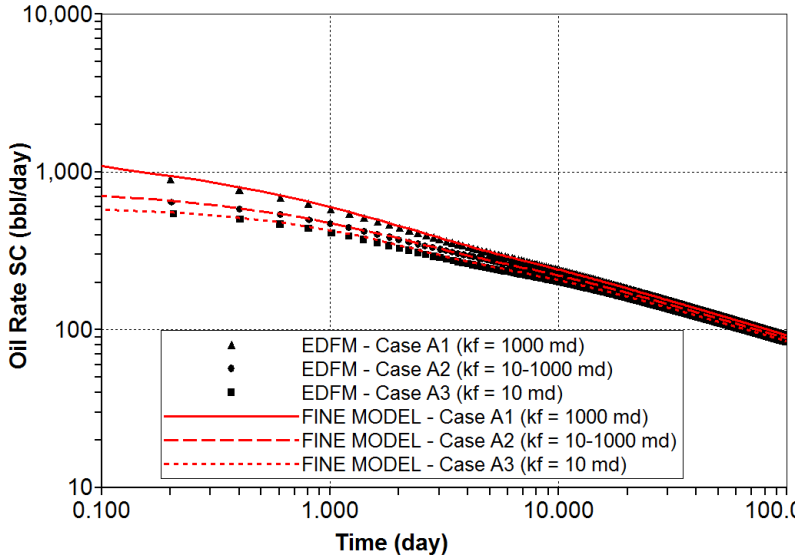

Figure 4.8: Results for verification of the EDFM and the fine model: Cases 1, 2, and 3.

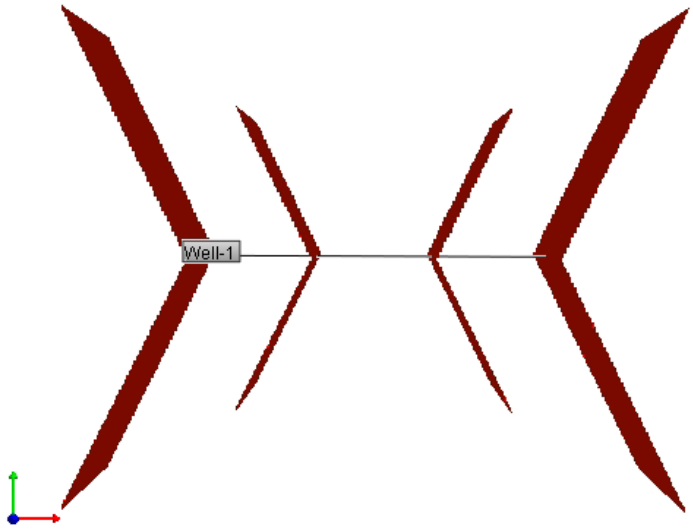

Figure 4.9: Illustration of the case with 4 non-planar fractures.

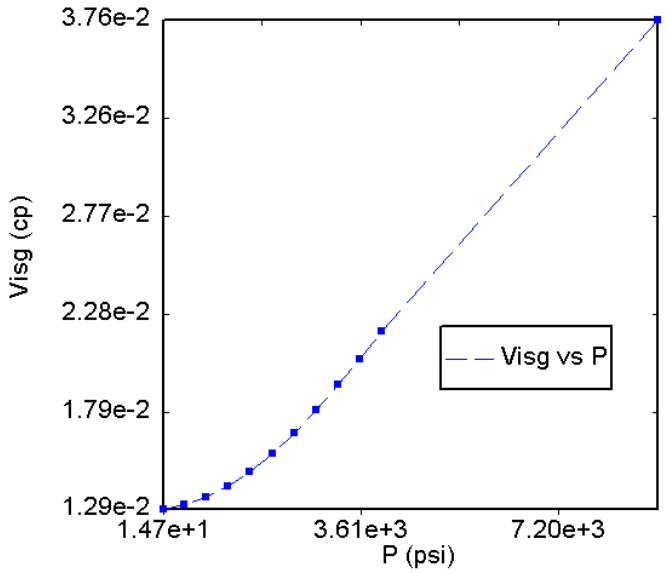

Figure 4.10: Gas viscosity as a function of pressure for the non-planar fracture case.

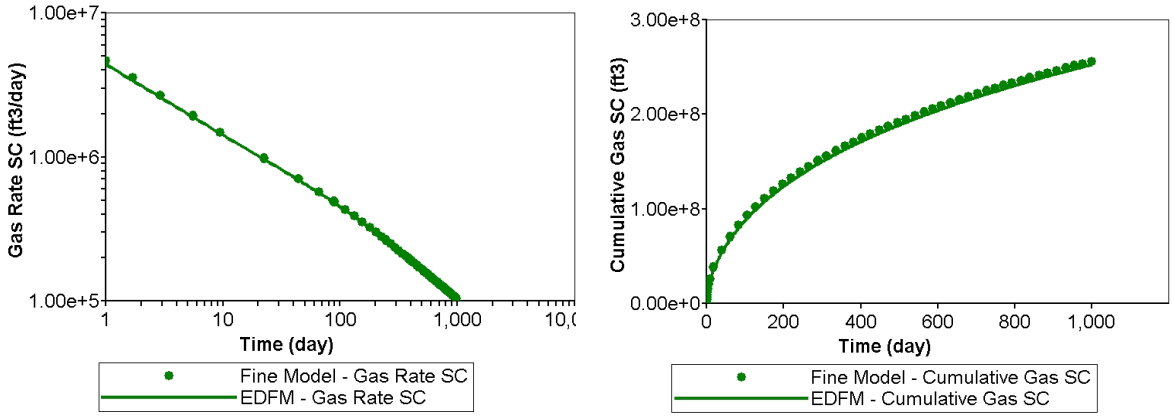

(a) **(b)**

Figure 4.11: Verification of non-planar fractures: (a) log-log plot of the gas production rate and (b) cumulative gas production.

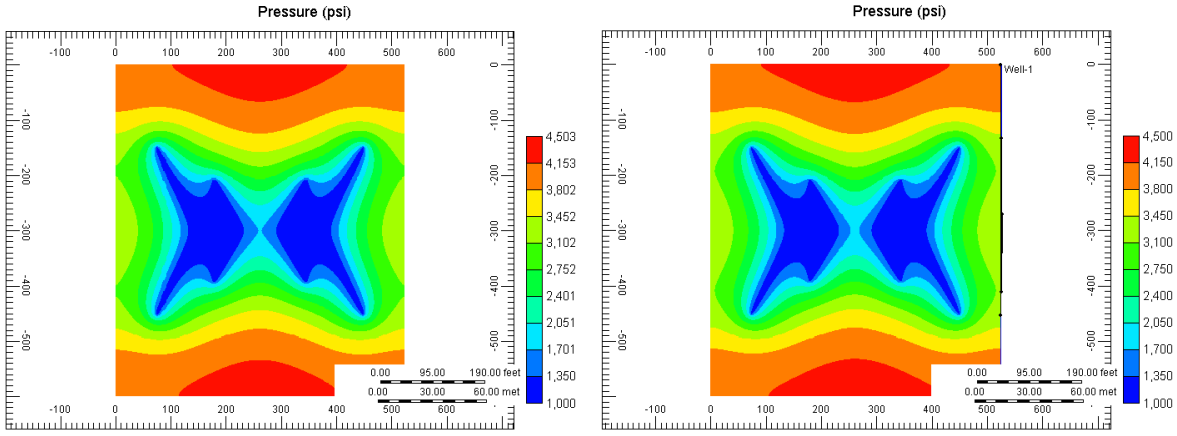

(a) (b)

Figure 4.12: Verification of non-planar fractures: (a) pressure map for the fine model and (b) pressure map for the EDFM.

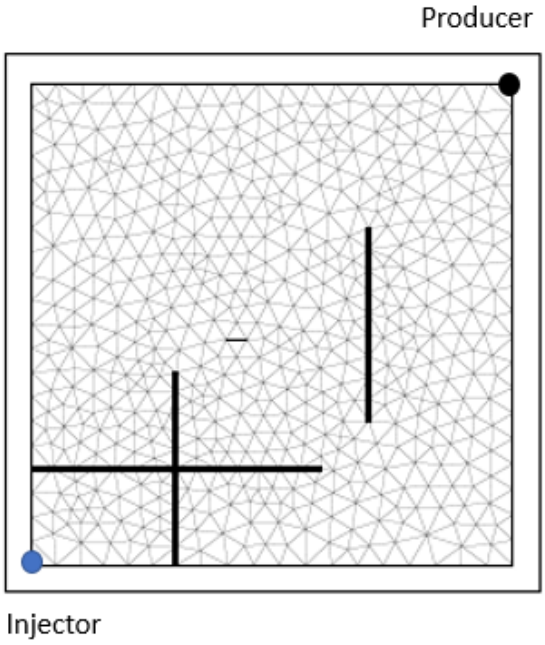

Figure 4.13: Unstructured grid used in Karimi-Fard and Firoozabadi's (2003) work.

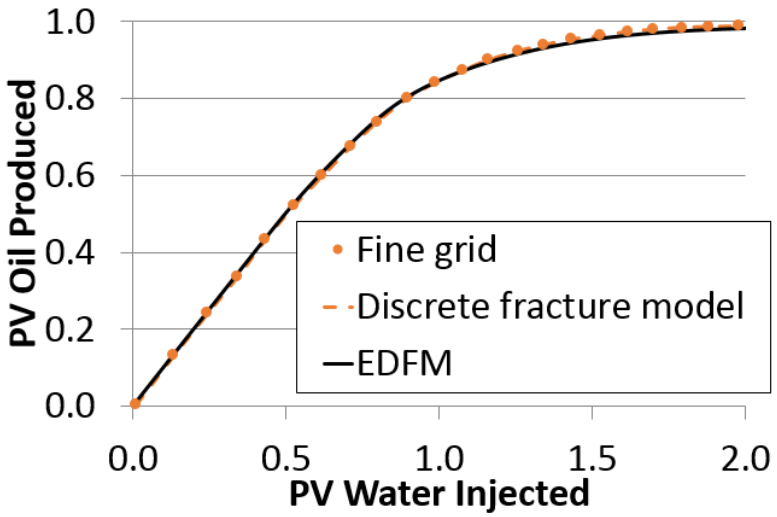

Figure 4.14: Verification of the EDFM against Karimi-Fard and Firoozabadi's (2003) unstructured grid case: PV oil produced .

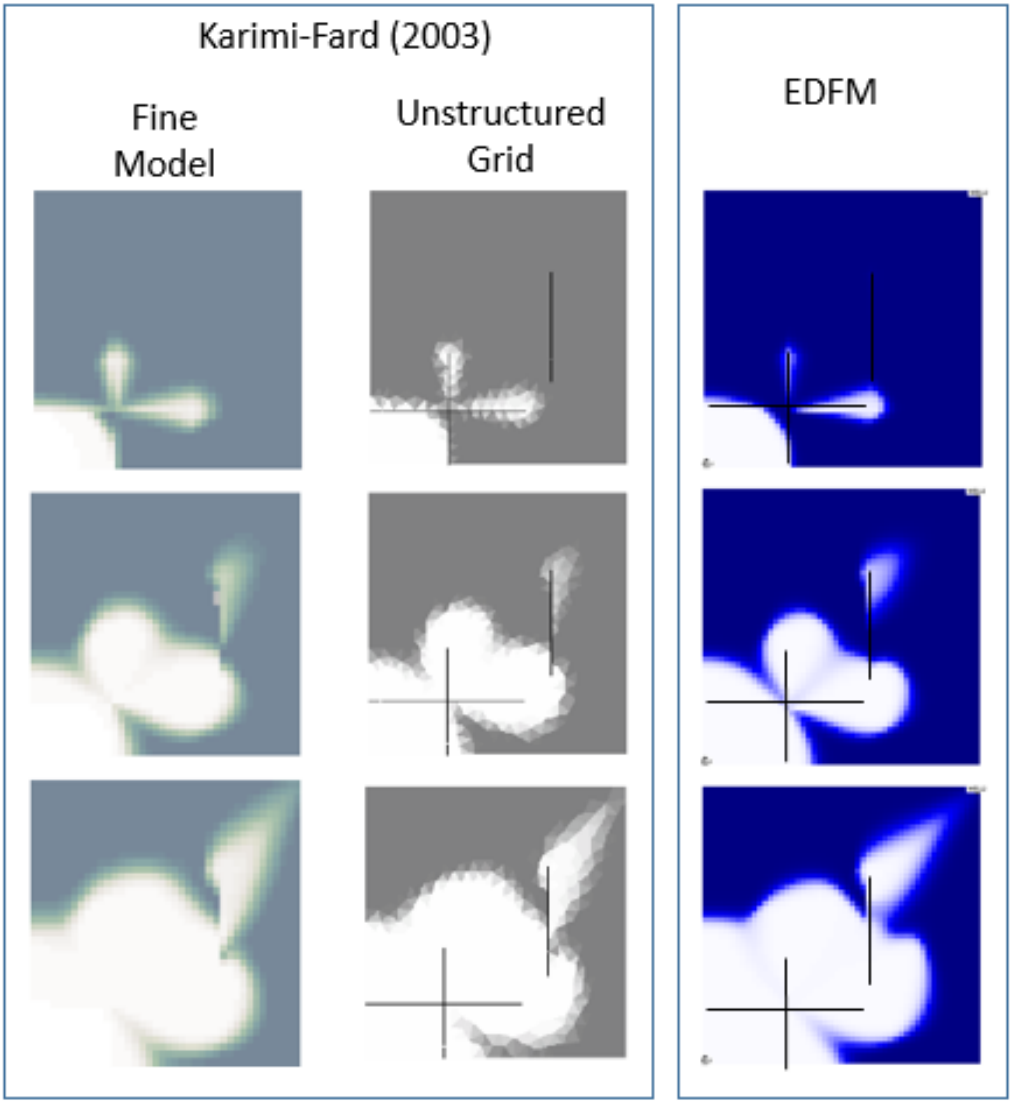

Figure 4.15: Water saturation map of Karimi-Fard and Firoozabadi's (2003) fine model and unstructured grid case compared to EDFM results.

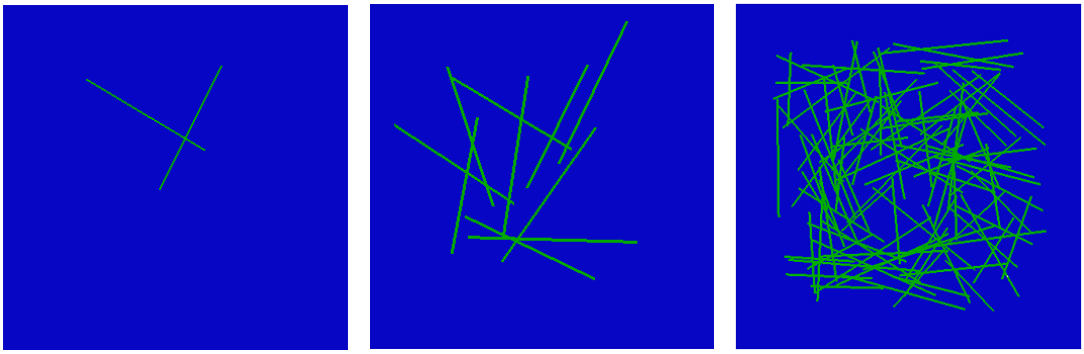

(a) 2 Fractures (b) 10 Fractures (c) 100 Fractures

Figure 4.16: Representation of fractures in fine grid, 2D model (commercial simulator).

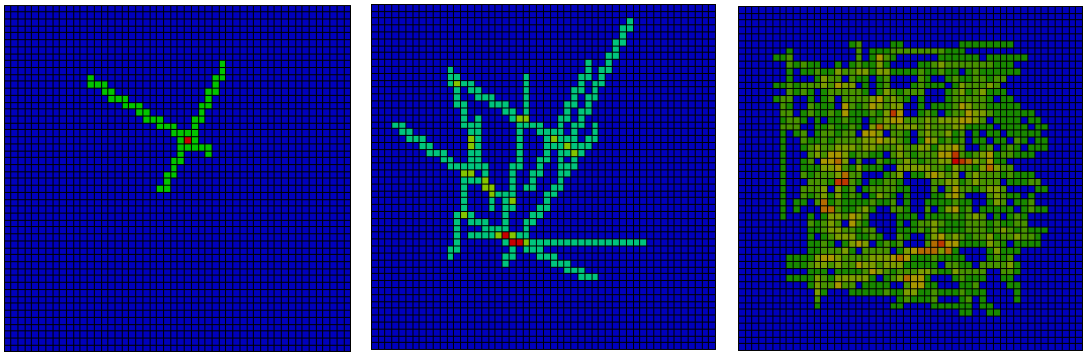

(a) 2 Fractures (b) 10 Fractures (c) 100 Fractures

Figure 4.17: Representation of fractures in fine grid, 2D model (EDFM).

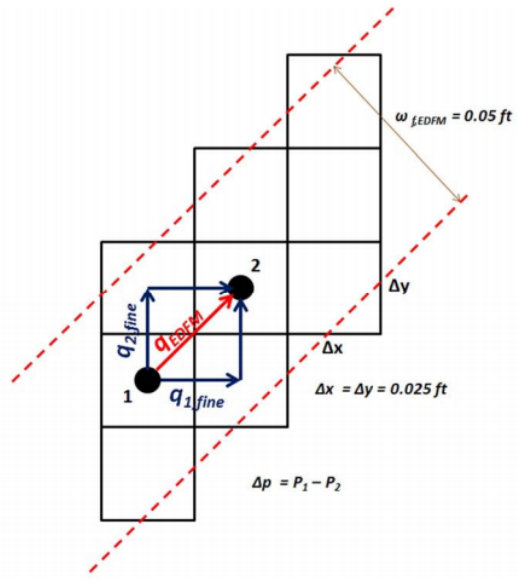

(a) Moinfar et al. (2013)

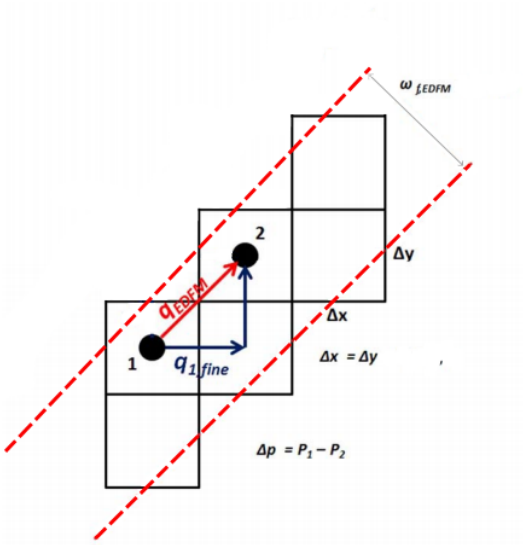

(b) Moinfar et al. (2013) modified

Figure 4.18: Stair step representation of fractures in single porosity fine models.

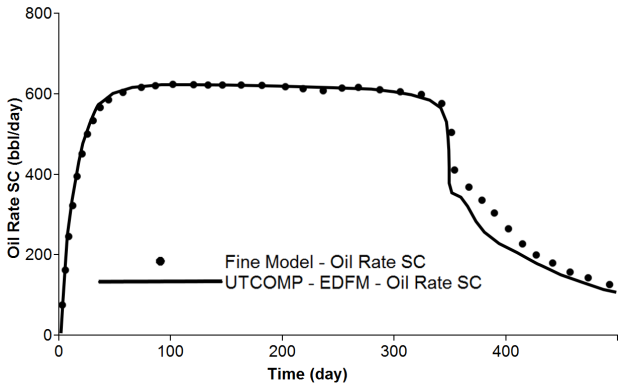

(a) 2 Fractures

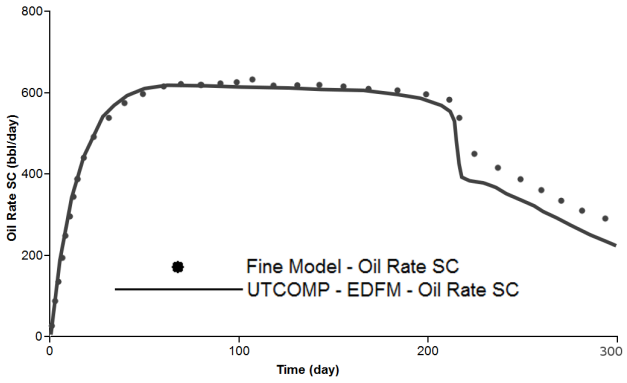

(b) 10 Fractures

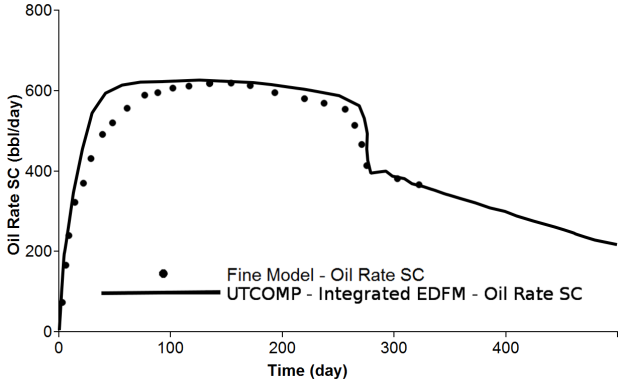

(c) 100 Fractures

Figure 4.19: Comparison of oil production for water injection case: Fine Model, EDFM (2 and 10 fractures) and integrated EDFM (100 fractures).

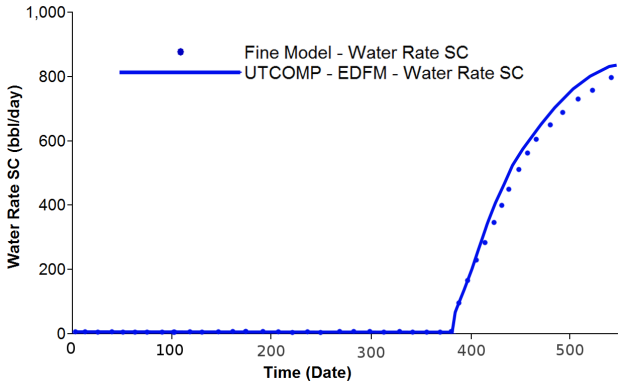

(a) 2 Fractures

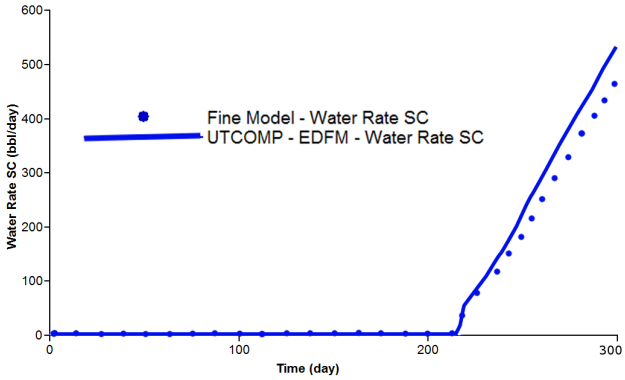

(b) 10 Fractures

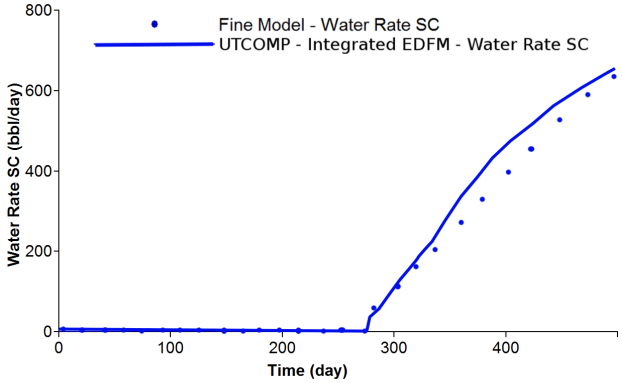

(c) 100 Fractures

Figure 4.20: Comparison of water production for water injection case: Fine Model, EDFM (2 and 10 fractures) and integrated EDFM (100 fractures).

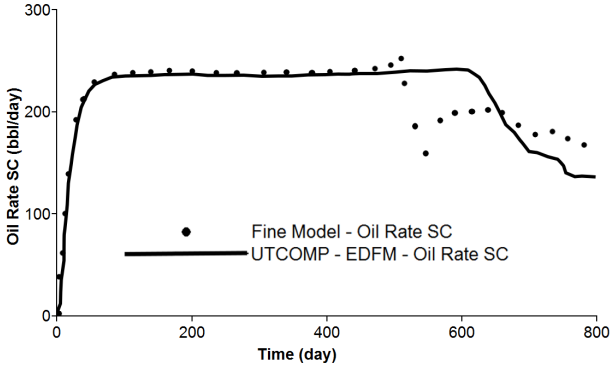

(a) 2 Fractures

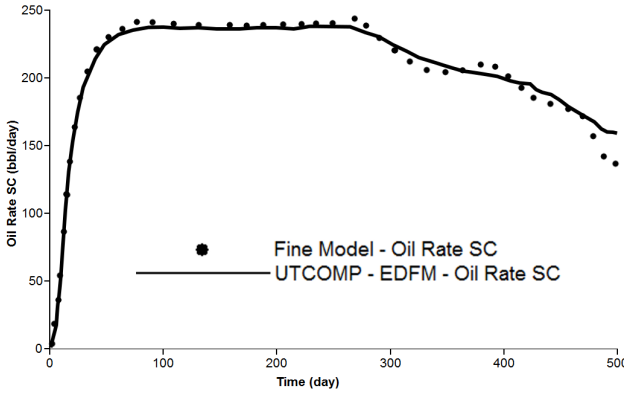

(b) 10 Fractures

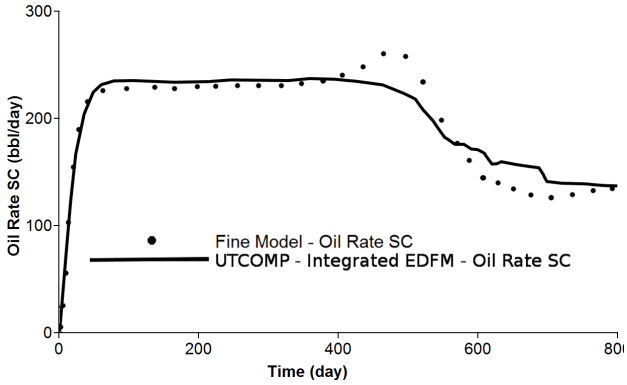

(c) 100 Fractures

Figure 4.21: Comparison of oil production for gas injection case (50% CO_2, 50% CH4): Fine Model, EDFM (2 and 10 fractures) and integrated EDFM (100 fractures).

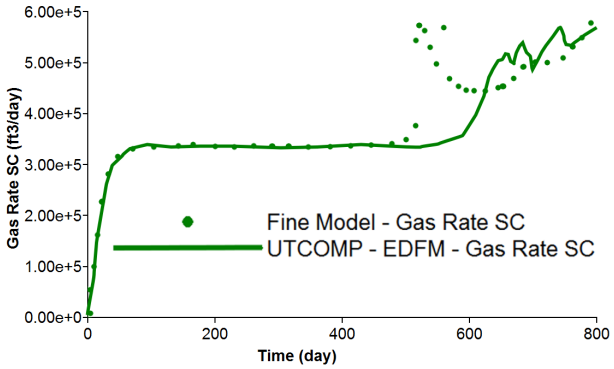

(a) 2 Fractures

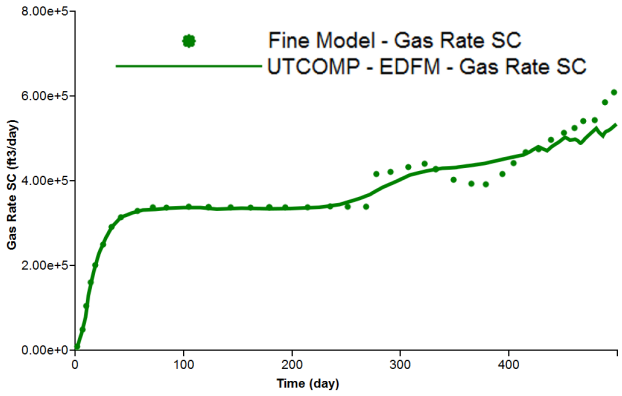

(b) 10 Fractures

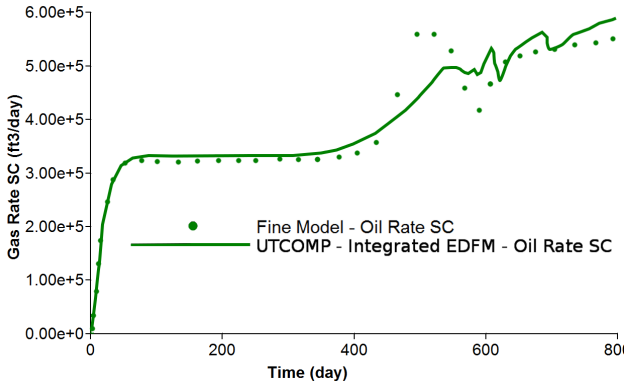

(c) 100 Fractures

Figure 4.22: Comparison of gas production for gas injection case (50% CO_2, 50% CH4): Fine Model, EDFM (2 and 10 fractures) and integrated EDFM (100 fractures).

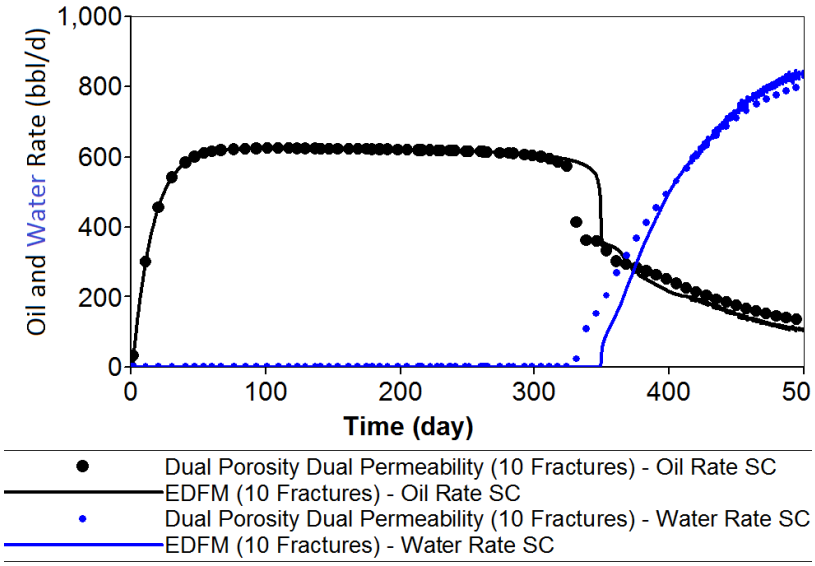

Figure 4.23: Comparison of the EDFM and conventional dual porosity formulations for a reservoir with 10 fractures.

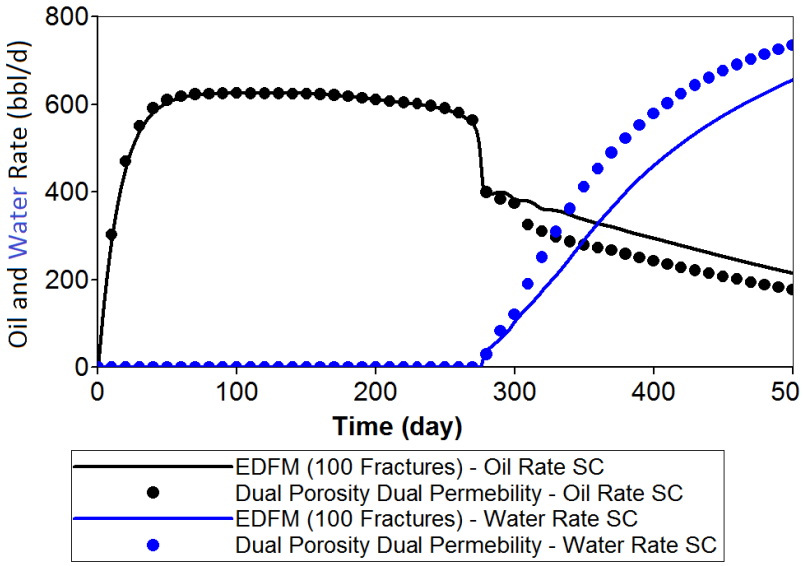

Figure 4.24: Comparison of the integrated EDFM and conventional dual porosity formulations for a reservoir with 100 fractures.

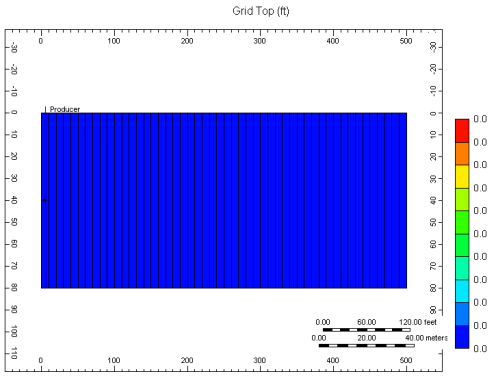

(a) Horizontal

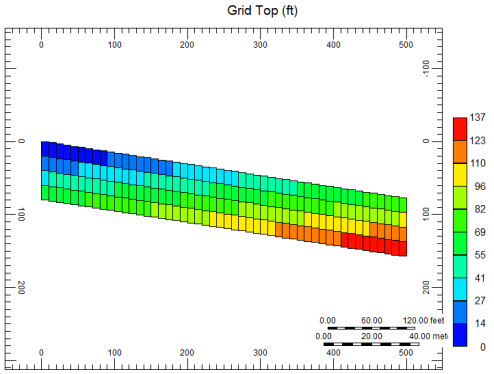

(b) Dipping

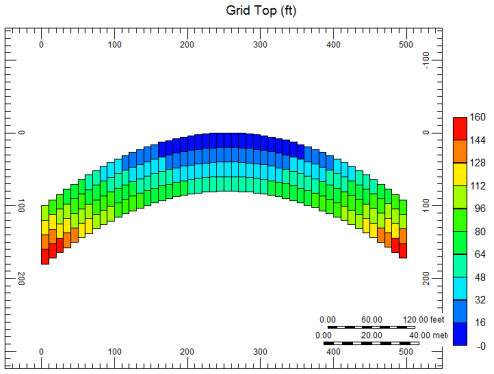

(c) Anticline

Figure 4.25: Horizontal, dipping and anticline NFR reservoirs; 3D grids expanded from 100 fractures case.

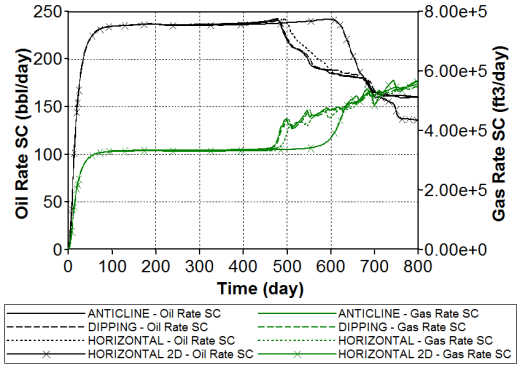

(a) 2 fractures

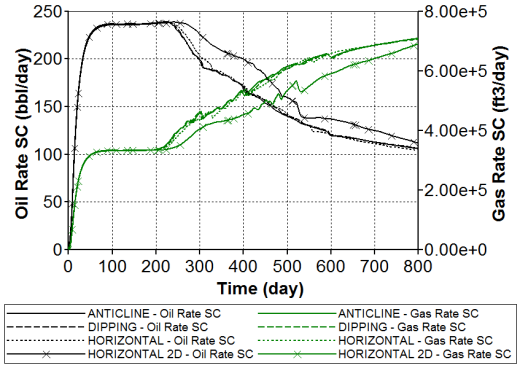

(b) 10 fractures

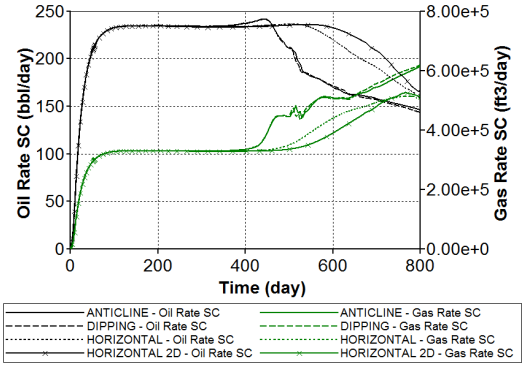

(c) 100 fractures

Figure 4.26: Gas injection in anticline, dipping and horizontal reservoirs: 2, 10, and 100 fractures.

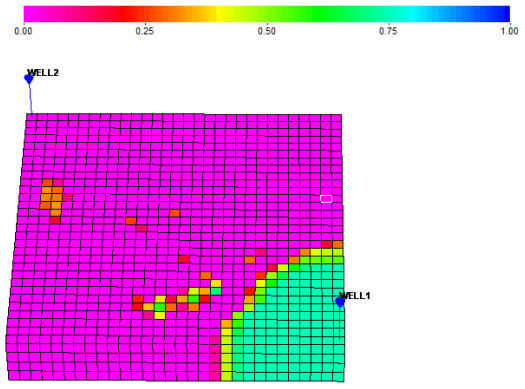

(a) Horizontal

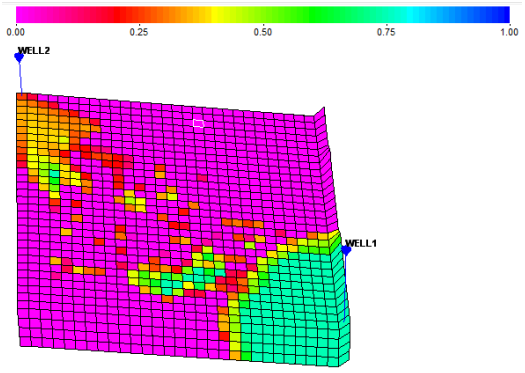

(b) Dipping

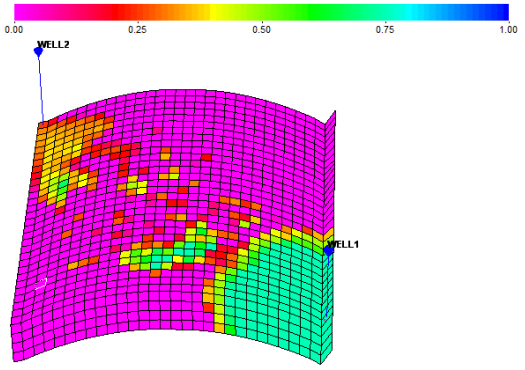

(c) Anticline

Figure 4.27: Gas saturation map after 600 days of production for the 100 fractures case in a horizontal, dipping and anticline reservoirs (3D grid); gravity effects may be noted.

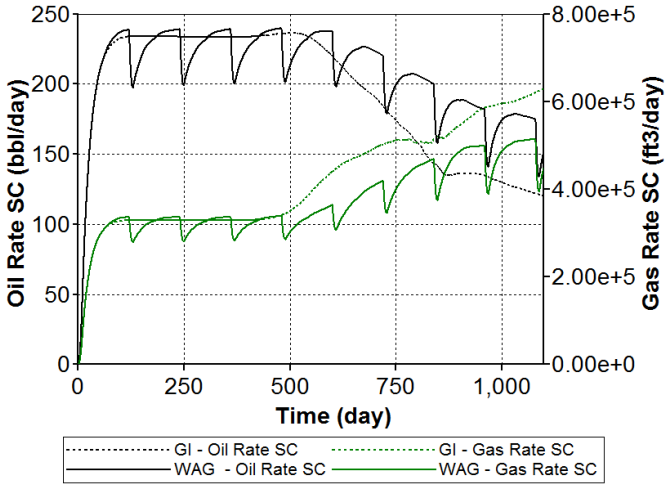

Figure 4.28: Continuous gas and WAG injections comparison (production rates) for horizontal 3D reservoir model. There was no water production in all cases.

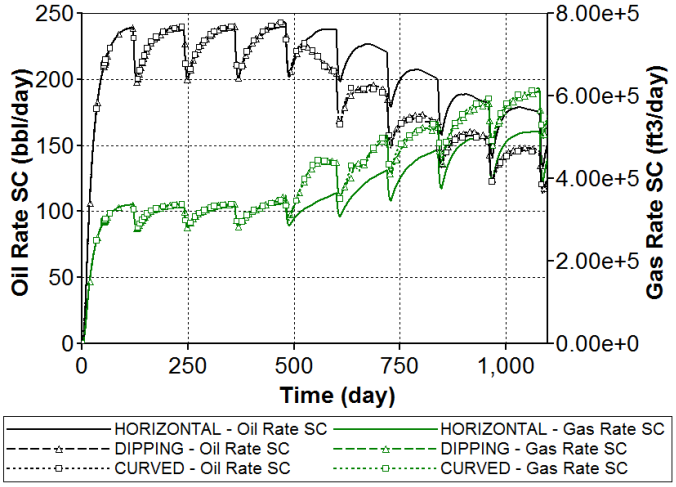

Figure 4.29: Continuous gas and WAG injections comparison (production rates) for dipping 3D reservoir model. There was no water production in all cases.

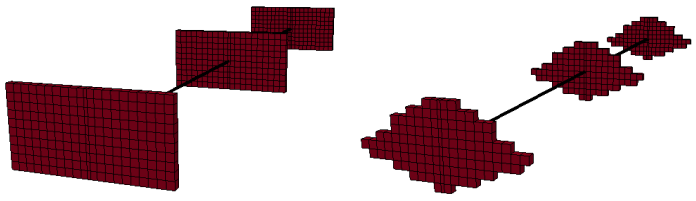

Figure 4.30: Hydraulic fractures of Case 1a and 1b.

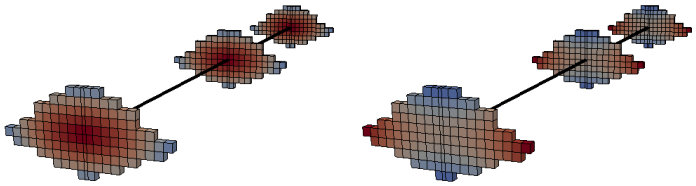

Figure 4.31: Hydraulic fractures of Case 2a and 2b.

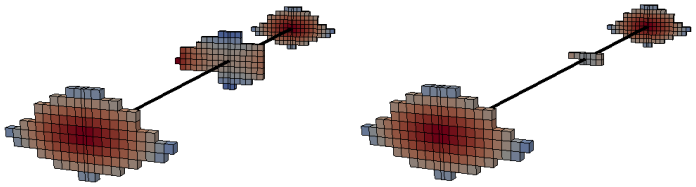

Figure 4.32: Hydraulic fractures of Case 3a and 3b.

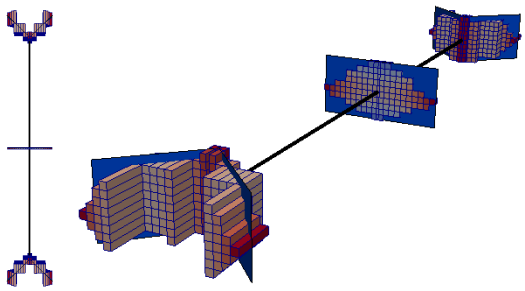

Figure 4.33: Hydraulic fractures of Case 4: top view on the left and 3D view on the right.

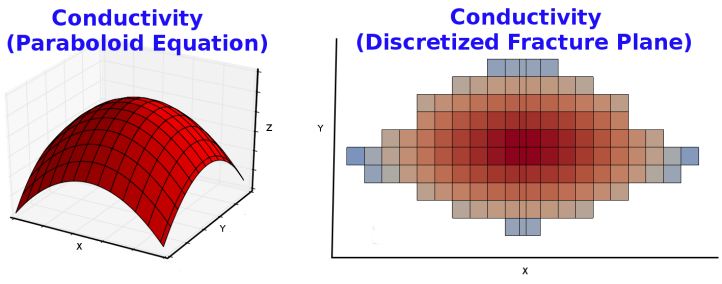

Figure 4.34: Example of a paraboloid surface used to model conductivity: plot of the analytical surface in the left and representation of the discretized fracture plane on the right.

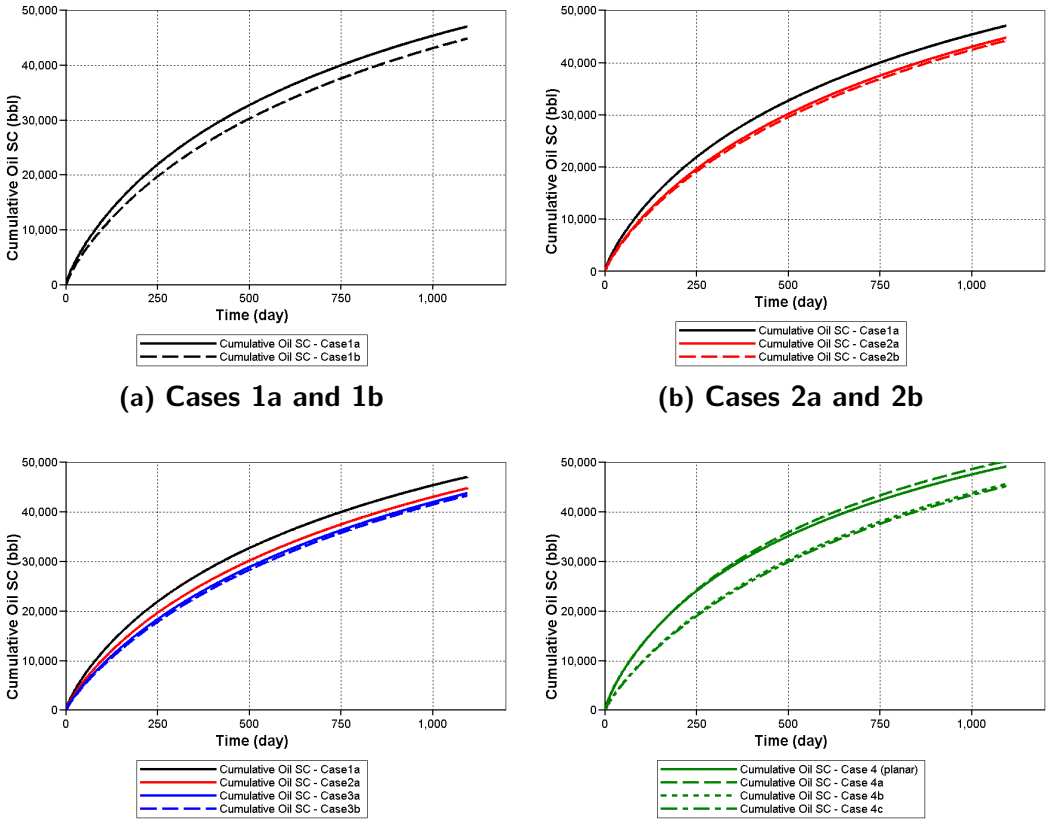

(a) Cases 1a and 1b **(b) Cases 2a and 2b**

(c) Cases 3a and 3b **(d) Cases 4a, 4b and 4c**

Figure 4.35: Cumulative oil production for cases 1, 2, 3, and 4.

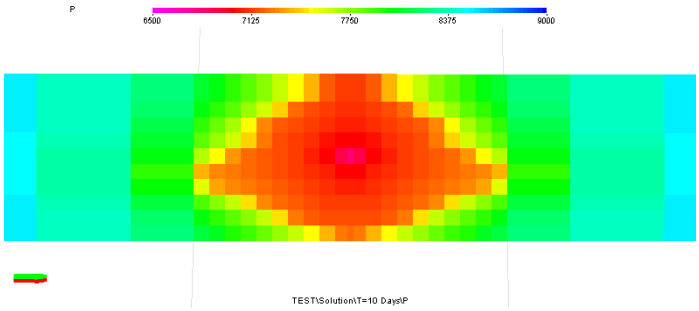

(a) 10 days

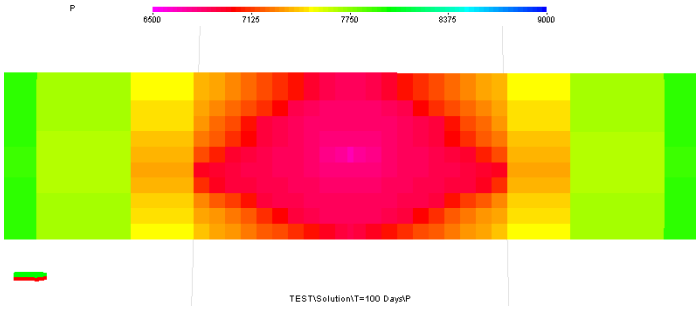

(b) 100 days

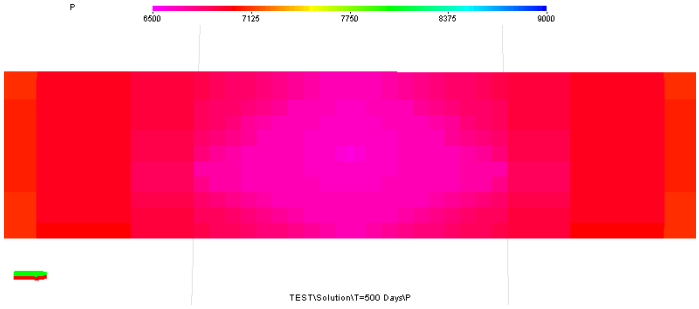

(c) 500 days

Figure 4.36: Pressure map for 10, 100 and 500 days in a complex hydraulic fracture (Case 2a).

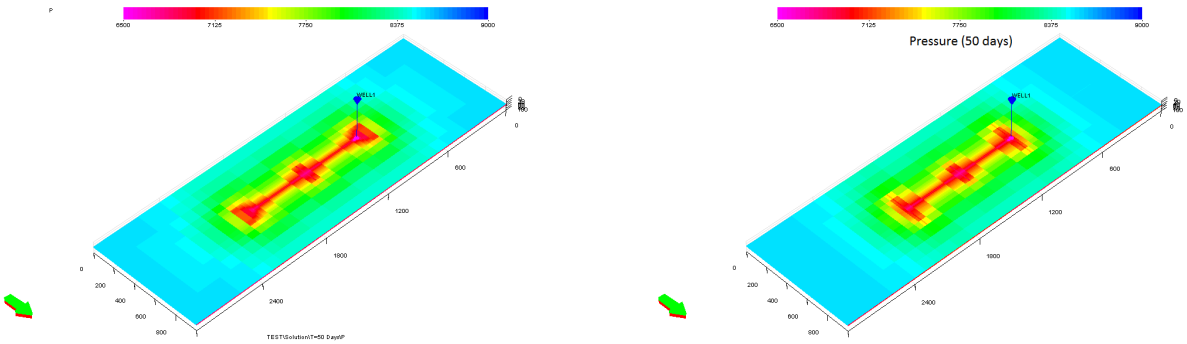

(a) Non-planar (50 days)

(b) Planar (50 days)

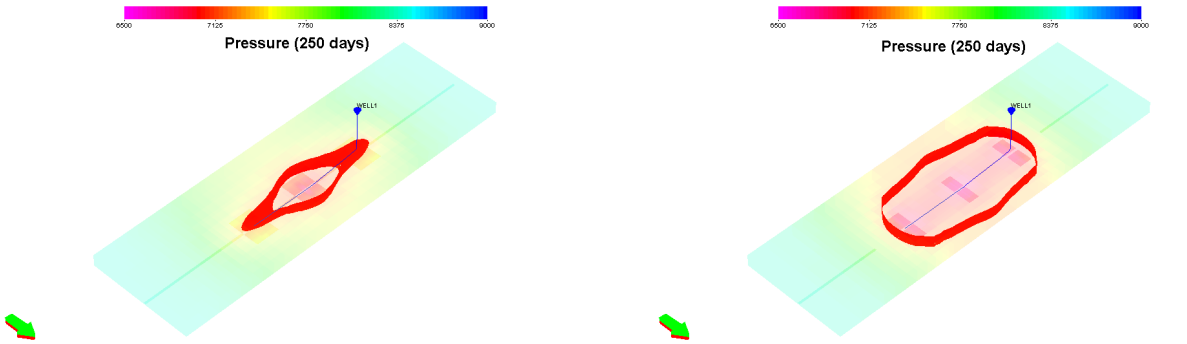

(c) Non-planar (250 days)

(d) Planar (250 days)

Figure 4.37: Pressure map (top view) for non-planar and planar fractures.

Chapter 5

Application of the EDFM to Multilateral Well Stimulation[1]

5.1 Introduction

The definition of a fishbone well presented at Schlumberger Oilfield Glossary (2014) is the following: "A series of multilateral well segments that trunk off a main horizontal well. The appearance closely resembles the ribs of a fish skeleton trunking off the main backbone." Many works in the literature describe the application of multilateral stimulation to increase well productivity in field projects. Those wellbore laterals are created using different methods such as mechanical drilling from the main wellbore using small drill bits or high velocity fluid injection to perforate the formation by diversion and dissolution.

Freyer and Shaoul (2011); Rice *et al.* (2014) described a multilateral stimulation technology (MST) known as fishbones technology. The technology was made possible by the development of a liner sub which houses four small-diameter high strength tubes called needles, each measuring 40 feet. Fishbones are created when the liner sub is hanged off into the wellbore with a standard liner hanger and HCl fluid is pumped jetting out of the nozzles located in each needle. Lateral tunnels of half to a quarter inches are created by diversion and dissolution. Although the needles exit the sub at 40^o angle the bending located at the exit port

[1]Cavalcante Filho, J. S. D. A., Xu, Y., Sepehrnoori, K., & Hogstol, H. (2015). Modeling Fishbones Using the Embedded Discrete Fracture Model Formulation: Sensitivity Analysis and History Matching. In SPE Annual Technical Conference and Exhibition. Society of Petroleum Engineers. Cavalcante Filho is the writer and main author, Xu is a collaborator and a reviewer, Sepehrnoori is the supervisor, and Hogstol is the provider of the production data.

results in laterals of approximately 90^o angle relative to the wellbore. This multilateral stimulation technology may be applied to compartmentalized, layered, or naturally fractured reservoirs. In the well screening process the presence of geological barriers is not an issue as it is in hydraulic fracturing. This stimulation technique is applicable to depleted reservoirs even when the accuracy of the depth is insufficient for sweet spot well placement (Rice *et al.*, 2014).

Figure 5.1 shows a schematic of the equipment used for fishbones installation (Carvajal *et al.*, 2015). A fishbone sub having 4 needles with 1/2 inch in diameter and 40 feet in length is the tool used to create fishbone laterals. Injected acid flows through the needles and is injected into the formation by nozzles located at the tip of the needle. As the acid is injected holes are created by diversion and dissolution; the needle is displaced in the direction of the formation like a hydraulic piston providing directionality and avoiding fluid loss to the formation. The pressure that displaces the needle is created by a valve located in the backbone anchor, which is positioned at the end of the column. Figure 5.1 shows that there is an angle between the injected needle and the formation, which is approximately 90 degrees after the needle is fully extended.

Numerical simulation must be used to assess the performance of multilateral stimulation and to evaluate the economic objective functions such as the net present value (NPV). A few numerical models are available in the literature for simulating fishbone wells, some of them using conventional reservoir simulation and fine grid models. Freyer and Shaoul (2011) attempted to model the fishbones using a single porosity model in a 3D reservoir simulator and computational fluid dynamics (CFD) modeling. In a high temperature gas/condensate reservoir consisting of layered and faulted sandstones, the fishbone's lateral extensions presented a productivity increase of 20-30% (compared to the base case well). A case of a hydraulic fracture was used for comparison and the fishbones produced less water due to the limited height of the branches and the evenly distributed connection with the reservoir. In a

low permeability sandstone gas reservoir, the fishbones stimulation proved to be as efficient as 2 longitudinal propped fractures. When longer needles were used, the Fishbones performance was comparable to 3 propped fractures. Freyer and Shaoul's (2011) used computer fluid dynamics (CFD) to estimate the friction pressure of a fluid flowing through a fishbone laterals. The calculated pressure loss was less than 0.07 MPa (10 psi) in all simulations performed. Rice *et al.* (2014) presented the results of a pilot well producing from the Austin Chalk formation, a tight limestone formation with porosity of 5% and 0.5 mD permeability located in Brazos County, Texas. Sixty laterals with 40 ft penetration length were successfully installed. Results showed a 8.3 times increase in IP-30 (cumulative production of first 30 days) and an 30 times increase in the well productivity index.

In this work we assume that wellbore laterals created with the fishbone technology may be modeled as fractures because of their small diameter and length. That assumption allows the application of the embedded discrete fracture model (EDFM) for fishbones modeling. The objective of this chapter is to apply the EDFM to model multilateral stimulation using wellbore laterals created by acid injection. A new EDFM connection between the wellbore lateral and the reservoir matrix was proposed assuming radial flow from the matrix to the lateral. A history match of the first fishbones pilot (Rice *et al.*, 2014) was accomplished using an in-house compositional IMPEC simulator and our EDFM preprocessor. Additional sensitivity analyses were performed to evaluate the number of fishbone laterals and the use of fishbone laterals in different reservoirs producing under primary production.

5.2 Results and Discussion

5.2.1 Fishbones' Pilot History Match

The fishbones' technology first pilot was performed in a well producing from the Austin Chalk formation. The Austin Chalk formation is a tight limestone

formation with 5% porosity and 0.5 mD permeability located in Brazos County, Texas. In this section we explain how the history match of the pilot data was conducted using our fishbones' modeling approach and an automated history match tool. The initial pressure of the reservoir was assumed to be 2500 psi, which gives a depletion of approximately 2000 psi compared to original hydrostatic pressure (4500 psi). The Initial water saturation (S_{wi}) is greater than the connate water saturation (S_{wc}); hence, the mobile water saturation is greater than zero. The reservoir properties (maximum and minimum values) used in the history match are given in Table 5.1.

The composition of the fluid used in this study is shown in Table 5.2 and is based on Whitson and Sunjerga's (2012) work. Assuming the fluid composition from the literature, a separator test was performed using a thermodynamic software in order to evaluate the properties of the fluid. The critical properties of the heaviest components were used to match the expected properties of oil and gas. We used the Peng-Robinson equation of state (EOS) and the Lorentz-Bray-Clark (LBC) viscosity correlation. The phase envelope for the fluid composition was obtained with regression as shown in Figure 5.2, where the green point represents the critical point and the red point represents the reservoir initial condition; the fluid is a retrograde gas.

5.2.1.1 Sensitivity Analysis

Before the history match, reservoir properties were evaluated in the expected range of variations as shown in Table 5.1. A total of $2n + 1$ simulations were performed to evaluate the sensitivity of each parameter using the conventional "One at a Time" sensitivity analysis method. Figure 5.3 shows the sensitivity analysis of the reservoir properties of the Austin Chalk formation on the water cumulative production. Two parameters have the most influence in the cumulative water production: the exponent of the water relative permeability curve (N_w) and the mobile water saturation (S_{wm}). N_w shows an inversely proportional relationship to

the total amount of produced water because a decrease in that parameter increases the area below the relative permeability curve, increasing the water mobility. S_{wm} shows a direct proportional relationship to the total amount of produced water because an increase in this parameter increases the mobile water saturation (defined as the difference between the initial and the connate water saturation). S_{wm} and the permeability of the matrix (k) show a greater influence on the cumulative oil production (Figure 5.4) and the cumulative gas production (Figure 5.5). S_{wm} presents an inversely proportional relationship for both oil and gas cumulative productions because an increase in this parameter decreases the initial volume of the oil phase. The permeability of the matrix presents a directly proportional relationship because an increase in this parameter increases the mobility of the produced fluids.

5.2.1.2 History Match

The history match was performed using an automated tool and the Simplex optimization algorithm. The Simplex method has been used to minimize the difference between simulated and history data as described by Nelder and Mead (1965). The method adapts itself to the local solution space contracting to a final minimum value, does not assume any smoothness for the solution, and may reach a local minimum depending on the initial guess. To use the automated history match we coupled the Simplex method, our EDFM preprocessor, and the numerical simulator to allow sequential runs in our Linux server. The procedure is presented in Figure 5.6.

The objective function is shown in Equation 5.1,

$$OF = \sum_{i=1}^{n} |X_{history,i} - X_{simulation,i}|, \tag{5.1}$$

where OF is the objective function, $X_{history,i}$ is the parameter to be matched from the

history data, $X_{simulation,i}$ is the simulation result to be adjusted at each automated history match step, and n is the number of points to be considered in the history match, each at a different simulation run time. The parameter used for the history match was the water production rate.

Figure 5.7 shows the evolution of the history match using the Simplex method. The water and gas rates at surface conditions were used as history match parameters. The water rate was the most sensitive parameter and was highly dependent on the initial water saturation and relative permeability curve. The automated history match was interrupted after 50 simulation runs because no further enhancement in the objective function was observed. Several cases provided reasonable history match. In this paper, three cases were selected to illustrate the results. Table 5.3 shows the reservoir properties of each case. The properties defined for the optimization process converged to similar values. Figure 5.8 presents the oil production rate of the pilot and the simulation (used as a constraint for the history match).

Figure 5.9 shows a good agreement for late time water production rates; for early times the simulation shows lower water production rates than the history. This difference in early time water production is due to a transient production of water both from inside the well and from a region near the wellbore. The gas production rate of the pilot and the simulation are shown in Figure 5.10. A good agreement between the history and the simulation data was obtained. The gas-oil ratio was constant because the reservoir was above the dew point during production. The selection of these cases was based on the match of the cumulative water production shown in Figure 5.11. A good agreement between the history and the simulation data was obtained. Figure 5.12 shows the cumulative gas production, where a good agreement between simulation results and history data can be observed.

5.2.1.3 Evaluation of the History Match assuming NFR

The presence of natural fractures in the Austin Chalk reservoir was evaluated using a triple porosity system composed of matrix, natural fractures and fishbones' laterals. Two hundred fractures aligned to the NE-SW direction (dip angle of 90^o and strike angle varying from 40^o to 50^o) and with 110 ft of average length (Figure 5.13) were defined. Fracture directions in the Austin Chalk formation were reported in Schnerk and Madeen's (1990) work. The fractures were embedded in the simulation grid using a dual continuum approach, allowing the simulation of a triple porosity reservoir composed of the matrix, natural fractures and fishbones. Figure 5.14 shows the comparison of history and simulated data for the water rate (the constraint is the oil rate). The water rate match was improved compared to cases without fractures (Figure 5.9). With the increase of reservoir connectivity, the water rate was able to stabilize faster after each oil rate change. Figure 5.15 shows the comparison of history and simulated data for the gas rate, where one may note a good agreement between the simulation results and the data. Figure 5.16 and Figure 5.17 show the comparison of history and simulated data for the cumulative water and gas productions. Results show a good match for both cumulative water and gas production.

5.2.2 Additional Sensitivity Analysis

To further study the application of the fishbones technology in carbonate reservoirs under depletion we evaluated the number of fishbones' subs and the reservoir characteristics using synthetic cases. The number of fishbones' subs varied from 4 to 15 subs (16 to 60 fishbone laterals) to investigate the behavior of different number of laterals on the well production. Different types of reservoirs were also studied, such as isotropic, anisotropic, and fractured. The influence of the reservoir characteristics on the cumulative oil production of a fishbone well with 15 subs (60 fishbone laterals) was evaluated using a different approach for each reservoir; after the analyzes were performed the averaged cumulative oil production was used to

determine in which type of reservoir the fishbones technology had a better performance.

We used a two-phase (oil and water) flow model (oil viscosity of 1 cp and water viscosity of 0.8 cp). The production well produces at a drawdown of 500 psi. Reservoir properties are as follows: porosity of 10%, permeability of 1 mD, mobile water saturation of 30%, endpoint of the water relative permeability curve of 1.0, and exponent of water relative permeability curve of 1.5. The parameters used for all cases and types of reservoirs are shown in Table 5.4. The analyses performed in each reservoir are described.

5.2.2.1 Number of Fishbone Subs

The influence of the number of fishbone subs is presented in Figure 5.18. An increase in the number of subs from 4 to 8 gives a greater volume of additional oil than when the number of subs is increased from 8 to 15. Extrapolating this tendency, one may note that as the number of subs increases the volume of additional produced oil drops, which indicated the existence of an optimal number of subs that gives a greater oil production at a lower operational cost. We define the fishbone production saturation point (FPSP) in the curve of the cumulative oil production against the number of subs. The FPSP corresponds to a point on the curve where a further increase in the number of fishbone subs does not increase oil production any further. Table 5.5 shows the well productivity index for oil and total fluids (oil + water). The well productivity index increases when the number of subs increases (well productivity index of the case of 15 subs is 3.3 times greater than the case with no subs).

The main objective of the pilot evaluated in this work was to test the mechanical installation of the fishbone; hence, the economic feasibility of the pilot was not taken as a decision parameter. We performed a simplified economical evaluation of the fishbones to qualitatively analyze the behavior of the plot of an economical objective function against the number of fishbone subs.

Figure 5.19 shows the economic evaluation for the cases with 4, 8, and 15 subs using an estimative of the cost of this fishbone operation and using different oil prices; note that an increase in the number of subs from 4 to 8 reduces the NPV (additional oil does not pay the use of an additional sub) being 4 subs the FESP for those examples. The plot of the net present value (NPV) against the number of subs would gives us a point similar to the FPSP, which we refer to as the fishbone economical saturation point (FESP). The FESP will appear when the number of fishbone sub increases and the additional produced oil is not sufficient to pay the cost of an additional sub.

5.2.2.2 Different Types of Reservoir

Isotropic, Homogeneous Reservoir

A linear regression model was used to fit the simulation results and evaluate the influence of the reservoir permeability in the oil production. The plot of the cumulative oil production against the logarithm of the permeability is presented in Figure 5.20. As the permeability increases, the cumulative oil production decreases because of a greater amount of water produced.

Anisotropic, Heterogeneous Reservoir

Different anisotropic reservoirs were constructed using the Dykstra-Parson coefficient as a measure of anisotropy; a linear regression model was used to fit the simulation results and evaluate the influence of the geometric average of the permeability of all layers in the oil production. Figure 5.21 presents a plot of the cumulative oil production against the Dykstra-Parsons coefficient. Note that both parameters present a weak linear correlation ($R^2 = 0.65$). Figure 5.22 shows a plot of the cumulative oil production against the weighted geometric average of the permeability (GEOK); the linear correlation was $R^2 = 0.84$. A comparison between Figure 5.20 and Figure 5.22 shows that the production from fishbones' laterals is

more sensitive in anisotropic reservoirs, where a smaller increase in GEOK results in a bigger loss in terms of oil production due to water production.

Fractured Reservoir

The fractured reservoir case needs a more complete evaluation, since several parameters of the fracture model may affect the reservoir connectivity. The following parameters of the fracture network model were evaluated: number of fractures, fracture length, fracture conductivity, dip and strike angle. A uniform probabilistic distribution was assigned for each parameter. The Latin Hypercube Experimental Design was used to sample 10 combinations of the parameters; note that the amount of 10 combinations is adequate for a sensitivity analysis study, but a greater number of samples is needed for history matching or uncertainty analysis studies using response surface models. A sensitivity analysis was performed using the regression analysis technique (Helton *et al.*, 2006). The linear surface equation shown in Equation 5.2 was used to match the cumulative oil production using least squares regression. Helton *et al.* (2006) reported that the coefficients of the linear surface equation are not used for sensitivity analysis for two reasons: coefficients are influenced by the units of each parameter in the equation and they do not carry any information on the distribution assigned for each parameters. For that reason, the coefficients were transformed using Equation 5.3, which provides a reliable measure of the parameter importance when all parameters are independent. A tornado plot was then built to show the influence of each variable.

$$\hat{y} = b_0 + \sum_{j=1}^{n} b_j x_j, \tag{5.2}$$

$$\hat{b_j} = \frac{b_j \hat{s_j}}{\hat{s}}, \tag{5.3}$$

where $\hat{s}$ is the standard deviation.

Figure 5.23 shows a tornado plot with the number (N_f), length (L_f), conductivity (C_d), dip and strike angle of fractures against the cumulative oil and water production. The parameters that most strongly influence the cumulative oil and water production are related to the fracture geometry: the dip angle, strike angle, and length of the fractures. An increase in the dip angle increases the area of the fracture into the reservoir (assuming fractures penetrate the whole reservoir) and increases reservoir connectivity. The strike angle is related to the fracture positioning, which determines whether or not the fishbone lateral intersects a given fracture. A change in the fracture length changes the fracture area. Fracture characterization was found to greatly affect the results, being also the biggest source of uncertainties.

We compared the effect of presence of fractures in a more permeable reservoir producing from a fishbone well by increasing the matrix permeability and comparing the coefficients obtained after the regression of the data to a linear surface equation. Although the coefficients of the linear surface equation cannot be directly used for sensitivity analysis, the comparison of their absolute magnitude in the cases of low and high matrix permeability allows the qualitative measurement of the effect of the fractures in both cases. Figure 5.24 shows the absolute magnitude of the coefficients of the linear surface equation for the cumulative oil and water production for both cases with low (1 mD) and high matrix (100 mD) permeability. Note that the absolute magnitude of the coefficients is higher for the case of low matrix permeability. The presence of fractures has a greater impact on low permeability reservoirs.

Figure 5.25 compares the average cumulative oil production for the isotropic, anisotropic, and fractured reservoir cases. A greater cumulative oil production was observed for the application of the fishbone technology in the case of a fractured reservoir. These results are due to a greater spreading of the pressure drawdown over the fracture network during production, which reduces the water channeling effect.

The well productivity index for the case with fractures was 3 times greater than the isotropic case of 15 subs presented in Table 5.5.

5.3 Summary

- The use of equivalent fractures allows effective modeling of multilateral well stimulation. A new well to matrix connection was proposed based on the Peaceman's equation which assumes radial flow from the matrix to the wellbore laterals.

- The sensitivity analysis of reservoir parameters on the water cumulative production showed the Nw exponent and the Swi as the most strongly influencing parameters, denoting an inversely and directly proportional relationship, respectively; the cumulative oil production and the cumulative gas production had k and S_{wi} as the most influencing parameters.

- An automated history match procedure was used to match a fishbone pilot performed in the Austin Chalk. The water rate and cumulative water production were the most sensitive production parameters. The main matching parameters were the water relative permeability curve and the initial water saturation. When natural fractures were added the water production rate showed a better match.

- As the number of fishbone subs increases the well productivity index and the oil recovery increases. Extrapolating this tendency one may determine the optimal number of subs which gives the greater oil production at the lowest operational cost. The Fishbone Production Saturation Point (FPSP) was defined as the point where an increase in the number of subs does not increase oil production.

- The dip and strike angles of the fractures were the most strongly influencing parameters as observed in the sensitivity analysis of the fractured reservoirs;

these results show that the fracture characterization is a source of uncertainty and reinforces the importance of an appropriate fracture modeling for reliable results.

- Fractured reservoirs are the best scenario for fishbones application. The connection of the fishbone laterals to a natural fracture network increases the well to reservoir connectivity, allowing greater cumulative oil production.

Table 5.1: Reservoir properties range used in this work.

Property	Min	Max
Porosity (%)	5	10
Permeability (k_{matrix}, mD)	0.50	1.50
Mobile Water Saturation (S_{wm})	0.15	0.50
Water Relative Permeability End-point (k^o_{rw})	0.50	1.00
Exponent for Water Relative Permeability (N_w)	1.50	3.00

Table 5.2: Composition of the fluid used in this study.

Pseudo-Component	Global Molar Fraction
CH4	0.6996
CO2	0.0136
H2S-C2H6	0.1163
C3H8	0.0471
IC4-FC6	0.0256
NC4-IC5-NC5	0.0356
C7+	0.0622

Table 5.3: Reservoir properties of Cases 1, 2, and 3.

Properties	Case 1	Case 2	Case 3
Porosity (%)	6.1	6.1	6.2
Permeability (mD)	0.975	1.042	1.066
Mobile Water Saturation	0.291	0.284	0.290
Krw@Sor	0.827	0.806	0.789
Nw	1.339	1.316	1.316

Table 5.4: Reservoir properties of the cases used for the sensitivity analysis on different reservoirs.

Reservoir	Isotropic	Anisotropic	Fractured				
Case	k_{matrix}	DP Coef.	N_f	L_f	C_d	Dip	$Strike$
1	105	0.42	126	223.99	0.35	67.94	12.51
2	669	0.61	43	180.41	14.82	53.80	129.59
3	430	0.75	190	207.63	27.33	63.19	61.89
4	42	0.76	165	144.31	62.36	50.50	51.24
5	978	0.37	162	116.50	53.07	57.95	77.32
6	337	0.46	21	152.38	59.46	76.67	92.62
7	540	0.67	135	57.04	26.37	74.91	117.75
8	771	0.49	73	95.61	6.75	71.17	140.75
9	272	0.61	85	82.34	16.14	62.10	154.69
10	850	0.27	108	244.54	14.76	81.32	39.71

Table 5.5: Well productivity index for cases with different number of subs.

Cases	Total PI (bpd/PSI)
0 Subs (No Fishbones)	0.17
4 Subs	0.32
8 Subs	0.44
15 Subs	0.56

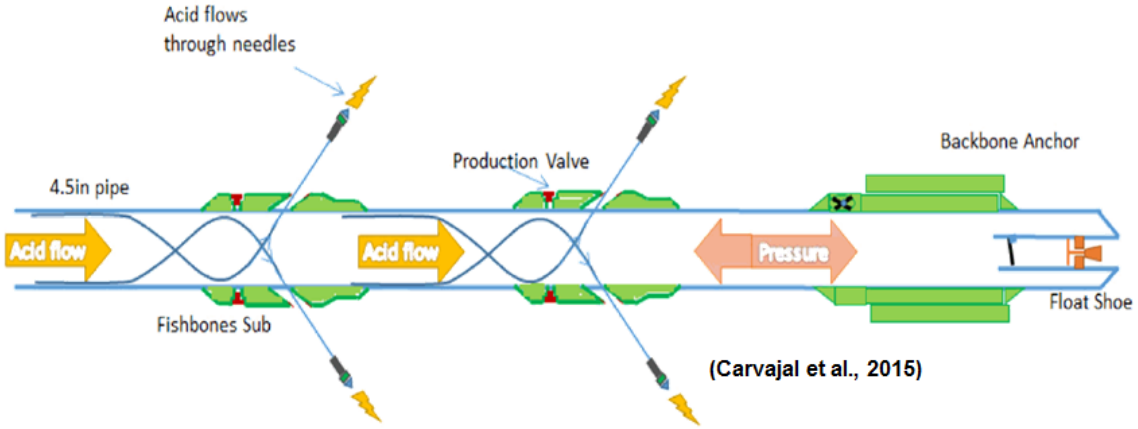

Figure 5.1: Schematic of the installation of multilateral branches using the fishbones' technology (Carvajal et al., 2015).

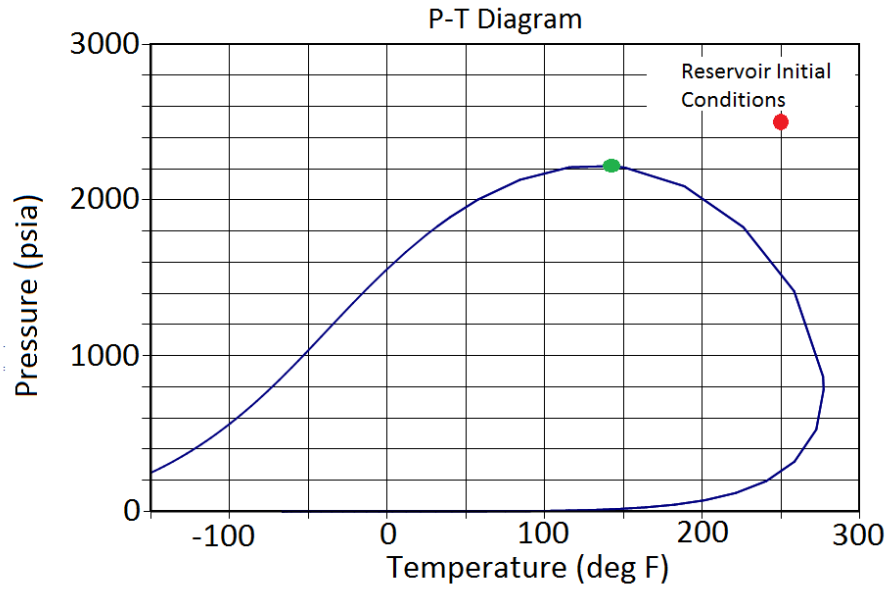

Figure 5.2: P-T phase envelope of the EOS: the green dot is the critical point and the red dot is the reservoir initial condition.

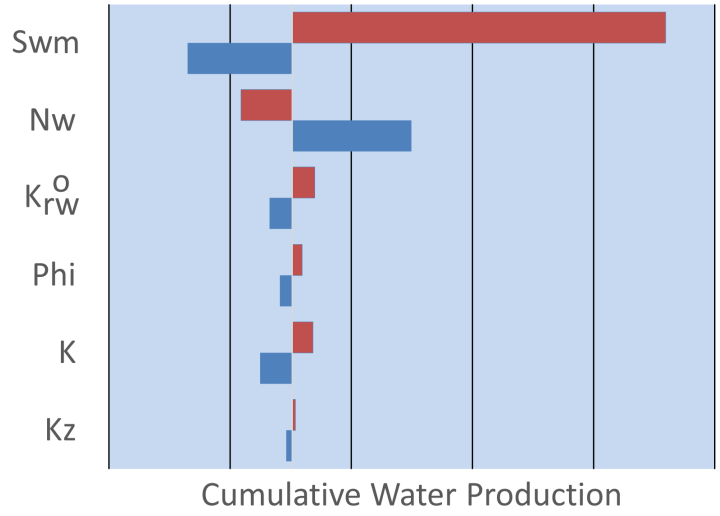

Figure 5.3: Sensitivity analysis: cumulative water production (STB).

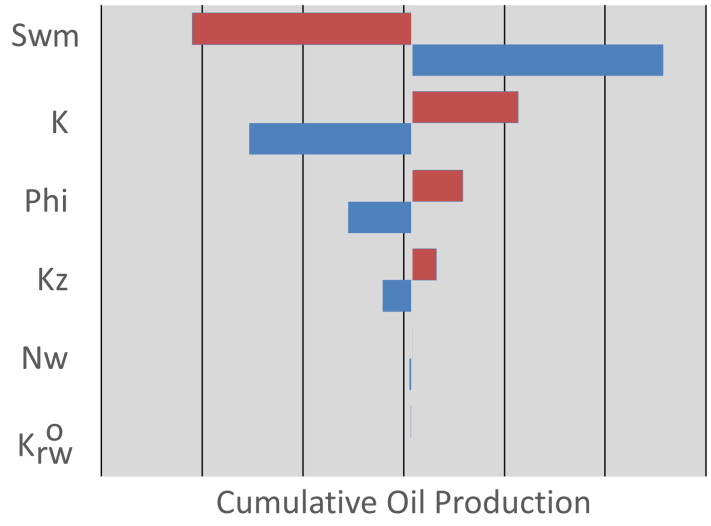

Figure 5.4: Sensitivity analysis: cumulative oil production (STB).

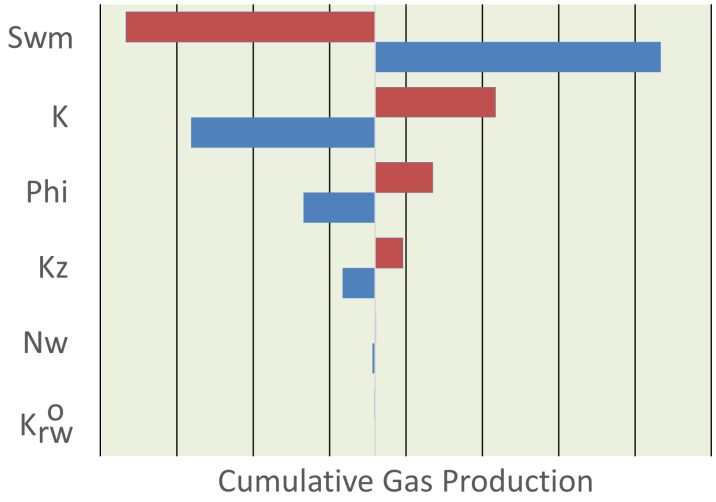

Figure 5.5: Sensitivity analysis: cumulative gas production (SCF).

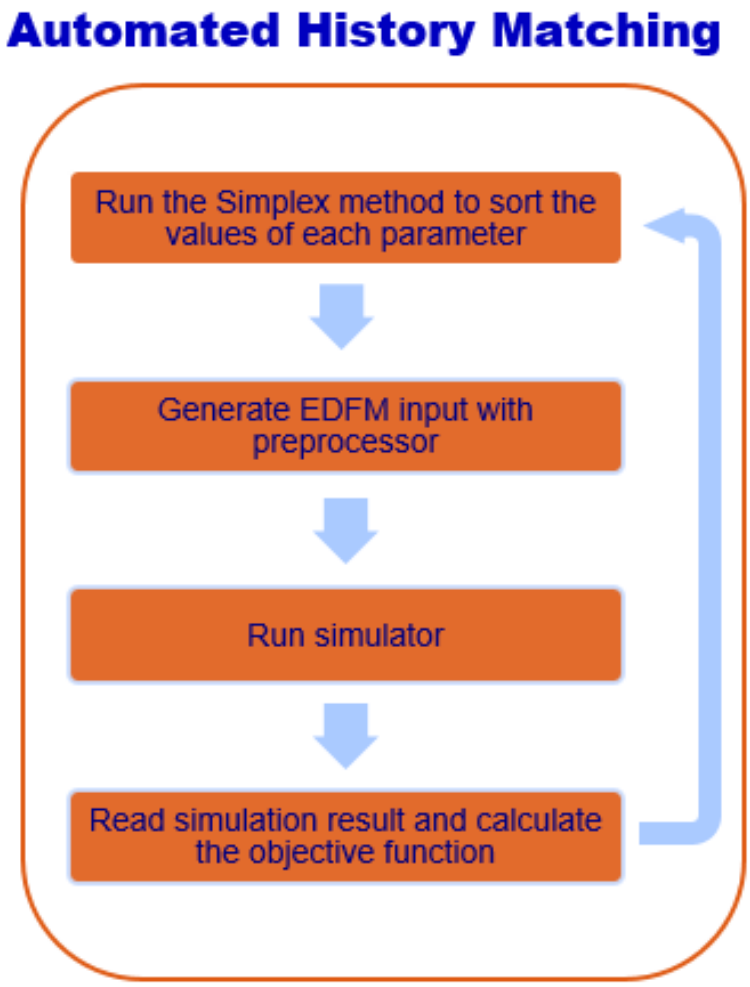

Figure 5.6: Workflow for the automated history matching of the pilot case.

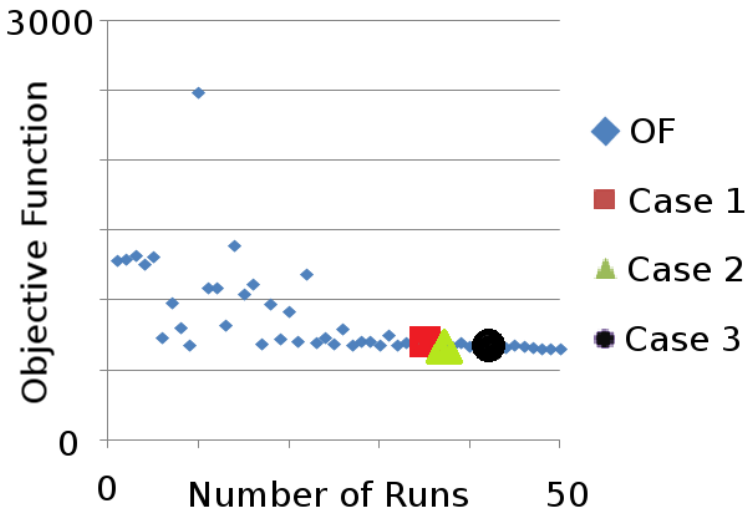

Figure 5.7: Evolution of the objective function in the automated history match.

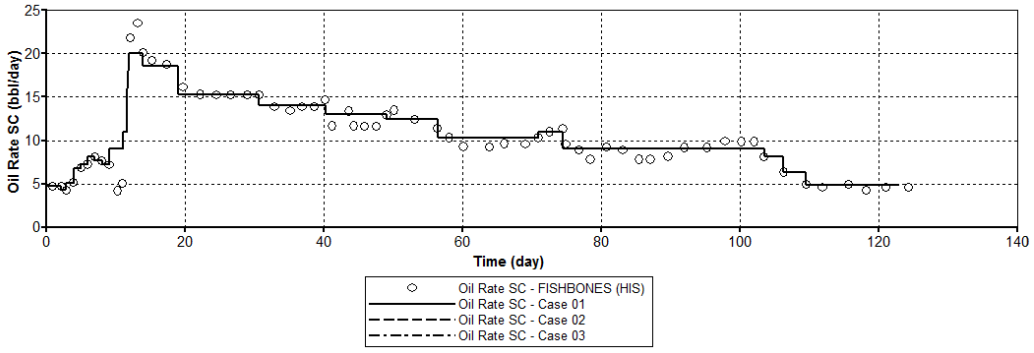

Figure 5.8: Oil production from history and simulation (Cases 1, 2, and 3); oil production was informed to the simulator.

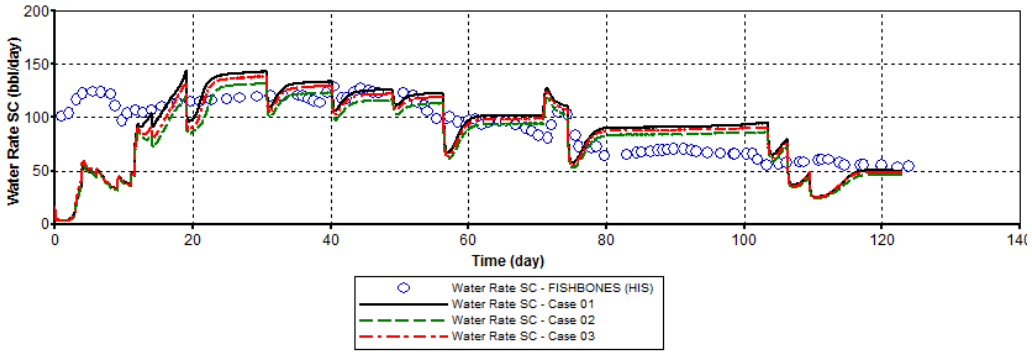

Figure 5.9: Water production from history and simulation (Cases 1, 2, and 3); the most sensitive parameter in the history matching.

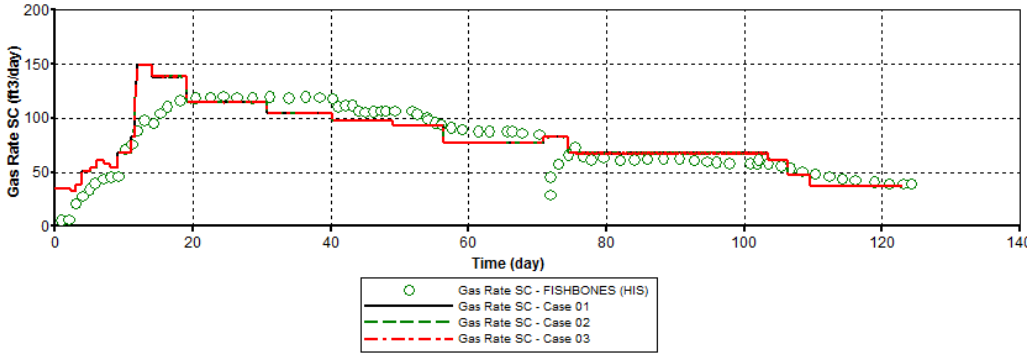

Figure 5.10: Gas production from history and simulation (Cases 1, 2, and 3).

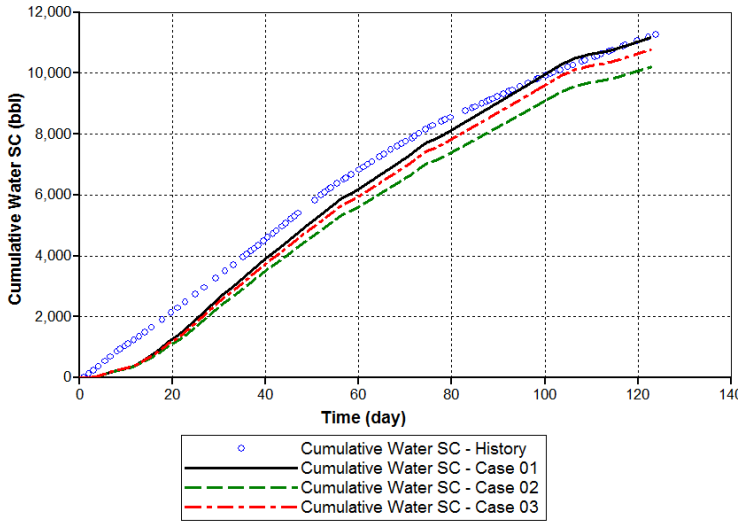

Figure 5.11: Cumulative water production from history and simulation (Cases 1, 2, and 3).

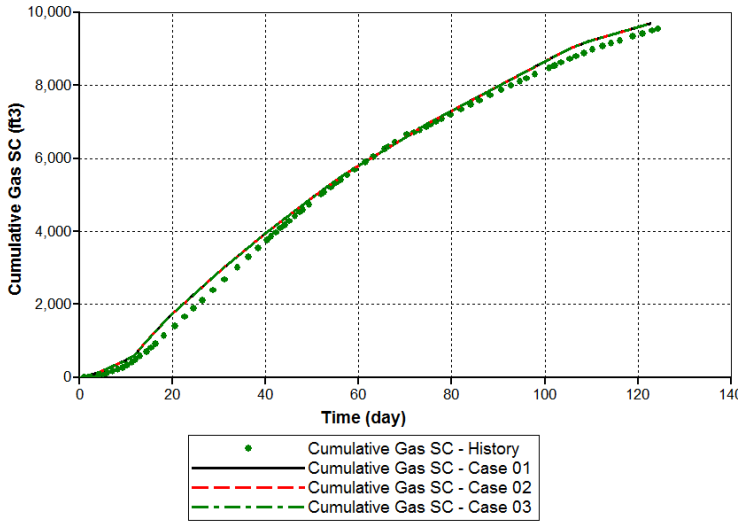

Figure 5.12: Cumulative gas production from history and simulation (Cases 1, 2, and 3).

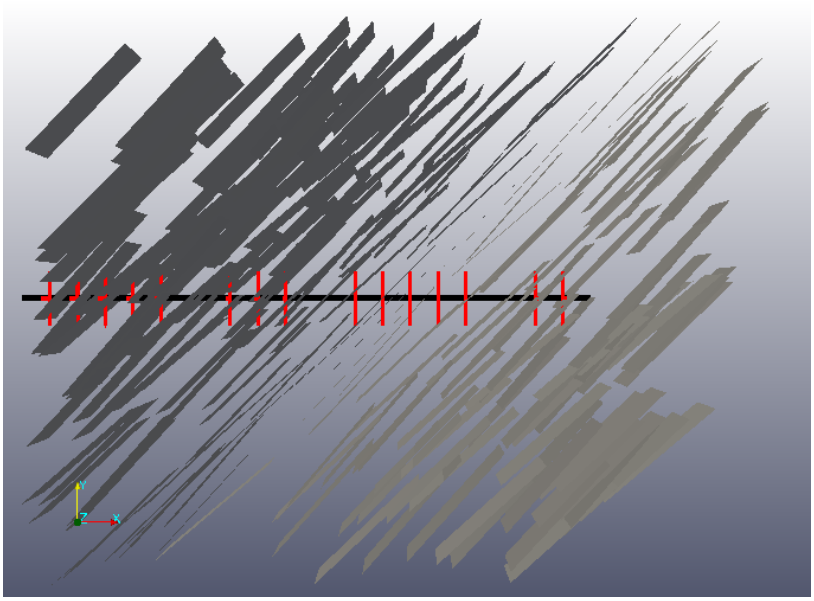

Figure 5.13: Distribution of the 200 fractures used to evaluate the fishbones' pilot using the triple porosity EDFM formulation.

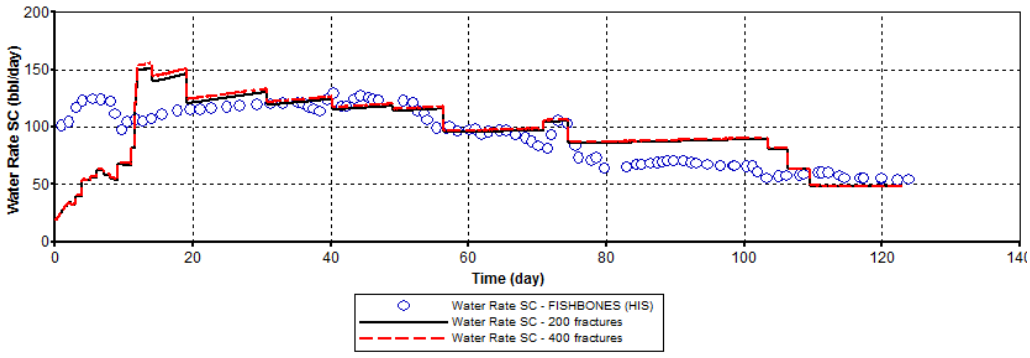

Figure 5.14: Water production from history and simulation (200 fractures case); the most sensitive parameter in the history matching.

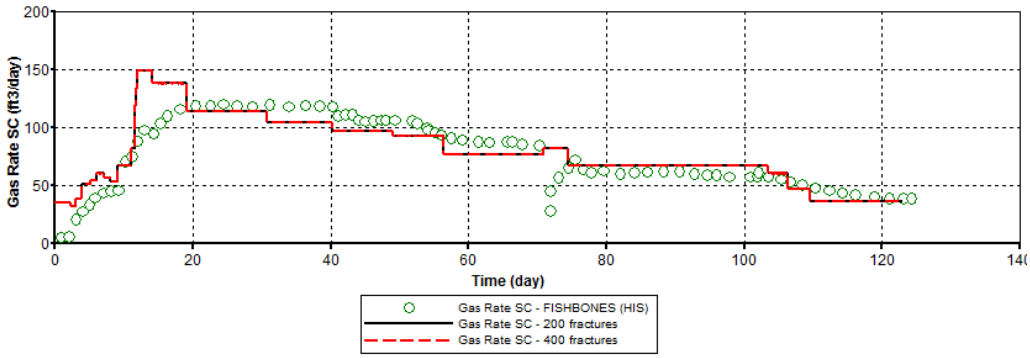

Figure 5.15: Gas production from history and simulation (200 fractures case).

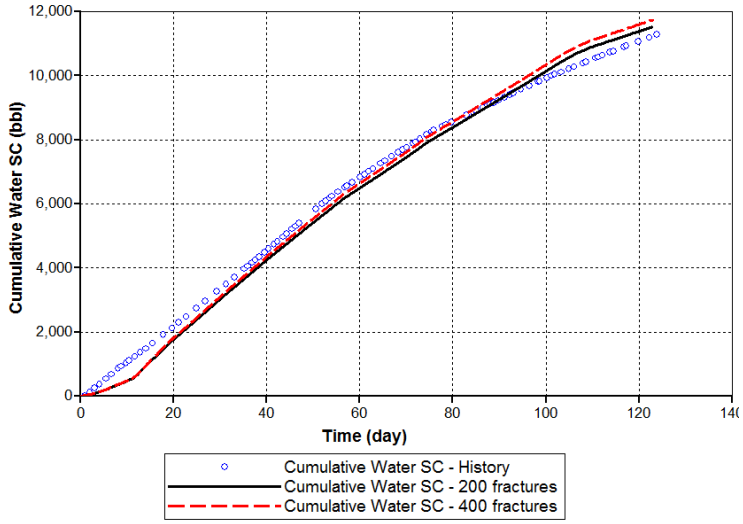

Figure 5.16: Cumulative water production from history and simulation (200 fractures case).

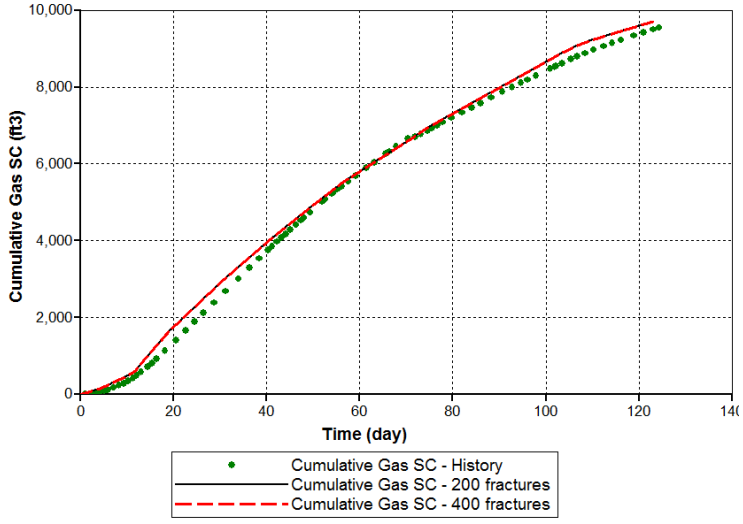

Figure 5.17: Cumulative gas production from history and simulation (200 fractures case).

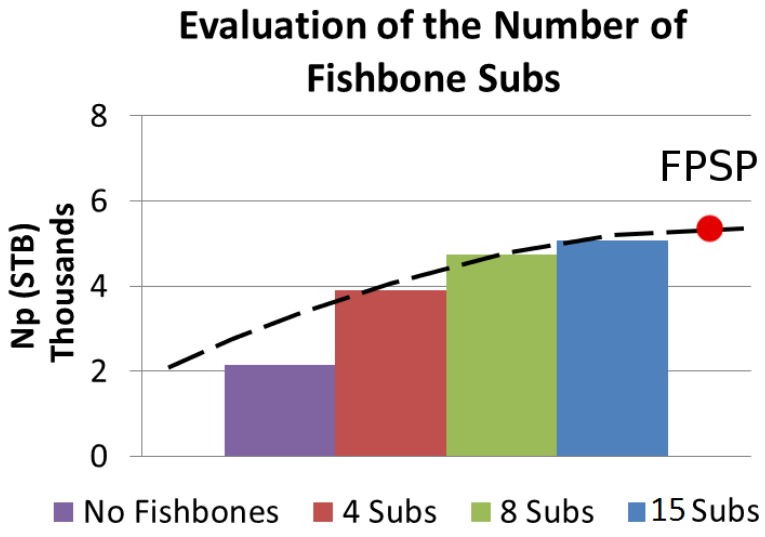

Figure 5.18: Evaluation of number of Fishbone Subs: cumulative oil production; the fishbones saturation point (FSP) is displayed in the extrapolated curve.

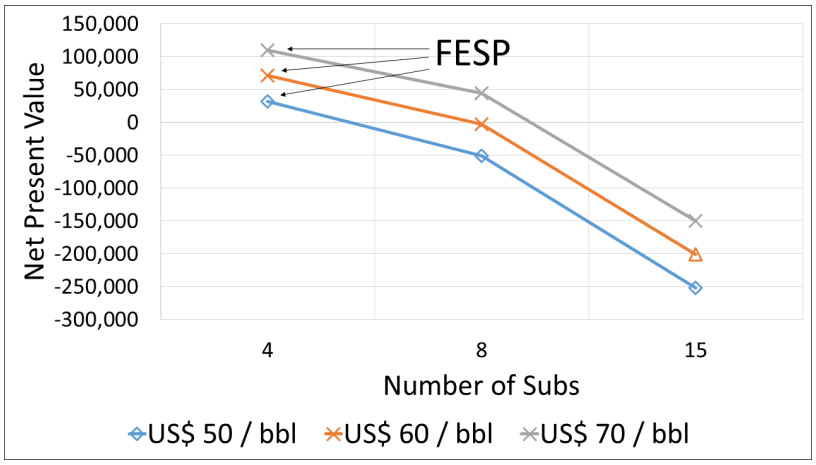

Figure 5.19: Evaluation of number of Fishbone Subs: net present value (NPV).

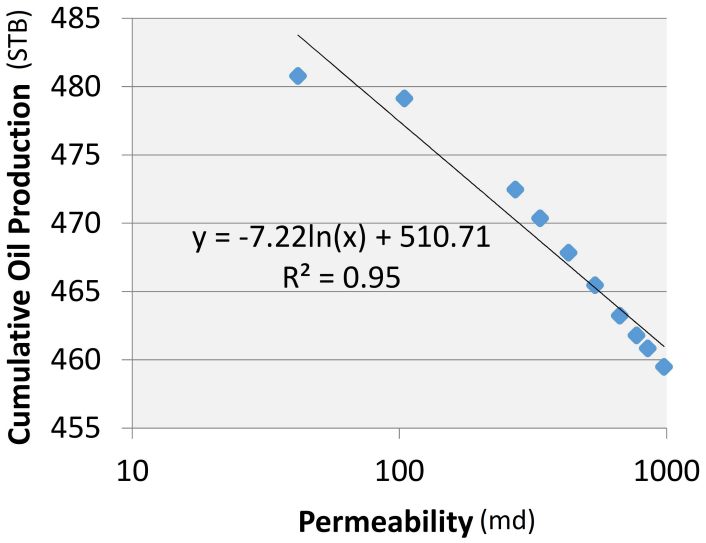

Figure 5.20: Correlation between the matrix permeability and the cumulative oil production for an isotropic reservoir.

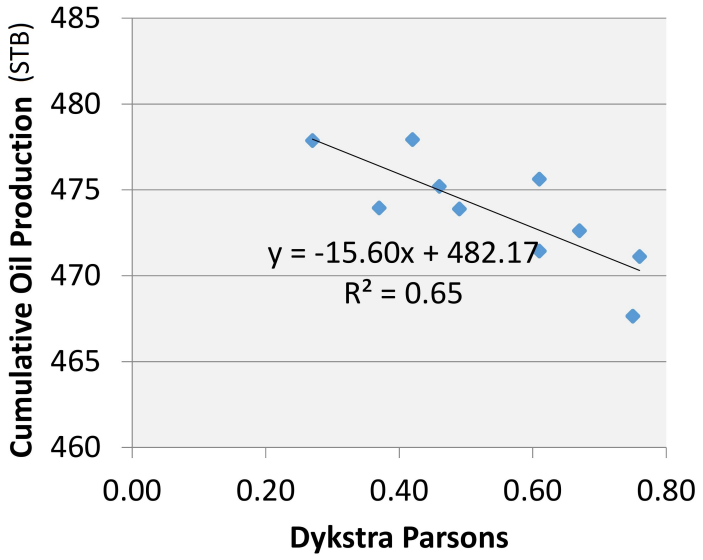

Figure 5.21: Correlation between the Dykstra-Parson's coefficient and the cumulative oil production for an anisotropic reservoir.

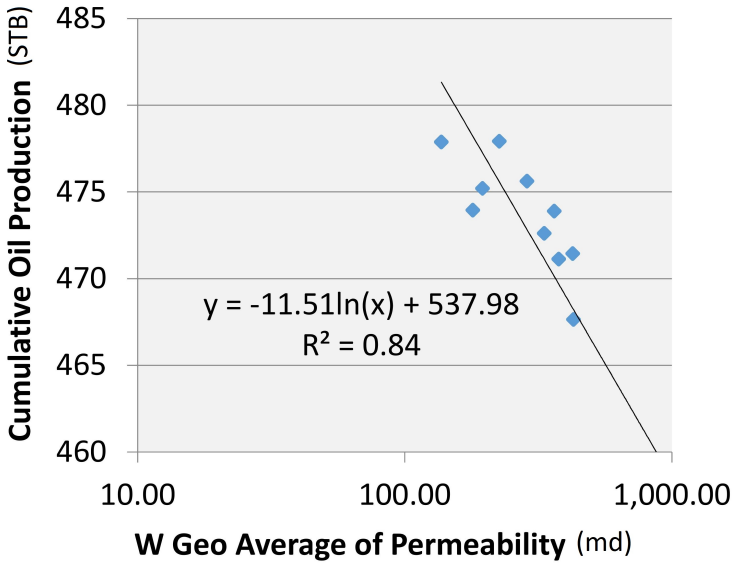

Figure 5.22: Correlation between the geometric average of the permeability weighted by the layer thickness and the cumulative oil production for an anisotropic reservoir.

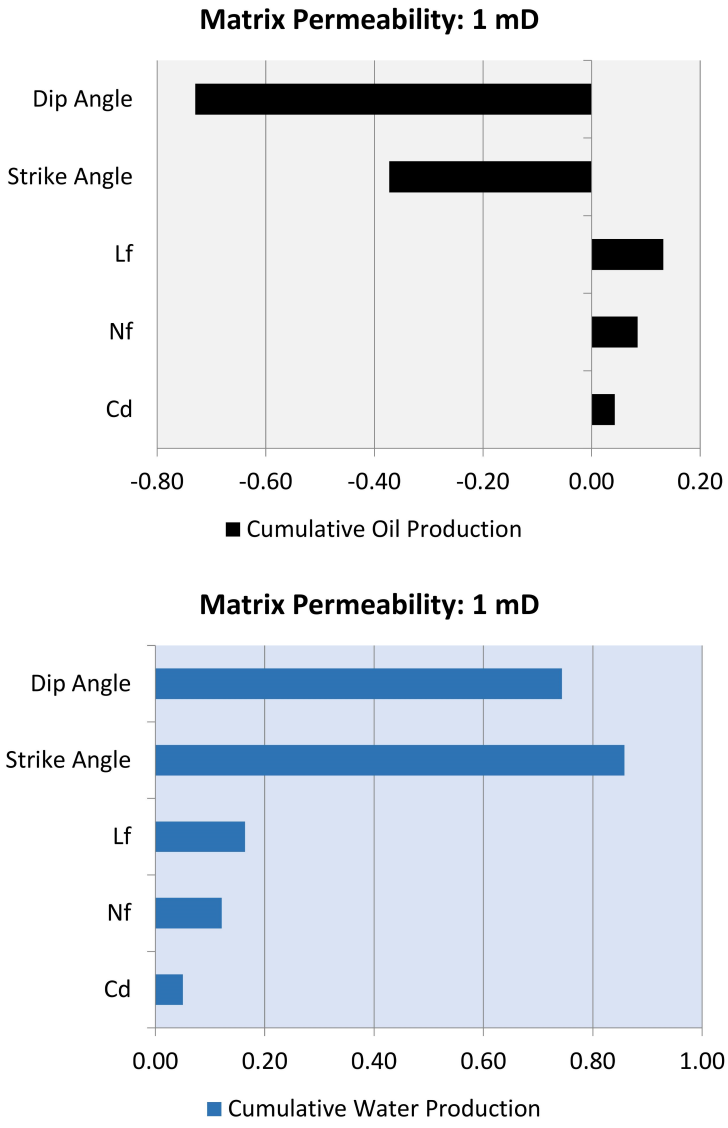

Figure 5.23: Tornado plot for cumulative oil and water production; dip and strike angle are the most influencing parameters.

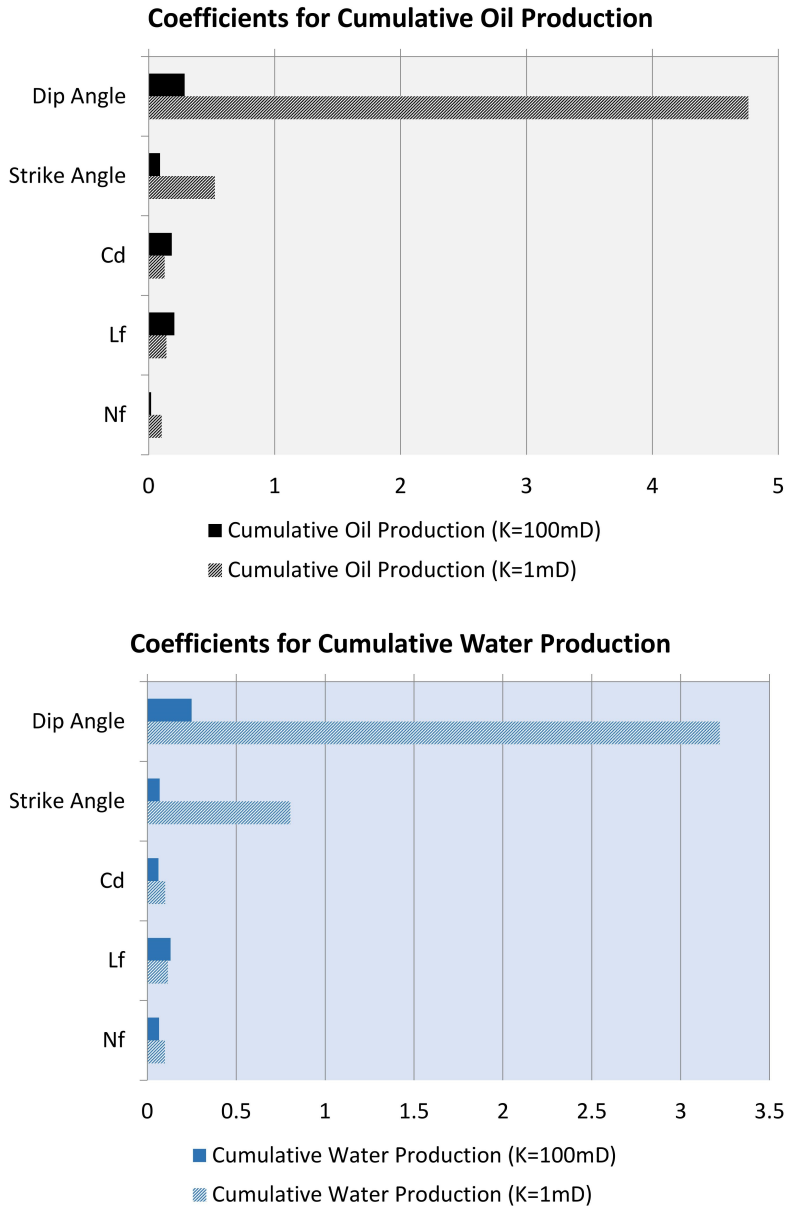

Figure 5.24: Coefficients linear response surface model for reservoirs with matrix permeability of 1 mD and 100 mD; note that the effects of the fractures are greater for a low permeability reservoir.

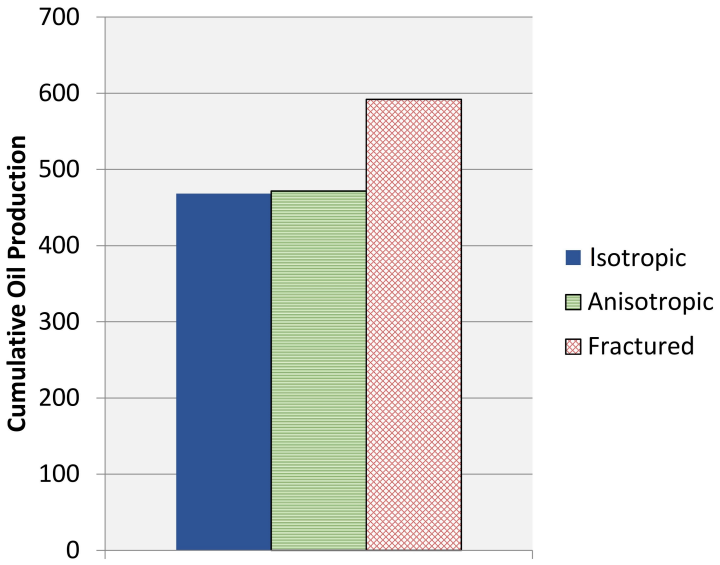

Figure 5.25: Application of fishbones in different scenarios; fractured reservoir resulted in greater cumulative oil production.

Chapter 6

Verification of the Foam Model[1]

6.1 Introduction

The high contrast of conductivity between matrix and fracture reduces the performance and the efficiency of improved oil recovery methods as the injected fluids prefers to flow through fractures. Mobility control methods are used to delay injected fluid breakthrough, increase sweep efficiency, and reduce gravity effects. Many works in the literature have attempted to evaluate the use of foam as a mobility reduction agent. Foam is a colloidal dispersion composed of a gas phase dispersed in a liquid phase and stabilized by a surfactant which is adsorbed at the gas/liquid interface (Kovscek and Radke, 1994). The foam is composed of the lamella (thin liquid phase film which separates the gas phase) and the plateau border (connection of three lamella at a 120 degree angle). Foam quality is defined as the ratio of gas volume to the total volume of gas and liquid. Given the difficulty of measuring foam quality in the porous media, injection foam quality is used as a reference.

Many studies in the literature have shown the advantages of using foam as a mobility control agent in gas injection projects (Farajzadeh *et al.*, 2010; Ashoori and Rossen, 2010, 2012; Haugen *et al.*, 2012), and compared its performance to other EOR methods (Srivastava *et al.*, 2009; Abbasi Asl *et al.*, 2010; Kharrat *et al.*, 2012).

[1]Cavalcante Filho, J. S. D. A., Delshad, M., & Sepehrnoori, K. (2016). Estimation of Foam Flow Parameters for Local-Equilibrium Methods using Steady-State Flow Experiments and Optimization Algorithms. In SPE Improved Oil Recovery Conference. Society of Petroleum Engineers. Cavalcante Filho is the writer and main author, Delshad is a collaborator and a reviewer, and Sepehrnoori is the supervisor.

The efficiency of the foam as a gas mobility control agent in naturally fracture reservoirs (NFR) is evaluated by the use of numerical models, which are capable to represent foam flow in matrix and fracture. Commercial simulators currently use local equilibrium models for foam flow (STARS, 2011; ECLIPSE, 2014). The population balance model provides a mechanistic representation of the foam flow process (Kovscek and Radke, 1994; Kovscek *et al.*, 1993, 1994, 1997; Apaydin and Kovscek, 2000). To simplify the numerical solution and make the population balance model suitable to real field models Chen *et al.* (2010) assumed local equilibrium between foam generation and coalescence rates. Rossen *et al.* (1994, 1999); Cheng *et al.* (2000); Delshad *et al.* (2002) described an empirical foam model that assumes local-equilibrium known as P_c* or UT model. Originally developed for the high quality regime the model also exhibits reasonable results for the low quality regime.

In this chapter we verify both the population balance model assuming local equilibrium (LE) and the P_c* model, both described in Section 3.3. We use experimental data from the literature to verify our population balance (LE) implementation and we also match the P_c^* model for comparison purposes. We propose and apply an automated method for fitting foam parameters of the population balance (LE) and P_c^* model, described in Section 3.3.3,and we compare results in terms of effective foam viscosity and fractional flow curves.

6.2 Results and Discussion

6.2.1 Verification of the Foam Models

In this section we present the history matching of experimental data from the literature (Chen *et al.*, 2010; Kovscek and Radke, 1994) performed to verify the population balance (LE) and the P_c* model. Our objective is to use experimental results to verify the population balance (LE) model and to compare our results to the P_c* model. We provide a brief description of the experiments performed by Chen

et al. (2010) and Kovscek and Radke (1994). As the experiments performed by both authors are similar we explain the experiment using Chen *et al.*'s (2010) work as a reference.

A schematic of the experiment apparatus is shown in Figure 6.1 The apparatus allows the simultaneous injection of gas and foaming solution and the measurement of flow parameters such as phase saturation, pressure drop, and texture of effluent foam bubbles. The core used in the center of the apparatus has a diameter of 5.08 cm and length of 60 cm. A mass flow controller and a piston pump supplying nitrogen and foamer solution, respectively, allow to control the fluid injection. Foam quality at injection is zero since there is no foam pre-generator. Pressure is measured using seven differential pressure transducers. A dome-loaded back-pressure regulator is used to control the exit pressure. Although both steady-state and transient foam flow experiments are reported by the author, we use the transient experiment to validate our implementation. Before each experiment, the cores are pre-flushed with large volumes of brine to remove all the gas and surfactant; the brine is then replaced by a 1 wt% active surfactant which is injected to avoid surfactant loss to the rock during the experiments. During the transient experiment (after the preflush) gas and a surfactant-solution mixture are injected into the core. The foam front is tracked by pressure and saturation measurements, and also by a visualization system.

Table 6.1 shows the two-phase flow parameters used assumed for each experiment. Figure 6.2 and Figure 6.3 show the water saturation and pressure gradient versus fluid velocity profiles measured in each experiment and used for the history matching with our compositional simulator.

6.2.1.1 Population Balance (LE) Model

Figure 6.4 shows the history match of water saturation for both experiments. The match for Chen *et al.* (2010) (Figure 6.4a) shows that we were not able to capture the S_w^* observed in the experiment. That difference is explained by the lack

of capillary pressure effects (imbibition) since capillary pressure is assumed to be zero in the simulations. We define the coalescence rate as function of S_w^* and not P_c^*. The population balance model (LE) presents a better agreement for S_w^* in the data presented by Kovscek and Radke (1994) (Figure 6.4b). Note that in Kovscek and Radke's (1994) experiments the core has greater permeability, which reduces capillary effects and increases the influence of viscous effects. The match for the pressure drop profile is shown in Figure 6.5. We observe a good agreement between the published experimental data and the simulated data for both experiments. Table 6.2 shows the foam model parameters for both experiments.

6.2.1.2 $Pc*$ Model

Figure 6.6 shows the history match of water saturation for both experiments. The match for Chen *et al.* (2010) (Figure 6.6a) shows that we were not able to capture the Sw^* observed in the experiment. That difference is explained by the lack of capillary pressure effects (imbibition), since capillary pressure is assumed to be zero. Our population balance model (LE) presents a better agreement for the S_w^* in the data presented by Kovscek and Radke (1994) (Figure 6.6b). As mentioned above, in Kovscek and Radke's (1994) experiments the core had greater permeability, which reduces the effect of capillary effects and increases the influence of viscous effects. The match for the pressure gradient profile is shown in Figure 6.7. We observe a good agreement between the experimental data from the literature and the simulated data. Table 6.3 shows the foam model parameters for both experiments.

Comparing Tables 6.2 and 6.3, we note that both models were provided similar values for S_w^*. In history matching Chen *et al.*'s (2010) experiment the population balance (LE) model used a S_w^* of 0.38 while P_c^* model used 0.4; for Kovscek and Radke's (1994) experiments S_w^* used in the population balance model was 0.26 while for the P_c^* model we used 0.25. The population balance (LE) model has 8 foam model parameters that allow a great flexibility during history matching. An analytical

method is needed to help determine foam parameters from experimental data and compare different foam models.

6.2.2 Fitting Foam Parameters

Few works in the literature have attempted to develop a method to estimate foam model parameters from experimental data (Cheng *et al.*, 2000; Boeije and Rossen, 2013a,b; Ma *et al.*, 2013). In Section 3.3.3 we present an algorithm capable of estimating foam parameters for local equilibrium foam models such as the population balance (LE) and the P_c* based on steady-state experiments. To evaluate our algorithm, we estimated foam parameters for experiments presented by Alvarez *et al.* (2001). Alvarez *et al.* (2001) proposed an unified model to describe the foam behavior in acid-well stimulation and gas diversion improved oil recovery. The authors performed a series of experiments to validate their assumptions. The schematic of the experimental apparatus is shown in Figure 6.8. Gas and surfactant solution were injected and foam was generated by a foam generator. The foam was observed upstream and downstream of the core. Pressure drop along the core was measured by a pressure transducer. Figure 6.9 shows the pressure gradient versus fluid velocity of each experiment. For further details on the experiment apparatus and procedures refer to Alvarez *et al.* (2001).

Experiment UG5

Here we present the results for fitting of foam parameters for experiment UG5 from Alvarez *et al.* (2001). We performed fitting for the population balance (LE) and the P_c^* model. The population balance (LE) model needs a greater number of parameters to be fitted; hence, the need for a robust optimization algorithm. During the fitting the Simplex method successfully reduced the objective function for both models. Figure 6.10 shows the behavior of the objective function during the optimization of the population balance (LE) model; the algorithm was

able optimize the parameter in 500 iterations. The convergence of the optimization process strongly depends on the initial guess. The time spent for optimization is of the order of minutes. Table 6.4 shows the initial guess and final results for the optimized parameters of the population balance (LE) model.

We show the evolution of the objective function for the optimization of the parameters of the P_c^* model in Figure 6.11. Since the P_c^* only has 3 parameters to be fitted, the convergence is faster than for the case of the population balance (LE) model. Table 6.5 shows the initial guess and the final results for the foam model parameters. Although both foam models presented a good match with the experimental data the values assigned for the S_w^* are different. That difference is related to the different number of parameters needed for both models. Since the P_c^* model has only 3 parameters, S_w^* becomes important and an attempt to match the experiment restraining the range of variation of that variable will result in a poor match. An optimization using weighted objective functions may be done to constraint any of the optimized parameters to a given value range.

The plots of the pressure gradient as function of gas and liquid velocities for the population balance (LE) and the P_c^* models are presented in Figure 6.12. The gradients plotted are 6, 11, and 15 KPa/m. A good match is observed for both models and the experimental data. The effective viscosity of both foam models are presented in Figure 6.13. The population balance (LE) model provides different effective viscosity curves for each pressure gradient due to the foam density and relative permeability calculation; note that the trapped foam saturation depends on the pressure gradient. The effective viscosity curves caculated with the P_c^* model are superposed because this model does not account for variations in the pressure gradient. Figure 6.14 shows the water fractional flow for each pressure gradient. The population balance (LE) provides a different fractional flow curve for each pressure gradient, while for the P_c^* model all pressure gradients are superposed. Figure 6.15 presents the foam density for each pressure gradient. At $f_g^* = 0.73$ we observe that the

foam density varies from 1.0 to 1.4 $\times 10^{12} m^{-3}$. The foam density increases with the pressure gradient showing that the population balance (LE) is capable to represent the foam generation at greater pressure gradients. Figure 6.16 shows the relative permeability curves for the foam calculated with both models. Figure 6.16a shows the effect of the pressure gradient in the foam relative permeability when modeled with the population balance (LE) model; note that at low pressure gradients there is more trapped foam (lower relative permeability), while for greater pressure gradients the trapped foam is mobilized and the relative permeability increases. The foam relative permeability curves calculated with the P_c^* model are shown in Figure 6.16b, where we observe that the relative permeability curves for each pressure gradient are superposed.

Experiment UG14

Figure 6.17 shows the plots of the pressure gradient as a function of gas and liquid velocities for the population balance (LE) and the P_c^* models. The gradients plotted are 2, 4, 6, 9, and 11 KPa/m. A good match is observed for both models and the experimental data. Figure 6.18 shows a good match between the effective viscosities of the experimental data and both foam models. We observe differences in the effective viscosity for each pressure gradient due to different relative permeabilities (as explained in the previous subsection) and foam density values. Figure 6.19 presents the foam density for each pressure gradient. At $f_g^* = 0.6$ we observe that the foam density varies from 0.8 to 1.0 $\times 10^{12} m^{-3}$. Figure 6.20a shows the relative permeability curves where the effect of the trapped foam is observed in the population balance (LE) model. Figure 6.20b presents the superposition of relative permeability curves for different pressure gradients calculated with the P_c^* model.

In this experiment we observed variation in the effective viscosity at high-quality regime. Although the effective viscosity calculated with the P_c^* model

presented an overall good match with the experimental data, a better match is obtained if we use a variable R_f and S_w^*. We propose the use of a linear correlation of R_f and S_w^* with the pressure gradient, as shown in Figure 6.21. We performed a linear regression of R_f and S_w^* against the pressure gradient and applied the obtained linear equation to recalculate the effective foam viscosities. Results are presented in Figure 6.22, where we observe a better match of the proposed model with the experimental data in the high quality regime. Figure 6.23 shows a better match using the proposed approach for the fractional flow curve (especially for the 2 KPa/m curve).

6.3 Summary

- We implemented the population balance (LE) model in a compositional reservoir simulator assuming the foam coalescence rate as a function of S_w^*.
- The population balance (LE) implementation was verified against two experimental data from the literature.
- A good match was observed for the saturation and pressure profiles between simulated and experimental data.
- Assuming capillary pressure equals to zero resulted in a poor estimation of S_w^* in the first experiment.
- An automated method using optimization algorithms was proposed and used to fit foam model parameters to steady-state experiments. The method may be applied to any local-equilibrium foam model and allows the determination of foam model parameters, as well as quantitative and qualitative comparison of each foam model.
- The population balance (LE) model is capable of modeling the foam and its regimes in different pressure gradients by calculating the foam density (texture)

and assuming the fraction of flowing foam as a function of the pressure gradient. Different effective viscosities and fractional flow curves were observed for each pressure gradient.

- The P_c^* model was insensitive to the pressure gradient variations because it consists of an empirical alteration of the gas relative permeability triggered by the S_w^* and surfactant concentration. The pressure differential is not in the equations used to calculate the foam relative permeability, therefore it has no impact on foam mobility predictions. It is worth mentioning that even without considering the pressure differential to calculate the foam mobility the P_c^* model may be used to model foam behavior when the pressure gradient has small impact on the foam flow.

- The ϵ parameter of the P_c^* model directly influences the transition zone between the low and the high quality zone; low values of ϵ will result in a L-shaped iso-pressure gradient line.

- To overcome the absence of the pressure differential on foam behavior modeled with the P_c^* equations we propose an extension of the P_c^* model by assuming R_f and S_w^* as linear functions of the pressure gradient. The linear function relating R_f and S_w^* and the pressure differential may be obtained with the proposed method for foam parameters fitting.

Table 6.1: Foam experimental data.

Two-phase flow parameters	Chen *et al.* (2010)	Kovscek and Radke (1994)
k	0.3 μm^2	1.3 μm^2
ϕ	0.18	0.25
n_w	3	3
k^0_{rw}	0.7	0.7
n_g	3	3
k^0_{rg}	1	1
S_{wc}	0.38	0.25
μ_w	$1 \cdot 10^{-3}\ Pa \cdot s$	$1 \cdot 10^{-3}\ Pa \cdot s$
μ_g	$1.8 \cdot 10^{-5}\ Pa \cdot s$	$1.8 \cdot 10^{-5}\ Pa \cdot s$
u_w	0.125 m/d	0.046 m/d
u_g	1.125 m/d	0.430 m/d

Table 6.2: Parameters after history matching using the population balance (LE) model.

Model Parameters	Chen *et al.* (2010)	Kovscek and Radke (1994)
S^*_w	0.38	0.26
$n^*\ (ft^{-3})$	2.80×10^{10}	1.10×10^{10}
$k^o_{-1}\ (ft^{-1})$	3.05	304.00
$k^o_1\ \ (day^{1/3} ft^{-13/3})$	9.58×10^{12}	3.80×10^{11}
$\alpha\ (cp\ day^{-1/3} ft^{10/3})$	4.00×10^{-14}	1.00×10^{-14}
ψ	1.40	1.40
f_c	0.25	0.25
η	0.18	0.33

Table 6.3: Parameters after history matching using the P^*_c model.

Model Parameters	Chen *et al.* (2010)	Kovscek and Radke (1994)
R_f	600	40,000
S^*_w	0.4	0.25
ϵ	1.00×10^{-3}	1.00×10^{-2}

Table 6.4: Parameters before and after optimization for the population balance (LE) model.

Model Parameters	Initial Guess	Optimization Results
S_w^*	0.47	0.35
n^* (ft^{-3})	1400×10^9	1000×10^9
k_{-1}^o (ft^{-1})	0.0051	0.0056
k_1^o $(day^{1/3} ft^{-13/3})$	55×10^{11}	22×10^{12}
α $(cp\ day^{-1/3} ft^{10/3})$	1.6×10^{-15}	6×10^{-15}
ψ	1.40	1.41
f_c	0.25	0.24
η	0.35	0.40

Table 6.5: Parameters before and after optimization for the P_c^* (LE) model.

Model Parameters	Initial Guess	Optimization Results
R_f	10,000	4,800
S_w^*	0.3	0.47
ϵ	0.001	0.03

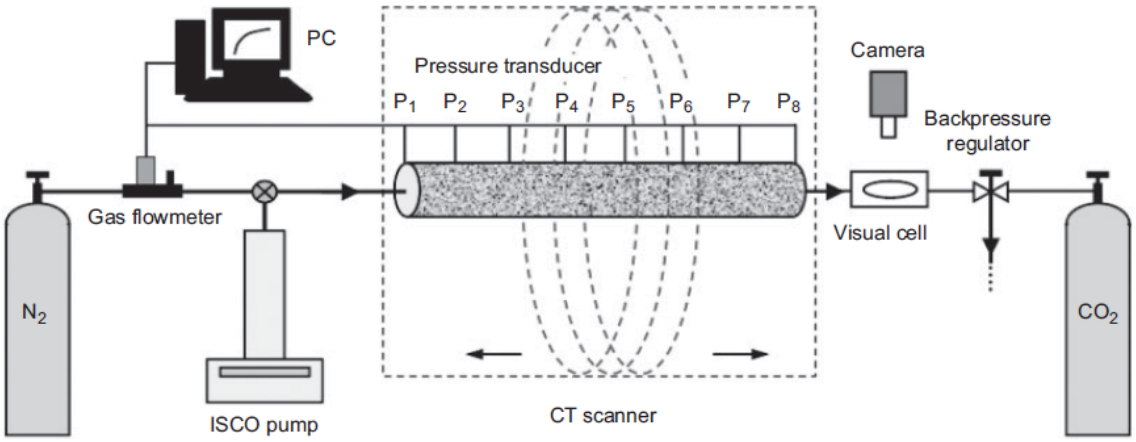

Figure 6.1: Schematic representation of the experiment performed by Chen et al. (2010).

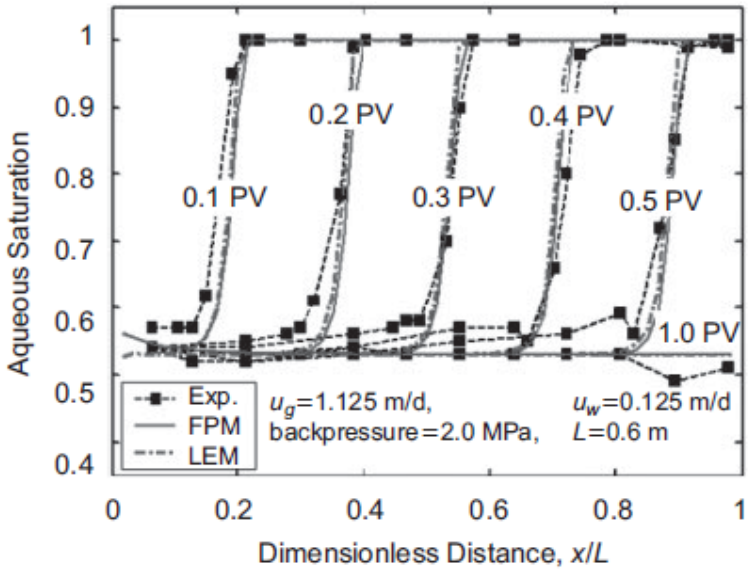

(a) Chen et al. (2010)

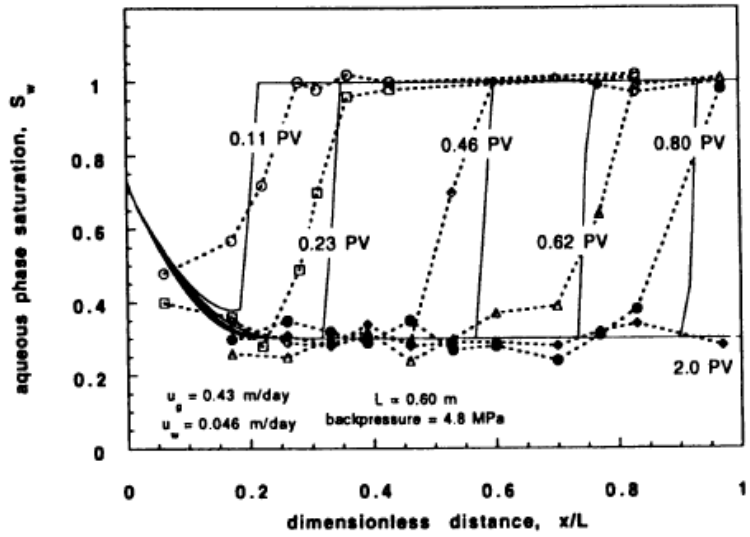

(b) Kovscek and Radke (1994)

Figure 6.2: (a) Water saturation profile from Chen et al. (2010) and (b) Kovscek and Radke (1994).

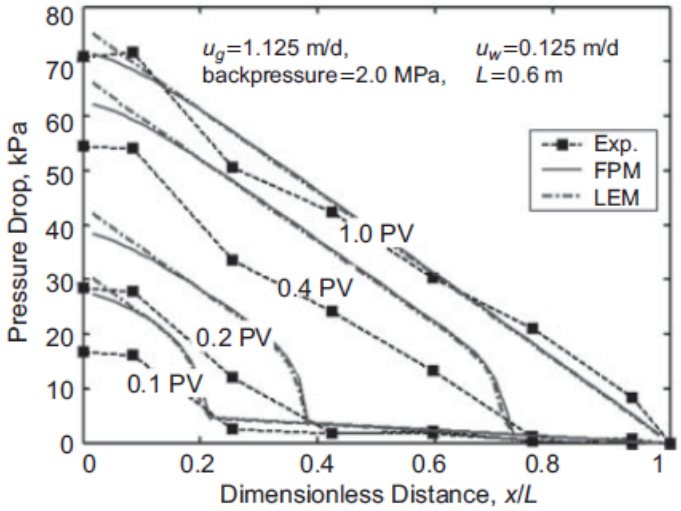

(a) Chen et al. (2010)

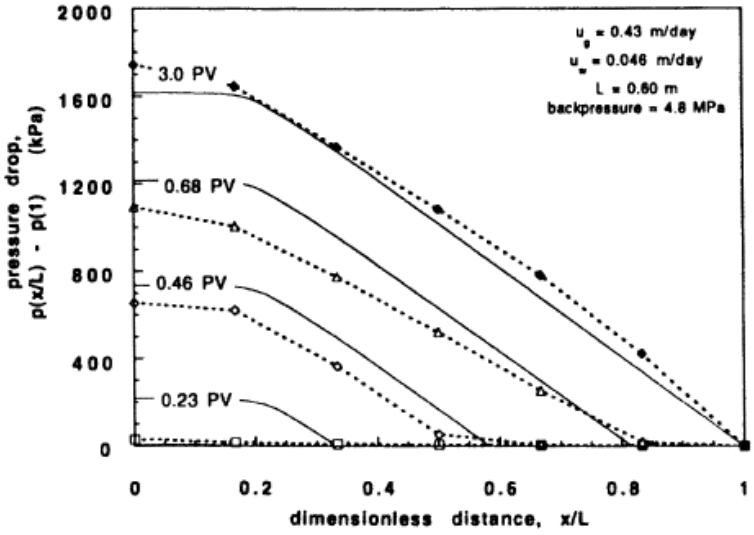

(b) Kovscek and Radke (1994)

Figure 6.3: (a) Pressure drop versus fluid velocity profile from Chen et al. (2010) and (b) Kovscek and Radke (1994).

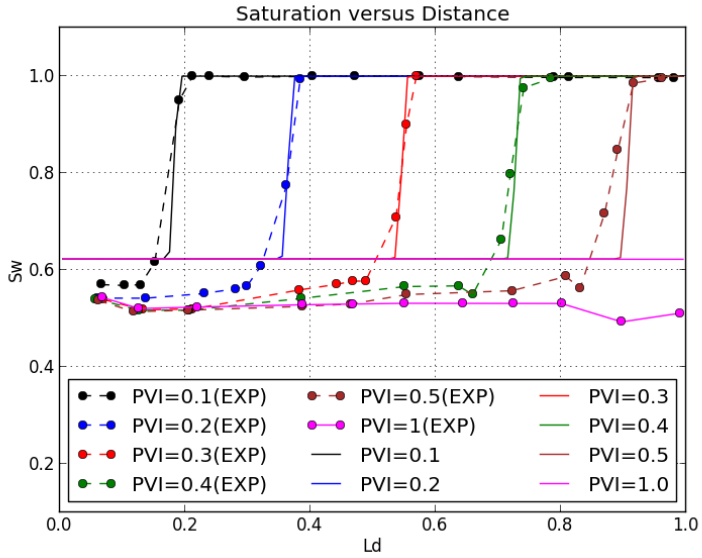

(a) Chen et al. (2010)

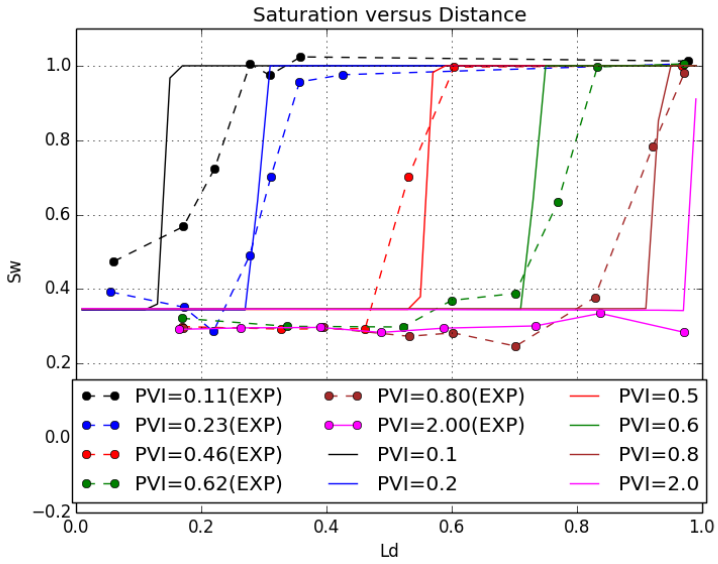

(b) Kovscek and Radke (1994)

Figure 6.4: Verification of the population balance (LE) model: (a) history match of water saturation from experimental data presented by Chen et al. (2010) and (b) Kovscek and Radke (1994).

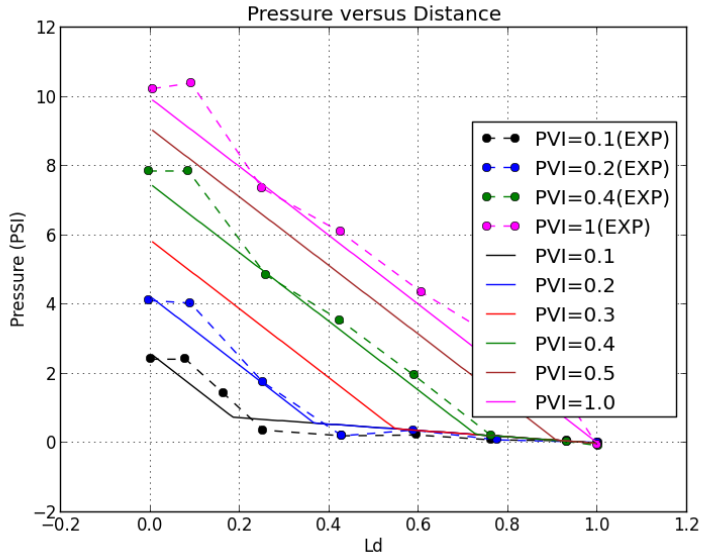

(a) Chen et al. (2010)

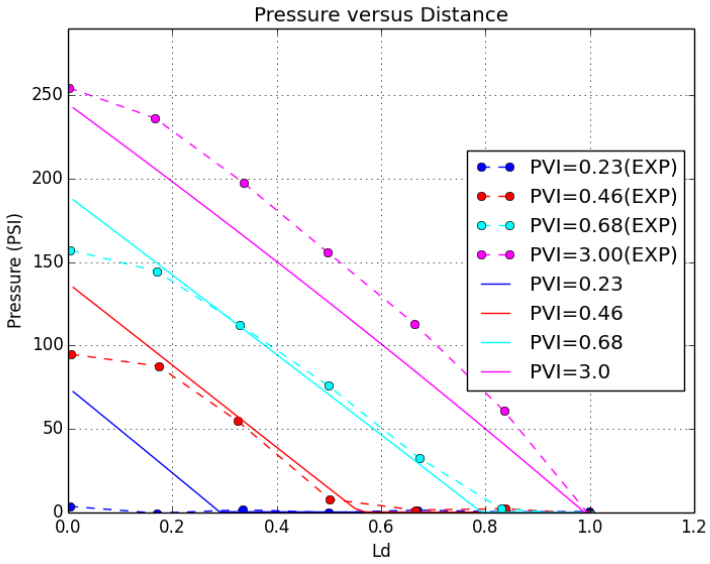

(b) Kovscek and Radke (1994)

Figure 6.5: Verification of the population balance (LE) model: (a) history match of pressure drop from experimental data presented by Chen et al. (2010) and (b) Kovscek and Radke (1994).

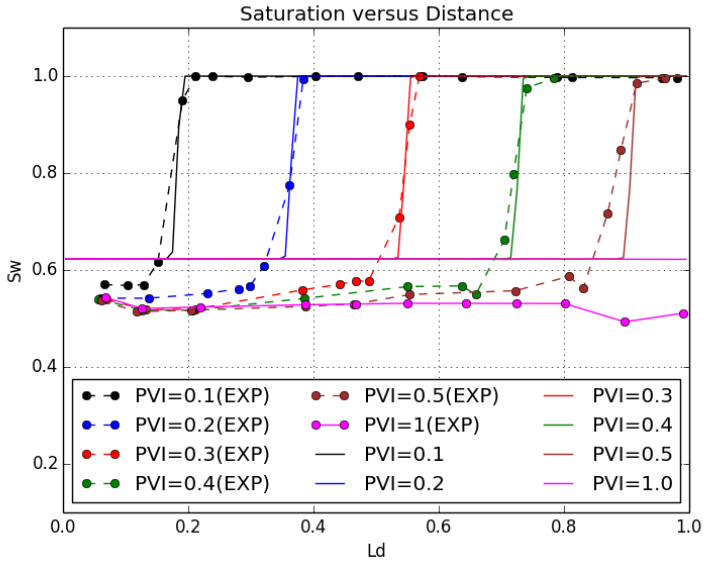

(a) Chen et al. (2010)

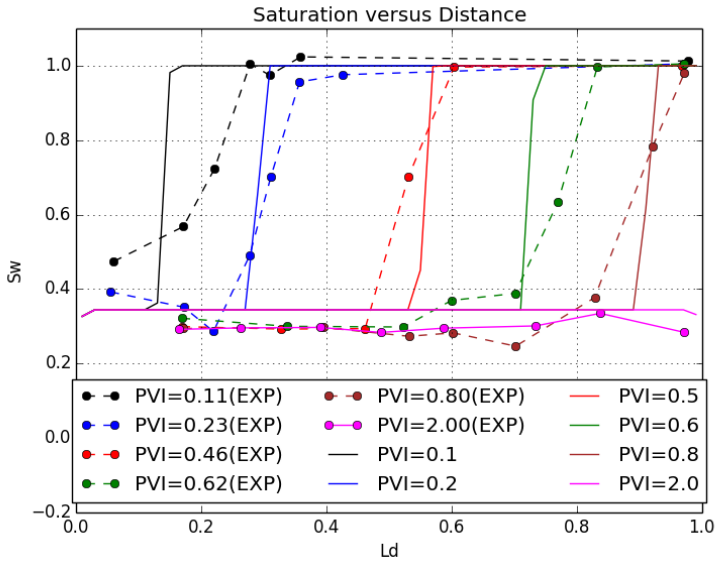

(b) Kovscek and Radke (1994)

Figure 6.6: Verification of the P_c* model: history match of water saturation from experimental data presented by Chen et al. (2010) (a) and Kovscek and Radke (1994) (b).

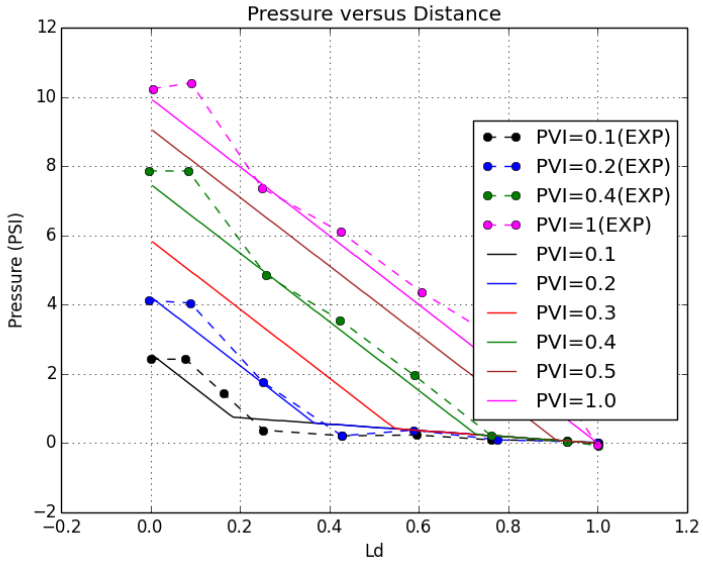

(a) Chen et al. (2010)

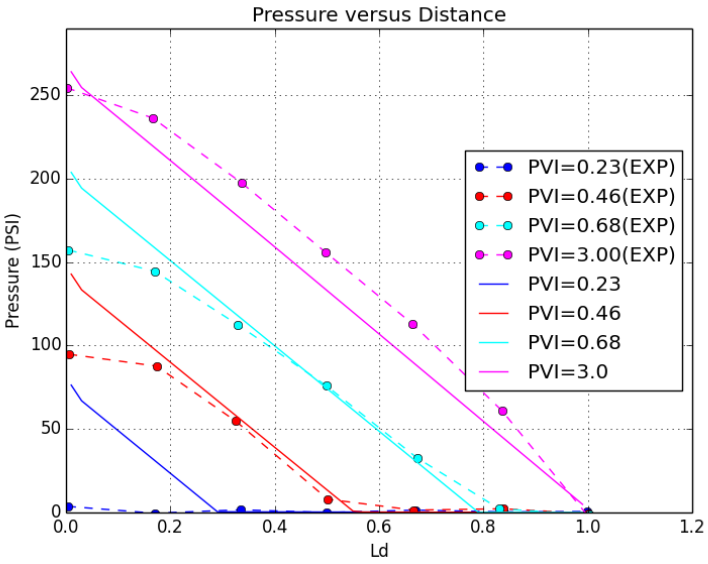

(b) Kovscek and Radke (1994)

Figure 6.7: Verification of the P_c* model: history match of pressure drop from experimental data presented by Chen et al. (2010) (a) and Kovscek and Radke (1994) (b).

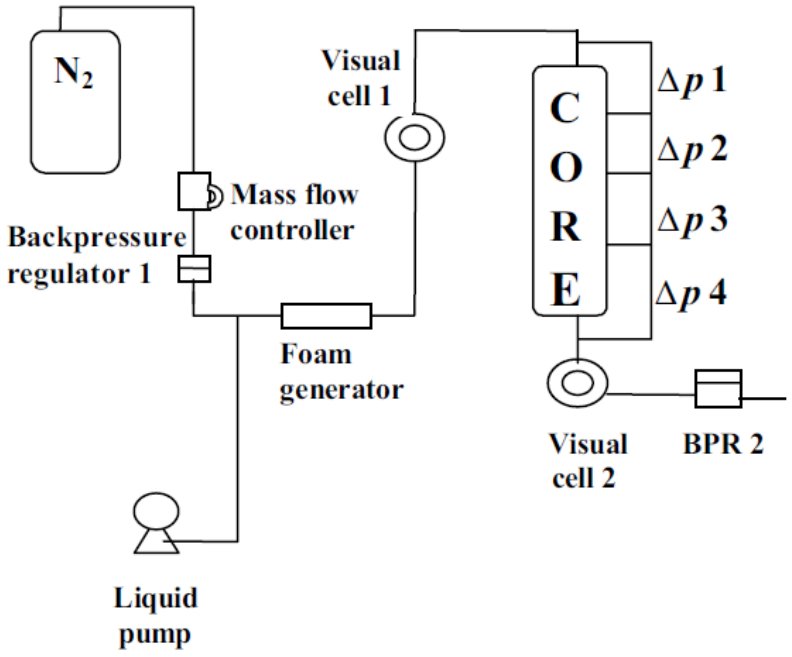

Figure 6.8: Schematic representation of the experiment performed by Alvarez et al. (2001).

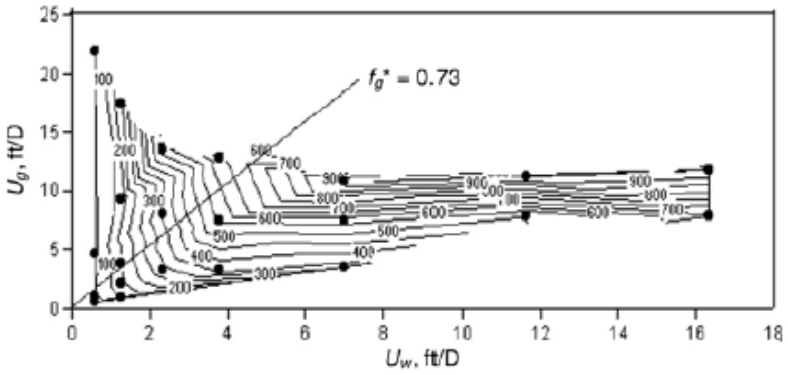

(a) Experiment UG5

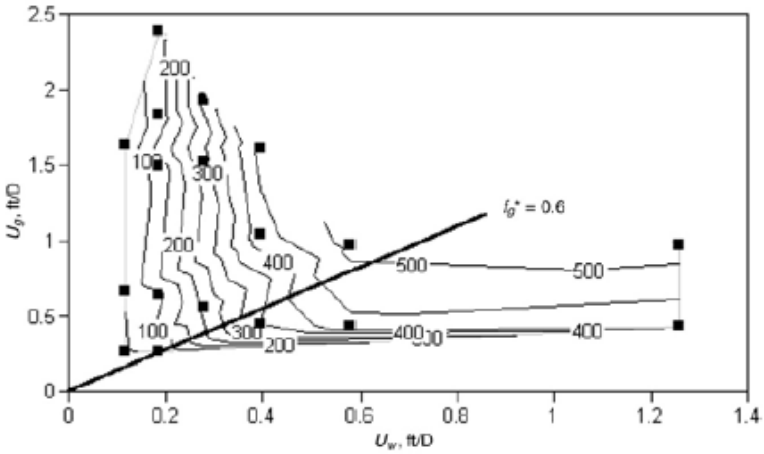

(b) Experiment UG14

Figure 6.9: Experimental data used to apply the methodology proposed to fit foam model parameters (Alvarez et al., 2001): pressure gradient in psi/ft.

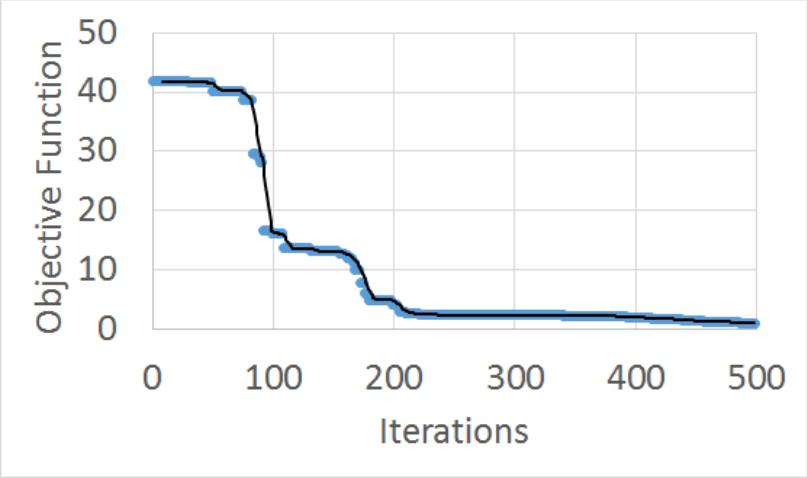

Figure 6.10: Behavior of the objective function during optimization of the foam parameters for the population balance model (LE).

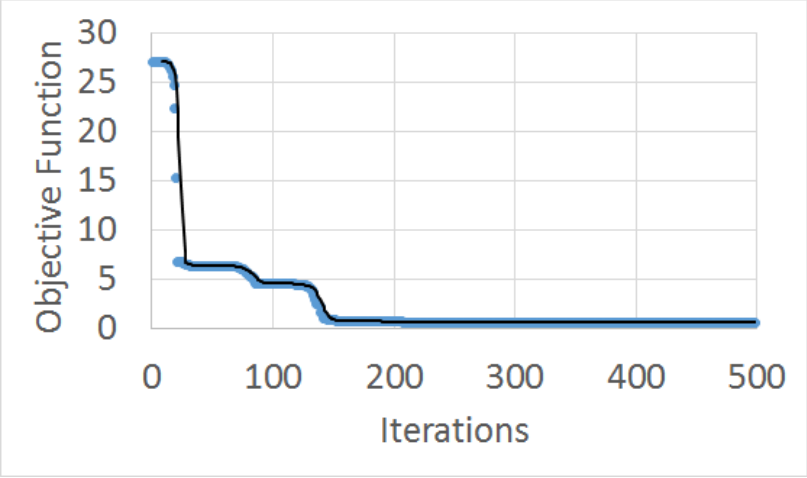

Figure 6.11: Behavior of the objective function during optimization of the foam parameters for the P_c^* model.

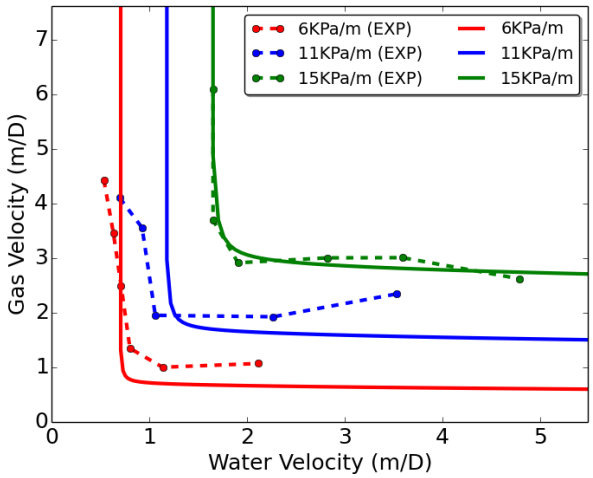

(a) LE

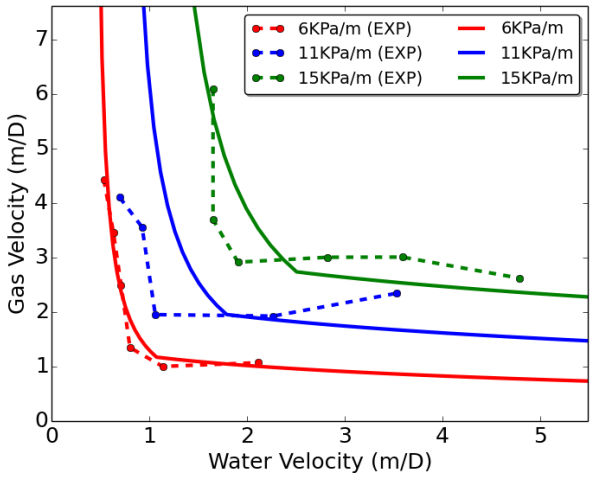

(b) Pc^*

Figure 6.12: Isogradient pressure lines for experiment UG5.

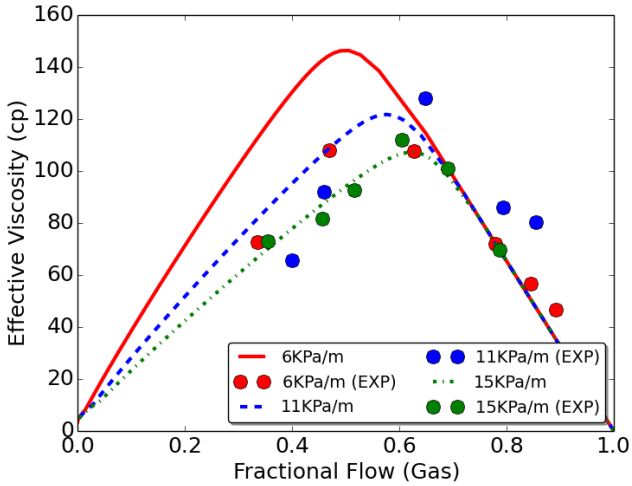

(a) LE

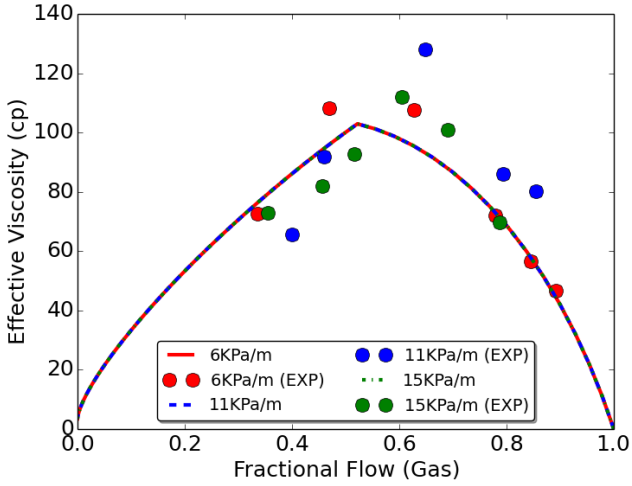

(b) Pc^*

Figure 6.13: Effective viscosities for experiment UG5.

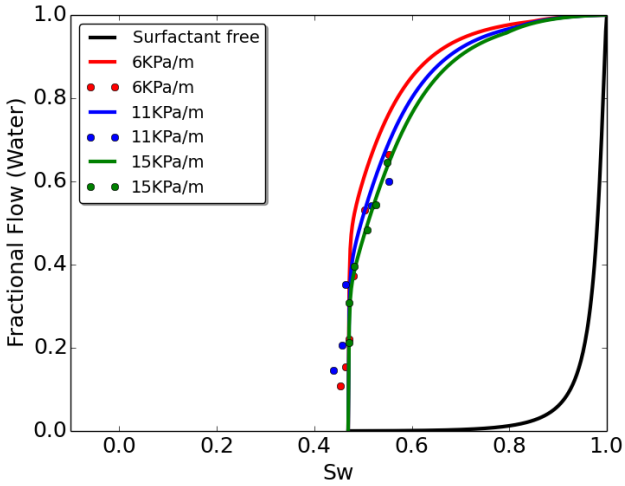

(a) LE

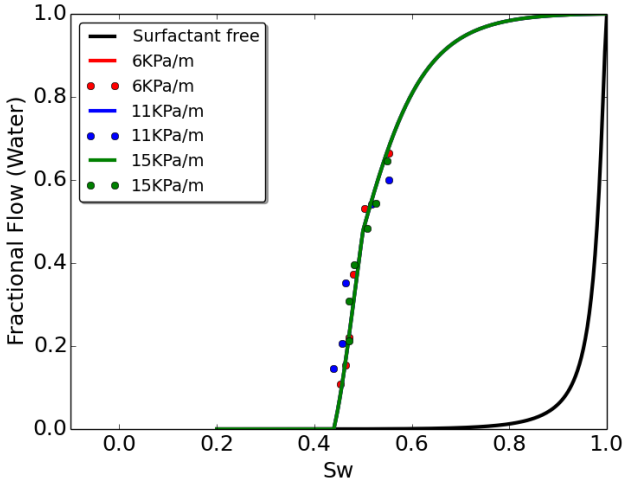

(b) Pc^*

Figure 6.14: Water fractional flow for experiment UG5.

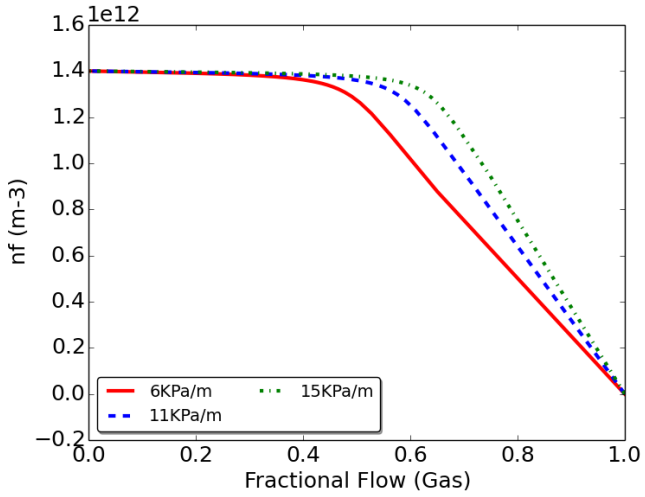

Figure 6.15: Foam density for experiment UG5.

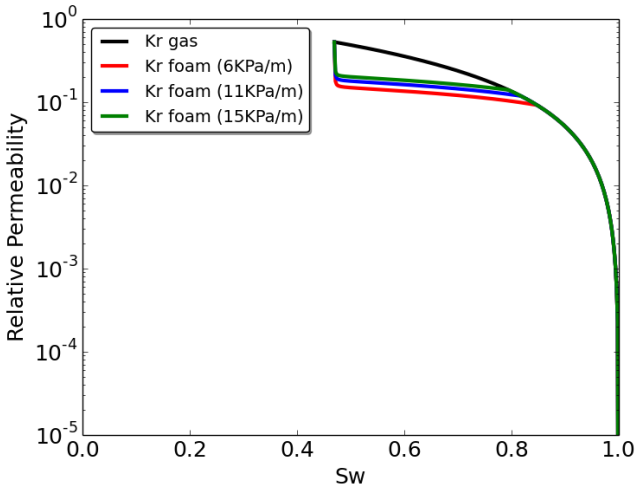

(a) LE

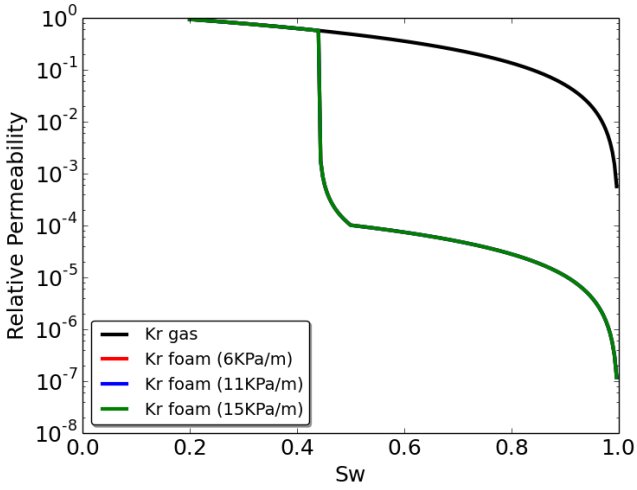

(b) Pc^*

Figure 6.16: Relative permeabilities for gas and foam for experiment UG5.

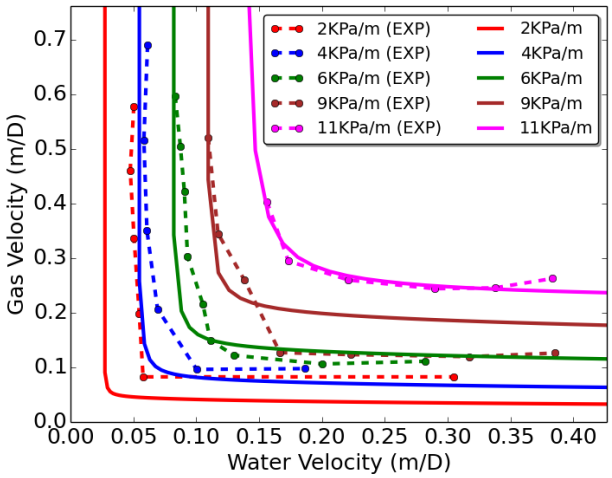

(a) LE

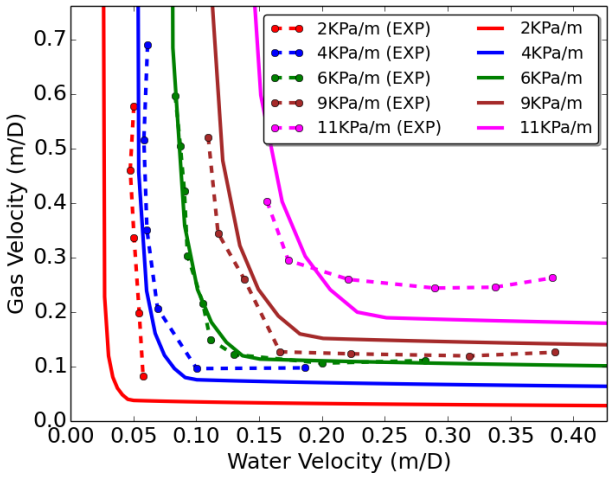

(b) Pc^*

Figure 6.17: Isogradient pressure lines for experiment UG14.

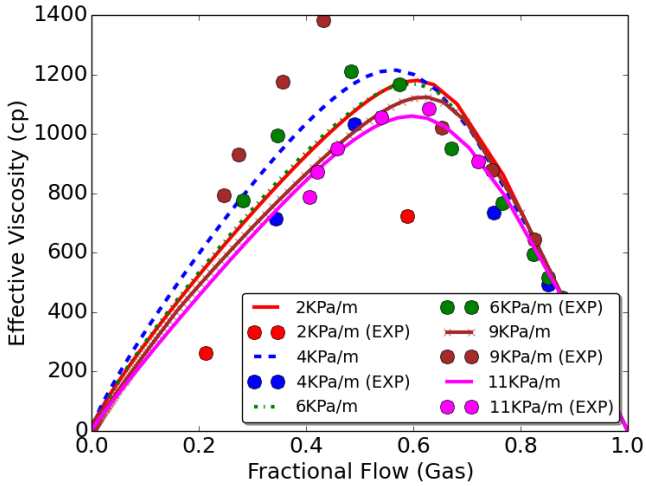

(a) LE

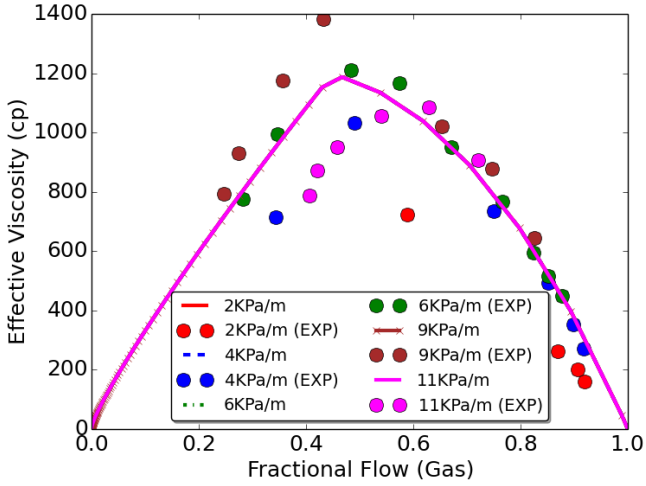

(b) Pc^*

Figure 6.18: Effective viscosities for experiment UG14.

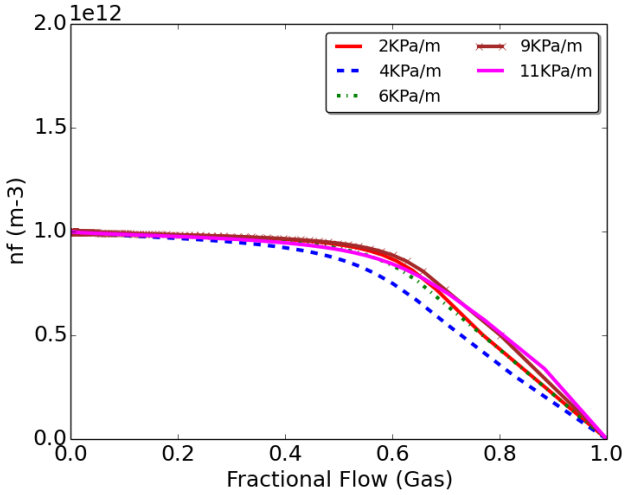

Figure 6.19: Foam density calculated with the population balance (LE) model for experiment UG14.

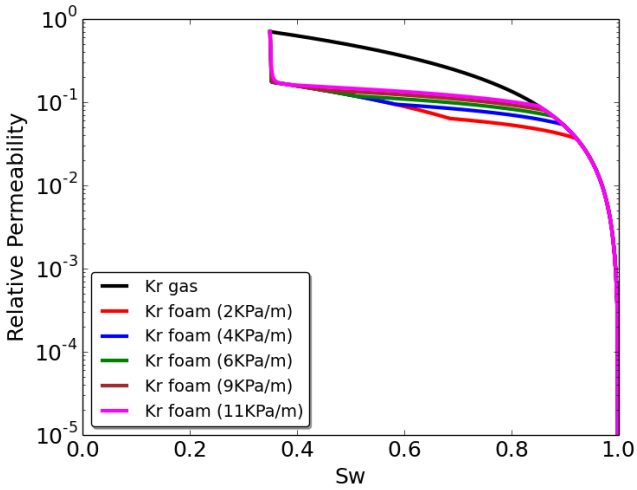

(a) LE

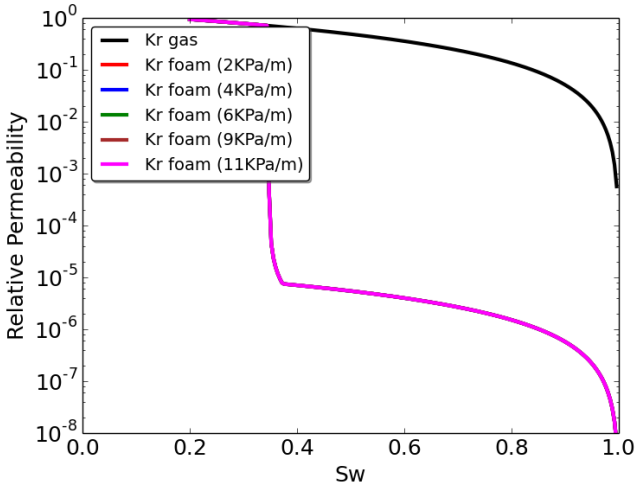

(b) Pc^*

Figure 6.20: Relative permeabilities for gas and foam for experiment UG14.

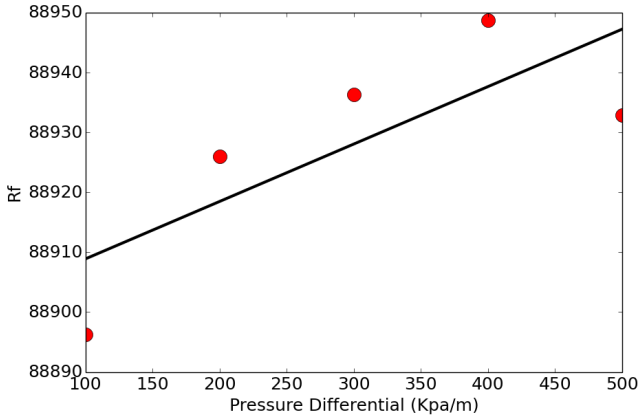

(a) Linear correlation of R_f

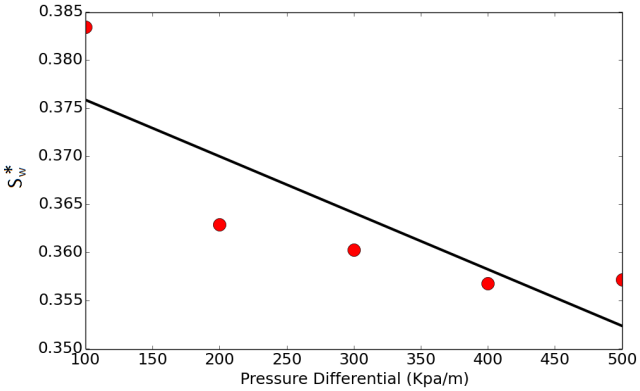

(b) Linear correlation of S_w^*

Figure 6.21: Linear correlation for R_f and S_w^*.

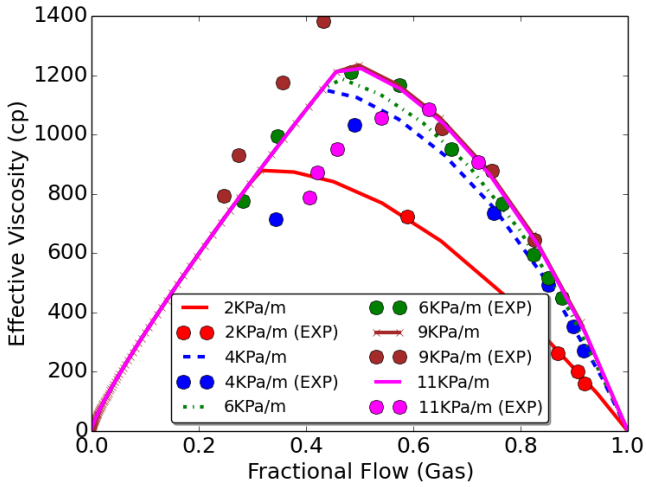

Figure 6.22: Match of the effective viscosity after using linear correlations for R_f and S_w^*.

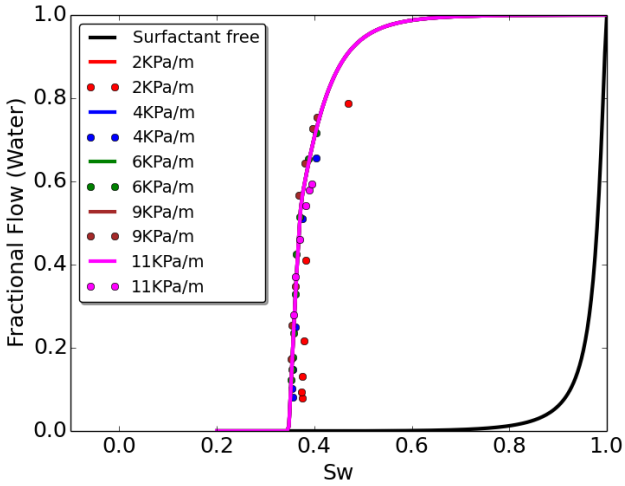

(a) Constant R_f and S_w^*

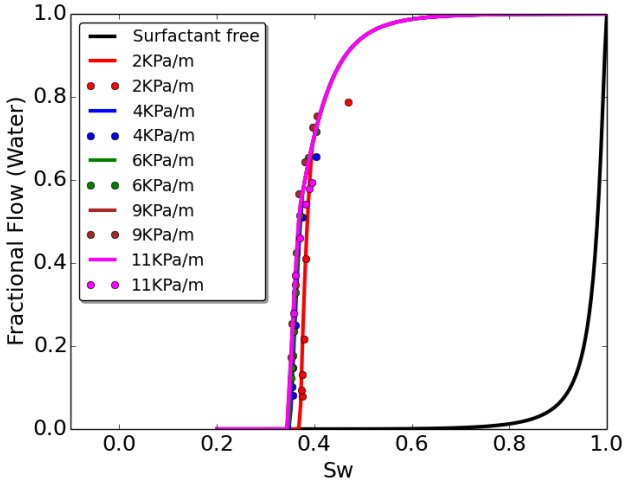

(b) Linear correlation of R_f and S_w^*

Figure 6.23: Match of the fractional flow after using linear correlations for R_f and S_w^*.

Chapter 7

Modeling and Application of Foam Injection in Fractured Reservoirs

7.1 Introduction

In this chapter we evaluate the use of foam as a mobility control agent in fractured and heterogeneous reservoirs. We study two types of reservoirs: a low permeability homogeneous reservoir with 10 fractures and a high permeability heterogeneous reservoir with 4 conductive faults and high permeability layers. In the low permeability homogeneous reservoir, we evaluate the population balance (LE) and the P_c^* models by running a continuous foam injection case and comparing results from both models; we also study water alternated gas injection (WAG) and foam assisted water alternated gas injection (FAWAG). The high permeability heterogeneous reservoir is derived from a real field located offshore in Brazil; we performed a case study to evaluate the application of continuous foam injection. The case study was conducted in two steps: the first step evaluates the continuous foam injection assuming that the foam does not interact with oil and the second step analyzes the foam model parameters and the effect of oil saturation on foam. We quantify the impact of oil saturation on the cumulative oil production obtained with the continuous foam injection.

7.2 Case 1 - Low Permeability Homogeneous Reservoir

We assumed a 2D, low permeability, reservoir with 10 fractures; the initial water saturation equals the connate water saturation, which leads us to a two-phase

flow problem (gas/foam and oil). The composition of the injected gas is 50% CO_2 and 50% methane and we obtain partial miscibility between oil and injected gas. Reservoir and fluid properties used in this study are described in Section 4.2.1.4 and Appendix A. A representation of the reservoir and its fractures is shown in Figure 4.17.

7.2.1 Continuous Foam Injection

We used foam model parameters obtained with the match of the transient experiment described in Chen *et al.* (2010) (Section 6.2.1) to evaluate a continuous foam injection project and compare solutions of the population balance (LE) and P_c^* models. Foam model parameters used to match Chen *et al.*'s (2010) experiment using the population balance (LE) and the P_c^T* model are found in Table 6.2 and Table 6.3, respectively.

Figure 7.1 compares the oil production rate of gas injection and the continuous foam injection modeled with the population balance (LE) and the P_c^* model. We keep the reservoir pressure above the saturation pressure of the fluid; the reason for oil production decline is the breakthrough of the injected gas. The gas injection presents an earlier breakthrough than the cases with foam. The foam injection modeled with the population balance (LE) model resulted in a stronger foam than the case modeled with the P_c^* model. This difference is related to the S_w^* used in both models; while the population balance (LE) models needed a S_w^* of 0.38 to match the experimental data, the P_c^* model needed a S_w^* of 0.40. In terms of foam creation and destruction that means that the foam will coalesce earlier in the P_c^* model, hence a weaker foam. Another reason for the difference of behavior is that Tang and Kovscek's (2006) equation, used in our population balance (LE) model, relates the percentage of flowing foam with the pressure gradient ($\propto |\nabla p|^{\eta}$), while in the P_c^* model the foam strength is a function of R only. Figure 7.2 shows the gas saturation map for the cases with no foam and with foam modeled with the population balance (LE) and

the P_c^* model. In the P_c^* model the foam coalescence happens earlier and the foam is not able to reduce gas mobility in the gas saturation front. Figure 7.3 presents the relative foam mobility ($K_{r,foam}/\mu_{foam}$) for the P_c^* and the population balance (LE) models. The population balance (LE) model results in lower foam relative mobilities than the P_c^*. The P_c^* results in low gas mobilities close to injection well rather than at the saturation front, while population balance (LE) shows low foam mobility behind and at the front, with foam coalescence happening in between.

7.2.2 Foam Assisted Water Alternated Gas

We evaluated the WAG and FAWAG injection. The WAG injection is well known as a mobility control IOR method that works by alternated injection of fluids with different densities and viscosities, such as water and gas. The injection of each fluid in cycles allows the saturation fronts of both fluids to move slower both by gravity and by viscous forces effects. In order to evaluate the WAG injection with and without foam, we neglect the gravity effects and focus on the viscous force effects by using a 2D dimensional model.

Table 4.2 shows the well operation constraints for producers and injectors. The injection cycles were spaced for 90 days, alternating from gas to water injection. Figure 7.4 shows the oil production for the WAG and FAWAG with the foam modeled with the population balance (LE) and P_c^* models. After the breakthrough of the injected fluid, different decline rates are observed in each curve, being the smaller decline rate being the case with no foam. We expect the foam to decrease gas mobility and increase oil production by smoothing the gas injection saturation front and increasing the sweep efficiency, but water injected in alternated cycles may breakthrough any moment. Figure 7.5 shows the gas production rate and we observe that the gas production was reduced for the two cases using foam, which we expected to happen since the foam reduces gas mobility. Around 1273 days a peak of oil production and a sudden reduction in production are observed in

the case using the P_c^* model because of an abrupt reduction in gas mobility. We also observe an increase in the reservoir pressure, as presented in Figure 7.6, due to an increasing saturation of trapped gas. But what happens to the water injected? Figure 7.7 shows the water production rate and we observe that the water breakthrough of the FAWAG case happened earlier than in the WAG case. This happens because once we reduce gas mobility using foam, the water becomes the fluid with greater mobility and, conducted by the fractures, reaches the producer sooner. An alternative to avoid the earlier water breakthrough is to use polymer to increase water viscosity and reduce water velocity into the porous medium, but care should be taken once the reservoir pressure tends to increase (specially around the wellbore) as the injected fluids move slower into the porous media.

7.3 Case 2 - High Permeabililty Heterogeneous Reservoir

The reservoir model used in this evaluation is derived from a real carbonate reservoir located offshore in Brazil. A section of the model, originally run in a commercial simulator, was subtracted to evaluate the use of foam as a mobility control agent during continuous foam injection. The reservoir contains 4 main faults and 2 layers of high permeability (layers 7 and 14). We evaluate the effect of those faults on the fluid flow. There are 4 wells, 1 injector (Well 1) and 3 producers (Well 2, Well 3, and Well 4). Figure 7.8 shows the porosity and the permeability of one layer of the reservoir to illustrate the heterogeneity, as well as the position of each well. Figure 7.9 presents the relative permeability curves of the reservoir.

We converted the simulation model to a simplified Cartesian grid and defined the fault planes to be embedded in the matrix using the EDFM preprocessor, as illustrated in Figure 7.10. We assumed a fracture permeability of 10 Darcy and aperture of 0.01 ft, which results in a fracture conductivity of $100md \cdot ft$.

7.3.1 Continuous Foam Injection

We used foam model parameters obtained with the match of the transient experiment described in Chen *et al.* (2010) (Section 6.2.1) to evaluate a continuous foam injection project. We assumed $S_w^* = 0.05$.

Results showed that the foam was effective to increase oil production and delay the gas breakthrough. Figure 7.11 shows the cumulative oil production for cases with no foam and with foam modeled with the P_c^* an the population balance (LE) models; the use of foam as a mobility control agent increased the cumulative oil production of about 11%. The cumulative gas production was reduced in both cases where foam was used, as presented in Figure 7.12. The 4 conductive faults were added and modeled using the EDFM but they did not affect the simulation results because of the low permeability contrast between the matrix and the fracture. The high permeability layers had a greater impact than the faults, as shown in Figures 7.13 and 7.14, which show the gas saturation map for the cases with no foam and with foam. Both layers 7 and 14 are responsible for the gas breakthrough when the gas injected in Well 1 reaches Well 2. The foam reduces the mobility of gas and reduces gas production through Well 2. The side effect of the reduction in gas production is the increase of average reservoir pressure, led by an increase in the pressure around the injection well (Figure 7.15).

7.3.1.1 Evaluating the Effect of the Presence of Oil

To evaluate the effect of the presence of oil in our reservoir model we used the population balance (LE) model with the effect of the oil saturation in the foam creation. We solved Equation 3.49 by applying the methodology described in Figure 3.24. The relative permeability data used in the evaluation are presented in Table 7.1 (derived from Figure 7.9). We used 2 different values for $S_{o,lim}$ (0.1 and 0.25), k_2^0 equals to 0.1, and maximum fraction of trapped foam ($X_{t,max}$) equals to 0.75. We

assumed a matrix permeability of 400 md, oil viscosity of 0.7 cp, and gas viscosity of 0.02 cp.

The methodology described in Figure 3.24 applies to experiments of gas displacing water. Since we want to model the effects of the oil saturation on foam creation/destruction, we assume an experiment where the core has the initial water saturation equal to the connate water saturation ($S_{wi} = S_{wc}$) and the initial oil saturation equal to the complement of the initial water saturation ($S_{oi} = 1 - S_{wi}$). Under this initial saturation profile, gas and foaming solution are injected at one end of the core and oil is produced across the other end until $S_o = 1 - S_{wi} - S_{or}$.

Figure 7.16 shows the relative permeability of the foam for the cases of $S_{o,lim} = 1.00$, $S_{o,lim} = 0.25$, and $S_{o,lim} = 0.10$. We observe that the foam is generated faster in the case of $S_{o,lim} = 1.00$, since foam is formed only when $S_o < S_{o,lim}$. Although the foam is generated earlier for the case where $S_{o,lim} = 1.00$, relative permeabilities are the same for $S_{o,lim} = 1.00$ and $S_{o,lim} = 0.25$ in the saturation regions where the foam is formed ($S_o < 0.25$). That can be explained by Figure 7.17, which presents the foam texture values for each case. Foam texture gradually converges to the same value in all cases as the water saturation approaches the limiting oil saturation ($S_{o,lim}$); hence we conclude that $S_{o,lim}$ has a small influence in foam texture. Foam texture is influenced by the constant k_2^0; Figure 7.18 shows the foam texture calculated for $k_2^0 = 0.1$, $k_2^0 = 10$ and $k_2^0 = 100$ and we observe that as k_2^0 increases the foam generation occurs at a lower rate, compared to small values of k_2^0. As observed in Equation 3.48, for different foam texture values we obtain different foam relative permeabilities (if the fraction of flowing foam is smaller than $1 - X_{t,max}$).

Figure 7.19 presents the effective foam viscosity for each case. As we include the effect of oil saturation the overall effective viscosity of foam is reduced and the gas fractional flow at which the foam effective viscosity is maximum is moved. The effect of oil presence in the water fractional flow curve is shown in Figure 7.20, where we observe a discontinuity at the point where foam is formed (at the foam front).

That discontinuity observerd for $S_{o,lim} = 0.25$ marks the existence of foam and the abrupt transition in gas mobility (Figure 7.20b).

We evaluated the effect of the presence of oil on the foam injection for the field case using a $k_2^0 = 0.1$. We defined $S_{o,lim} = 0.1$ and $S_{o,lim} = 0.25$; for the case of $S_{o,lim} = 0.1$ the cumulative oil production was reduced in 14%, while for the case of $S_{o,lim} = 0.25$ the cumulative oil production was reduced in 10%. The effect of the oil saturation on foam stability is important and must be considered when evaluating a foam injection project.

7.4 Summary

7.4.1 Case 1 - Low Permeability Homogeneous Reservoir

- The use of foam successfully reduces gas mobility increasing oil recovery and delaying the gas breakthrough.
- The population balance (LE) model resulted in a stronger foam in the fractures because it relates the pressure differential to the foam relative permeability.
- The P_c^* model resulted in a weaker foam in the saturation front; among other reasons we assumed a greater S_w^* than the one used in the population balance (LE) model.
- In FAWAG injection the foam was able to reduce gas mobility and delay the gas breakthrough, but the reduction in gas mobility resulted in an earlier water breakthrough.
- An appropriate characterization of the foam behavior must be performed prior to the evaluation of any foam injection project.

7.4.2 Case 2 - High Permeability Heterogeneous Reservoir

- The foam was able to reduce gas mobility and increase oil recovery.

- Conductive faults with conductivity of $100md \cdot ft$ did not impact the flow behavior into the reservoir due to low contrast with the matrix permeability.
- High permeability layers were responsible for the gas breakthrough and foam successfully diverted the gas increasing the vertical sweep efficiency.
- The evaluation of the foam model parameters considering the effects of oil saturation denoted the importance of the $S_{o,lim}$ and K_2^0 parameters, the latter the most influential.
- Including the oil saturation effect in the simulation reduced the cumulative oil production by more than 10%.

Table 7.1: Relative permeability data used to evaluate foam model parameters and the influence of oil saturation om foam behavior.

S_{wr}	0.05
S_{or}	0.05
k_{rwo}	0.3
k_{row}	0.6
k_{rgl}	0.22
n_o	3
n_g	3
n_w	3

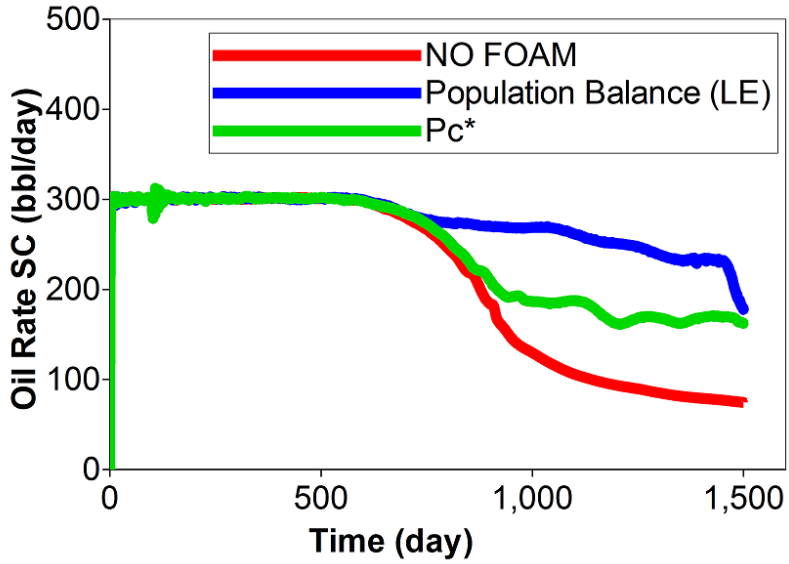

Figure 7.1: Oil production for the gas injection with no foam and with foam modeled with the population balance(LE) and P_c^* model; oil production decline occurs because of the gas breakthrough in all cases.

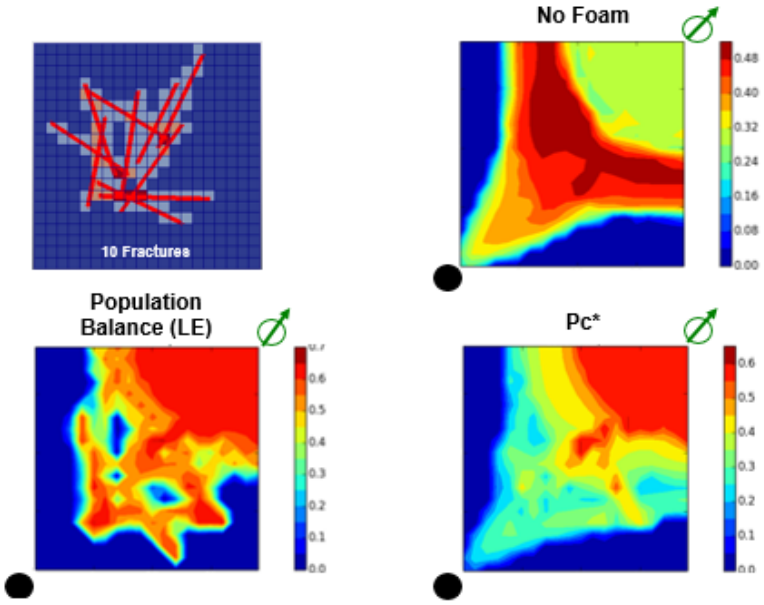

Figure 7.2: Gas saturation map for the gas injection with no foam and with foam modeled with the population balance (LE) and the P_c^* model; population balance (LE) results in stronger foam into the fractures.

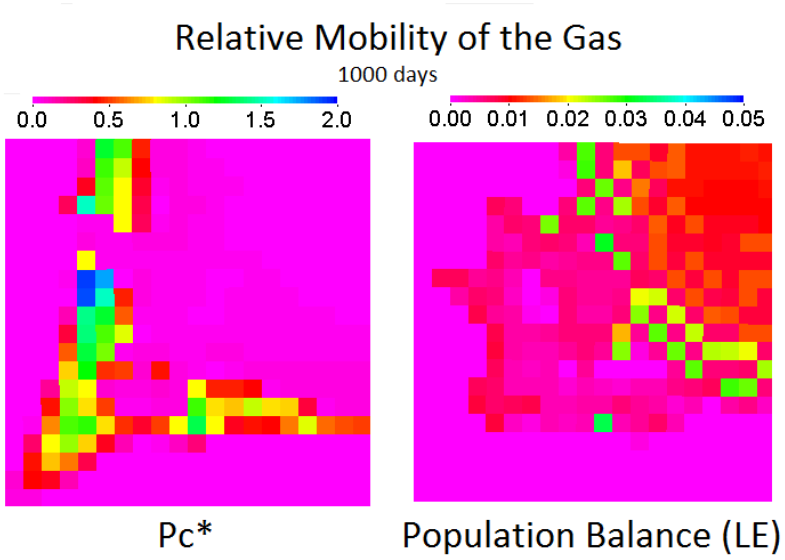

Figure 7.3: Relative mobility ($K_{r,foam}/\mu_{foam}$) map for the gas injection with foam modeled with the population balance (LE) and the P_c^* model; population balance (LE) results in overall lower mobilities.

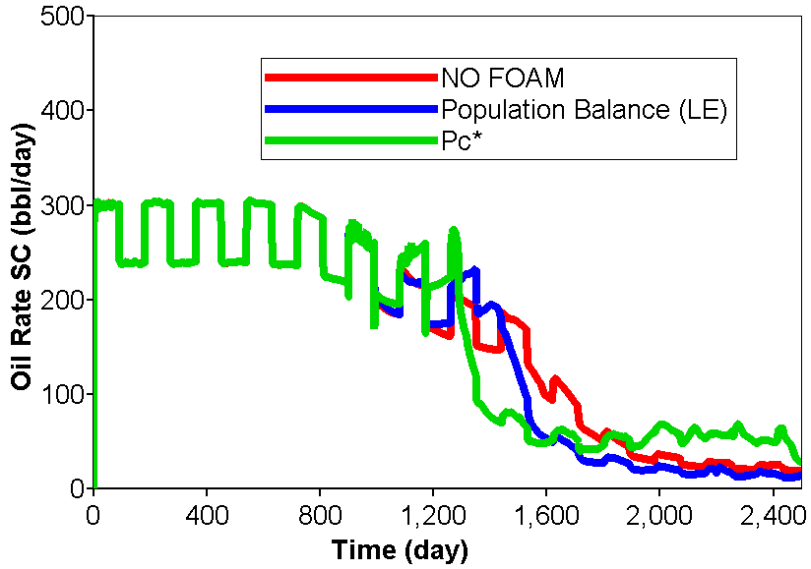

Figure 7.4: Oil production for the WAG injection with no foam and with foam modeled with the population balance(LE) and P_c^* model; oil production decline occurs because of the gas and water breakthrough in all cases.

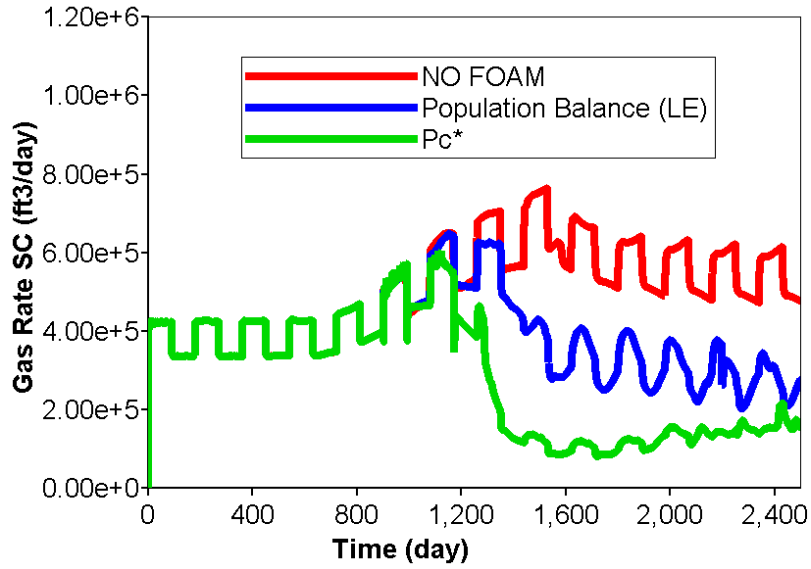

Figure 7.5: Gas production for the WAG injection with no foam and with foam modeled with the population balance(LE) and P_c^* model.

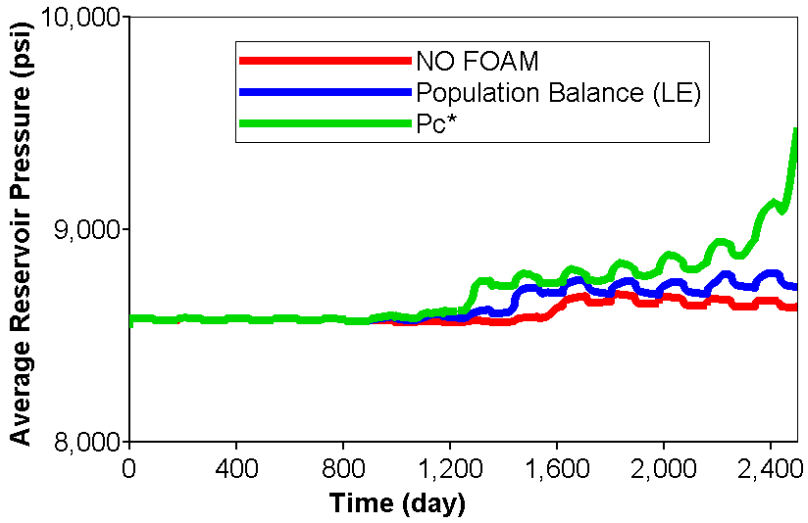

Figure 7.6: Average reservoir pressure for the WAG injection with no foam and with foam modeled with the population balance(LE) and P_c^* model.

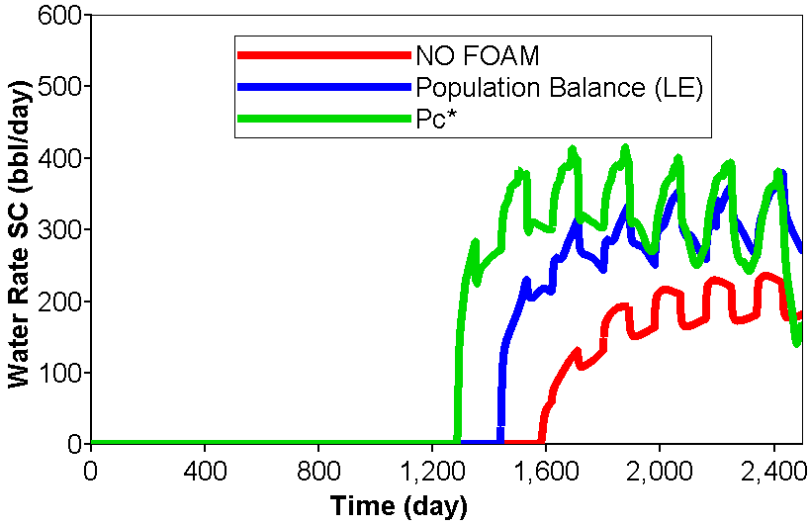

Figure 7.7: Water production for the WAG injection with no foam and with foam modeled with the population balance(LE) and P_c^* model.

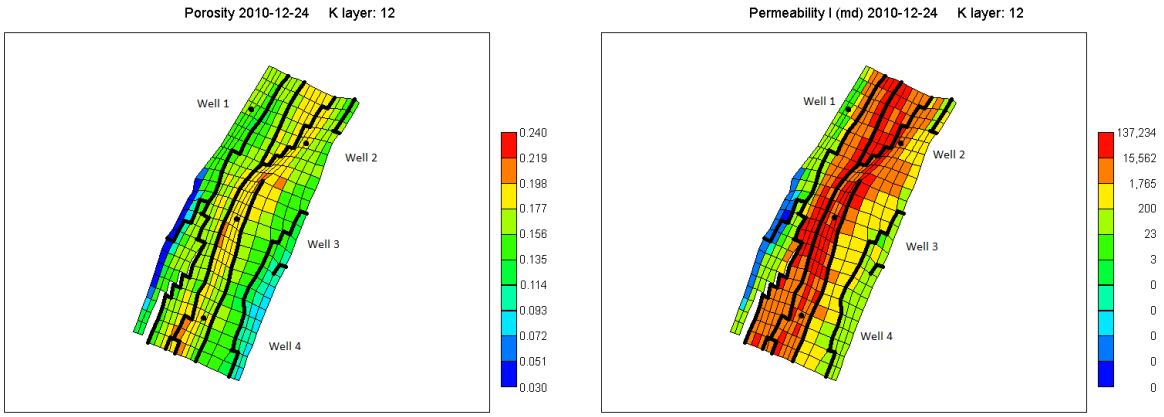

(a) (b)

Figure 7.8: High permeability heterogeneous reservoir: (a) porosity and (b) permeability of layer 12.

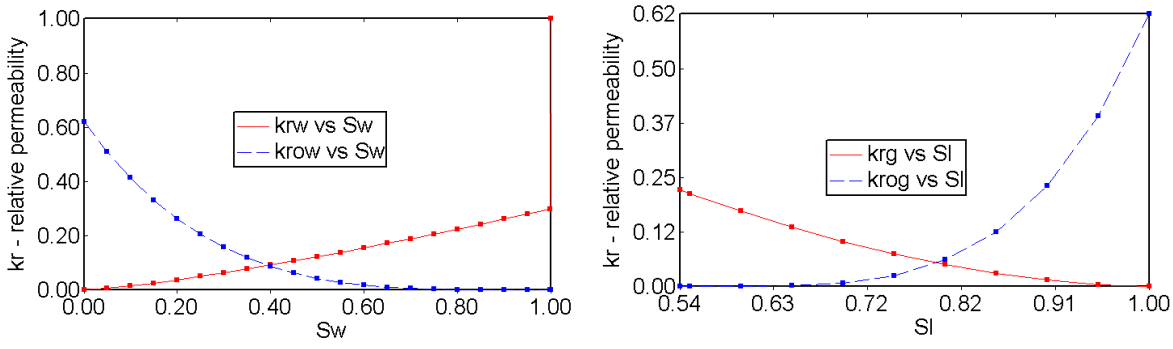

(a) (b)

Figure 7.9: High permeability heterogeneous reservoir relative permeability curves.

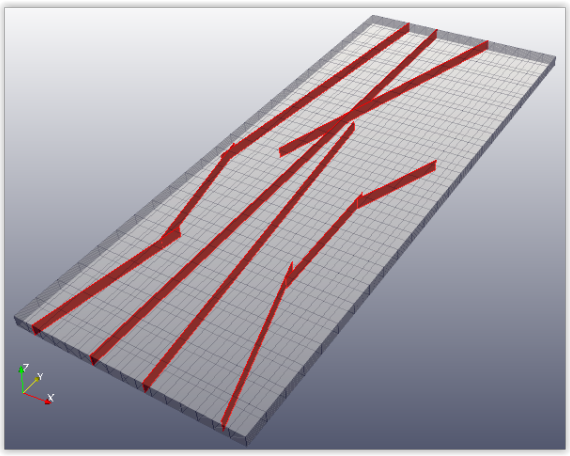

Figure 7.10: Cartesian reservoir model derived for the real field model.

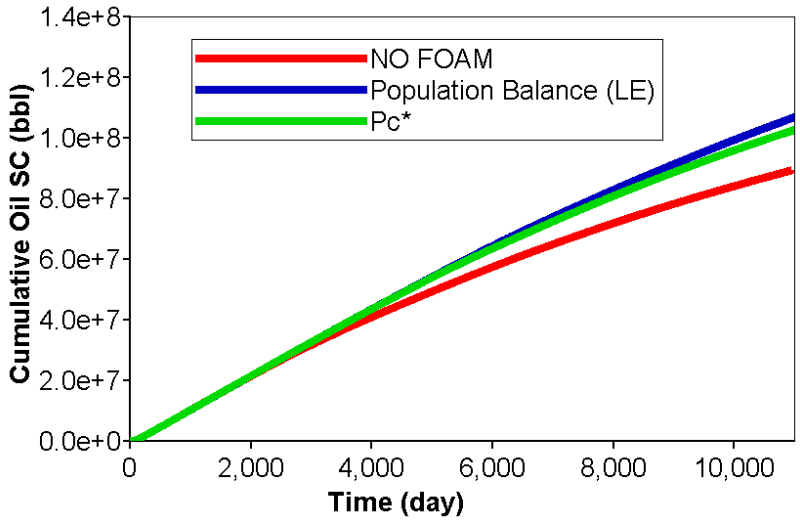

Figure 7.11: Cumulative oil production of the field model: cases with no foam and with foam modeled by the P_c^* and population balance (LE) model.

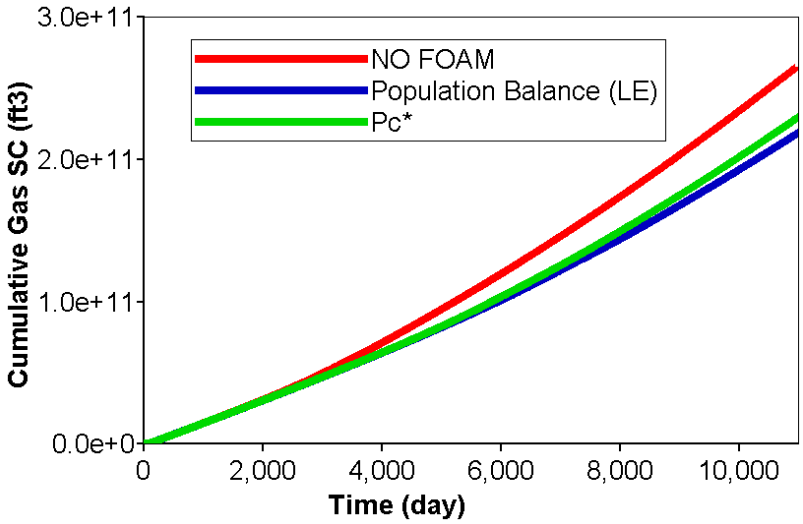

Figure 7.12: Cumulative gas production of the field model: cases with no foam and with foam modeled by the P_c^* and population balance (LE) model.

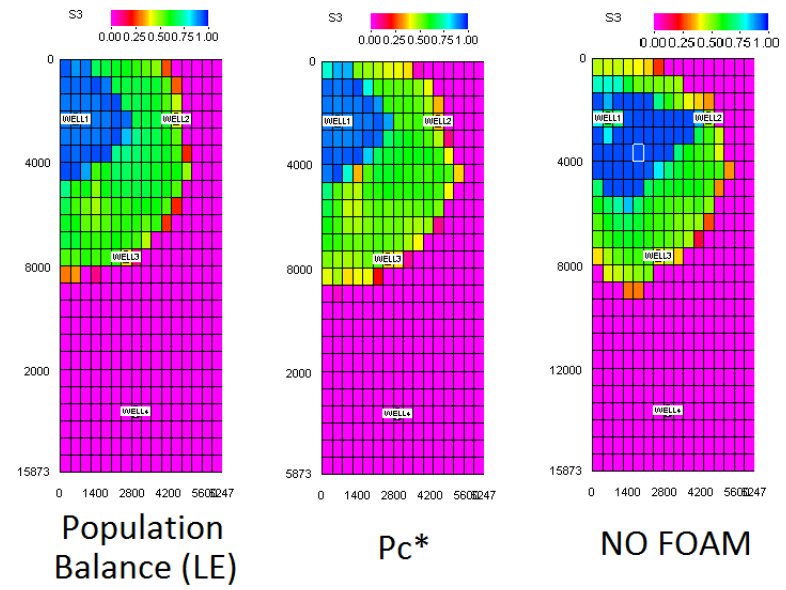

Figure 7.13: Gas saturation map for layer 7.

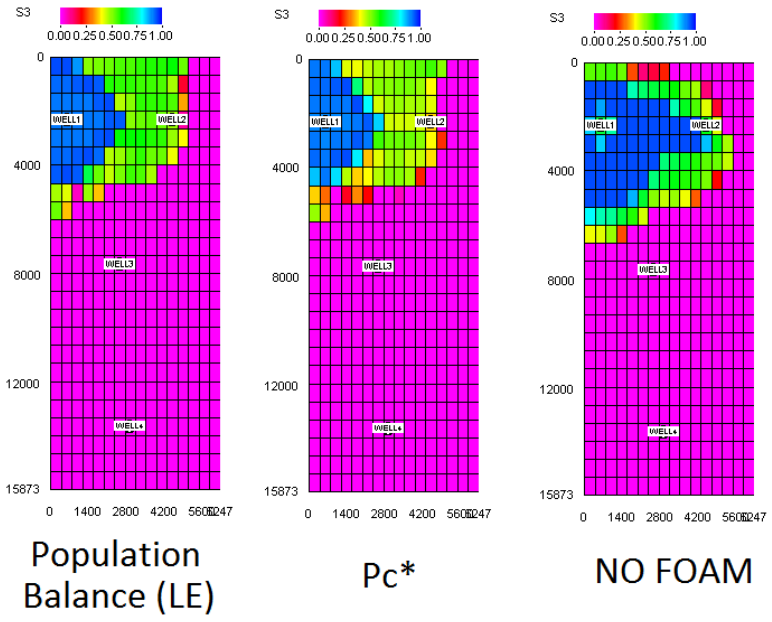

Figure 7.14: Gas saturation map for layer 14.

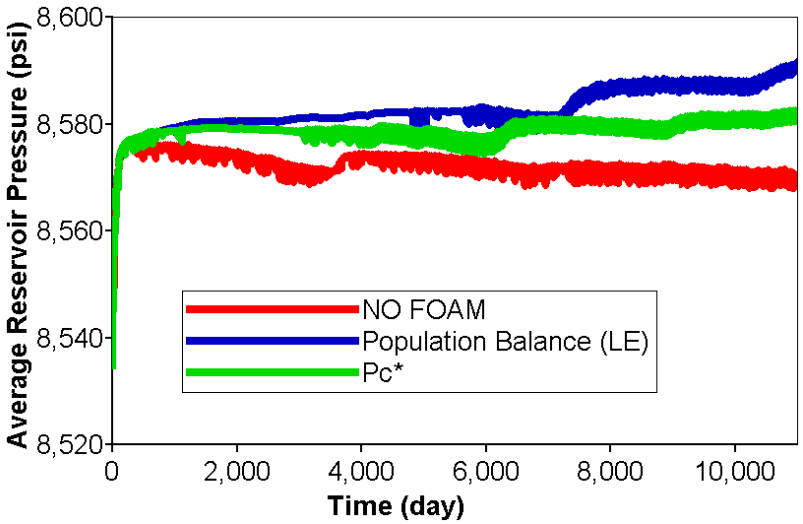

Figure 7.15: Average reservoir pressure of the field model: cases with no foam and with foam modeled by the P_c^* and population balance (LE) model.

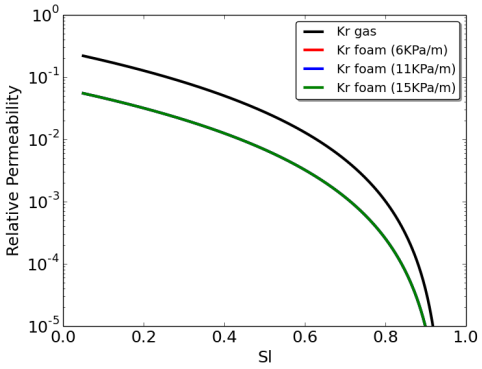

(a) $S_{o,lim} = 1.00$

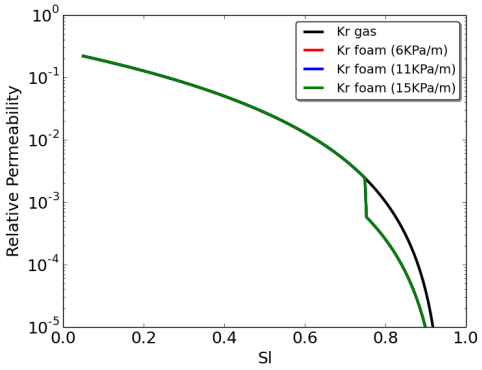

(b) $S_{o,lim} = 0.25$

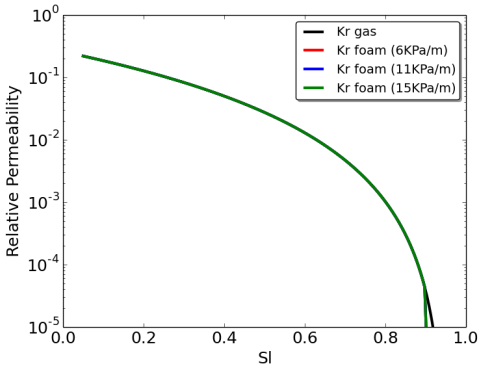

(c) $S_{o,lim} = 0.10$

Figure 7.16: Relative permeability for different $S_{o,lim}$.

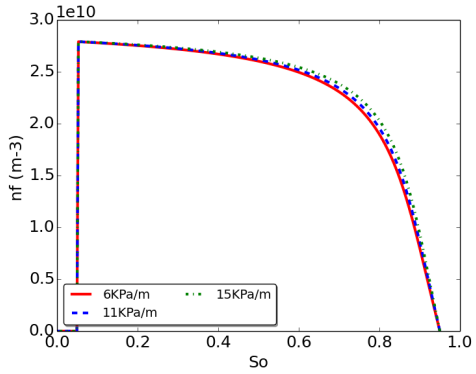

(a) $S_{o,lim} = 1.00$

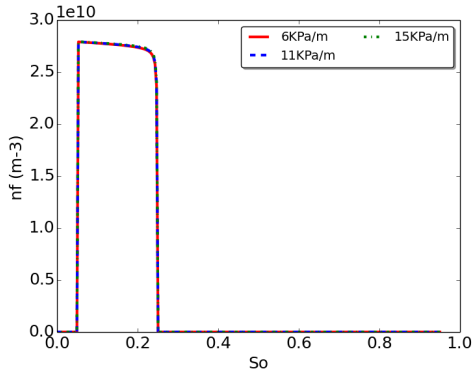

(b) $S_{o,lim} = 0.25$

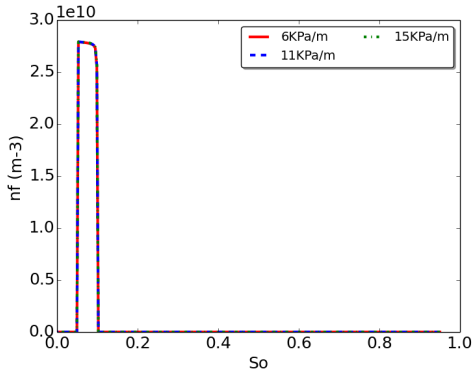

(c) $S_{o,lim} = 0.10$

Figure 7.17: Foam texture for different $S_{o,lim}$.

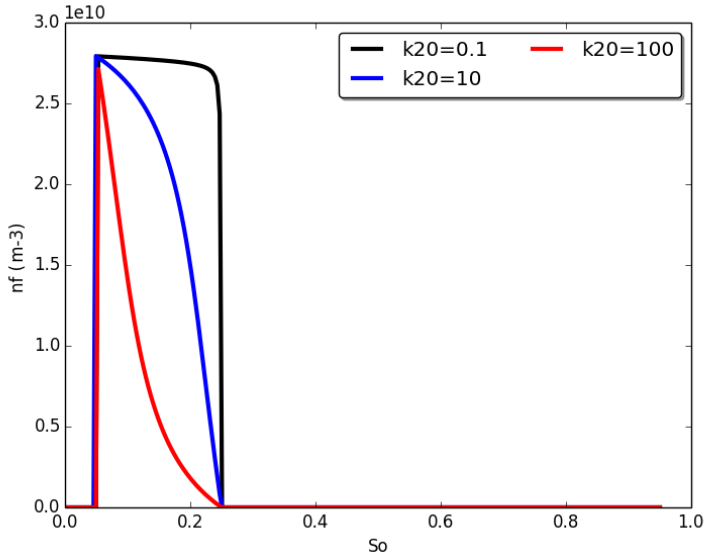

Figure 7.18: Foam texture for $k_2^0 = 0.1$, $k_2^0 = 10$, and $k_2^0 = 100$.

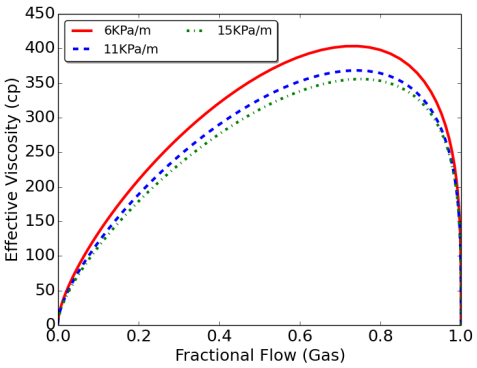

(a) $S_{o,lim} = 1.00$

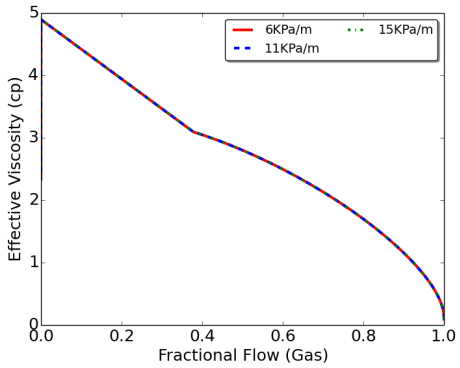

(b) $S_{o,lim} = 0.25$

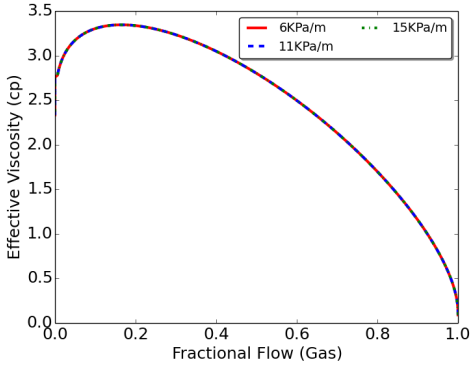

(c) $S_{o,lim} = 0.10$

Figure 7.19: Effective viscosity for different $S_{o,lim}$.

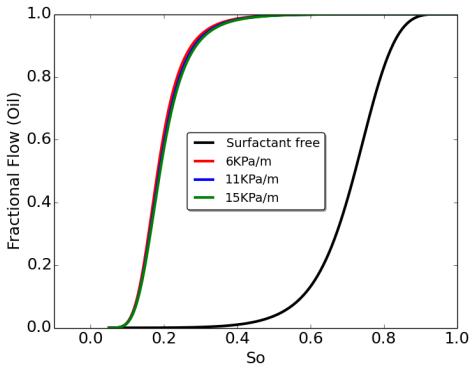

(a) $S_{o,lim} = 1.00$

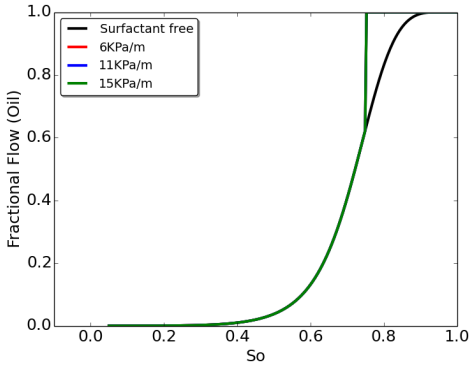

(b) $S_{o,lim} = 0.25$

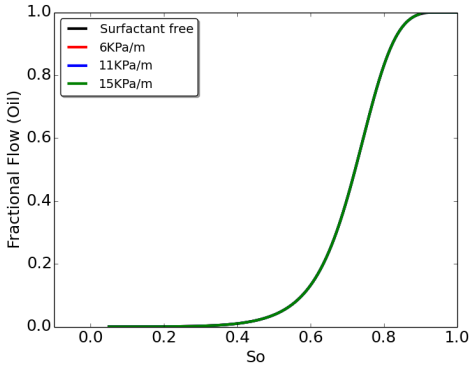

(c) $S_{o,lim} = 0.10$

Figure 7.20: Fractional flow for different $S_{o,lim}$.

Chapter 8

Modeling and Application of Nanoparticle Transport in Foam Injection Projects

8.1 Introduction

In this chapter we evaluate the implementation of the transport of nanoparticles model in an IMPEC compositional simulator. First we validate our implementation using experimental data from Murphy (2012). After the validation we evaluate the impact of the nanoparticle transport in foam generation and stabilization by comparing the results of a foam injection project in a homogeneous reservoir using nanoparticles and a surfactant, the latter modeled as an inert tracer.

8.2 Nanotechnology and Nanoparticles

Nanotechnology was first introduced by the Nobel Laureate Richard P. Feynman in 1959 in the lecture "There's Plenty of Room at the Bottom," given at the California Institute of Technology. Nanotechnology focus on the development and application of materials, methods and devices ranging from a few nanometers to submicron dimensions. Those applications are derived from the use of physical, chemical and biological systems occurring in nanoscale to perform a given task. The nanotechnology also investigates the integration of nanoparticles and nanostructures into larger systems as well as the study of matter to individual atoms (Sobolev and Gutiérrez, 2005). The earlier definition of nanotechnology was provided by Drexler *et al.* (1991): "the control of matter based on molecule-by-molecule control of products and byproducts through high-precision systems as well as the products

and processes of molecular manufacturing, including molecular machinery."

Sobolev and Gutiérrez (2005) describes three groups of nanomaterial classified by their geometry/shape: quantum well (one nanosized dimension), quantum wire (two nanosized dimensions), and quantum dot (three nanosized dimensions). The nanoparticle is classified as a quantum dot and is one important structural unit in nanotechnology. The decreased size of nanoparticles results in a greater surface area and a greater number of atoms located in the surface. The reduction of the dimensions from macro to nanosize and changes electronic conductivity, optical absorption, chemical reactivity and mechanical properties.

8.2.1 Application of Nanoparticles in the Petroleum Industry

Nanoparticles have a broad application in the oil industry. Krishnamoorti *et al.* (2006) mentioned that refining and conversion of fossil fuels have been using nanoparticles as nanocatalysts successfully for the past 30 years. The authors mentioned that drilling engineers have been using nanopartciles for decades in drilling muds, which are composed of clays and 1-nm-thick discs of aluminosilicates; these nanoparticles improve rheological properties of drilling muds. The use of nanoparticles for reservoir conformance was also mentioned based on the alteration of nanoparticle mechanical and flow properties. Sensing and imaging are other application of the nanoparticles because of the alteration in the optical, magnetic, and electric properties and the ability to form percolated structures. The use of nanoparticles for foam stabilization and generation was mentioned by Jikich *et al.* (2012). The authors stated that there are problems with surfactant-based foams: they require continuous generation, surfactant is adsorbed onto the rock surface increasing the costs with chemicals, and degradation of surfactant in severe reservoir conditions. Nanoparticles are mentioned as a solution for foam stabilization because of their chemical stability at adverse reservoir conditions and their capability to be selective adsorbed in fluid-to-fluid interfaces. For nanoparticle-stabilized foam

generation a threshold shear rate is required; once high-shear rates are associated with high permeability zones in the field this property allows the selective reduction of gas mobility where gas flows at higher velocities, such as fractures and gravity override regions that contain little oil. The use of nanoparticles to stabilize CO_2 foam was studied by Espinoza *et al.* (2010); supercritical CO_2 foam presented greater viscosities than pure CO_2 improving sweep efficiency.

8.2.2 Nanoparticle Transport Models

Because of their nanoscale diameter, usually much smaller than typical pore throats, nanoparticles are able to flow through pore throats. First assumption to model nanoparticles is that adsorption and filtration are neglected, hence the transport will be similar to the transport of an inert tracer. We assume that the advection-dispersion equation is accurate and can be used to model the transport of nanoparticles. Equation 8.1 shows a one dimensional advection-dispersion equation (x direction), which is derived based in the following assumptions: homogeneous porous medium, fluid and rock compressibility are negligible, fluid flow at constant rate, reservoir is under isothermal conditions, dispersion occurs only in the longitudinal direction, there is no chemical reaction, and there is no adsorption.

$$\frac{\partial c}{\partial t} = D\frac{\partial^2 c}{\partial x^2} - v_p\frac{\partial c}{\partial x}, \tag{8.1}$$

where where c is the dispersion concentration $[M/L^3]$, D is the dispersion coefficient $[L^2/t]$, x is the distance in x direction, t is time, and v_p is the interstitial velocity $[L/t]$.

Zhang (2012) validated that hypothesis by comparing the results of the advection-dispersion equation with the continuous-random walk model (Figure 8.1). The author mentions that the good match between both models suggests that the heterogeneity effect on tracer transport is negligible (in the measuring range of the experiments) and the advection-dispersion equation is accurate enough to describe

tracer transport.

However, nanoparticle's increased surface area results in strong van der Walls attraction with the rock surface, which causes physicochemical filtration. Physicochemical filtration is mainly governed by the physical and chemical interactions between particles and solid phase. There are two alternatives to model nanoparticle transport in porous media (Zhang, 2012): one based on colloid filtration and other based on chemical adsorption.

Colloid particle deposition in porous media is modeled by Equations 8.2 and 8.3.

$$\frac{\partial c}{\partial t} + \frac{\rho_b}{\phi}\frac{\partial S}{\partial t} = D\frac{\partial^2 c}{\partial x^2} - v_p\frac{\partial c}{\partial x}, \tag{8.2}$$

$$\frac{\rho_b}{\phi}\frac{\partial S}{\partial t} = k_{dep}c, \tag{8.3}$$

where c is the dispersion concentration $[M/L^3]$, k_{dep} is the deposition rate coefficient $[1/t]$, S is the nanoparticle retention concentration $[M_{nanoparticle}/M_{porous\ medium}]$, ρ_b is the bulk density of the porous medium $[M/L^3]$, ϕ is the porosity of the medium, D is the dispersion coefficient $[L^2/t]$, and v_p is the interstitial velocity $[L/t]$. This colloid filtration model calculates increasing retention when the dispersion concentration is above zero and assumes irreversible deposition of suspended particles. Permeability of the rock will decrease steadily with the increase in the amount of retained particles.

For some nanoparticles with diameters smaller than 10 nm the adsorption is driven by the chemical potential gradient between the nanoparticle and the rock surface. In that case the adsorption is balanced with desorption as represented by Equation 8.4.

$$\frac{\partial S}{\partial t} = k_a\left(1 - \frac{S}{S_{max}}\right)c - k_d\frac{S}{S_{max}}, \tag{8.4}$$

where s_{max} is the maximum adsorption capacity of the rock surface $[M/L^2]$, k_a is the adsorption rate coefficient $[L/t]$, and k_d is the desorption rate coefficient $[M/L^2/t]$. An maximum capacity (the monolayer capacity, as in the Langmuir type of adsorption), s_{max}, is assumed in that model. k_a and k_d have a first order influence on the nanoparticle transport. Since desorption is assumed to happen the adsorption is considered to be reversible. Nanoparticles concentration propagates as a travelling front governed by the injected concentration of nanoparticles and adsorption capacity.

Zhang's (2012) work evaluated different models for modeling nanoparticle flow in porous media. Among the studies models are the Two Site and Two Rate models.

8.2.2.1 Two Site Model

The Two Site model assumes that nanoparticle adsorption may occur in two different sites in the reservoir rock, in one site the adsorption is reversible and in the other site the adsorption is irreversible, and that the adsorption assumes a monolayer configuration. Reversible and irreversible adsorptions have different capacities, independent of each other, and their summation is equal to the monolayer coverage density. The desorption rate depends of the reservoir surface geometry at which the nanoparticle is adsorbed. Equations 8.5, 8.6, and 8.7 are used to model nanoparticle adsorption using the Two Site model.

$$\frac{\rho_b}{\phi}\frac{\partial S}{\partial t} = \frac{\rho_b}{\phi}\frac{\partial S_1}{\partial t} + \frac{\rho_b}{\phi}\frac{\partial S_2}{\partial t}, \tag{8.5}$$

$$\frac{\rho_b}{\phi}\frac{\partial S_1}{\partial t} = k_{in}\left(1 - \frac{S_1}{S_{1,max}}\right)c, \tag{8.6}$$

$$\frac{\rho_b}{\phi}\frac{\partial S_2}{\partial t} = k_{ra}\left(1 - \frac{S_2}{S_{2,max}}\right)c - \frac{\rho_b}{\phi}k_{rd}S_2, \tag{8.7}$$

where S_1 and S_2 are the reversible and irreversible concentrations of adsorbed nanoparticles, $S_{1,max}$ and $S_{2,max}$ are the capacities for irreversible and reversible adsorption, k_{irr} is the irreversible adsorption rate coefficient $[1/t]$, k_{ra} is the reversible adsorption rate coefficient $[1/t]$, and k_{rd} is the desorption rate coefficient $[1/t]$.

8.2.2.2 Two Rate Model

The Two Rate model assumes two kinds of nanoparticle adsorption: a irreversible one at rates faster than the flow rate but that reaches equilibrium instantaneously and a reversible one based on a dynamic process that does not reach equilibrium instantaneously. In the fast adsorption the adsorbed concentration is proportional to the dispersion concentration, while for the slow adsorption the adsorbed concentration follows the Langmuir-type. The Two Rate model is represented by Equations 8.8, 8.9, and 8.10.

$$\frac{\partial c}{\partial t} + \frac{\rho_b}{\phi}\frac{\partial (S_1 + S_2)}{\partial t} = -v_p \frac{\partial c}{\partial x} + D\frac{\partial^2 c}{\partial x^2}, \tag{8.8}$$

$$\frac{\rho_b}{\phi}\frac{\partial S_1}{\partial t} = k_{ads}\left(1 - \frac{S_1}{S_{max}}\right)c - k_{des}M_p\frac{S_1}{S_{max}}, \tag{8.9}$$

$$\frac{\rho_b}{\phi}S_2 = k_f c, \tag{8.10}$$

where k_{ads} is the adsorption rate coefficient $[t^{-1}]$, k_{des} is the desorption rate coefficient $[t^{-1}L^{-3}]$, S_{max} is the retention capacity, M_p is the mass of a single nanoparticle $[M]$, and k_f is the retardation factor $[t^{-1}]$.

Calculating $\frac{\partial (S_2)}{\partial t}$ from Equation 8.10 we obtain $\frac{\partial (S_2)}{\partial t} = \frac{\phi}{\rho_b}k_f\frac{\partial c}{\partial t}$. Combining $\frac{\partial (S_2)}{\partial t}$ with Equation 8.8 we obtain Equation 8.11. For calculating $\frac{\partial (S_2)}{\partial t}$ we assume ρ_b, ϕ, and k_f are constant in time, or that the fast adsorption represented by k_f is

irreversible.

$$(1+k_f)\frac{\partial c}{\partial t}+\frac{\rho_b}{\phi}\frac{\partial S_1}{\partial t}=-v_p\frac{\partial c}{\partial x}+D\frac{\partial^2 c}{\partial x^2}. \tag{8.11}$$

8.3 Methodology

We implemented the nanoparticle transport in an IMPEC compositional compositional simulator. Equations used in the implementation are described in Section 8.2.

For the Two Site model we discretized Equations 8.5, 8.6, and 8.7. Equations 8.12 and 8.13 presents the calculations of the gradients in time of the reversible and irreversible concentrations of adsorbed nanoparticles, respectively. The summation of both equations gives the net molar mass of nanoparticles ($\Delta S = \Delta S_1 + \Delta S_2$) after reversible and irreversible adsorption takes place in a given time step (Δt).

$$\Delta S_1 = \Delta t \times \left[k_{in}\left(1-\frac{S_1}{S_{1,max}}\right)c\frac{\phi}{\rho_b}\right], \tag{8.12}$$

$$\Delta S_2 = \Delta t \times \left[k_{ra}\left(1-\frac{S_2}{S_{2,max}}\right)c\frac{\phi}{\rho_b}-k_{rd}S_2\right], \tag{8.13}$$

For the Two Rate model Equations 8.9 and 8.11 are solved numerically assuming steady-state and neglecting dispersion. We add $k_f\frac{\Delta c}{\Delta t}$ and the right side of Equation 8.9 to the accumulation term of the tracer transport equation, as in Equation 8.11.

Although we implement filtration models to model the adsorption and desorption of nanoparticles, the permeability alteration due to the filtration was not taken into account.

8.4 Validation

The validation was performed using experimental data from the literature. The experiment number 66 (Murphy, 2012) was modeled using our IMPEC compositional simulator and the parameters of the Two Site model, used to model nanoparticle transport, were adjusted using an automated optimization tool.

Experiment 66 was performed by injecting 3 PV of 5 wt% Salt Tolerant 3M nanoparticles into a 1 ft column of 95 wt% 177-210 μm Boise sandstone, mixed with 5 wt% kaolinite at 10 mL/min. The core plud had a diameter of 0.43 in. The experiment was done to evaluate slug size sensitivity and test high flow rate nanoparticle retention in the presence of kaolinite. Figure 8.2 shows the effluent history of experiment 66.

8.4.1 Two Site Model

Figure 8.3 shows the match obtained with the Two Site model using our IMPEC compositional simulator. Table 8.1 shows the model parameters obtained from the match.

8.4.2 Two Rate Model

Figure 8.4 shows the match obtained with the Two Rate model using our IMPEC compositional simulator. Table 8.2 shows the model parameters obtained from the match. As observed, to match the data in experiment 66 the dispersion coefficient was greatly increased in comparison to the dispersion coefficient needed for the Two Site model.

To further verify the utilization of the Two Rate model we match the experiment 60 described in Yu (2012). The core used in this experiment has 6 in length and diameter of 1 in; porosity of the plug is 0.278, permeability is 864 mD. Nano particle is injected at a rate of 0.1017 ft^3/d at a concentration of 5,000 ppm. Figure 8.5 shows a good match between the numerical model and the experimental

data. We present the parameters used in the Two Rate model in Table 8.3.

Figure 8.5 shows the match between the experimental data and the simulated data for experiment 60 (Yu, 2012). A good match is observed between the experimental and simulated data. We obtained a low dispersivity value (compared to the experiment 66). The k_{des} was a thousand times greater than the k_{ads}, otherwise the amount of adsorbed nanoparticles in the simulation would be greater than the observed in the experiment.

8.5 Application

In this section we evaluate the injection of foam injection using surfactant and nanoparticles as foam stabilizing agents. The surfactant stabilized foam was modeled using a inert tracer model (without dispersion and without adsorption) for the surfactant transport and the population balance (LE) and the parameters used were obtained with the matching of Chen *et al.*'s (2010) experimental data (Table 6.2). To simulate the nanoparticle stabilized foam we used the Two Site model with parameters shown in Table 8.1 and the population balance model (LE) with parameters obtained with the matching of Chen *et al.*'s (2010) experimental data (Table 6.2). To stabilize the foam we inject 50 ppm of the stabilizing agent (surfactant or nanoparticles) for 500 days and we assume that foam will be formed in the presence of gas, water, and stabilizing agent. We neglect the effect of the oil saturation in foam stability.

We assumed a 2D low permeability reservoir with properties described in Table 8.4. Reservoir dimensions used are 500 ft x 500 ft x 80 ft. Porosity was 0.3 and permeability 10 md. The initial water saturation equals the connate water saturation, which leads us to a two-phase flow problem (gas/foam and oil). The initial reservoir pressure is 8534 psi. The composition of the injected gas is 50% CO_2 and 50% methane and we obtain partial miscibility between the oil and the injected gas. Fluid

properties used in this study are described in Appendix A.

8.5.1 Homogeneous Reservoir

Figures 8.6 and 8.7 show the oil production rate and gas production rate, respectively, for the homogeneous reservoir under gas injection with no foam, surfactant stabilized foam, and nanoparticle stabilized foam. As observed the foam delayed the breakthrough of the injected gas for the cases of surfactant and nanoparticle foams. Results using surfactant and nanoparticles were similar. To further evaluate the foam injection with nanoparticle and surfactant foam we plotted in Figure 8.8 the average reservoir pressure of both cases; similar results in terms of average reservoir pressure are observed. For this case the dispersivity and adsorption parameters did not impact the foam efficiency as a mobility control agent. Future works should model and evaluate the effect of the adsorption and dispersivity in nanoparticle transport and foam stabilization with a greater range of experimental data.

8.6 Summary

- We presented two models for nanoparticle transport in porous media (Zhang, 2012) based on colloid filtration and chemical adsorption.
- Zhang's (2012) work evaluated different models for modeling nanoparticle flow in porous media: the Two Site model and the Two Rate model.
- The Two Site model assumes that nanoparticle adsorption may occur in two different sites in the reservoir rock, in one site the adsorption is reversible and in the other site the adsorption is irreversible, and that the adsorption assumes a monolayer configuration. The Two Rate model assumes two kinds of nanoparticle adsorption: a irreversible one at rates faster than the flow rate

but that reaches equilibrium instantaneously and a reversible one based on a dynamic process that does not reach equilibrium instantaneously.

- We implemented the Two Site and the Two Rate model in a compositional IMPEC reservoir simulator. The implementation was successfully validated against experimental data from the literature.

- We simulated a foam injection in a synthetic reservoir to illustrate the modeling of surfactant and nanoparticles stabilized foam injection. Surfactant transport was modeled as an inert tracer, while nanoparticles transport was modeled using the Two Site model.

- The foam was successful to delay the injected gas breakthrough. Results of surfactant and nanoparticles stabilized foam were similar, although we expected differences because the nanoparticle modeling includes adsorption and dispersivity.

Table 8.1: Two Site model parameters

k1	S2max	S1max	k2	k3	ROCKDNNP	Dispersion
0.0393	0.00478	3.15e-05	1350.577	187.294	162.24	1

Table 8.2: Two Rate model parameters for experiment 66

k_{ads}	S_{max}	k_{des}	M_p	k_f	Dispersion
24.885	1114.621	2158.552	1e-20	0.395	40.632

Table 8.3: Two Rate model parameters for experiment 60

k_{ads}	S_{max}	k_{des}	M_p	k_f	Dispersion
1.92	0.02	1951.41	1e-20	0.08	1.41

Table 8.4: Properties of models for the application of the nanoparticles stabilized foam injection.

Reservoir Dimension	500 ft x 500 ft x 80 ft
Initial Pressure	8534 psi
Reservoir Temperature	147.2^o F
Porosity	0.3
Permeability	10 mD
Irreducible Water Saturation	0.25
Residual Oil Saturation for Water Injection	0.25
End Point for Water Relative Permeability Curve	0.5
Corey Exponent for Water Relative Permeability Curve	3
End Point for Oil Relative Permeability Curve	1.0
Corey Exponent for Oil Relative Permeability Curve	3
End Point for Gas Relative Permeability Curve	0.5
Corey Exponent for Gas Relative Permeability Curve	3

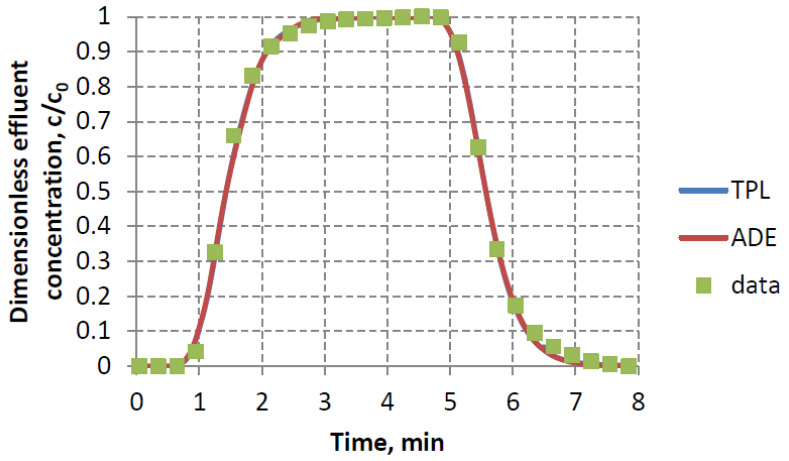

Figure 8.1: Validation of the advection-dispersion equation with the continuous-random walk model (Zhang, 2012).

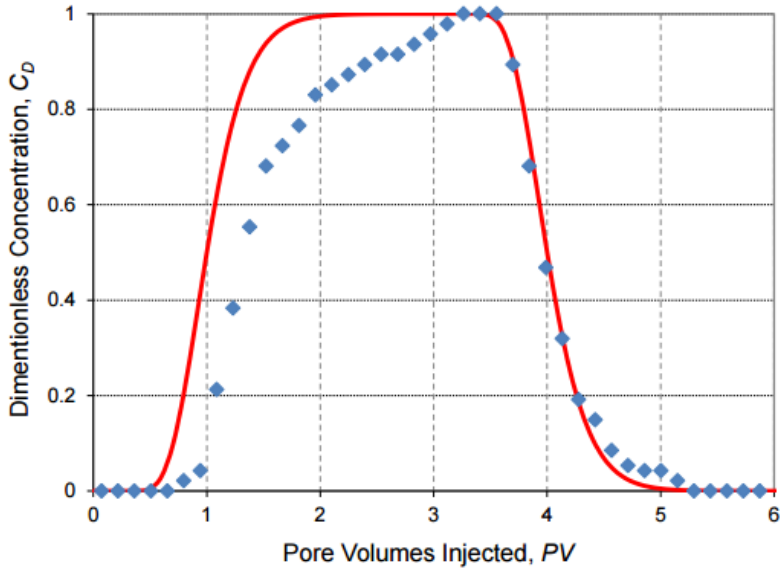

Figure 8.2: Effluent history of experiment 66 (Murphy, 2012).

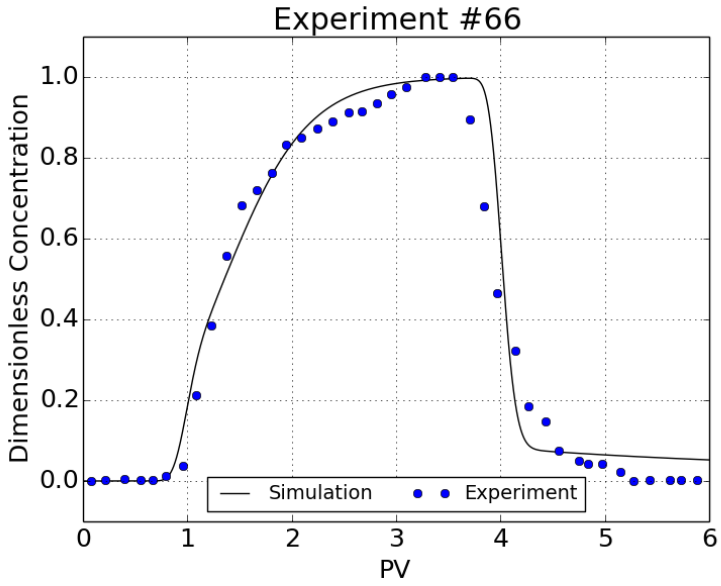

Figure 8.3: Effluent history of experiment 66 (Murphy, 2012) and the results obtained in the simulation: a good match is observed for the Two Site model.

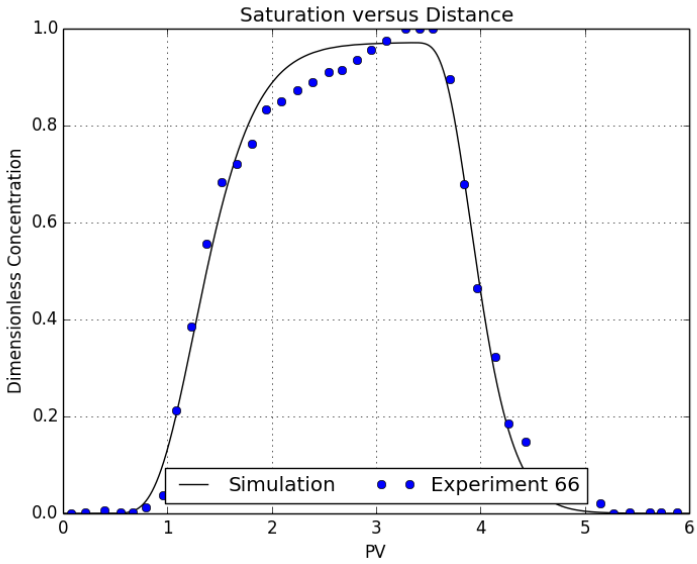

Figure 8.4: Effluent history of experiment 66 (Murphy, 2012) and the results obtained in the simulation: a good match is observed for the Two Rate Model.

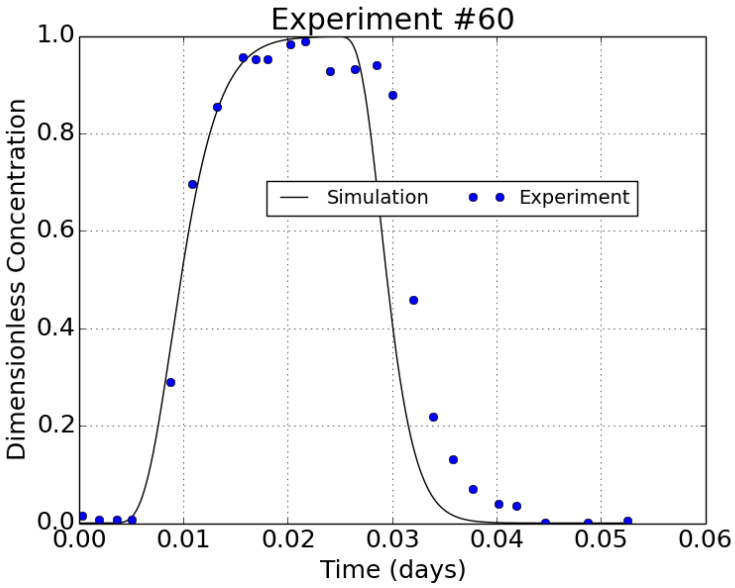

Figure 8.5: Effluent history of experiment 60 (Murphy, 2012) and the results obtained in the simulation: a good match is observed for the Two Rate Model.

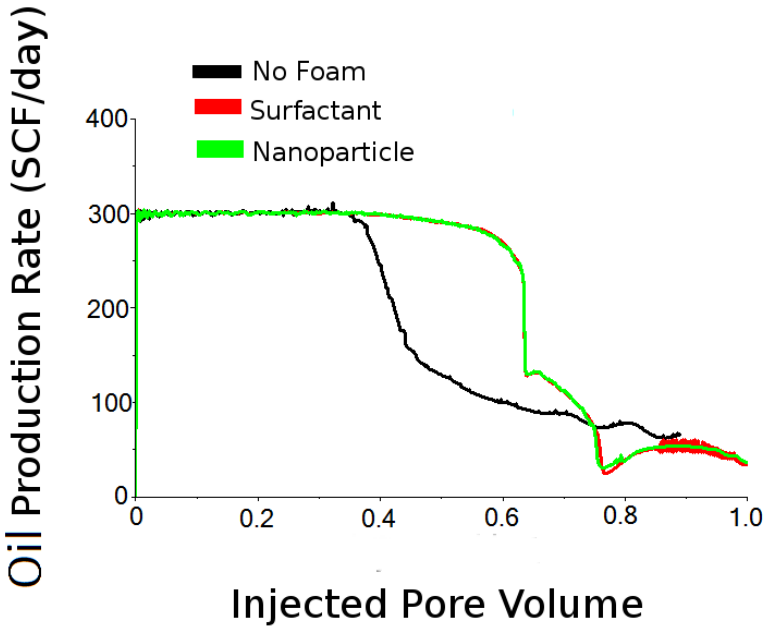

Figure 8.6: Oil production rate for the homogeneous reservoir cases.

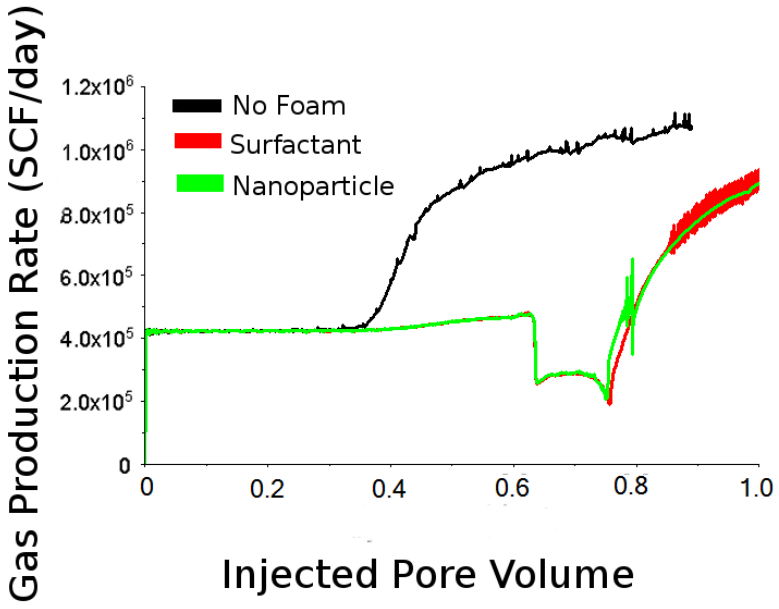

Figure 8.7: Gas production rate for the homogeneous reservoir cases.

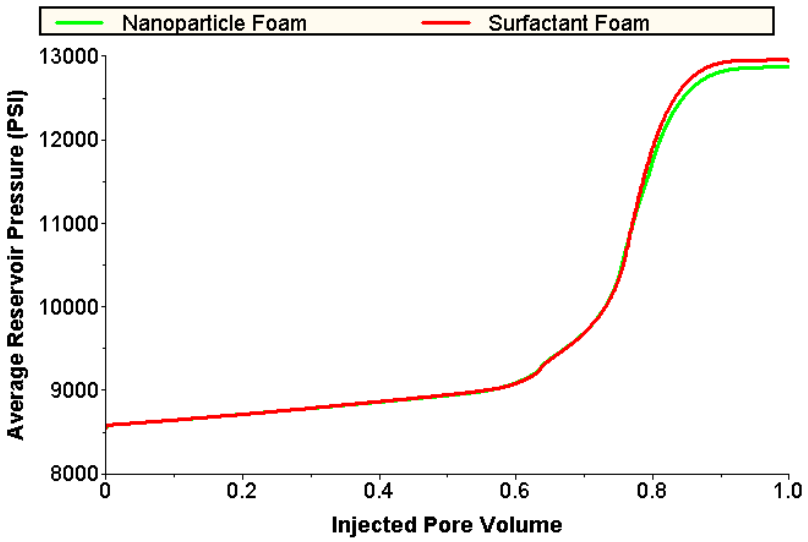

Figure 8.8: Average reservoir pressure for the homogeneous reservoir: nanoparticle and surfactant foam cases.

Chapter 9

Summary, Conclusions, and Recommendations

In this section we present the summary and conclusions of each topic addressed in this research. We also present recommendations and opportunities for future research related to this work.

9.1 Embedded Discrete Fracture Model

9.1.1 Summary

In this work we developed a computational tool called the EDFM preprocessor which is able to discretize multiple fractures in different input formats. Cartesian grids were assumed to model reservoir matrix. Although originally developed to be used with our in-house IMPEC reservoir simulator, the EDFM preprocessor output data can be converted for use in commercial simulators.

The equations used to calculate all the transmissibilities involved in the simulation of flow through fractures are explained in Chapter 3. We assume a linear pressure behavior in the matrix; we also assume that the fracture pressure follows the same pressure gradient of the matrix. The full permeability tensor of the matrix can be used in our calculations to allow the transformation of the flux vector to be perpendicular to the fracture plane. For partially penetrating fractures we extend the fracture area to calculate the characteristic distance and assume that the transmissibility of the partially penetrating fracture is linearly proportional to the area of the fracture into the gridblock. We derived and proposed a new equation for the transmissibility between two fracture blocks of a same fracture that allows the

modeling of complex fracture with varying conductivity. We explained how the transmissibility between intersecting fractures are calculated and we modified the previous method; our equation takes into account all the fracture segments intersecting the gridblock, neglecting small segments as needed. We propose a new equation to calculate the transmissibility (or well index) of an horizontal well intersecting a planar fracture which assumes radial flow from the fracture to the well.

In terms of the integrated EDFM approach, which was proposed as an extension of the EDFM assuming a dual continuum media, we explained how the average permeability of a set of fractures was calculated using Oda's method. We assume that the fracture system is highly connected. To compare the integrated EDFM with the conventional dual porosity formulation we estimated the shape factor of each fracture block using the average distance between fractures; fracture permeability of the conventional dual porosity model was calculated using Oda's method.

We identified the need to translate fracture properties in the space to allow the coupling of the EDFM with fracture propagation tools. The approach is important to model non-planar complex fractures. In the proposed method we define a local system of coordinates for the fracture plane using dimensionless variables. This local system can be translated in space to any fracture plane in any position and dimensions.

Due to restrictions imposed by the IMPEC formulation, a porosity cut-off was applied to fracture blocks to avoid low pore volumes and the simulation run time was reduced about 10 times without loss in the results quality and precision.

9.1.2 Conclusions

We concluded that the EDFM can be used to model complex fractures in reservoirs producing under depletion, water injection, or gas injection miscible. We

verified our EDFM preprocessor against an unstructured grid model (Karimi-Fard and Firoozabadi, 2003) and a good match was observed for the cumulative production and water saturation maps. The EDFM was verified against fine models ran in a commercial simulator for water and miscible gas injection. We verified multi-fractured horizontal wells with different fracture properties (homogeneous, heterogeneous and non-planar fractures) and naturally fractured reservoirs with 2, 10, and 100 fractures. A good match between the EDFM and fine model results was observed.

We observed that the gravity effect is important in low permeability reservoir when a highly connected network of fractures is present. Different application case studies were investigated upon which the gravity effect was highlighted when the 2D models were converted to 3D grid. Gravitational effect was not pronounced for models with low number of fractures because of the low matrix permeability. Although water alternated gas injection (WAG) is idealized to reduce gravity override, our simulations show a lower oil production for anticline and dipping reservoirs producing under alternated injection; gravity effects in WAG injection are associated to the reservoir geometry. WAG provides a better mobility control when compared to continuous gas injection, but it may have its efficiency reduced depending on the reservoir geometry.

9.2 Multilateral Well Stimulation

9.2.1 Summary

The EDFM preprocessor was extended to model multilateral well stimulation techniques. Wellbore laterals are modeled as equivalent fractures and a new transmissibility equation (based on Peaceman's equation) was proposed and used to calculate the connection between wellbore laterals and the reservoir matrix. To verify our approach for multilateral well stimulation modeling we performed a sensitivity analysis and a history matching to the data of a pilot test of the Fishbones technology, conducted in the Austin Chalk Formation. The history matching was performed using an in-house automated tool.

9.2.2 Conclusions

After performing a sensitivity study on the reservoir properties of the Austin Chalk Formation we concluded that the N_w exponent and the S_{wi} were the most strongly influencing parameters on the water cumulative production, denoting an inversely and directly proportional relationship, respectively; the cumulative oil production and the cumulative gas production had k and S_{wi} as the most influencing parameters. The water rate and cumulative water production were the most sensitive production parameters during the history match. The main matching parameters were the water relative permeability curve and the initial water saturation. When natural fractures were added the water production rate showed a better match, which leads us to onclude that the presence of natural fractures must be evaluated in low permeability reservoirs candidates to the use of multilateral well stimulation.

As the number of fishbone subs increases the well productivity index and, consequently, the cumulative oil production increases. We conclude that an optimal number of wellbore laterals, which gives greater oil production at the lowest operational cost, may be determined through a simulation study using the EDFM. The Fishbone Production Saturation Point (FPSP) was defined as the point were an increase in the number of subs does not increase oil production.

Fracture modeling is an important parameter in multilateral well stimulation evaluation. The dip and strike angles of the fractures were the most strongly influencing parameters as observed in the sensitivity analysis for fractured reservoirs; these results show that the fracture characterization is a source of uncertainty and reinforces the importance of an appropriate fracture modeling and uncertainty analysis for reliable results.

Fractured reservoirs are the best scenario for multilateral well stimulation. The connection of the wellbore lateral to a natural fracture network increases the well to

reservoir connectivity, allowing greater cumulative oil production.

9.3 Foam Modeling and Application

9.3.1 Summary

We implemented the population balance (LE) model in a compositional reservoir simulator assuming the foam coalescence rate as a function of the S_w^*. The population balance (LE) implementation was verified against two experimental data from the literature. A good match was observed for the saturation and pressure profiles between simulated and experimental data. An automated method using optimization algorithms was proposed and used to fit foam model parameters to steady-state experiments. The method may be applied to any local-equilibrium foam model and allows quantitative and qualitative comparison of each foam model.

We applied foam injection in two different reservoirs, a low permeability homogeneous reservoir and a high permeability heterogeneous fractured reservoir, the latter was derived from a real field located in Brazil. For the Low Permeability Homogeneous Reservoir case we evaluated continuous foam injection and the foam assisted water alternated gas injection (FAWAG). The continuous injection of foam successfully reduced gas mobility, increasing oil recovery and delaying the breakthrough of the injected gas when compared to gas injection with no foam. In FAWAG injection the foam was able to reduce gas mobility and delay the gas breakthrough, but the reduction in gas mobility resulted in an earlier water breakthrough. For the High Permeability Heterogeneous Reservoir case, the foam was able to reduce gas mobility and increase oil recovery. Conductive faults (conductivity of $100md \cdot ft$) did not impact the flow behavior into the reservoir due to low contrast with the matrix permeability. High permeability layers were responsible for the gas breakthrough and foam successfully diverted the gas increasing the vertical sweep efficiency.

9.3.2 Conclusions

We conclude that the assumption of foam coalescence rate as a function of the S_w^* allows the use of the population balance (LE) model in complex simulation cases. Assuming capillary equal to zero resulted in a poor estimation of the S_w^*, as observed in our validation with experimental data. Non-zero capillary pressure tends to increase oil recovery due to natural imbibition in mixed and water wet reservoirs.

There is a need of an accurate and practical method to allow the characterization of foam parameters used in local equilibrium foam models. Although the population balance (LE) needs a greater number of foam paraters than the P_c^* model, our foam fitting method allowed not only to determine foam parameters but also to evaluate the foam behavior under different pressure differentials. It is also important to evaluate foam model parameters considering the effects of the oil saturation; we mention the importance of the $S_{o,lim}$ and k_2^0 parameters on cumulative oil production.

We observed that the population balance (LE) generates stronger foam than the P_c^* model. The population balance (LE) model relates the pressure differential to the foam relative permeability, hence foam strength. The pressure differential is related to the absolute rock permeability, once for a constant flow rate a greater pressure differential is observed in a rock with lower permeability. We conclude that the population balance (LE) model is able to model foam behavior under different pressure differentials. The P_c^* model resulted in a weaker foam in the saturation front because this model assumes constant foam parameters, while foam parameters should be a function of reservoir properties, such as permeability. An appropriate characterization of the foam behavior must be performed prior to the evaluation of any foam injection project.

9.4 Nanoparticles Modeling for Foam Stabilization

9.4.1 Summary

Zhang's (2012) work evaluated different models for modeling nanoparticle flow in porous media assuming adsorption and filtration: the Two Site model and the Two Rate model. The Two Site model assumes that nanoparticle adsorption may occur in two different sites in the reservoir rock, in one site the adsorption is reversible and in the other site the adsorption is irreversible, and that the adsorption assumes a monolayer configuration. The Two Rate model assumes two kinds of nanoparticle adsorption: a irreversible one, at rates faster than the flow rate but that reaches equilibrium instantaneously, and a reversible one, based on a dynamic process that does not reach equilibrium instantaneously. We implemented the Two Site and the Two Rate model in a compositional IMPEC reservoir simulator. The implementation was successfully validated against experimental data from the literature.

9.4.2 Conclusions

We conclude that nanoparticles transport may be modeled and coupled to foam models to evaluate the injection of nanoparticles stabilized foam. We simulated foam injection in a synthetic reservoir to illustrate the injection of nanoparticles stabilized foam. Surfactant transport was modeled as an inert tracer, while nanoparticles transport was modeled using the Two Site model. The foam was successful to delay the injected gas breakthrough. Results of surfactant and nanoparticles stabilized foam were similar.

9.5 Recommendations

1. Extend the EDFM preprocessor to embed fracture planes in a Corner Point Grid (CPG). The EDFM preprocessor must be able to read all the 8 corners of each gridblock and calculate all the fracture plane intersections needed for

transmissibility calculations despite the block orthogonality (up to a limit, once even in CPGs a certain degree of orthogonality must be honored). If the fault is assumed a main fault during grid generation it will not cross any gridblock, but it will be positioned in between gridblocks. In that case the fracture plane cannot be embedded because of the lack of intersection between the fracture plane and the matrix gridblock.

2. Simulate fracture corridors using the EDFM. Fracture corridors are composed of a main fault and its associated small scale fractures, which increases permeability and creates a permeability channel.

3. Extend the multilateral well stimulation feature to model lateral in arbitrary directions; perform sensitivity and uncertainty analysis on the installation of the Fishbone's lateral using physical or economical objective functions.

4. Evaluate the use of multilateral well stimulation in unconventional reservoirs, such as coal-bed methane reservoirs. The EDFM preprocessor may be modified to allow the coupling of EDFM fracture blocks with dual porosity fracture blocks in commercial simulators. An EDFM fracture would then be connected to the matrix gridblock and to the fracture gridblock modeled with the conventional dual porosity formulation, allowing flow from the matrix to the EDFM fracture, from the matrix to the dual porosity fracture, and between the EDFM and dual porosity fractures.

5. Implement the P_c^* model with the proposed modification and evaluate its accuracy and performance using experimental data from the literature. As the foam parameters are treated as function of the pressure differential we expect the foam to become stronger in the high quality regime.

6. Evaluate the foam flow into fractures using the EDFM and the population balance (LE) assuming the coalescence term as a function of the critical

capillary pressure. Experimental data should be used to validate and guide the evaluation.

7. Model the adsorption of trapped surfactant and evaluate the impact of the adsorption of the trapped surfactant on trapped foam stability.

8. Investigate the effect of adsorption and dispersivity on nanoparticle transport and foam stability using foam models such as the population balance (LE) and P_c^*. Experimental data should be used to validate and guide the evaluation.

9. Implement the permeability reduction due to nanoparticles filtration and evaluate its effect on foam stability using the population balance (LE) and P_c^* foam models.

10. Extend the implementation of the EDFM to model dispersivity into fracture blocks.

11. Evaluate and model nanoparticle transport in fractures assuming adsorption and dispersivity in fracture walls.

Appendices

Appendix A

Compositional Modeling

PVT data from a real field located in Brazil were used to model the Equation of State (EOS) and to simulate gas (CO_2 and methane) injection processes. The Peng-Robinson (PR) EOS was used to model the volumetric behavior, while for the viscosity the Lorentz-Bray-Clark (LBC) correlation was used. To lump the pseudo components and characterize the plus fraction, the procedure described in Pedersen *et al.* (2012) was used. The plus fraction characterization consists of determining the mole fraction and density distributions of components with carbon number greater than the plus fraction by the use of correlations. Pseudo-components are lumped with approximately equal weight fraction. Mixing rules are used to calculate the properties of pseudo-components. The mole fraction distribution is determined by the A and B coefficients in Equation A.1a, which are calculated by an analytical method proposed by Khan *et al.* (1992). Equation A.1b was used to calculate the molecular weight (M_w) of each component. The relation between density and the carbon number is given by Equation A.1c.

$$lnz_i = A + BC_{ni}, \tag{A.1a}$$

$$M_{wi} = 14C_{ni} - 4, \tag{A.1b}$$

$$\rho_i = C + DlnC_{ni}, \tag{A.1c}$$

where z_i is the global mole fraction of the component i, M_{wi} is the molecular weight of component i, ρ_i is the density of component i, and C_{ni} is the number of carbon atoms of each component i. A, B, C, and D are coefficients determined by the analytical

procedure developed by Khan *et al.* (1992).

Critical properties were calculated using the Pedersen *et al.* (1988) correlations for the PR EOS, which are shown in Equation A.2. The coefficients to be used in that equation are presented in Table A.1.

$$T_{ci} = c_1\rho_i + c_2 ln M_{wi} + c_3 M_{wi} + \frac{c_4}{M_{wi}}, \tag{A.2a}$$

$$lnP_{ci} = d_1 + d_2\rho_i^{d_5} + \frac{d_3}{M_{wi}} + \frac{d_4}{M_{wi}^2}, \tag{A.2b}$$

$$m = e_1 + e_2 M_{wi} + e_3\rho_i + e_4 M_{wi}^2, \tag{A.2c}$$

where T_{ci} is the critical temperature of component i and P_{ci} is the critical pressure of component i. For the PR EOS, m is related to the accentric factor (Ω) as $m = 0.37464 + 1.54226\Omega - 0.26992\Omega^2$. Critical volumes ($V_c$) can be calculated using Riazi and Daubert (1980) correlation (Equation A.3), or Pitzer correlation (Equation A.4).

$$T_{boil,i} = -265.6055 + 1056.0353 * log(C_{ni}), \tag{A.3a}$$

$$V_{ci} = 7.5214 \times 10^{-3} T_{boil,i}^{0.2896} \rho_i^{-0.7666} M_{wi}, \tag{A.3b}$$

where $T_{boil,i}$ is the boiling temperature of component i.

$$Z_{ci} = 0.2091 - 0.0879\Omega, \tag{A.4a}$$

$$V_{ci} = \frac{Z_{ci} T_{ci} R}{P_{ci}}, \tag{A.4b}$$

where Z_{ci} is the critical compressibility factor of component i and R is the universal gas constant.

The parachor of component i (ψ_i) for C_1 to C_6 may be calculated as function of carbon number as $\psi_i = 40C_{ni} + 31$, assuming all component are normal alkanes. Since reservoir fluids are not normal alkanes, for carbon numbers higher than 6, Khan *et al.* (1992) developed a correlation assuming a linear relationship between parachor

and log C_n (Equation A.5), which fits the data from Firoozabadi (1988),

$$\psi_i = -797.68 + 1179.17 log C_{ni}. \tag{A.5}$$

Binary interaction coefficients (δ) were calculated by using a correlation developed for a low-temperature West Texas oil, which is a function of the carbon number and temperature (Equation A.6). Different values for δ may be needed for different areas; Equation A.6 is used in this application since there is no correlation available for this field.

$$\delta_{CO_2-i} = 2.0919 e^{-0.03465 T_{res}},\ i < 7,\ 83 \leq T_{res} \leq 110^o F, \tag{A.6a}$$

$$\delta_{CO_2-i} = 0.095, \tag{A.6b}$$

where T_{res} is the reservoir temperature.

Volume shift of component i (V_{si}) parameters are available in literature for CO_2 and C_1 to C_6. For the C_{7+} fraction, Khan *et al.* (1992) proposed a correlation presented in Equation A.7,

$$V_{si} = -0.3773 + 0.4359 log(C_{ni}). \tag{A.7}$$

The mixing rules used in pseudo-components grouping were proposed by Pedersen *et al.* (1985). In Equation A.8, $X = P_c,\ T_c,\ \Omega,\ V_c,\ V_s$, and ψ, i is the pseudo-component index and j is the component index within a pseudo-component. Equation A.9 shows the mixing rule for the molecular weight.

$$X_i = \frac{\sum_j z_j MW_j X_j}{\sum_j z_j MW_j}, \tag{A.8}$$

$$MW_i = \frac{\sum_j z_j MW_j}{\sum_j z_j}. \tag{A.9}$$

A commercial thermodynamic software was used to match the PR EOS results with experimental data. Table A.2 shows the pseudo-components used and the initial reservoir fluid composition (molar fraction). Figure A.1 shows the comparison of the experimental data to the tuned EOS, where a good agreement may be observed not only for the volumetric properties, but also for the viscosity correlation. Miscibility pressures for the initial fluid composition and the injected solvent (50% CO_2 and 50% CH4) were calculated using the Cell to Cell method. Results have shown that the multiple contact miscibility pressure is expected to be at 8,498 psi, while the first contact miscibility pressure is expected to be at 10,937 psi. The reservoir is expected to be at multiple contact miscibility for the whole simulation run time.

Table A.1: Coefficients for critical properties correlations from Pedersen et al. (2012)

Subindex	**1**	**2**	**3**	**4**	**5**
c	7.340×10	9.735×10	6.187×10^{-1}	-2.059×10^{3}	-
d	7.284×10^{-2}	2.188	1.639×10^{2}	-4.043×10^{3}	1/4
e	3.737×10^{-1}	5.492×10^{-3}	1.179×10^{-2}	-4.930×10^{-6}	-

Table A.2: Compositional fluid: pseudo-components and molar fraction

Pseudo-component	Molar Fraction
CO_2	0.13
$C1 - C3$	0.59
$C4 - C6$	0.05
$C7 - C19$	0.14
$C20 - C37$	0.06
$C37 - C80$	0.03

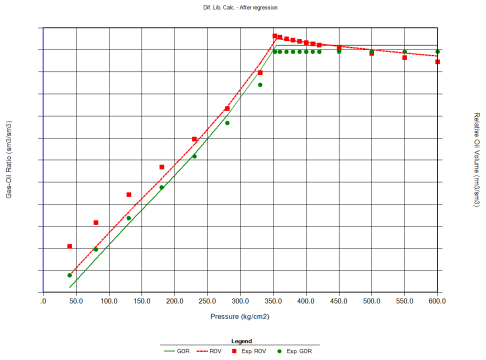

(a) Bo and GOR

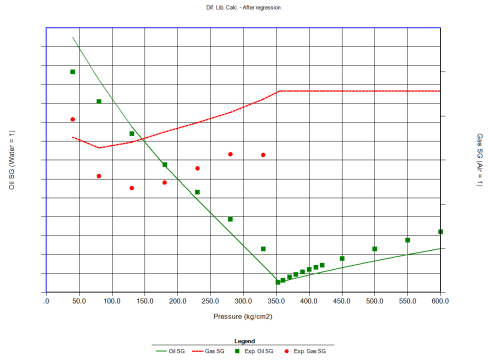

(b) Oil and gas specific gravity

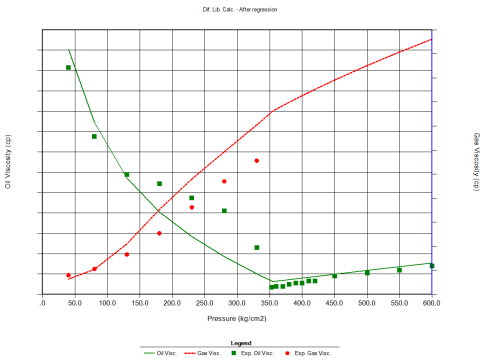

(c) Oil and gas viscosity

Figure A.1: PVT tuning using PR EoS and LBC viscosity correlation.

Appendix B

Dual Porosity Well Test Results in Fine Models

In this section we show that dual porosity derivative pattern may be obtained from single porosity fine models of fractured media. We simulated a drawdown test (9 days of duration) using a single porosity fine model of a fractured media with 800 fractures using a commercial compositional simulator. Wells were completed in the fracture, once the dual porosity model assumes flow from matrix to fracture, and fractures to well. Reservoir properties used are: reservoir dimension is 500 x 500 x 80 ft, number of blocks is 250 x 250 x 1, matrix porosity is 0.3, matrix permeability is 2 md, and fracture to matrix permeability ratio is 100.. Figure B.1a shows permeability map of the NFR and Figure B.1b shows the derivative of the results of the simulated drawdown test calculated by first and higher order methods. The dual porosity derivative obtained from the simulated well test is observed in Figure B.1b.

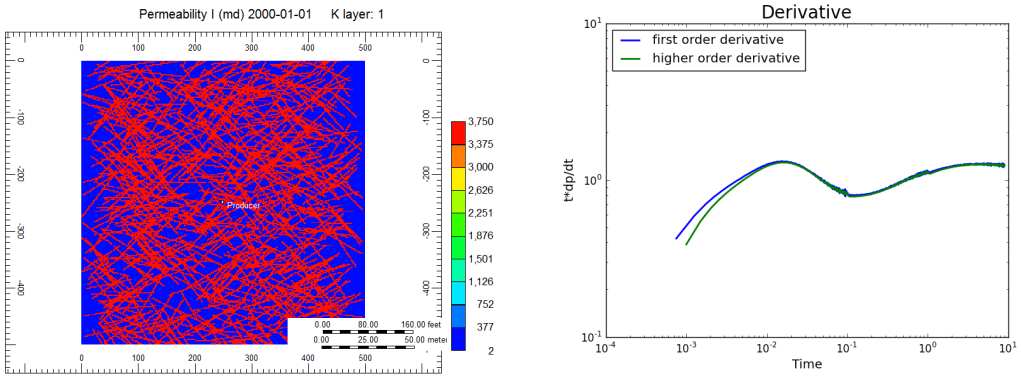

(a) Permeability Map for NFR **(b) Well Test - Dual Porosity**

Figure B.1: Dual porosity well test signature in a naturally fractured reservoir with 800 fractures represented with a single porosity fine model.

Appendix C

Evaluation of Solver Preconditioners for EDFM Simulations

In this section we describe two solvers implemented in a commercial simulation. The reference used for this description is ECLIPSE (2014).

C.1 Nested Factorization Preconditioning

Some commercial simulators use the Nested Factorization preconditioner to accelerate simulation runs. ECLIPSE (2014) describes this preconditioner as the fastest iterative technique and mentions that off banded terms created by non-neighboring connections (used in faults and local grid refinement, for example) are efficiently handled. Typically, the direction of greater transmissibility is chosen during the preconditioning stage, but off band elements destroy the simple structure of bands. The generalization of the definition of the bands usually solves that issue. In few words, the Nested Factorization preconditioner solves the pressure equation for each plane until y is known for each plane. At the end of the procedure the equations are solved as block tri-diagonal equations.

C.2 Constrained Pressure Residual (CPR)

The CPR preconditioner is used by the CPR solver to work with the linear equations involved in reservoir simulation, which are of mixed character (pressure equations are often elliptic while saturation equations are often hyperbolic). The preconditioner rearranges the equations handling firts pressure equation terms and

subsequently saturation equation terms. After the preconditioning, the Jacobian matrix is composed by the following terms: pressure terms (A_{pp}), saturation terms (A_{ss}), and pressure-saturation coupling terms (A_{ps} and A_{sp}). Equation C.1 shows the matrix after the preconditioning with each term. Note that both the solution (x) and residual (R) vectors are also decomposed.

$$\begin{bmatrix} A_{pp} & A_{ps} \\ A_{sp} & A_{ss} \end{bmatrix} \begin{bmatrix} x_p \\ x_s \end{bmatrix} = \begin{bmatrix} R_p \\ R_s \end{bmatrix} \tag{C.1}$$

In the first stage of the preconditioner the system is restricted to the pressure system. The reduced pressure system is solved (using GMRES solver, for example) to a given accuracy. As the solution of the pressure is obtained it is expanded to the full system and a correction to the original residual is applied. In a second stage, to find a another correction to the solution of the pressure system a nested factorization is applied to the remaining residual. Combination of the first and second stages provide a CPR preconditioned vector.

The two stage CPR is more expensive than hte single stage nested factorization preconditioner, but convergence with the CPR usually needs less iterations. The CPR preconditioner is suitable to fully implicit simulations or when the default linear solver fails to converge.

C.3 Comments on the Applications of Both Solver in EDFM Problems

For cases with orthogonal fractures both solvers are capable to solve the imposed problem in reasonable simulation run times. The CPR presents a slightly better performance. For cases with slanted fractures (fractures are not aligned to the main axis of the grid), the Nested Factorization preconditioner took days to solve the problem, while the CPR was able to run in a matter of minutes.

Since the EDFM involves high transmissibility fracture blocks added to the

solution matrix as off band terms, we conclude that the use of the CPR preconditioner (and CPR solver) has a better performance due to its efficient rearraging of the equation in the solution matrix.

Appendix D

EDFM Preprocessor

D.1 Structure of the EDFM Preprocessor

The EDFM preprocessor uses an input file to perform its runs. The structure is the following:

1. All input files must be located in a folder called *preprocessor_input*, located in the same folder as the EDFM preprocessor executable file
2. The EDFM preprocessor must be called and the results will be printed in a folder located in the same level as the executable file

D.2 Reference Manual for the EDFM Preprocessor

- FOLDER/folder: folder at which the EDFM preprocessor will save the results
- GRID/grid: type of Cartesian grid, regular or irregular.
- GRIDORIGIN/gridorigin: coordinated of the origin of the grid.
- NX/nx: number of blocks in x direction for the matrix.
- NY/ny: number of blocks in y direction for the matrix.
- NZ/nz: number of blocks in z direction for the matrix.
- LX/lx: length of the matrix grid (x direction).
- LY/ly: length of the matrix grid (y direction).

- LZ/lz: length of the matrix grid (z direction).
- TOP/top: depth of the top. If CON/con, define a constant depth. If VAR/var, define an array with depth of all blocks in the matrix grid
- NWELL/nwell: number of wells
- WELLRADIUS/wellradius: well radius
- WCOORD/wcoord: coordinates of the well, defined as a line. Two points (X1,Y1,Z1) and (X2,Y2,Z2) must be given in the following manner: X1 Y1 Z1 X2 Y2 Z2
- FILEHF/filehf: name of the file containing the fracture information
- FRACPORCUTOFF/fracporcutoff: value of porosity cut-off to be applied in fracture blocks
- MATRIXPERM/matrixperm: permeability of the matrix assuming Kx=Ky
- MATRIXPERMZ_MULTIPLIER/matrixpermz_multiplier: multiplier to be applied for the permeability in the z direction.
- MATRIXPOR/matrixpor: porosity of the matrix.
- DUALCONTINUUM/dualcontinuum: 1 to activate the integrated EDFM calculations, 0 to deactivate.
- FILENF/filenf: name of the file containing fracture information for the integrated EDFM.
- ODAHTENSOR/odahtensor: 1 to print full permeability tensor, 0 to deactivate. The average permeability of the fracture network is calculated using the Oda's method even when this functionality is deactivated.

- EQSHAPEFACTOR/eqshapefactor: 1 to activate the calculation of equivalent shape factor for conventional dual porosity dual permeability formulations, 0 to deactivate.
- TESTCONN/testconn: 1 to activate the connectivity test to ensure transmissibilities are properly defined, 0 to deactivate. Useful for UTCOMP/UTCHEM only.

D.3 Input File

```
folder case3_planargeomheterosame (string)

grid 2
>1 for regular
>2 for irregular (must provide array with dz,dy,dz)
>3 for cornerpoint
gridorigin 0. 0. 0. (origin of the grid)

nx 31 (int)
ny 33 (int)
nz 10 (int)

lx 1000 (int)
ly 3000 (int)
lz 100 (int)
>only used for regular grids

top con 0.
```

```
dx var (var)
100 100 100 60 40 10 10 10 10 10 10 10 10 10 8 4 8 10 10 10 10 10 10
10 10 10 40 60 100 100 100
/

dy var (var)
200 200 100 100 100 95 80 60 40 20 10 40 100 210 100 40 10 40 100 210
100 40 10 20 40 60 80 95 100 100 100 200 200
/

dz var (var)
10 10 10 10 10 10 10 10 10 10
/

>>>>>
>>well
>>>>>
nwell 1 (int)
wellradius con 0.1 (float) >for now only constant
wcoord (x1 y1 z1 x2 y2 z2) >one line for each well
500 1000 50 500 2011 50

>>>>>>>>>>>>>
>>hydraulic fracture
>>>>>>>>>>>>>
filehf <Fracture input file> (string)
>extension .fab or .ut
```

```
fracporcutoff 1e-4

matrixperm con .1 (con or array)

matrixpermz_mutiplier .1

matrixpor con 0.15 (con or array)

heterofracinput 1 (0 to not use input file, 1 to use it)
heterogeneous_fracture_properties.txt (Map of Prop. for Fracture)

>>>>>>>>>>>>
>>natural fracture
>>>>>>>>>>>>
dualcontinuum 0 (int)
>0 for deactivate
>1 for activate

filenf <Fracture input file> (string)
>extension .fab or .ut

odahtensor 0 (int)
>0 for deactivate
>1 for activate

eqshapefactor 0 (int)
>0 for deactivate
>1 for activate (only id dualcontinuum = 1)
```

```
testconn 0 (int)
>0 for deactivate
>1 for activate (only id dualcontinuum = 1)
```

D.4 Fracture input (UT format)

```
nfrac 3
uf1
400 1000 0
400 1500 0
400 2000 0
uf2
600 1000 100
600 1500 100
600 2000 100
dip
90
90
90
perm
1000
1000
1000
aperture
0.01
0.01
0.01
```

D.5 Map of Properties of an Heterogeneous Fracture

```
frac 1 (header with the number of the fracture)
0.03 0.95 -999 -999 (x_local y_local aperture permeability)
0.08 0.95 -999 -999
0.13 0.95 -999 -999
0.18 0.95 -999 -999
0.23 0.95 -999 -999
0.28 0.95 -999 -999
0.33 0.95 -999 -999
0.38 0.95 -999 -999
0.43 0.95 0.1 377.8
0.47 0.95 0.1 389.8
0.5 0.95 0.1 392.5
0.53 0.95 0.1 389.8
0.58 0.95 0.1 373.3
0.63 0.95 -999 -999
0.68 0.95 -999 -999
0.73 0.95 -999 -999
0.78 0.95 -999 -999
0.83 0.95 -999 -999
0.88 0.95 -999 -999
0.93 0.95 -999 -999
0.98 0.95 -999 -999
.
.
.
```

Bibliography

Abbasi Asl, Y., Pope, G., and Delshad, M. (2010). Mechanistic modeling of chemical transport in naturally fractured oil reservoirs. In *SPE Improved Oil Recovery Symposium*, Tulsa, Oklahoma, USA. Society of Petroleum Engineers.

Afonja, G., Hughes, R., Nagineni, V. G., and Jin, L. (2012). Simulation study for optimizing injected surfactant volume in a miscible carbon dioxide flood. In *SPETT 2012 Energy Conference and Exhibition*, Port-of-Spain, Trinidad. Society of Petroleum Engineers. SPE 158220-MS. http://dx.doi.org/10.2118/158220-MS.

Aguilera, R. (1995). *Naturally Fractured Reservoirs*. PennWell Publishing Company.

Allan, J. and Sun, S. Q. (2003). Controls on recovery factor in fractured reservoirs: Lessons learned from 100 fractured fields. In *SPE Annual Technical Conference and Exhibition*, Denver, Colorado, USA. Society of Petroleum Engineers.

Alvarez, J., Rivas, H., and Rossen, W. (2001). Unified model for steady-state foam behavior at high and low foam qualities. *SPE journal*, 6(03):325–333. SPE-74141-PA. http://dx.doi.org/10.2118/74141-PA.

Ameri Ghasrodashti, A., Farajzadeh, R., Suicmez, V., and Bruining, J. (2012). Experimental and numerical investigation on the performance of gas oil gravity drainage at different miscibility conditions. In *SPE Improved Oil Recovery Symposium*, Tulsa, Oklahoma, USA. Society of Petroleum Engineers.

Apaydin, O. and Kovscek, A. (2000). Transient foam flow in homogeneous porous media: Surfactant concentration and capillary end effects. In *SPE/DOE Improved Oil Recovery Symposium*, Tulsa, Oklahoma, USA. Society of Petroleum Engineers.

Aronson, A., Bergeron, V., Fagan, M., and Radke, C. (1994). The influence of disjoining pressure on foam stability and flow in porous media. *Colloids and Surfaces A: Physicochemical and Engineering Aspects*, 83(2):109–120. http://dx.doi.org/10.1016/0927-7757(94)80094-4.

Ashoori, E. and Rossen, W. (2010). Can formation relative permeabilities rule out a foam EOR process? In *SPE Annual Technical Conference and Exhibition*, Florence, Italy. Society of Petroleum Engineers.

Ashoori, E. and Rossen, W. (2012). Can formation relative permeabilities rule out a foam EOR process? *SPE Journal*, 17(2).

Babadagli, T. (2001). Selection of proper EOR method for efficient matrix recovery in naturally fractured reservoirs. In *SPE Latin American and Caribbean Petroleum Engineering Conference*, Buenos Aires, Argentina. Society of Petroleum Engineers.

Balan, H. O., Balhoff, M. T., and Nguyen, Q. P. (2012). Modeling of foamed gas mobility in permeable porous media. In *SPE Improved Oil Recovery Symposium*. Society of Petroleum Engineers. http://dx.doi.org/10.2118/154233-MS.

Bertin, H. (2000). Foam diversion modeling using a bubble-population correlation. In *SPE/DOE Improved Oil Recovery Symposium*.

Bertin, H., Apaydin, O., Castanier, L., and Kovscek, A. (1999). Foam flow in heterogeneous porous media: Effect of cross flow. *SPE Journal*, 4(2):75–82.

Bertin, H., Quintard, M., and Castanier, L. (1998a). Development of a bubble-population correlation for foam-flow modeling in porous media. *SPE Journal*, 3(4).

Bertin, H., Quintard, M., and Castanier, L. (1998b). Modeling transient foam flow in porous media using a bubble population correlation. In *SPE Annual Technical*

Conference and Exhibition, New Orleans, Louisiana, USA. Society of Petroleum Engineers.

Blaskovich, F., Cain, G., Sonier, F., Waldren, D., and Webb, S. (1983). A multicomponent isothermal system for efficient reservoir simulation. In *Middle East Oil Technical Conference and Exhibition*.

Boeije, C. and Rossen, W. (2013a). Fitting foam simulation model parameters to data. In *IOR 2013-17th European Symposium on Improved Oil Recovery*.

Boeije, C. and Rossen, W. (2013b). Fitting foam simulation model parameters to data. In *IOR 2013-17th European Symposium on Improved Oil Recovery*.

Carvajal, A., Ivan, E., Caline, Y., Rylance, M., Rice, J. K., Waters, J., and Wells, S. (2015). Open-hole completion based mechanical diversion of acid/chemical stimulation operations: Design, deployment and field trial results. In *SPE Hydraulic Fracturing Technology Conference*. Society of Petroleum Engineers. http://dx.doi.org/10.2118/173355-MS.

Chang, Y. (1990). *Development of a three-dimensional, equation-of-state compositional reservoir simulator for miscible gas flooding*. PhD dissertation, Ph. D. Dissertation, The University of Texas at Austin.

Chen, Q. (2009). *Assessing and improving steam-assisted gravity drainage: Reservoir heterogeneities, hydraulic fractures, and mobility control foams*. PhD dissertation, Ph. D. Dissertation, Stanford University.

Chen, Q., Gerritsen, M., and Kovscek (2010). Modeling foam displacement with the local-equilibrium approximation: Theory and experimental verification. *SPE Journal*, 15(1).

Cheng, L., Reme, A., Shan, D., and Coombe, D. (2000). Simulating foam processes at high and low foam qualities. In *SPE/DOE Improved Oil Recovery Symposium*, Tulsa, Oklahoma, USA. Society of Petroleum Engineers.

Dahi-Taleghani, A. and Olson, J. E. (2011). Numerical modeling of multistranded-hydraulic-fracture propagation: Accounting for the interaction between induced and natural fractures. *SPE J*, 16(3):575–581. SPE-124884-PA. http://dx.doi.org/10.2118/124884-PA.

Dean, R. and Lo, L. (1986). Development of a naturally fractured reservoir simulator and examples of its use, spe 14110. In *International Meeting on Petroleum Engineering, Beijing, China, March*, pages 17–20.

Delshad, M., Kazuhiro, A., Pope, G., and Sepehrnoori, K. (2002). Simulations of chemical and microbial enhanced oil recovery methods. In *SPE/DOE Improved Oil Recovery Symposium*, Tulsa, Oklahoma, USA. Society of Petroleum Engineers.

Ding, Z., Liu, Y., Gong, Y., and Xu, N. (2012). A new technique: Fishbone well injection. *Petroleum Science and Technology*, 30(23):2488–2493. http://dx.doi.org/10.1080/10916466.2010.518196.

Drexler, K. E., Peterson, C., and Pergamit, G. (1991). Unbounding the future. *William Morrow, New York*, page 294.

ECLIPSE (2014). *Eclipse reservoir simulation software - Tehcnical Description*. Schlumberger, version 2014.2 edition.

Edwards, D. A., Cheng, N., Dombrowsky, T. P., Bowen, G., and Nasvik, H. (2013). Representing hydraulic fractures using a multilateral, multisegment well in simulation models. In *SPE Reservoir Simulation Symposium*, The Woodlands, Texas, USA. Society of Petroleum Engineers. http://dx.doi.org/10.2118/163644-MS.

Emadi, A., Sohrabi, M., Jamiolahmady, M., Irland, S., and Robertson, G. (2011). Mechanistic study of improved heavy oil recovery by CO_2-foam injection. In *SPE Enhanced Oil Recovery Conference*.

Espinoza, D. A., Caldelas, F. M., Johnston, K. P., Bryant, S. L., Huh, C., *et al.* (2010). Nanoparticle-stabilized supercritical co2 foams for potential mobility control applications. In *SPE Improved Oil Recovery Symposium*. Society of Petroleum Engineers. SPE-129925-MS. http://dx.doi.org/10.2118/129925-MS.

Falls, A., Hirasaki, G., Patzek, T., Gauglitz, D., Miller, D., and Ratulowski, T. (1988). Development of a mechanistic foam simulator: The population balance and generation by snap-off. *SPE Reservoir Engineering*, 3(3).

Farajzadeh, R., Wassing, B., and Boerrigter, P. (2012). Foam assisted gas oil gravity drainage in naturally-fractured reservoirs. *Journal of Petroleum Science and Engineering*.

Farajzadeh, R., Wassing, L. B., and Boerrigter, P. (2010). Foam assisted gas oil gravity drainage in naturally-fractured reservoirs. In *SPE Annual Technical Conference and Exhibition*, Florence, Italy. Society of Petroleum Engineers.

Firoozabadi, A. (1988). Reservoir-fluid phase behavior and volumetric prediction with equations of state (includes associated papers 18400 and 18579). *Journal of Petroleum Pechnology*, 40(04):397–406. SPE-17653-PA. http://dx.doi.org/10.2118/17653-PA.

Freyer, R. and Shaoul, J. R. (2011). Laterals stimulation method. In *Brasil Offshore Conference and Exhibition*, Macae, Brazil. Society of Petroleum Engineers. SPE-143381-MS. http://dx.doi.org/10.2118/143381-MS.

Friedmann, F. and Jensen, J. (1986). Some parameters influencing the formation and propagation of foams in porous media. In *SPE California Regional Meeting*, Oakland, California, USA. Society of Petroleum Engineers.

Fung, L.-K., Hiebert, A. D., Nghiem, L. X., and others (1992). Reservoir simulation with a control-volume finite-element method. *SPE Reservoir Engineering*, 7(03):349–357. http://dx.doi.org/10.2118/21224-PA.

Gilman, J. and Kazemi, H. (1983). Improvements in simulation of naturally fractured reservoirs. *Old SPE Journal*, 23(4):695–707.

Hajibeygi, H., Karvounis, D., and Jenny, P. (2011). A hierarchical fracture model for the iterative multiscale finite volume method. *Journal of Computational Physics*, 230(24):8729–8743. http://dx.doi.org/10.1016/j.jcp.2014.08.019.

Haugen, s., FernÃ¸, M., Graue, A., and Bertin, H. (2012). Experimental study of foam flow in fractured oil-wet limestone for enhanced oil recovery. *SPE Reservoir Evaluation & Engineering*, 15(2).

Helton, J. C., Johnson, J. D., Sallaberry, C. J., and Storlie, C. B. (2006). Survey of sampling-based methods for uncertainty and sensitivity analysis. *Reliability Engineering & System Safety*, 91(10):1175–1209. http://dx.doi.org/10.1016/j.ress.2005.11.017.

Hill, A. and Thomas, G. (1985). A new approach for simulating complex fractured reservoirs. In *Middle East Oil Technical Conference and Exhibition*.

Hou, Q., Zhu, Y., Luo, Y., and Weng, R. (2012). Studies on foam flooding eor technique for daqing reservoirs after polymer flooding. In *SPE Improved Oil Recovery Symposium*.

Hui, M.-H., Mallison, B., Fyrozjaee, M., and Narr, W. (2013). The upscaling of discrete fracture models for faster, coarse-scale simulations of ior and eor processes for fractured reservoirs. In *SPE Annual Technical Conference and Exhibition*.

Jiang, J., Shao, Y., and Younis, R. M. (2014). Development of a multi-continuum multi-component model for enhanced gas recovery and CO_2 storage in fractured

shale gas reservoirs. In *SPE Improved Oil Recovery Symposium*, Tulsa, Oklahoma, USA. Society of Petroleum Engineers. SPE-169114-MS. http://dx.doi.org/10.2118/169114-MS.

Jiang, J., Younis, R., *et al.* (2015). Hybrid coupled discrete-fracture/matrix and multicontinuum models for unconventional-reservoir simulation. *SPE Journal*. SPE-178430-PA. http://dx.doi.org/10.2118/178430-PA.

Jikich, S. J. *et al.* (2012). Co2 eor: Nanotechnology for mobility control studied. *Journal of Petroleum Technology*, 64(07):28–31. SPE-1106-0024-JPT. http://dx.doi.org/10.2118/0712-0028-JPT.

Jimenez-Laguna, A. (1991). *Stability of thin liquid films: Theory and application to foam flow in porous media*. PhD dissertation, University of California. Copyright - Copyright UMI - Dissertations Publishing 1991; Last updated - 2014-05-14; First page - n/a.

Kam, S., Nguyen, Q., Li, Q., and Rossen, W. (2007). Dynamic simulations with an improved model for foam generation. *SPE Journal*, 12(1).

Kam, S. and Rossen, W. (2003). A model for foam generation in homogeneous media. *SPE Journal*, 8(4).

Karimi-Fard, M. and Firoozabadi, A. (2003). Numerical simulation of water injection in fractured media using the discrete-fracture model and the galerkin method. *SPE Reservoir Evaluation & Engineering*, 6(2). SPE-83633-PA. http://dx.doi.org/10.2118/83633-PA.

Kazemi, H., Gilman, J., and Elsharkawy, A. (1992). Analytical and numerical solution of oil recovery from fractured reservoirs with empirical transfer functions (includes associated papers 25528 and 25818). *SPE Reservoir Engineering*, 7(02):219–227. http://dx.doi.org/10.2118/19849-PA.

Kazemi, H., L.S., M., Porterfield, K., and Zeman, P. (1976). Numerical simulation of water-oil flow in naturally fractured reservoirs. *Society of Petroleum Engineers Journal*, 16(6).

Khalil, F. and Asghari, K. (2006). Application of CO_2-foam as a means of reducing carbon dioxide mobility. *Journal of Canadian Petroleum Technology*, 45(5).

Khan, S., Pope, G., and Sepehrnoori, K. (1992). Fluid characterization of three-phase CO_2/oil mixtures. In *SPE/DOE Enhanced Oil Recovery Symposium*, Tulsa, Oklahoma, USA. Society of Petroleum Engineers. SPE-24130-MS. http://dx.doi.org/10.2118/24130-MS.

Kharrat, R., Mahdavi, S., and Ghorbani, D. (2012). A comprehensive EOR study of a highly fractured matured field- case study. In *SPE Europec/EAGE Annual Conference*, Copenhagen, Denmark. Society of Petroleum Engineers.

Khatib, Z., Hirasaki, G., and Falls, A. (1988). Effects of capillary pressure on coalescence and phase mobilities in foams flowing through porous media. *SPE Reservoir Engineering*, 3(3).

Kiani, M., Kazemi, H., Ozkan, E., and Wu, Y.-S. (2011). Pilot testing issues of chemical EOR in large fractured carbonate reservoirs. In *SPE Annual Technical Conference and Exhibition*, Denver, Colorado, USA. Society of Petroleum Engineers.

Kovscek, A., Patzek, T., and Radke, C. (1993). Simulation of foam transport in porous media. In *SPE Annual Technical Conference and Exhibition*, Houston, Texas, USA. Society of Petroleum Engineers.

Kovscek, A., Patzek, T., and Radke, C. (1994). Mechanistic prediction of foam displacement in multidimensions: A population balance approach. In *SPE/DOE Improved Oil Recovery Symposium*, Tulsa, Oklahoma, USA. Society of Petroleum Engineers.

Kovscek, A., Patzek, T., and Radke, C. (1995). A mechanistic population balance model for transient and steady-state foam flow in boise sandstone. *Chemical Engineering Science*, 50(23):3783–3799.

Kovscek, A. and Radke, C. (1994). Fundamentals of foam transport in porous media. In *Foams: Fundamentals and Applications in the Petroleum Industry*, volume 242 of *Advances in Chemistry*, pages 115–163. American Chemical Society.

Kovscek, A., Tadeusz, W., and Radke, C. (1997). Mechanistic foam flow simulation in heterogeneous and multidimensional porous media. *SPE Journal*, 2(4).

Krishnamoorti, R. *et al.* (2006). Extracting the benefits of nanotechnology for the oil industry. *Journal of petroleum technology*, 58(11):24–26. SPE-1106-0024-JPT. http://dx.doi.org/10.2118/1106-0024-JPT.

Lee, S. H., Jensen, C. L., and Lough, M. F. (2000). Efficient finite-difference model for flow in a reservoir with multiple length-scale fractures. *SPE Journal*, 5(03):268–275. SPE-65095-PA. http://dx.doi.org/10.2118/65095-PA.

Lee, S. H., Lough, M. F., and Jensen, C. L. (2001). Hierarchical modeling of flow in naturally fractured formations with multiple length scales. *Water Resources Research*, 37(3):443–455. http://dx.doi.org/10.1029/2000WR900340.

Li, L. and Lee, S. (2006). Efficient field-scale simulation for black oil in a naturally fractured reservoir via discrete fracture networks and homogenized media. In *International Oil and Gas Conference and Exhibition*, Beijing, China. Society of Petroleum Engineers.

Li, L. and Lee, S. (2008). Efficient field-scale simulation of black oil in a naturally fractured reservoir through discrete fracture networks and homogenized media. *SPE Reservoir Evaluation & Engineering*, 11(4). SPE-103901-PA. http://dx.doi.org/10.2118/103901-PA.

Lim, K. and Aziz, K. (1995). Matrix-fracture transfer shape factors for dual-porosity simulators. *Journal of Petroleum Science and Engineering*, 13(3):169–178. http://dx.doi.org/10.1016/0920-4105(95)00010-F.

Ma, K., Lopez-Salinas, J. L., Puerto, M. C., Miller, C. A., Biswal, S. L., and Hirasaki, G. J. (2013). Estimation of parameters for the simulation of foam flow through porous media. part 1: the dry-out effect. *Energy & Fuels*, 27(5):2363–2375. http://dx.doi.org/10.1021/ef302036s.

Ma, K., Ren, G., Mateen, K., Morel, D., and Cordelier, P. (2015). Modeling techniques for foam flow in porous media. *SPE Journal*, 20(3). SPE 169104-PA. http://dx.doi.org/10.2118/169104-PA.

Maricic, N., Mohaghegh, S. D., and Artun, E. (2008). A parametric study on the benefits of drilling horizontal and multilateral wells in coalbed methane reservoirs. *Reservoir Evaluation and Engineering*, 11(06):976–983. SPE-96018-PA. http://dx.doi.org/10.2118/96018-PA.

Moinfar, A. (2013). *Development of an efficient embedded discrete fracture model for 3D compositional reservoir simulation in fractured reservoirs.* PhD dissertation, The University of Texas, Austin, Texas, USA. http://pge.utexas.edu/images/pdfs/theses13/moinfa.pdf.

Moinfar, A., Narr, W., Hui, M.-H., Mallison, B., and Lee, S. H. (2011). Comparison of discrete-fracture and dual-permeability models for multiphase flow in naturally fractured reservoirs. In *SPE Reservoir Simulation Symposium*, The Woodlands, Texas, USA. Society of Petroleum Engineers. SPE-142295-MS http://dx.doi.org/10.2118/142295-MS.

Moinfar, A., Varavei, A., Sepehrnoori, K., and Johns, R. (2012). Development of a novel and computationally-efficient discrete-fracture model to study IOR

processes in naturally fractured reservoirs. In *SPE Improved Oil Recovery Symposium*, Tulsa, Oklahoma, USA. Society of Petroleum Engineers. SPE-154246-MS. http://dx.doi.org/10.2118/154246-MS.

Moinfar, A., Varavei, A., Sepehrnoori, K., and Johns, R. T. (2013). Development of a coupled dual continuum and discrete fracture model for the simulation of unconventional reservoirs. In *SPE Reservoir Simulation Symposium*, The Woodlands, TX, USA. Society of Petroleum Engineers. SPE-163647-MS. http://dx.doi.org/10.2118/163647-MS.

Mukherjee, J., Norris, S., Nguyen, Q., Scherlin, J., Vanderwal, P., and Abbas, S. (2014). Co2 foam pilot in salt creek field, natrona county, wy: Phase i: Laboratory work, reservoir simulation, and initial design. In *SPE Improved Oil Recovery Symposium*. Society of Petroleum Engineers. http://dx.doi.org/10.2118/169166-MS.

Murphy, M. J. (2012). *Experimental analysis of electrostatic and hydrodynamic forces affecting nanoparticle retention in porous media*. PhD dissertation, The University of Texas, Austin, Texas, USA. https://repositories.lib.utexas.edu/bitstream/handle/2152/ETD-UT-2012-05-5576/MURPHY-THESIS.pdf.

Narr, W., Schechter, D. S., and Thompson, L. B. (2006). *Naturally Fractured Reservoir Characterization*. Society of Petroleum Engineers.

Nelder, J. A. and Mead, R. (1965). A simplex method for function minimization. *The computer journal*, 7(4):308–313. SPE-169104-MS. http://dx.doi.org/10.1093/comjnl/7.4.308.

Norris, S. O., Scherlin, J. M., Mukherjee, J., Vanderwaal, P., Abbas, S., Nguyen, Q. P., *et al.* (2014). Co2 foam pilot in salt creek field, natrona county, wy: Phase

ii: Diagnostic testing and initial results. In *SPE Annual Technical Conference and Exhibition*. Society of Petroleum Engineers. http://dx.doi.org/10.2118/170729-MS.

Oda, M. (1985). Permeability tensor for discontinuous rock masses. *Geotechnique*, 35(4):483–495.

Olson, J. (2008). Multi-fracture propagation modeling: Applications to hydraulic fracturing in shales and tight gas sands. In *The 42nd US rock mechanics symposium (USRMS)*, volume 29. American Rock Mechanics Association. ARMA-08-327.

Osterloh, W. and Jante Jr, M. (1992). Effects of gas and liquid velocity on steady-state foam flow at high temperature. In *SPE/DOE Enhanced Oil Recovery Symposium*. Society of Petroleum Engineers. SPE 24179-MS. http://dx.doi.org/10.2118/24179-MS.

Panfili, P., Cominelli, A., and Scotti, A. (2013). Using embedded discrete fracture models (EDFMs) to simulate realistic fluid flow problems. In *Second Workshop on Naturally Fractured Reservoirs*. EAGE. http://dx.doi.org/10.3997/2214-4609.20132026.

Peaceman, D. W. (1983). Interpretation of well-block pressures in numerical reservoir simulation with nonsquare grid blocks and anisotropic permeability. *Society of Petroleum Engineers Journal*, 23(3):531–543. SPE-10528-PA. http://dx.doi.org/10.2118/10528-PA.

Pedersen, K., Thomassen, P., and Fredenslund, A. (1988). Characterization of gas condensate mixtures. Technical report, New York, NY; American Institute of Chemical Engineers.

Pedersen, K. S., Christensen, P. L., and Shaikh, J. A. (2012). *Phase behavior of petroleum reservoir fluids*. CRC Press.

Pedersen, K. S., Thomassen, P., and Fredenslund, A. (1985). Thermodynamics of petroleum mixtures containing heavy hydrocarbons. 3. efficient flash calculation procedures using the SRK equation of state. *Industrial & Engineering Chemistry Process Design and Development*, 24(4):948–954. http://dx.doi.org/10.1021/i200031a009.

Ponting, D. K. (1989). Corner point geometry in reservoir simulation. In *ECMOR I-1st European Conference on the Mathematics of Oil Recovery*.

Pruess, K. and Narasimhan, T. N. (1985). A practical method for modeling fluid and heat flow in fractured porous media. *Old SPE Journal*, 25(1):14–26.

Ransohoff, T., Radke, C., *et al.* (1988). Mechanisms of foam generation in glass-bead packs. *SPE reservoir engineering*, 3(02):573–585. http://dx.doi.org/10.2118/15441-PA.

Ren, G., Zhang, H., and Nguyen, Q. P. (2011). Effect of surfactant partitioning between co2 and water on co2 mobility control in hydrocarbon reservoirs. In *SPE Enhanced Oil Recovery Conference*. Society of Petroleum Engineers. http://dx.doi.org/10.2118/145102-MS.

Riazi, M. R. and Daubert, T. E. (1980). Prediction of the composition of petroleum fractions. *Industrial & Engineering Chemistry Process Design and Development*, 19(2):289–294. http://dx.doi.org/10.1021/i260074a016.

Rice, K., Jorgensen, T., and Waters, J. (2014). First installation of efficient and accurate multilaterals stimulation technology in carbonate oil application. In *SPE Eastern Regional Meeting*, Charleston, WV,USA. Society of Petroleum Engineers. SPE-171021-MS. http://dx.doi.org/10.2118/171021-MS.

Roof, J. (1970). Snap-off of oil droplets in water-wet pores. *Society of Petroleum Engineers Journal*, 10(1):85–90. SPE 2504-PA. http://dx.doi.org/10.2118/2504-PA.

Rossen, W., Zeilinger, S., Shi, J., and Lim, M. (1994). Mechanistic simulation of foam processes in porous media. In *SPE Annual Technical Conference and Exhibition*, New Orleans, Louisiana, USA. Society of Petroleum Engineers.

Rossen, W., Zeilinger, S., Shi, J., and Lim, M. (1999). Simplified mechanistic simulation of foam processes in porous media. *SPE Journal*, 4(3).

Rossen, W. and Zhou, Z. (1995). Modeling foam mobility at the limiting capillary pressure. *SPE adv. Technol*, 3(1):146–153. SPE-22627-PA. http://dx.doi.org.ezproxy.lib.utexas.edu/10.2118/22627-PA.

Saidi, A. (1983). Simulation of naturally fractured reservoirs. In *SPE Reservoir Simulation Symposium*.

Schlumberger Oilfield Glossary (2014). Fishbone wells. http://glossary.oilfield.slb.com/en/Terms/f/fishbone_wells.aspx (accessed 25 November 2014).

Schnerk, G. and Madeen, C. (1990). The austin chalk: Simulation of horizontal wells in a heterogeneous formation. In *SPE Annual Technical Conference and Exhibition*. Society of Petroleum Engineers. SPE-20716-MS. http://dx.doi.org/10.2118/20716-MS.

Schramm, L. L. and Wassmuth, F. (1994). Foams: Basic principles. In *Foams: Fundamentals and Applications in the Petroleum Industry*, volume 242 of *Advances in Chemistry*, pages 3–45. American Chemical Society.

Shakiba, M. (2014). Modeling and simulation of fluid flow in naturally and hydraulically fractured reservoirs using embedded discrete fracture model (EDFM). Msc thesis, The University of Texas at Austin, Austin, Texas, USA. http://pge.utexas.edu/images/pdfs/theses14/shakiba.pdf.

Siriwardane, H. and Layne, A. (1991). Improved model for predicting multiple hydraulic fracture propagation from a horizontal well. *SPE*, 23448:22–25. SPE-23448-MS. http://dx.doi.org/10.2118/23448-MS.

Skoreyko, F., Villavicencio, A., Rodriguez Prada, H., and Nguyen, Q. (2011). Development of a new foam EOR model from laboratory and field data of the naturally fractured cantarell field. In *SPE Reservoir Characterisation and Simulation Conference and Exhibition*, Abu Dhabi, UAE. Society of Petroleum Engineers.

Skoreyko, F., Villavicencio, A., Rodriguez Prada, H., and Nguyen, Q. (2012). Understanding foam flow with a new foam EOR model developed from laboratory and field data of the naturally fractured cantarell field. In *SPE Improved Oil Recovery Symposium*, Tulsa, Oklahoma, USA. Society of Petroleum Engineers.

Sobolev, K. and Gutiérrez, M. F. (2005). How nanotechnology can change the concrete world. *American Ceramic Society Bulletin*, 84(10):14.

Spirov, P., Rudyk, S., and Khan, A. (2012). Foam assisted WAG, snorre revisit with new foam screening model. In *North Africa Technical Conference and Exhibition*, Cairo, Egypt. Society of Petroleum Engineers.

Srivastava, M., Zhang, J., Nguyen, Q., and Pope, G. (2009). A systematic study of alkaline-surfactant-gas injection as an EOR technique. In *SPE Annual Technical Conference and Exhibition*, New Orleans, Louisiana, USA. Society of Petroleum Engineers.

STARS (2011). *STARS advanced Process and Thermal Reservoir Simulator*. Computer Modeling Group Ltd., version 2011 edition.

Sydansk, R. D. and Romero-Zeron, L. (2011). *Reservoir conformance improvement*. Society of Petroleum Engineers.

Taheri, A., Hoier, L., and Torsaeter, O. (2013). Miscible and immiscible gas injection for enhancing of condensate recovery in fractured gas condensate reservoirs. In *75th EAGE Conference and Exhibition incorporating SPE EUROPEC*, London, United Kingdom. SPE. SPE 164934-MS. http://dx.doi.org/10.2118/164934-MS.

Talebian, S. H., Masoudi, R., Mohamad Tan, I., and Zitha, P. L. J. (2013). Foam assisted CO_2-EOR; concepts, challenges and applications. In *SPE Enhanced Oil Recovery Conference*, Kuala Lumpur, Malaysia. Society of Petroleum Engineers.

Tang, G.-Q. and Kovscek, A. (2006). Trapped gas fraction during steady-state foam flow. *Transport in porous media*, 65(2):287–307. http://dx.doi.org/10.1007/s11242-005-6093-4.

Tarahhom, F. (2008). *Development of an implicit full-tensor dual porosity compositional reservoir simulator*. PhD dissertation, The University of Texas, Austin, Texas, USA. (December 2008).

Thomas, L., Dixon, T., and Pierson, R. (1983). Fractured reservoir simulation. *Old SPE Journal*, 23(1):42–54.

Vassenden, F., Holt, T., *et al.* (2000). Experimental foundation for relative permeability modeling of foam. *SPE Reservoir Evaluation & Engineering*, 3(02):179–185. SPE 62506-PA. http://dx.doi.org/10.2118/62506-PA.

Warren, J. and Root, P. (1963). The behavior of naturally fractured reservoirs. *Society of Petroleum Engineers Journal*, 3(3).

Wasan, D., Koczo, K., and Nikolov, A. (1994). Mechanisms of aqueous foam stability and antifoaming action with and without oil. In *Foams: Fundamentals and Applications in the Petroleum Industry*, volume 242 of *Advances in Chemistry*, pages 47–114. American Chemical Society.

Weng, X., Kresse, O., Cohen, C., Wu, R., and Gu, H. (2011). Modeling of hydraulic-fracture-network propagation in a naturally fractured formation. *SPE Production and Operations*, 26(4):368. SPE-140253-PA. http://dx.doi.org/10.2118/140253-PA.

Whitson, C. H. and Sunjerga, S. (2012). Pvt in liquid-rich shale reservoirs. In *SPE Annual Technical Conference and Exhibition*, San Antonio, Texas, USA. Society of Petroleum Engineers. SPE-155499-MS. http://dx.doi.org/10.2118/155499-MS.

Wu, K. and Olson, J. E. (2013). Investigation of the impact of fracture spacing and fluid properties for interfering simultaneously or sequentially generated hydraulic fractures. *SPE Production & Operations*, 28(04):427–436. SPE-163821-PA. http://dx.doi.org/10.2118/163821-PA.

Wu, K. and Olson, J. E. (2014). Mechanics analysis of interaction between hydraulic and natural fractures in shale reservoirs. In *SPE/AAPG/SEG Unconventional Resources Technology Conference*. Society of Petroleum Engineers. urtec-2014-1922946. http://dx.doi.org/10.15530/urtec-2014-1922946.

Xiance, Y., Guo, B., Ai, C., and Bu, Z. (2009). A comparison between multi-fractured horizontal and fishbone wells for development of low-permeability fields. In *Asia Pacific Oil and Gas Conference & Exhibition*, Jakarta, Indonesia. Society of Petroleum Engineers. SPE-120579-MS. http://dx.doi.org/10.2118/120579-MS.

Xu, Y. (2015). Implementation and Application of the Embedded Discrete Fracture Model (EDFM) for Reservoir Simulation in Fractured Reservoirs. Master's thesis, The University of Texas at Austin, Austin, Texas.

Xun, C. (2013). Development and application of horizontal well drilling technologies with liaohe oilfield's characteristics. In *IPTC 2013: International Petroleum Technology Conference*, Beijing, China. https://www.onepetro.org/conference-paper/IPTC-16900-MS.

Yamamoto, K., Shimamoto, T., and Sukemura, S. (2004). Multiple fracture propagation model for a three-dimensional hydraulic fracturing simulator. *International Journal of Geomechanics*, 4(1):46–57. http://dx.doi.org/10.1061/(ASCE)1532-3641(2004)4:1(46).

Yan, W., Miller, C. A., and Hirasaki, G. J. (2006). Foam sweep in fractures for enhanced oil recovery. *Colloids and Surfaces A: Physicochemical and Engineering Aspects*, 282:348–359.

Yanze, Y. and Clemens, T. (2012). The role of diffusion for nonequilibrium gas injection into a fractured reservoir. *SPE Reservoir Evaluation & Engineering*, 15(1).

Yu, H. (2012). *Transport and retention of surface-modified nanoparticles in sedimentary rocks*. PhD dissertation, The University of Texas, Austin, Texas, USA. https://repositories.lib.utexas.edu/handle/2152/22237.

Zhang, T. (2012). *Modeling of nanoparticle transport in porous media*. PhD dissertation, The University of Texas, Austin, Texas, USA. https://repositories.lib.utexas.edu/bitstream/handle/2152/ETD-UT-2012-08-6044/ZHANG-DISSERTATION.pdf.

Zhang, Y., Luo, P., and Huang, S.-S. (2010). Improved heavy oil recovery by CO_2 injection augmented with chemicals. In *International Oil and Gas Conference and Exhibition in China*.

Zhou, F., Shi, A., and Wang, X. (2014). An efficient finite difference model for multiphase flow in fractured reservoirs. *Petroleum Exploration and Development*, 41(2):262–266. http://dx.doi.org/10.1016/S1876-3804(14)60031-8.

Zhou, Z. and Rossen, W. (1995). Applying fractional-flow theory to foam processes at the ̈limiting capillary pressure. *SPE Advanced Technology Series*, 3(1):154–162.

Vita

Jose Sergio de Araujo Cavalcante Filho was born in Ladario, Mato Grosso do Sul, Brazil. He received the Bachelor of Science degree in Mechanical Engineering from the Federal University of Ceara in 2003. He was employed by Beicip-Franlab in December of 2005 as a Reservoir Modeling Specialist. He left Beicip-Franlab in July of 2006 and joined Petrobras as a Petroleum Engineer. In July of 2012 he applied to the University of Texas at Austin for enrollment in their Petroleum and Geosystem Engineering program. He was accepted and started his graduate studies in September, 2012.

Electronic mail address: jsergio@gmail.com

This dissertation was typeset with LaTeX[†] by the author.

[†]LaTeX is a document preparation system developed by Leslie Lamport as a special version of Donald Knuth's TeX Program.